



Universitat Autònoma de Barcelona

**ADVERTIMENT.** L'accés als continguts d'aquesta tesi queda condicionat a l'acceptació de les condicions d'ús establertes per la següent llicència Creative Commons:  [http://cat.creativecommons.org/?page\\_id=184](http://cat.creativecommons.org/?page_id=184)

**ADVERTENCIA.** El acceso a los contenidos de esta tesis queda condicionado a la aceptación de las condiciones de uso establecidas por la siguiente licencia Creative Commons:  <http://es.creativecommons.org/blog/licencias/>

**WARNING.** The access to the contents of this doctoral thesis it is limited to the acceptance of the use conditions set by the following Creative Commons license:  <https://creativecommons.org/licenses/?lang=en>



Universitat Autònoma  
de Barcelona

**Design, Synthesis and Applications of  
V-shaped  
Polycarboxylate *meta*-Carborane-Based  
Metal-Organic Frameworks**

**Lei Gan**

DOCTORAL THESIS

Ph. D. in Chemistry

Supervisor

**Dr. José Giner Planas**

Institut de Ciència de Materials de Barcelona (ICMAB)-CSIC

Departament de Química - Facultat de Ciències

**2020**



Thesis presented to aspire to the Doctorate in Chemistry degree by Lei Gan.

Dr. José Giner Planas

Tenured Scientist/Científico Titular

Consejo Superior de Investigaciones Científicas

INSTITUT DE CIÈNCIA DE MATERIALS DE BARCELONA-CSIC

Bellaterra, 20 de Julio de 2020







MINISTERIO  
DE ECONOMÍA  
Y COMPETITIVIDAD

El Doctor JOSÉ GINER PLANAS, Científico Titular del Consejo Superior de Investigaciones Científicas (CSIC) en el Instituto de Ciencia de Materiales de Barcelona (ICMAB),

CERTIFICA:

Que Lei Gan, licenciado en Química, ha realizado bajo su dirección la tesis doctoral titulada “**Design, Synthesis and Applications of V-shaped Polycarboxylate *meta*-Carborane-Based Metal-Organic Frameworks**” y que se recoge en esta memoria para optar al grado de Doctora en Química por la Universitat Autònoma de Barcelona.

Y para que así conste y tenga los efectos oportunos, firmo este certificado en Bellaterra, a 20 de Julio de 2020.

Dr. José Giner Planas

ICMAB-CSIC



This work has been financed by the Comisión Interministerial de Ciencia y Tecnología CICYT by the following projects CTQ2013-44670-R y CTQ2016-75150-R, and by the Generalitat de Catalunya (project 2014/SGR/149). L. Gan acknowledges the China Scholarship Council (CSC) for his PhD grant (201609110106). Some of the experiments were performed at the XALOC and NCD beamlines of the ALBA synchrotron with the support of ALBA staff.



The dissertation defense of the present work is scheduled for September 2020. The thesis Committee consists of the following members:

- President: Dr. Daniel Ruiz Molina, Institut Català de Nanociència i Nanotecnologia ICN2.
- Secretary: Dr. Ana Eva Platero Prats, Universidad Autónoma de Madrid.
- Chair: Dr. David Fairen Jimenez, University of Cambridge.

Committee substitutes:

- Substitute 1: Dr. Inmaculada Ratera Bastardas, Institut de Ciència de Materials de Barcelona-CSIC.
- Substitute 2: Dr. Jordi Cirera, Universitat de Barcelona.



*This thesis is dedicated to my parents.*





## Acknowledgement

I would like to take the opportunity to thank many people who have supported and contributed to my PhD study and this thesis. First, I would like to thank my supervisor Dr. José Giner Planas for providing me the opportunity to carry out research on carborane-based MOFs. Thanks for his enthusiastic and countless help and support to my research. Besides his careful and patient guidance in my study, his spirit of optimism and kindness has been deep infectious to me. During my four years in Spain, he has played a role like relatives and friends in my life and it makes me have precious memories of staying abroad.

I would also thank to Prof. Francesc Teixidor, Prof. Clara Viñas and Dr. Rosario Núñez for the support and help during my study in the research group, Inorganic Materials and Catalysis in ICMAB-CSIC. I am grateful to Prof. Francesc Teixidor, and Prof. Clara Viñas for helping me revise posters and papers many times. I am also grateful to Jordi Cortes for his support and his maintenance in the laboratory.

I also owe my thanks to Prof. Mark E. Light and Dr. Duane Choquesillo-Lazarte for their much-valued support related to single-crystal measurements and structure analysis. I would like to thank Eduardo Solano for the measurement of WAXS and SAXS experiments. I would also acknowledge Gantulga Norjmaa, Prof. Gregori Ujaque, and Prof. Hongliang Huang who performed the DFT calculations. I have to thank Julio Fraile for helping BET surface area measurements. I would like to acknowledge Eduardo Andrés-García and Guillermo Mínguez Espallargas from Universitat de València for the breakthrough experiments of gas mixtures. Then I would thank to Prof. Kyriakos C. Stylianou and Dr Arunraj Chidambaram for their strong help of the ABE separation and OPs adsorption.

Separate thanks to Prof. Jorge A. R. Navarro from Universidad de Granada for his allowing me to do experiments in his laboratory and his very kindness of providing guidance to my experiments.

Many thanks to my group members and friends: Dr. Isa Fuentes, Dr. Ines Bennour, Dr. Mahdi Chaari, Dr. Albert Ferrer-Ugalde, Dr. Zsolt Kelemen, Ana Begoña Buades, Miquel Nuez i Martínez, Joan Soldevila, Arpita Saha, Abhishek Saini, Isabel Guerrero Troyano, Sohini Sinha, Jewel Ann Maria Xavier, Fangchang Tan, Zhen Li, Dr Amirali Yazdi, Pol Gimeno Forquernié and Laura Hernández López for all the friendship and help during my PhD study.

Additionally, I would thank my country China and CSC grant to give me this opportunity and support me financially to study in Spain for 4 years. I would like to thank the support from ALBA Synchrotron Light Source to do SCXRD and WAXS/SAXS measurements. I would also like to thank all technicians from ICMAB and UAB who helped me do characterization measurements.

Moreover, I would thank my friends who also came from China to study in Spain: Teniger, Yajie Zhang, Yu Chen, HuanhuanSu, Yihua Chen and Ce Sun. Thank you for the accompany and encouragement. Also, special thanks to Dr Liuz for her support and help in the past years.

Finally, I must thank my parents for their support and encouragement especially respect for what I choose throughout my life.

The present PhD thesis has been carried out at the Laboratory of Inorganic Materials and Catalysis of the Materials Science Institute of Barcelona ICMAB (CSIC) following the doctoral program in Chemistry of the Autonomous University of Barcelona. According to the decision of the PhD commission, this Thesis is presented as a compendium of publications. Additionally, and with the idea of providing a more complete Thesis, some additional results obtained before the deposit of the present work and in process of publication are also included.

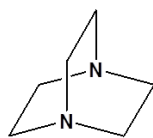
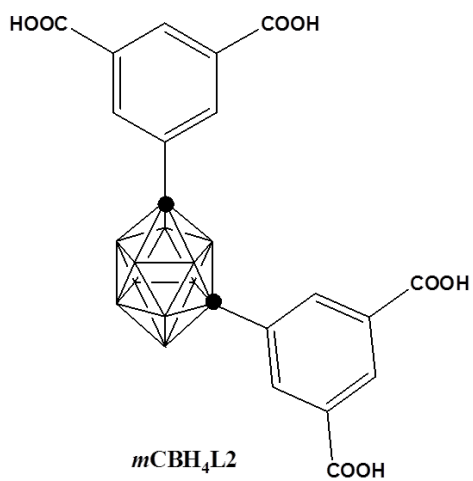
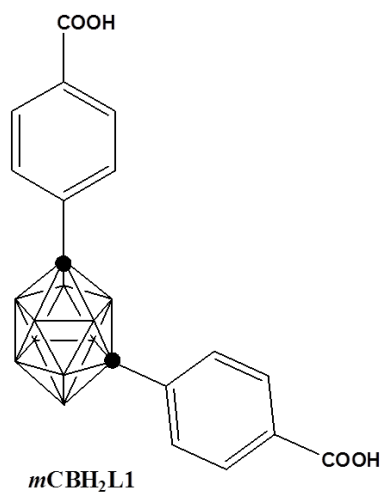
The publications accepted in the compendium are listed below in order of their appearance in the Thesis:

1) **L. Gan**, P. G. Fonquernie, M. E. Light, G. Norjmaa, G. Ujaque, D. Choquesillo-Lazarte, J. Fraile, F. Teixidor, C. Viñas and J. G. Planas, *Molecules* **2019**, *24*, 3204.

2) **L. Gan**, A. Chidambaram, P. G. Fonquernie, M. E. Light, D. Choquesillo-Lazarte, H. Huang, E. Solano, J. Fraile, C. Viñas, F. Teixidor, J. A. Navarro, K. Stylianou, J. G. Planas, *J. Am. Chem. Soc* **2020**, *142*, 8299-8311.



## Ligands used in this thesis



DABCO



## Compound List

Nomenclature	Formula
<b>1-DMF</b>	$[\text{Cu}_2(\text{mCB-L1})_2(\text{DMF})_2] \cdot 2\text{DMF} \cdot \text{H}_2\text{O}$
<b>1-DMA</b>	$[\text{Cu}_2(\text{mCB-L1})_2(\text{DMA})_2] \cdot \text{DMA} \cdot \text{H}_2\text{O}$
<b>1-MeOH</b>	$[\text{Cu}_2(\text{mCB-L1})_2(\text{MeOH})_2] \cdot 4\text{MeOH}$
<b>1'-MeOH-air</b>	$\text{Cu}_2(\text{mCB-L1})_2(\text{H}_2\text{O})(2\text{MeOH})$
<b>1'-CH<sub>2</sub>Cl<sub>2</sub>-air</b>	$\text{Cu}_2(\text{mCB-L1})_2(\text{H}_2\text{O})(\text{CH}_2\text{Cl}_2)$
<b>mCB-MOF-1</b>	$[\text{Cu}_2(\text{mCB-L1})_2(\text{DABCO})_{0.5}(\text{H}_2\text{O})] \cdot 2\text{DMF} \cdot 2\text{H}_2\text{O}$
<b>mCB-MOF-2</b>	$[\text{Zr}_6(\mu_3\text{-O})_4(\mu_3\text{-OH})_4(\text{OH})_4(\text{H}_2\text{O})_4(\text{mCB-L2})_2] \cdot 6\text{DMF} \cdot 3\text{H}_2\text{O}$





## Abbreviations

<b>1 or 2 or 3D</b>	1 or 2 or 3 dimensional
<b>MOFs</b>	metal-organic frameworks
<b>SBU</b>	Secondary building unit
<b>SC-SC</b>	single crystal to single crystal
<b><i>o</i>-carborane or <i>o</i>CB</b>	<i>ortho</i> -carborane
<b><i>m</i>-carborane or <i>m</i>CB</b>	<i>meta</i> -carborane
<b><i>p</i>-carborane or <i>p</i>CB</b>	<i>para</i> -carborane
<b>CB</b>	carborane
<b>Ph</b>	phenyl
<b><i>n</i>-BuLi</b>	<i>n</i> -butyl lithium
<b>EtOH</b>	ethanol
<b>CHCl<sub>3</sub></b>	chloroform
<b>CH<sub>2</sub>Cl<sub>2</sub></b>	dichloromethane
<b>C<sub>3</sub>H<sub>6</sub>O</b>	acetone
<b>MeOH</b>	methanol
<b>DMF</b>	dimethylformamide
<b>DMA</b>	dimethylacetamide
<b>THF</b>	tetrahydrofuran
<b>DABCO</b>	1,4-diazabicyclo[2.2.2]octane
<b>ATR-FTIR</b>	attenuated total reflectance fourier transform infrared spectroscopy
<b>BET</b>	Brunauer, Emmett and Teller

<b>DFT</b>	density functional theory
<b>GC</b>	gas chromatography
<b>WAXS</b>	wide-angle X-ray scattering
<b>SAXS</b>	small-angle X-ray scattering
<b>ICP</b>	inductively coupled plasma
<b>NMR</b>	nuclear magnetic resonance
<b>PXRD</b>	powder X-ray diffraction
<b>SCXRD</b>	single crystal X-ray diffraction
<b>SEM</b>	scanning electron microscopy
<b>TGA</b>	thermogravimetric analysis
<b>XRD</b>	X-ray diffraction
<b>UV-Vis</b>	ultra violet-visible
<b><math>\delta</math> (ppm)</b>	chemical shifts in parts per million

## Abstract

In this thesis, we present a study on the design and synthesis of V-shaped polycarboxylate *meta*-carborane-based linkers and the exploration of their resulting metal-organic frameworks (MOFs) with Cu or Zr clusters. These carborane-based MOFs show some properties such as extraordinary hydrolytic stability, as a result of the high hydrophobicity of the carborane moieties. Based on these properties, the first reported three-dimensional polycarboxylate *meta*-carborane-based MOFs exhibit good gas, liquid separation and capture of toxic phosphorous compound.

Chapter 1 gives a brief introduction on synthesis, properties of carboranes, and the most common functionalization routes. Then a history of MOF research, MOF synthesis and characterization, typical SBU design in carboxylate MOFs and carboxylate linker nature and *geometric mismatch* method for irregular structure design is introduced. Then it is given a brief description of potential applications and hydrolytic stability of MOFs. Finally, the chapter ends with a general account of reported carborane-based MOFs.

Chapter 2 states the general and specific objectives of this thesis based on polycarboxylate *meta*-carborane-based MOFs.

Chapter 3 describes a family of Cu-paddlewheel based coordination polymers constructed by a dicarboxylate *m*-carborane ligand ***mCB-H<sub>2</sub>L1***. All new compounds have been fully characterized and their structures are described. Chemical routes by MeOH and CH<sub>2</sub>Cl<sub>2</sub> exchange has been used to activate **1-DMF** and generate open metal sites (OMS). An unprecedented reversible phase transition has been observed on solvent exchange. Evidence is provided for the reversible process being the result of the formation/cleavage of weak but attractive B-H...Cu interactions by a combination of single-crystal (SCXRD), powder (PXRD) X-ray diffraction, Raman spectroscopy, and DFT calculations.

Chapter 4 describes a new 3D Cu-paddlewheel based MOF (***mCB-MOF-1***) constructed by mixed ligands ***mCB-H<sub>2</sub>L1*** and 1,4-diazabicyclo[2.2.2]octane (DABCO), that shows high hydrophobicity and water stability. The structure of ***mCB-MOF-1*** is a rare example of 5-connected (4<sup>4</sup>)(6<sup>6</sup>) topology (***sqp***) and represents the first example of such a topology in a Cu<sub>2</sub>-paddlewheel MOF. ***mCB-MOF-1*** exhibits excellent stability when immersed in organic solvents, water at 90 °C for at least two months, and acidic and basic aqueous solutions. The hydrolytic stability was examined by PXRD, N<sub>2</sub> adsorption, SEM and ICP measurements. ***mCB-MOF-1*** was studied for butanol recovery from the ABE (Acetone, Butanol, Ethanol) mixture in water (98%) by a combination of single-component adsorption experiments, IAST prediction, and breakthrough experiments, and compared with the hydrophobic MOF ZIF-8. GCMC simulation and DFT calculations are also performed to analyze the adsorption sites and interactions for both MOFs and to understand the influence of carborane in the ABE separation performance of ***mCB-MOF-1***.

Chapter 5 describes the CO<sub>2</sub>, CH<sub>4</sub>, N<sub>2</sub>, and H<sub>2</sub> adsorption and separation of the same hydrophobic MOF described in the previous chapter ***mCB-MOF-1***. Single-component gas adsorption experiments at various temperatures have been conducted. IAST selectivities of CO<sub>2</sub>/N<sub>2</sub> and CO<sub>2</sub>/CH<sub>4</sub> based on gas adsorption isotherms are calculated. The adsorption heat of gases has also been calculated to check their adsorption strength. Breakthrough experiments of CO<sub>2</sub>/N<sub>2</sub>, CO<sub>2</sub>/CH<sub>4</sub>, and C<sub>3</sub>H<sub>6</sub>/C<sub>3</sub>H<sub>8</sub> at 298 K are carried out in order to test the binary mixtures separation performance of ***mCB-MOF-1***. Finally, oil-water separations have also been tested by using a homemade device.

Chapter 6 describes the first 3D Zr<sub>6</sub> cluster based MOF constructed by a new tetracarboxylic acid *meta*-carborane ligand ***mCB-H<sub>4</sub>L2***. The new MOF (***mCB-MOF-2***) is a structural analogue of NU-1000 and contains typical hexagonal (1.2 nm) and triangular (0.8 nm) channels observed for the ***csq*** topology. Activated

***mCB-MOF-2'*** is porous and stable in both basic and strong acidic aqueous solutions as confirmed by PXRD and BET surface area measurements. Water sorption has also been investigated and shows a biporous system, with hydrophilic (triangular) and hydrophobic (hexagonal) pores. ***mCB-MOF-2'*** has been tested for the adsorptive removal of organophosphorus pesticides including Glyphosate (GP) and Glufosinate (GF). The new MOF shows a good recyclability and an overall performance for the capture of these pesticides. Organophosphorus nerve agents DIFP and DMNP are also tested for their catalytic degradation by ***mCB-MOF-2'***.



## Resumen

Este trabajo de Tesis está dedicado a la síntesis y diseño de ligandos V-shaped policarboxilato basados en la unidad *meta*-carborano y la exploración de las redes metal-órganicas (MOFs) de dichos ligandos con clústeres de Cu y Zr. Los MOFs basados en carborano presentan propiedades diversas, como es el caso de una extraordinaria hidrofobicidad que le confiere los fragmentos carborano. Motivados por estas propiedades, se presentan en esta tesis los primeros MOFs tridimensionales basados en policarboxilato derivados del *meta*-carborano y que presentan excelentes propiedades de separación, tanto de líquido como de gas y de captura de compuestos de fósforo tóxicos.

En el Capítulo 1, se hace una breve introducción sobre la síntesis y propiedades de los carboranos, así como las rutas de funcionalización más comunes. A continuación, se introduce una breve historia de la investigación en MOFs, las rutas sintéticas y caracterización, así como el diseño de estos materiales mediante SBU y ligandos carboxilato. Se introduce también muy brevemente el concepto de *desajuste geométrico* para el diseño de estructuras irregulares. El capítulo continúa con una breve descripción de posibles aplicaciones y la estabilidad hidrolítica de los MOFs. Finalmente, se exponen los MOFs basados en carborano, previos a esta tesis.

En el Capítulo 2, se introducen los objetivos generales y específicos de la presente tesis.

En el Capítulo 3, se describe la síntesis y caracterización de una familia de polímeros de coordinación basados en Cu-paddlewheel y un ligando dibarboxilato basado en *meta*-carborano **mCB-H<sub>2</sub>L1**. Los nuevos compuestos se han caracterizado completamente y se describen las estructuras cristalinas. Se han seguido rutas químicas para la activación de los polímeros y la generación de open metal sites (OMS), tales como el intercambio de DMF en **1-DMF** por MeOH y CH<sub>2</sub>Cl<sub>2</sub>. Se ha observado un cambio de fase reversible relacionado con la formación/ruptura de



interacciones débiles pero atractivas tipo B–H···Cu. Esto se ha dilucidado mediante la combinación de difracción de rayos X de cristal único, en polvo, espectroscopía de Raman y cálculos DFT.

En el Capítulo 4, se describe un nuevo MOF 3D basado en Cu-paddlewheel (**mCB-MOF-1**), construido por los ligandos **mCB-H<sub>2</sub>L1** y 1,4-diazabicyclo[2.2.2]octano (DABCO). Este nuevo MOF presenta una gran hidrofobicidad y estabilidad en agua. La estructura de **mCB-MOF-1** presenta un raro ejemplo de topología 5-connected (4<sup>4</sup>)(6<sup>6</sup>) (**sqp**), siendo la primera de este tipo en un MOF basado en Cu-paddlewheel. **mCB-MOF-1** muestra una excelente estabilidad en disolventes orgánicos, agua a 90°C durante al menos dos meses, así como en disoluciones acuosas ácidas y básicas. La estabilidad hidrolítica se ha examinado mediante medidas de difracción en polvo, adsorción de N<sub>2</sub>, SEM e ICP. Se ha estudiado además la separación de mezclas de ABE (Acetona, Butanol, Etanol) en agua (98%) mediante una combinación de experimentos: adsorción de un solo componente, predicciones IAST y experimentos de ruptura. Todos estos experimentos se han realizado también en el MOF ZIF-8. Se han realizado además simulaciones GCMC y cálculos DFT para analizar los posibles puntos de adsorción y las interacciones con ambos MOFs y así tratar de entender la influencia de las unidades carborano en la separación de ABE mediante **mCB-MOF-1**.

En el Capítulo 5, se describe la adsorción y separación de gases tales como CO<sub>2</sub>, CH<sub>4</sub>, N<sub>2</sub>, e H<sub>2</sub> mediante el mismo MOF hidrófobo **mCB-MOF-1**, descrito en el capítulo anterior. Se han realizado medidas de adsorción de un solo componente a varias temperaturas. Se han determinado los calores de adsorción de los gases y se han realizado experimentos de ruptura de mezclas CO<sub>2</sub>/N<sub>2</sub>, CO<sub>2</sub>/CH<sub>4</sub>, y C<sub>3</sub>H<sub>6</sub>/C<sub>3</sub>H<sub>8</sub> at 298 K con el fin de evaluar la separación de dichas mezclas binarias. Finalmente se han realizado separaciones aceite-agua mediante un dispositivo casero.

En el Capítulo 6, se describe el primer ejemplo de un MOF 3D construido con un clúster Zr<sub>6</sub> y un nuevo ligando tetracarboxylato **mCB-H<sub>4</sub>L2**. El nuevo MOF

**(mCB-MOF-2)** presenta una estructura análoga a la del MOF NU-1000, que contiene poros hexagonales (1.2 nm) y triangulares (0.8 nm) y una topología **csq**. Una vez activado **mCB-MOF-2'**, se ha estudiado la eliminación de pesticidas organofosforados, tales como Glifosato (GP) y Glufosinato (GF), mediante captura de los mismos en agua. El nuevo MOF presenta una buena reciclabilidad y respuesta a la captura de estos pesticidas. Se ha estudiado también la degradación catalítica de agentes nerviosos organofosforados mediante **mCB-MOF-2'**.



## Table of Content

<b>Chapter 1 Introduction .....</b>	<b>1</b>
1.1 Carboranes.....	1
1.1.1 Synthesis and Properties.....	2
1.1.2 Functionalization.....	6
1.2 Metal-Organic Frameworks (MOFs).....	8
1.2.1 Synthesis and Characterization .....	10
1.2.2 Linker and SBU design .....	11
1.2.3 Potential Applications and Hydrolytic Stability .....	15
1.3 Carborane-Based Metal-Organic Frameworks .....	19
1.4 References .....	26
<b>Chapter 2 Objectives.....</b>	<b>31</b>
<b>Chapter 3 A Reversible Phase Transition of 2D Coordination Layers by B–H•••Cu(II) Interactions in a Coordination Polymer .....</b>	<b>35</b>
3.1 Introduction .....	37
3.2 Results and Discussion.....	40
3.3 Conclusions .....	55
3.4 Experimental Section .....	56
3.4.1 Characterization and Methods.....	56
3.4.2 Materials.....	57
3.4.3 Crystallography .....	59
3.4.4 Computational Details.....	60
3.5 References .....	62
<b>Chapter 4 A Highly Water-Stable meta-Carborane-Based Copper Metal-Organic Framework for Efficient High-Temperature Butanol Separation.....</b>	<b>67</b>
4.1 Introduction .....	69
4.2 Results and Discussion.....	73
4.2.1 Crystal Structure and Characterization.....	73
4.2.2 Hydrolytic Stability and Hydrophobicity .....	78
4.2.3 Butanol Separation .....	83
4.3 Conclusions .....	90
4.4 Experimental Section .....	91
4.4.1 Characterization and Methods.....	91
4.4.2 Materials.....	93
4.4.3 Hydrothermal Stability Tests.....	94
4.4.4 Breakthrough Experiments.....	94
4.4.5 NMR Experiments.....	95
4.4.6 Adsorbate Location .....	95
4.4.7 Binding Energy Calculation .....	95
4.5 References .....	97

<b>Chapter 5 Selective Adsorptive Separation of Gases and Efficient Oil-Water Separation by a Hydrophobic Carborane-Based Metal-Organic Framework .....</b>	<b>101</b>
5.1 Introduction .....	103
5.2 Results and Discussion .....	104
5.2.1 Adsorption Isotherms of CO <sub>2</sub> , CH <sub>4</sub> , H <sub>2</sub> and N <sub>2</sub> on mCB-MOF-1 .....	105
5.2.2 IAST Predicted Adsorption Selectivities of CO <sub>2</sub> /N <sub>2</sub> and CO <sub>2</sub> /CH <sub>4</sub> on mCB-MOF-1 .....	108
5.2.3 Isosteric Heat of Adsorption .....	110
5.2.4 Breakthrough Experiments of Binary CO <sub>2</sub> /N <sub>2</sub> , CO <sub>2</sub> /CH <sub>4</sub> , and C <sub>3</sub> H <sub>8</sub> /C <sub>3</sub> H <sub>6</sub> Gas Mixtures on mCB-MOF-1 .....	111
5.2.5 Oil-water Separation .....	117
5.3 Conclusions .....	119
5.4 Experimental Section .....	120
5.4.1 Characterization and Methods .....	120
5.4.2 Materials .....	120
5.4.3 Breakthrough Experiments .....	121
5.5 References .....	122
<b>Chapter 6 Highly Efficient Adsorptive Removal of Toxic Organophosphorus Compounds by a New Carborane-Based Zirconium Metal-Organic Framework .....</b>	<b>125</b>
6.1 Introduction .....	127
6.2 Results and Discussion .....	129
6.2.1 Synthesis and Characterization .....	129
6.2.2 Water Adsorption .....	134
6.2.3 Removal of Organophosphorus Pesticides .....	137
6.2.4 Catalytic Hydrolysis of Organophosphorus Nerve Agent Simulants .....	143
6.3 Conclusions .....	148
6.4 Experimental Section .....	149
6.4.1 Characterization and Methods .....	149
6.4.2 Materials .....	150
6.4.3 Pesticides Adsorption Experiments .....	153
6.4.4 Organophosphorus Nerve Agent Simulants Degradation Experiments .....	153
6.5 References .....	155
<b>Supporting Information .....</b>	<b>159</b>
Supporting Information for Chapter 3 .....	161
Supporting Information for Chapter 4 .....	165
Supporting Information for Chapter 5 .....	179
Supporting Information for Chapter 6 .....	183
<b>General Conclusions .....</b>	<b>187</b>
<b>List of Publications .....</b>	<b>193</b>

# Chapter 1

---

## *Introduction*



## 1.1 Carboranes

Carboranes (“carbaboranes” in the formal nomenclature) are electron-delocalized clusters composed of boron, carbon and hydrogen atoms that may also contain other metallic and nonmetallic elements in the cluster framework [1]. These clusters are polyhedra or fragments of polyhedra, and can be classified as *closo*, *nido*, *arachno*, *hypho* structures based on whether the structure is a complete (*closo*) polyhedron, or a polyhedron that is missing one (*nido*), two (*arachno*) or three (*hypho*) vertices. Carboranes are a notable example of heteroboranes.

As early as 1923, carboranes had been present in some  $C_xB_yH_z$  products generated by experimentalists such as the great pioneer of boron hydride chemist, Alfred Stock. Afterwards carboranes had been envisioned by William Lipscomb, Roald Hoffmann, and others [1,2] from theoretical considerations before reports of the synthesis of any such compounds appeared. In 1995, Longuet-Higgins and coworkers calculated that two additional electrons would be required, stabilizing the icosahedron as a  $[B_{12}H_{12}]^{2-}$  dianion [3]. Then,  $[B_{12}H_{12}]^{2-}$  salts were isolated by Pitochelli and Hawthorne [4] and found to be incredibly stable, withstanding temperatures above 800 °C and exhibiting inertness toward most reagents. Its discovery strongly implied the viability of neutral  $C_2B_{10}H_{12}$  clusters, isoelectronic analogues of  $[B_{12}H_{12}]^{2-}$  in which two BH units are formally replaced by CH groups whose carbon atoms would be six-coordinate. The three well-known isomers of icosahedral charge-neutral *closo*-carboranes are *ortho*-, *meta*-, and *para*-carborane (respectively 1,2-, 1,7-, 1,12-  $C_2B_{10}H_{12}$ ) (Figure 1-1) which are particularly stable and are commercially available [5]. Since their discovery, carboranes have been found a wide range of applications, including luminescence materials, coordination polymers, medicine, liquid crystals or nanoscience, among others [6-9].



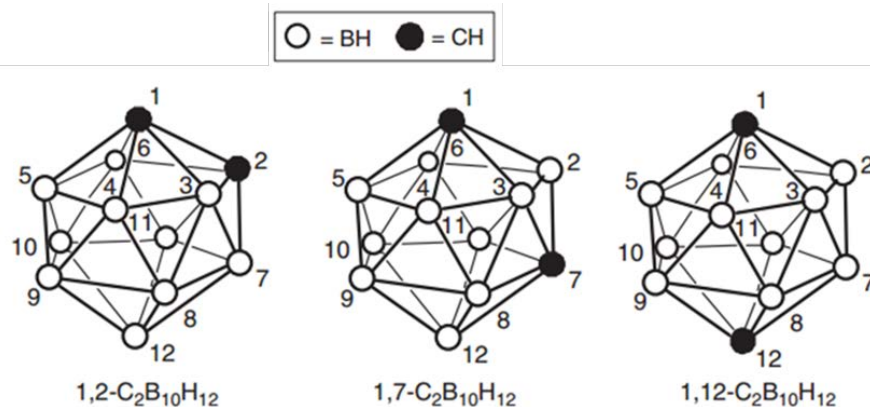
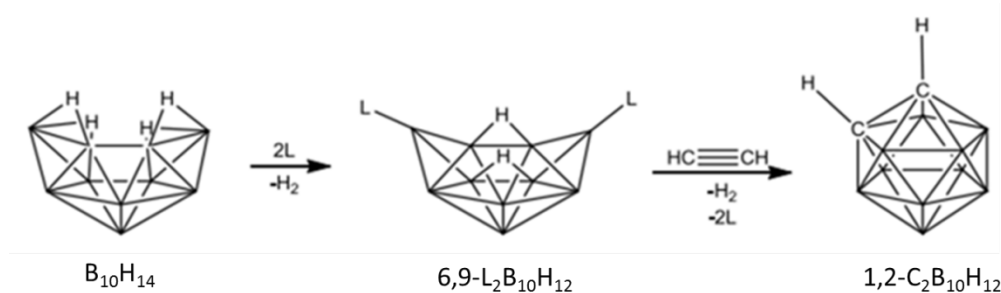


**Figure 1-1.** Structures and cage numbering for icosahedral carboranes( $C_2B_{10}H_{12}$ ), empty or black circles represent BH or CH, respectively.

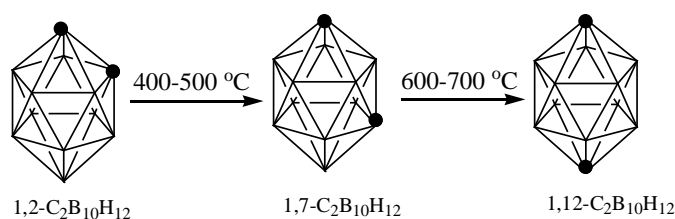
### 1.1.1 Synthesis and Properties

In late 1957, an extraordinarily stable compound characterized as 1, 2-  $C_2B_{10}H_{12}$ , had been isolated at the Reaction Motors Division of Thiokol Chemical Corporation from the reaction of  $B_{10}H_{14}$  derivatives with acetylene [10]. The original work on the icosahedral  $C_2B_{10}H_{12}$  carboranes was published in 1963 in a series of papers from the groups at Thiokol [11-15] and Olin-Mathieson [16-21]. The *o*-carborane was prepared by the addition of acetylenes to decaborane. Modern syntheses involve two stages, the first involving generation of an adduct of decaborane, the alkyne is then installed as the source of two carbon vertices in a second stage (Scheme 1-1). The two remaining isomers, 1, 7- and 1,12- $C_2B_{10}H_{12}$  (*m*- and *p*-carborane, respectively) were prepared by thermal cage-rearrangement of *o*-carborane (Scheme 1-2). When thermal isomerization from 1,2-  $C_2B_{10}H_{12}$  is conducted in vacuum atmosphere, nearly quantitative yields of *m*-carborane are obtained in 24-48 h; more rapid conversion time is achieved, in 98% yield, in a flow reactor at 600 °C [22]. During practical synthesis, the isomerization is accompanied by formation of bis(*m*-carboranyl), [(1,7- $C_2B_{10}H_{11}$ )<sub>2</sub>] isomers in the closed system [23]. For 1, 12- $C_2B_{10}H_{12}$ , the thermal rearrangement of *m*- to *p*-carborane takes place above 600 °C with some decomposition to intractable products. Continuous passage of *o*-carborane vapor in an

$\text{N}_2$  atmosphere through a heated tube at  $623\text{ }^\circ\text{C}$  affords *p*-carborane in ca. 25% yield along with ca. 75% *m*-carborane; separation of the isomers is achieved on basic alumina [22,24]. The latter synthetic and purification procedure make the price of *p*-carborane highly prohibitive, compared with their less symmetric isomers. The following are representative prices for the three isomers from US based companies at the time that this thesis was written: *o*-carborane, 75 \$/g; *m*-carborane, 150 \$/g and *p*-carborane, 895 \$/g.



**Scheme 1-1.** The synthesis procedure of *o*-carborane from  $\text{B}_{10}\text{H}_{14}$ .



**Scheme 1-2.** The transformation from *o*-carborane to *m*- and *p*-carborane.

As a key factor, the geometric nature of the boron atoms (Table 1-1) determines the carborane isomers properties [25]. As it can be seen in Table 1-1, the *o*- and *m*-carboranes have  $\text{C}_{2v}$  symmetry, while *p*-carborane has  $\text{D}_{5d}$  symmetry. The C-C bond distances range from  $1.62\text{ \AA}$  to  $3.06\text{ \AA}$  in these three isomers. Changes in the C-C distance also influence H-C-C-H angle. Thus, *ortho*-carborane shows ca.  $52^\circ$  calculated from crystal structure data [25], *meta*-carborane shows ca.  $115^\circ$  obtained from crystal structure data, neglecting a slight distortion [25], and *para*-carborane shows  $180^\circ$  obtained from crystal structure data [25]. The icosahedral shape measure ( $\text{S}_{\text{IC}}$ ) values (the higher the value, the greater the deviation from an ideal icosahedron)

## Introduction

shows the greatest deviation for *para*-carborane. The steric bulk of the carborane isomers can be demonstrated by comparing the van der Waals volume of 148, 143, and 141 Å<sup>3</sup> for *ortho*-, *meta*-, and *para*-carborane, with that of adamantane (136 Å<sup>3</sup>) and benzene (79 Å<sup>3</sup>) (Figure 1-2).

**Table 1-1.** Summary of geometric parameters of carboranes.

	<i>o</i> -carborane	<i>m</i> -carborane	<i>p</i> -carborane
symmetry	C <sub>2v</sub>	C <sub>2v</sub>	D <sub>5d</sub>
C-C distance (Å)	1.62	2.61	3.06
H-C-C-H angle (°)	52	115	180
S <sub>IC</sub> <sup>i</sup>	0.1	0.1	0.13
V <sub>vdW</sub> <sup>ii</sup> (Å <sup>3</sup> )	148	143	141

<sup>i</sup> icosahedral shape measure (see text for description). <sup>ii</sup> Van der Waals volume.

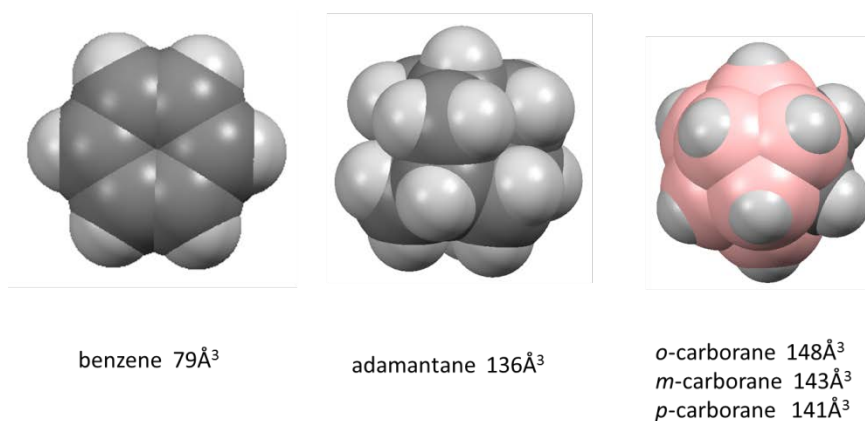


**Figure 1-2.** The comparison of van der Waals volume for carboranes, benzene and adamantine.

In carborane clusters, carbon and boron atoms adopt a six-bonded environment with five bonds to the cluster atoms and one exohedral bond to a hydrogen atom as a result of the low total electron count (26 skeletal electrons for 12 vertices). The delocalized electron density of the carborane isomers is not uniform and gives rise to differences in the electronic effects of the cluster on an exohedral substituent located on the carbon or boron atoms [26]. The presence of two different types of atoms in the cage and the icosahedral geometry of it, result in a large dipole moment of the *ortho*-carborane (4.53 D) and a significant dipole moment of the *meta*-carborane (2.85 D) compared to that of *para*-carborane (0 D). This unusual anisotropy is also manifested

in the anisotropy of the chemical properties of carborane derivatives [27]. Due to the higher electronegativity, the carbon atoms of carboranes are usually regarded as “electron withdrawing” [28,29], however, the boron atoms of the cluster are strongly electron donating [25,30]. This unusual electronic structure is often highlighted by regarding carboranes as inorganic three-dimensional “aromatic” analogs of arenes [31]. Stability, rigidity, tunable steric bulk, and electronic properties of carboranes make them a highly attractive organomimetic inorganic substituent platform [7,32,33]. The carboranes’ structures show a spherical shape of only slightly polarized H atoms. The presence of the hydride-like hydrogens at the B-H vertexes makes the clusters extremely hydrophobic. The hydrophobicity of carboranes increases in the order *ortho-* < *meta-* < *para-*carborane [34]. C-substituted compounds were most hydrophobic and even more hydrophobic than adamantane, while attachment of substituents to one of the boron atoms resulted in lower hydrophobicity than adamantane [35]. This interesting observation shows that the final hydrophobicity of the carborane compounds can be tuned not only by the choice of carborane isomer but also by choice of the vertex position for substitution in the cage.

Due to non-uniform electron distribution and different electronegativity of carbon and boron atoms, the protons attached to carbon atoms are relatively acidic. Two methods have been applied to determine the  $pK_a$  values of the cluster isomers. As shown in Table 1-2, two sets of  $pK_a$  values reveal the same trends of acidity of the CH vertices in carboranes in the order of *ortho-* > *meta-* > *para-*carborane. Since the  $pK_a$  values correlate with the inductive effects of the isomers, substituents at either the boron or the carbon atoms and the electronic nature of such substituents influence its acidity. For example, in clusters of halogen-substituted boron atoms, the acidity increases drastically. However, methyl group-substituted would decrease the acidity of the CH protons.

**Table 1-2.**  $pK_a$  values of CH vertices in carborane isomers

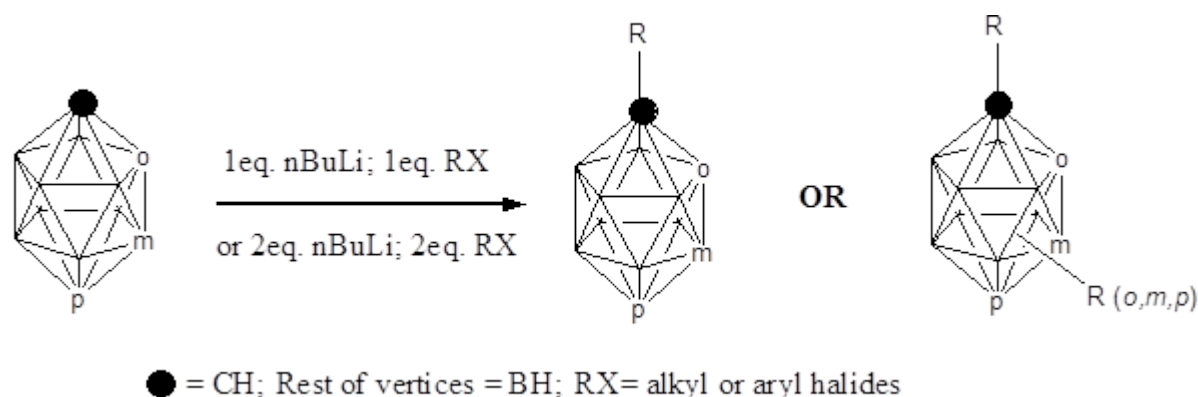
$pK_a$	<i>o</i> -carborane	<i>m</i> -carborane	<i>p</i> -carborane
<b>Streitwieser’s scale</b>	<b>23</b>	<b>28</b>	<b>30</b>

### **1.1.2 Functionalization**

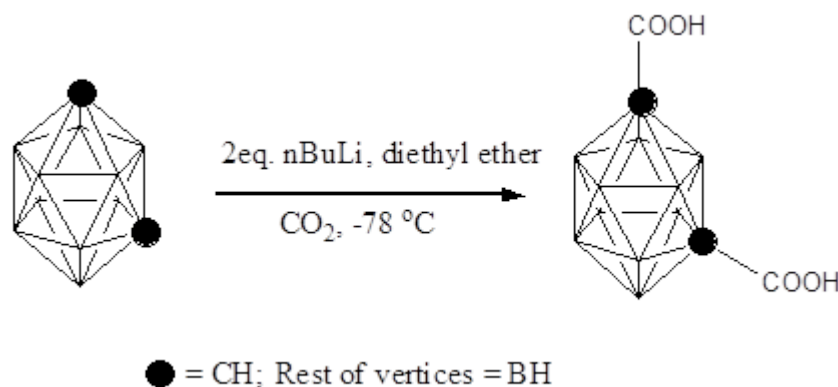
To date many of the standard methods have been described for derivatizing *ortho*-carborane by introducing substituents at the carbon and boron atoms, which are also applicable to *meta*- and *para*-carborane. However, there are clear differences between isomers. Compared with *ortho*-carborane, the lower polarity and the weaker inductive (*-I*) electron attraction in the *meta* and *para*-carborane, leads to reduced C-H acidity and lower reactivity toward metallation at carbon atoms in those isomers. The diminished *-I* effect in *m*- versus *o*-carborane is supported by measurement of the polarographic reduction potentials of many derivatives, which demonstrates the *m*- and *p*-carboranyl species are more difficult to reduce. In the following we will briefly outline the most common functionalization methods with some emphasis in carbon functionalization, which is the method used in the present thesis work.

The general synthetic route for substitution at the carbon atoms is showed as Scheme 1-3. Reactions are usually carried out in common organic solvents such as *n*-pentane, *n*-hexane, toluene, diethyl ether, dimethoxyethane, THF, etc. The acidic CH protons are removed with a base creating a carbaboranyl nucleophile. This nucleophile reacts with various electrophiles to form substituted derivatives. Although moderate bases can deprotonate carboranes, the strong lithium base *n*-butyllithium emerged as standard base for the reactions [36]. The property of moisture sensitive bases requires inert conditions, so anhydrous and anaerobic experiments are needed. During the reactions, the lithiated carborane precipitates from the reaction solution in a short time depending on the solvent. Most electrophiles used are halides, which result in formation of the corresponding lithium salts, that can be easily eliminated in the work up. The products are usually air-stable compounds and allow further purification and storage in air directly. The purification of carborane derivative is mostly based on column chromatography. Lithiation of carboranes is quantitative which suggests that

the yield of the reaction strongly depends on the electrophile. One example of carbon functionalization is the syntheses of carboxylic acid derivatives in Scheme 1-4. Such dicarboxylic derivative of *m*-carborane can be made quantitatively upon addition of the dilithium salt of the carborane to a slurry of dry ice or to CO<sub>2</sub> gas bubbled into the reaction, for 1h. The obtained dicarboxylic derivative is however not thermally stable and it does decarboxylates at 70 °C [37], which prevent its use as ligand in solvothermal reactions.



**Scheme 1-3.** General synthetic procedure for mono-substitution and di-substitution.

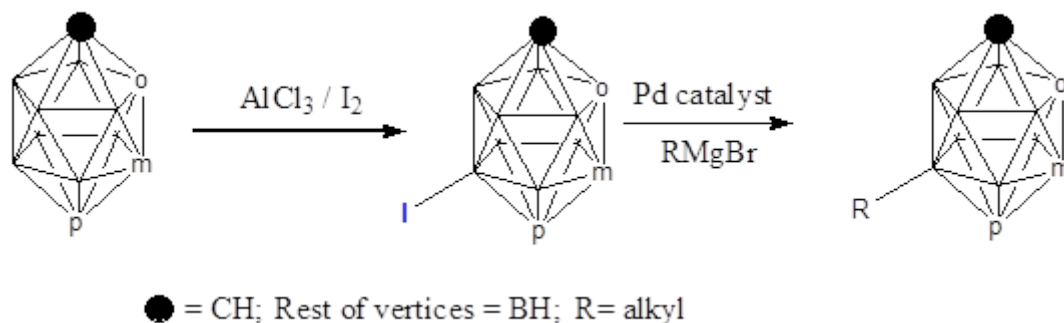


**Scheme 1-4.** Synthetic procedure for *meta*-carborane dicarboxylic acid.

Reactions at the boron atoms are generally different to those at the carbon atoms. Nucleophilic substitution reactions occur at the C-H vertices while electrophilic substitution reactions at the BH vertices. Compared to functionalization of the C-H

## Introduction

vertices, selective modification of ten B-H vertices is more difficult. The substitution reactions strongly depend on both the carborane isomer and the substituents to be added. B9/12 atoms (Figure 1-1) are easier to substitute than B3/6 atoms, which are less reactive. A comprehensive summary would exceed the capacity of this thesis, so we will only describe the important mono-substitution reactions at B9 atoms. As illustrated in Scheme 1-5, mild electrophilic aromatic substituents can be done to the selected boron vertices by using halides and  $\text{AlCl}_3$ . The boron halides can be further replaced by other residues in the presence of a catalyst such as a palladium catalyst. Our group has nicely summarized the methods to produce B-C, B-P, B-N and B-S bonds in boron clusters [38].

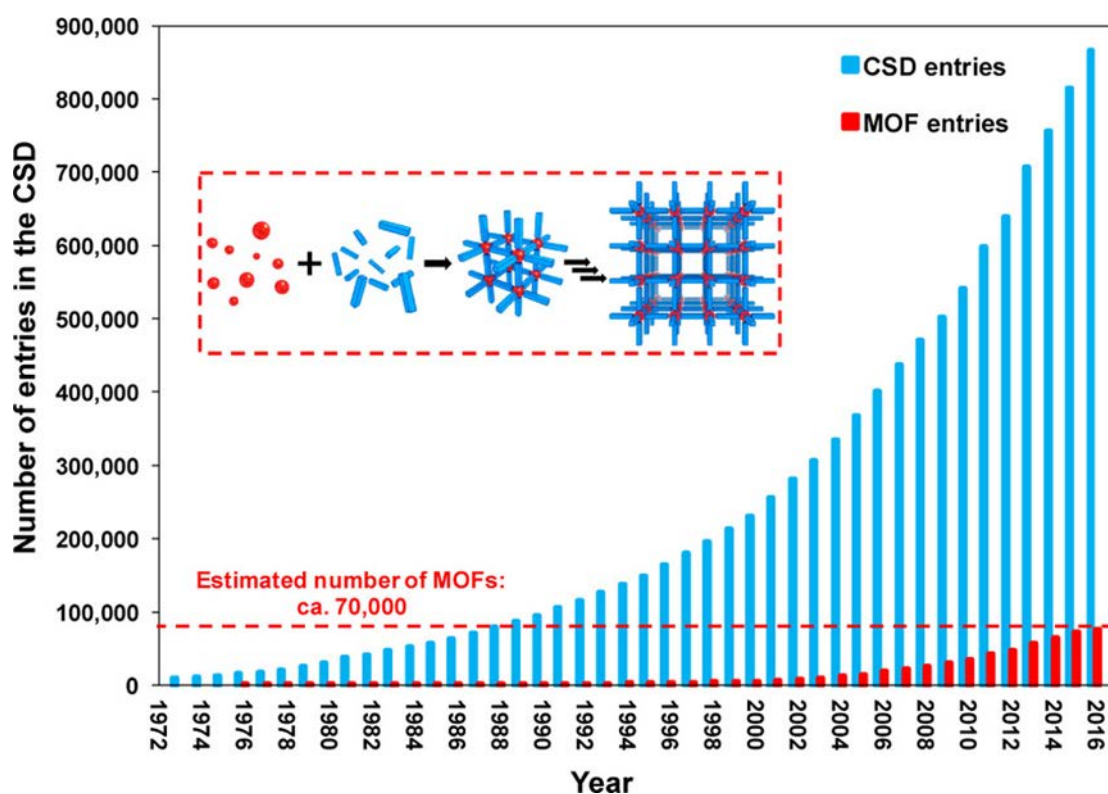


Scheme 1-5. B9-Substituted reactions.

## 1.2 Metal-Organic Frameworks (MOFs)

Metal-organic frameworks (MOFs), also known as coordination polymers (CPs), are porous crystalline materials that consist of metal ions or metal-containing inorganic clusters (usually called as secondary building units, SBUs) connected to multidentate organic ligands via metal coordination bonds. In 2013, IUPAC (The International Union for Pure and Applied Chemistry) recommended the definition of a metal-organic framework (MOF) as “a coordination network with organic ligands containing potential voids” [39]. The history of MOFs can be traced back to 1965,

when Tomic synthesized coordination polymers by carboxylic acid linkers and metals  $M^{n+}$  ( $n=2, 3, \text{ or } 4$ ) [40]. The thermal stabilities of the coordination polymers were studied and found to be dependent on the metals and linkers, which was the beginning to understand the properties of MOF materials. In 1990, a pioneering work was made by Hoskins and Robson, in which a wide range of scaffold-like materials with infinite 3D networks were synthesized and they predicted these materials with large empty cavities could be applied to molecular sieving, ion exchange, and catalysis [41]. Later, Yaghi and coworkers synthesized a crystalline and 3D framework material by hydrothermal synthesis, which then was firstly named the term metal-organic framework (MOF) [42]. In 1999, Yaghi and coworkers reported the first framework with permanent porosity after guest molecules removal, MOF-5 [43]. Soon after, G. Ferey and coworkers synthesized a stable MOF with large pores and high BET surface area guided by computational predictions and rational design [44]. Today there are more than 70 000 MOFs which have been reported according to the Cambridge Structural Database (CSD) (Figure 1-3) [45] and the numbers are continuously increasing from a variety of metal nodes or metal clusters and organic ligands or linkers.





## Introduction

**Figure 1-3.** Growth of the CSD and MOF entries since 1972. The inset shows the MOF self-assembly process from building blocks: metals (red spheres) and organic ligands (blue struts). Reprinted with permission from reference[45]. Copyright (2017) American Chemical Society.

### 1.2.1 Synthesis and Characterization

So far, MOFs have been generally synthesized via hydrothermal or solvothermal synthesis methods by electrical heating in small scales, which take reaction time from several hours to days. Efforts were primarily given to prepare high quality single crystals adequate for X-ray structural analysis in dilute liquid phase conditions. Alternative synthesis methods were attempted afterward in an effort to shorten the reaction times and to produce smaller and uniform products. Those include microwave-assisted [46-48], sonochemical [49-51], electrochemical [52,53], and mechanochemical [54-57] methods (Figure 1-4). There are alternative methods for introducing functional groups into prepared MOFs. Postsynthetic methods have been used to achieve the chemical modification of many organic and inorganic materials. That is, chemical modification can be performed on the fabricated material, rather than on the molecule precursors [58-60].

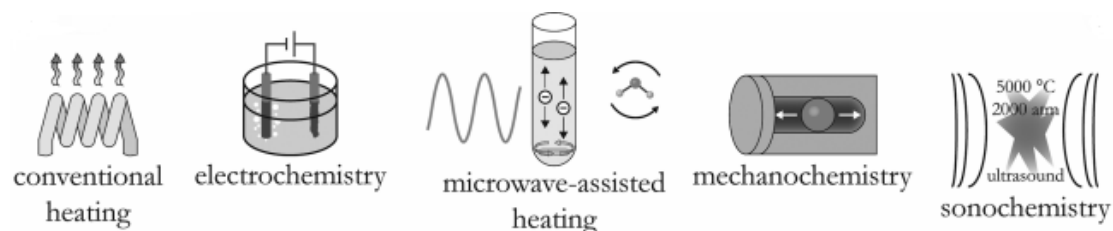


**Figure 1-4.** Summary of synthetic methods for MOF construction. Reprinted with permission from reference[61]. Copyright (2011) American Chemical Society.

For MOF characterization, single crystal X-ray diffraction (XRD) is used for obtaining exact structural information. Powder X-ray diffraction is used for checking crystallinity and phase purity of the materials. Nitrogen adsorption/desorption isotherms are used for texture properties and calculating surface area and porous

information. Other characterization techniques may include thermogravimetric analysis (TGA) for determining the MOF thermal stability, Fourier transform infrared (FTIR) for confirming active functional groups in the MOF, and scanning electron microscopy (SEM) for measuring crystal size and morphology. Usually these characterization techniques are used together for comprehensive understanding structural and porous information of the framework.

### **1.2.2 Linker and SBU design**

As previously mentioned, the construction of MOF involves the selection of inorganic and organic building units, commonly referred to as SBUs and linkers, respectively. The structural and chemical features of organic ligands will strongly affect the properties and potential applications of the resulting MOFs. According to the type of coordinating functional group, organic ligands are summarized into several representative categories as shown in Figure 1-5. Among these ligands, N-donor organic linkers and carboxylate-based ligands represent the most studied in MOF areas. In the mid-1990s, MOFs were constructed by using metal ions and di-, tri-, and poly-topic N-bound organic linkers such as 4, 4'-bipyridine [62,63]. However, compared to these neutral N-donor organic ligands, charged chelating linkers with binding groups such as carboxylate-based linkers are better choices for the formation of more rigid and diverse frameworks. Carboxylate groups favor the preparation of various polynuclear SBUs which provide directionality and endow the resulting multifunctional MOFs. In the present thesis, we will concentrate on carboxylate-based MOFs.

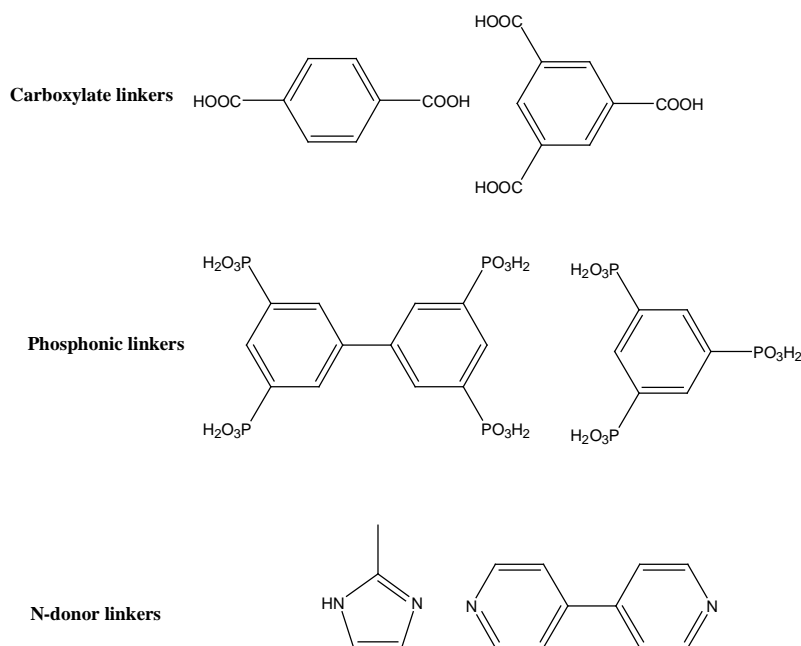
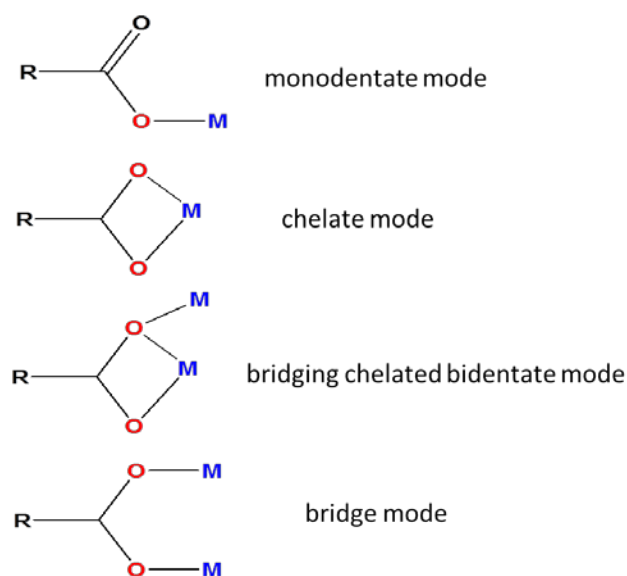


**Figure 1-5.** Representative categories of linkers used in MOFs.

There are several advantages for carboxylate-based linkers over neutral N-donor linkers: (i) the negative charged carboxylates neutralize the positive charged metal nodes, thus resulting in the formation of neutral structures without counter ions; (ii) the chelating nature of carboxylates allows for more rigidity and directionality of MOF structures; (iii) the metal ions are locked into polynuclear polyhedron by the carboxylate linkers which makes the resulting SBUs more rigid than the inorganic nodes with one metal ion; (iv) the abundance of SBUs and the multiple possible binding modes between carboxylates and metal ions provide the higher diversity of MOFs. Possible binding modes for carboxylate-based linkers are shown in Scheme 1-6.



**Scheme 1-6.** The possible binding modes for carboxylate-based linkers.

In addition to the carboxylate linkers, SBUs have to be taken also into consideration. Regarding SBUs formation, there are two methods. One is the *in-situ* preparation of the SBU, which is generated in the reaction mixture. This method is very easy and rapid for MOF construction and most MOFs have been synthesized by this way. However, the MOF reaction is dynamic, and different SBUs can be obtained from the same metal and linker combination. The second method involves the preformation of SBUs which is more predicable for MOF design. Ferey and coworkers reported that UiO-66 and its derivatives could also be synthesized by a prebuilt Zr cluster  $Zr_6O_4(OH)_4(OMc)_{12}$  ( $OMc$  = methacrylate) besides the conventional direct  $ZrCl_4$  addition [64]. Jin and coworkers demonstrated that the prebuilt Cu cluster  $Cu_2(ba)_4(MeOH)_2$  ( $ba$  = benzoic acid) could be used for the construction of a series of isostructural MOFs [65]. Therefore SBUs are crucial to the design of directionality for MOFs and to the accomplishment of robust structures. Some of the most common carboxylate-based SBUs are shown in Figure 1-6. Among these SBUs, the most common 4-connected SBU in MOFs is the dinuclear paddle-wheel cluster  $M_2(COO)_4$  ( $M = Zn^{2+}, Cu^{2+}, Co^{2+}$ ). In this SBU, two metal atoms are coordinated to four carboxylate and two terminal ligands in a square-pyramidal fashion. The

## Introduction

representative example of carboxylate-based MOF is HKUST-1 which consists of BTC linker and Cu paddle-wheel SBU. Additionally, the most frequently encountered SBU in Zr-MOFs is  $Zr_6O_8$ -core cluster. In this SBU, six Zr atoms are arranged at the vertices of an octahedron with  $u_3\text{-O}/u_3\text{-OH}$  capping the faces of the octahedron, the edges of the octahedron are capped by carboxylates and the Zr atoms from the equatorial edges may be capped by  $-\text{OH}$  or  $\text{H}_2\text{O}$ . According to different connectivity with carboxylate linkers, the common reported Zr-SBUs are 8-connected and 12 connected clusters in Zr-MOFs, which are found in NU-1000 and UiO-66, respectively.

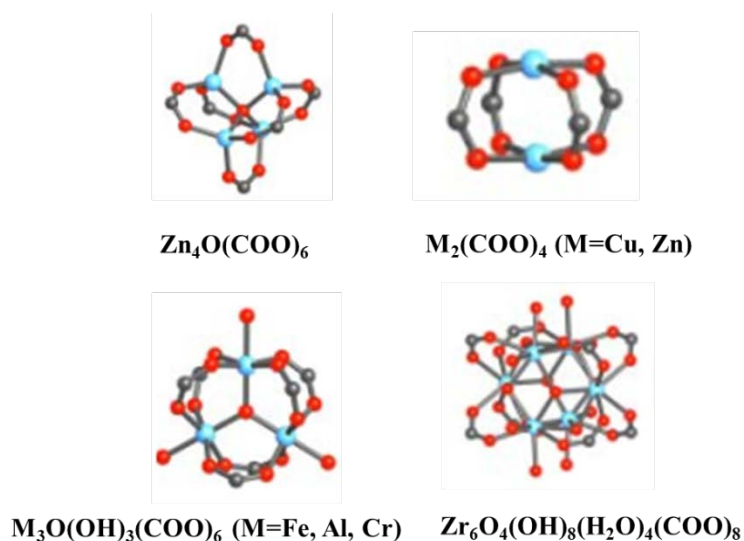


**Figure 1-6.** Some representative SBUs in carboxylate-based MOFs.

Regarding the carboxylate linker design, most efforts are focused on joining together compatible building blocks to form MOFs of predictable structures and topologies. Thus, the above mentioned SBUs are usually combined with symmetrical or linear linkers as a way to produce isorecticular families of MOFs with tailoring pore dimension[66]. An opposite strategy would be to combine apparently incompatible building blocks into structures and topologies, which would provide an opportunity to learn about their behavior and access unprecedented materials. Strategies to induce structural irregularity, by for example employing less symmetric organic linkers with

bend angles [67], introducing steric hindrance [68], or using zigzag-shaped ligands [69], are starting to emerge. These strategies have been termed as *geometric mismatch* [70]. Breaking the coplanarity or modifying the dicarboxylate angle in rectangular ligands creates geometry mismatch (Figure 1-7). Thus, by combining classical topology with these strategies, researchers are gradually elucidating the pre-requisites for designing MOFs with complex topologies [70].

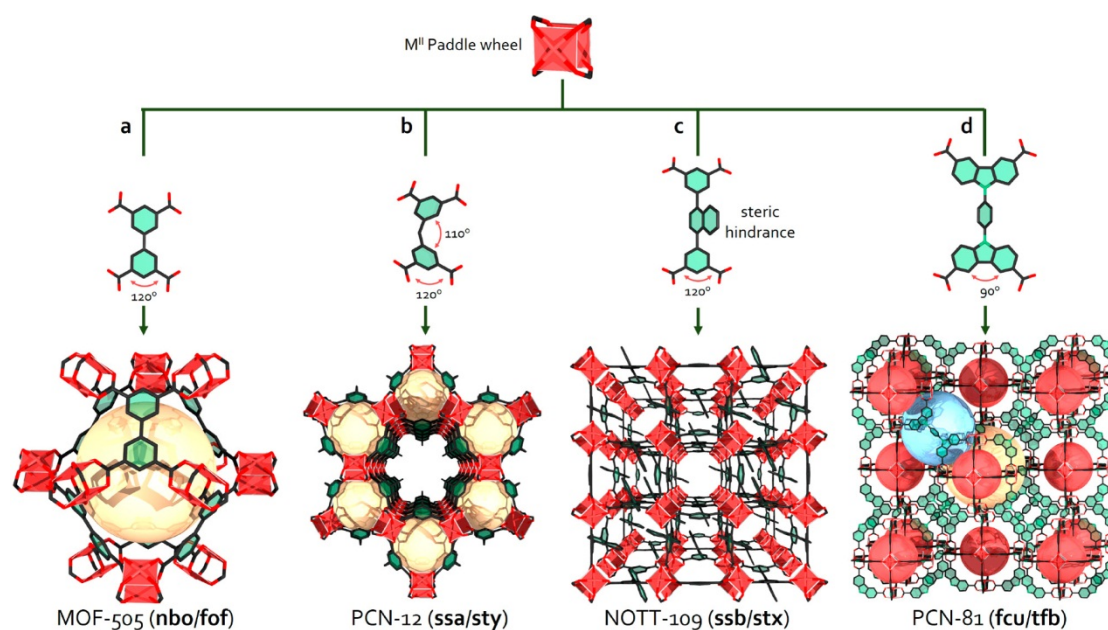


**Figure 1-7.** (a) Assembly of paddle wheels with square/rectangular ligands mainly affords pillared **kgl** layers in **nbo/fof**-type MOFs (MOF-505). (b) Introducing bending into the ligand yields a different type of pillaring, leading to the **ssa/sty** topology (PCN-12). (c) Steric hindrance leads to pillaring **sql** into **ssb/stx** MOFs (NOTT-109). (d) Reducing the bend-angle from 120° to 90° by replacing isophthalate moieties with carbazoles enables assembly of SBB-based **tfb**-MOF (PCN-81), whose underlying topology is **fcu**. Reprinted with permission from reference [70]. Copyright (2019) American Chemical Society.

### 1.2.3 Potential Applications and Hydrolytic Stability

Metal organic frameworks (MOFs) have emerged as a center of attention among the class of more traditional porous materials including zeolites, activated carbons, and

## *Introduction*

---

silica gels, due to their significantly larger pore volumes and tunability of pore geometries. The vast proportion of research based on the development of different types of MOF architectures has been devoted to the potential usefulness of these materials in applications like gas adsorption and separation, catalysis, sensing, conductivity, drug delivery, detection or removal of toxic compounds among others [71-76]. Compared to traditional porous materials, MOFs can be modified on an atomic scale, which will be conducive to precise chemical modifications for designative applications. Gaining precise MOF structural information during their applications facilitates the understanding of structure-property relationship, which conversely encourages the design and synthesis of new MOFs with outstanding application performance.

Gas storage and separation are closely related to various aspects in human society, such as environmental protection, energy utilization and industrial production. Compared to other porous materials (e.g. activated carbons, zeolites), the unique structural features of MOFs, such as high porosity, large surface area, tunable structure, and modifiable functionality, make them promising to be applied in gas storage and separation [77-79]. Specifically, carbon dioxide separation is crucial to the alleviation of greenhouse effect, thus the development of carbon capture and sequestration (CCS) technologies including MOF-based adsorbents that efficiently capture CO<sub>2</sub> from existing emission sources is very important. For example, MOF-505 was reported by Chen and coworkers which was constructed by 3,3',5,5'-biphenyltetracarboxylic acid and Cu paddle-wheel SBUs with liquid-assisted mechanochemical synthesis method [80]. After removing the guest and coordinated water molecules, MOF-505 exhibits exceptionally high CO<sub>2</sub> adsorption of 173 cm<sup>3</sup> g<sup>-1</sup> at 273 K and 0.95 bar, as well as good CO<sub>2</sub>/N<sub>2</sub> selectivity at 273 K due to high surface area and open metal sites (Figure 1-8). In regard to CO<sub>2</sub>/N<sub>2</sub> separation which is related to post-combustion carbon capture, Paolo and coworkers obtained the CO<sub>2</sub>/N<sub>2</sub> selectivity of ~101 at 298 K on the basis of experiments due to coordinatively unsaturated metal sites in HKUST-1 [81]. O. Farha and coworkers demonstrated the

CO<sub>2</sub>/N<sub>2</sub> selectivity of ~45 at 298 K in a Zn-paddle wheel MOF with highly polar ligands [82]. These polycarboxylate MOF materials exhibit promising gas sorption properties attributed to their high surface areas, tunable pore sizes and surface, and open metal sites.

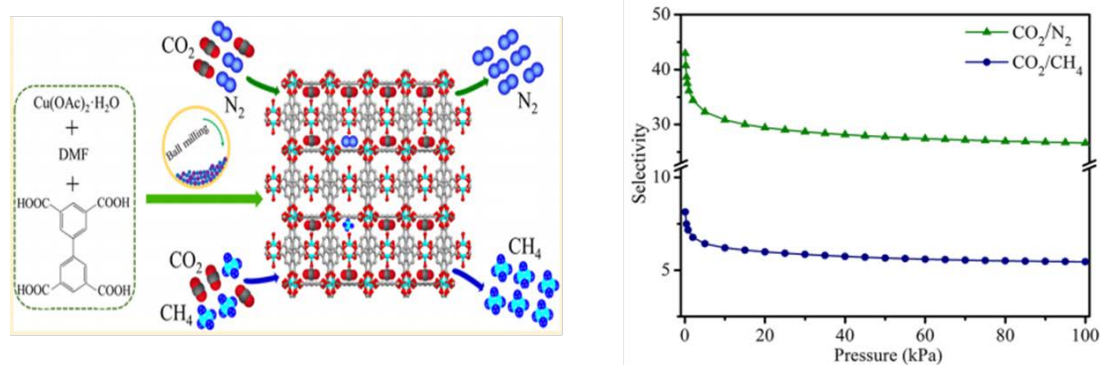


**Figure 1-8.** Structure diagram of MOF-505 (left); IAST CO<sub>2</sub>/N<sub>2</sub> and CO<sub>2</sub>/CH<sub>4</sub> selectivities (right). Reprinted with permission from reference [80]. Copyright (2018) American Chemical Society.

Materials applied for the safe and efficient capture or degradation of toxic chemicals, including chemical warfare agents (CWAs) and organophosphorus pesticides (OPs), are very important in the modern age because of continuous threats of these chemicals to human society, both directly and indirectly. MOFs have become a good alternative class of materials for the catalytic degradation CWAs and adsorptive removal of OPs due to reactive groups metal oxides/hydroxides (Figure 1-9). For example, Michael J. Katz and coworkers [83] reported MOF UiO-66 as a compelling biomimetic catalyst for the methanolysis and hydrolysis of two organophosphate CWA simulants, methyl paraoxon (dimethyl 4-nitrophenyl phosphate) and p-nitrophenyl diphenyl phosphate (PNPDPP). The results show that UiO-66 is an exceptionally active and selective catalyst for the hydrolysis of methyl paraoxon. The latter is due to the ability of the Zr-OH-Zr-containing node in UiO-66 to functionally mimic the binuclear Zn<sup>II</sup> active site of the phosphotriesterase enzyme. In the work from Zhu and coworkers [84], the removal of two representative OPs, glyphosate (GP) and glufosinate (GF), was



## Introduction

investigated by the stable Zr-MOF UiO-67. The adsorption capacities in UiO-67 approached as high as 3.18 mmol (537 mg)  $\text{g}^{-1}$  for GP and 1.98 mmol (360 mg)  $\text{g}^{-1}$  for GF, respectively.

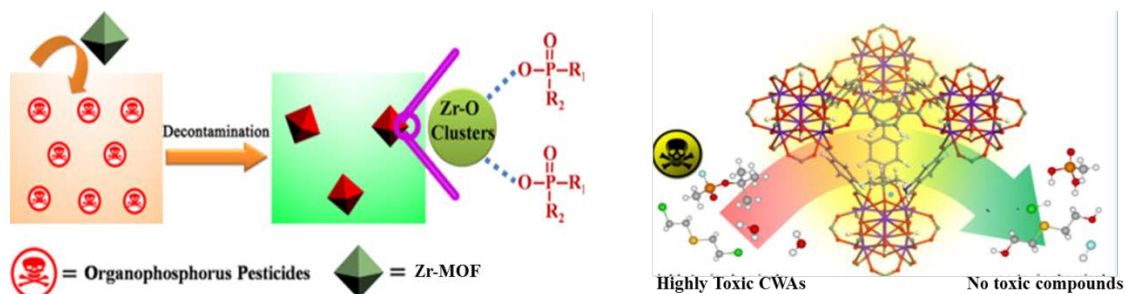


**Figure 1-9.** Diagram of OPs (left) and CWAs (right) interactions with Zr-MOFs. Reprinted with permission from reference [84] and [85]]. Copyright (2017 and 2014) American Chemical Society.

Despite numerous advantages as an emerging class of porous materials, realistic applications of MOFs are ultimately limited by their stability, especially hydrolytic stability. For example, there is inevitable 5-7%  $\text{H}_2\text{O}$  in a typical post-combustion flue gas. Thus for  $\text{CO}_2/\text{N}_2$  separation on MOF materials, their hydrolytic stability should be taken into consideration. OPs/CWAs capture also requires of high hydrolytic stable MOFs as the existing environment of these organophosphorus toxic compounds is aqueous solutions (either agricultural water or ground water). However, a majority of MOFs have been known to lose structural integrity in an aqueous medium (ambient moisture/water vapor, room temperature water, boiling water, steam, aqueous acidic/basic solutions, etc.), which has been considered as a major constraint regarding the potential usefulness of these materials [86-89]. If the nucleophile oxygen from a water molecule can coordinate to a metal cluster, the corresponding MOF will decompose and lose its original porosity due to the breakdown of the coordination bonds. Based on this, many important factors, such as the pKa value of the ligands, coordination number, coordination geometry, oxidation state of the metal centres, hydrophobicity group modifications, ligand rigidity and polymer/carbon coating, can govern the stability of MOFs and CPs [86-89]. For example, HKUST-1 and MOF-5 will decompose gradually when exposure to moisture in air [90,91]. In fact, water or

moisture usually exists in many industrial processes, which is also a major obstacle for large-scale MOF spread and commercialization from laboratory research to industrial application.

### 1.3 Carborane-Based Metal-Organic Frameworks

As mentioned above, carboranes exhibit several material-favorable properties including rigidity, hydrophobicity, thermal and chemical stability. Contrary to classical flat aromatic ligand based MOFs, spherical-shape linkers such as carboranes can access extensive conformational space by a combination of low-energy torsion of the substituents and by the spherical core of the ligand. Such spherical carborane based ligands can facilitate multiple supramolecular contacts that are of a different nature to those found in conventional planar carbon based ligands. These include B–H···A (A = H [92-94], I [95],  $\pi$  [96,97]) interactions. Thus designing and synthesizing carborane-based metal-organic frameworks can not only produce a variety of novel topological MOF materials with enhanced stability due to the hydrophobic backbone unit of the carborane cluster, but it can also be helpful for applications where the smaller pore size within carborane-based MOFs (in comparison with their phenyl-based analogues) or their non-conventional chemical nature introduce new functions or selectivities. Carborane based MOFs are not yet a widespread area and less than 20 papers has been published so far [65,98-115]. In the following we will summarize some of the most relevant reported metal-organic frameworks involving carborane-based ligands with an emphasis in linker modification (Figure 1-10).

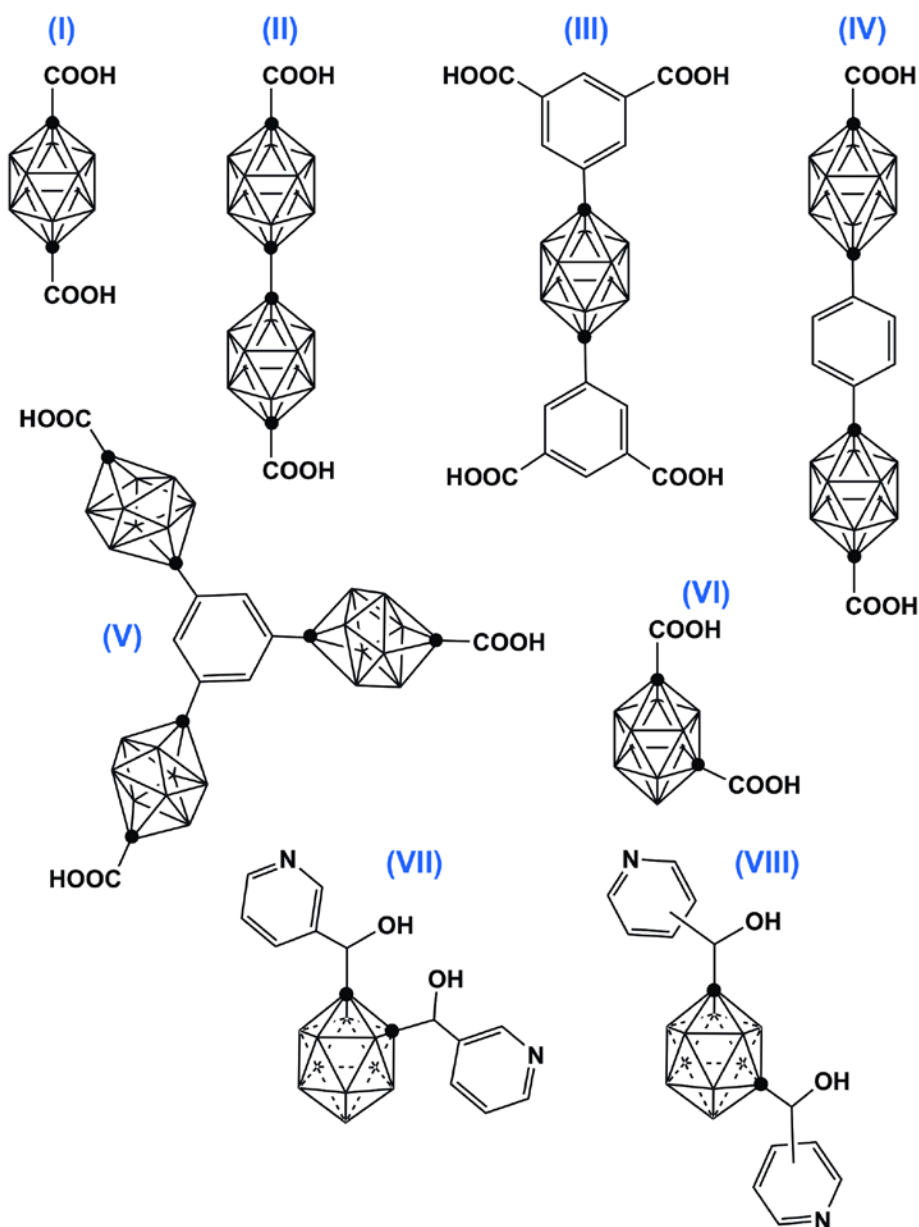


**Figure 1-10.** Summary of carborane-based linkers for MOF construction.

In 2007, J. Hupp and coworkers, from Northwestern University, reported the first carborane-based MOF which was built from 1,12-dihydroxylcarbonyl-1,12-para-*closo*-carborane (*p*-CDC, **I** in Figure 1-10) and  $\text{Zn}(\text{NO}_3)_2$  [98]. The authors argued that **I**, having approximately the same 2-D footprint as benzene-1,4-dicarboxylate (BDC), should provide an archetypal cubic framework compound similar to that of MOF-5  $[\text{Zn}_4\text{O}(\text{BDC})_3]_n$ . The structure of the *p*-carborane based MOF gave however a formula of  $[\text{Zn}_3(\text{OH})(p\text{-CDC})_{2.5}(\text{DEF})_4]_n$  indicating that it

was different with the expected MOF-5 type framework. Nevertheless, the guest-free framework exhibited high H<sub>2</sub> adsorption behaviors due to reduction of pore size and/or formation of open metal sites. Later in 2010, they extended the *p*-CDCH<sub>2</sub> ligand to form a bis(carborane) ligand (**II** in Figure 1-10) and a longer bis(carboranyl)benzene ligand (**IV** in Figure 1-10) for constructing two Zn-MOFs with different SBUs [111]. The results showed these two MOFs exhibited significantly higher surface areas than that of Zn-MOF with ligand **I**. The same group later used a tetradentate *para*-carborane based ligand 1,12-bis(3',5'-Bis(hydroxycarbonyl)phen-1'-yl)-1,12-dicarba-*closo*-caborane (**III** in Figure 1-10) to synthesize a Cu paddle-wheel MOF (NU-135) [101]. The later was the first highly porous carborane-based MOF which showed extremely high H<sub>2</sub> and CH<sub>4</sub> storage capacity. Furthermore, C. A. Mirkin and coworkers reported a tritopic *closo*-1,10-C<sub>2</sub>B<sub>8</sub>H<sub>10</sub> based ligand (**V** in Figure 1-10), which is closely related to the benzene based ligand 1,3,5-benzenetri-carboxylic acid (H<sub>3</sub>BTB)[112]. **V** and H<sub>3</sub>BTB provide isostructural Cu-based MOFs (NU-700 and NU-143, respectively; Figure 1-11), however, only the carborane analogue can be activated with retention of porosity and providing thus a demonstration that carboranes can act as general platforms for stabilization for difficult to activate MOFs. As mentioned in section 1.1.1, there is however a major drawback for using *para*-carborane (Figure 1-1) as the scaffold for ligand syntheses and MOF construction and that is its elevate price.

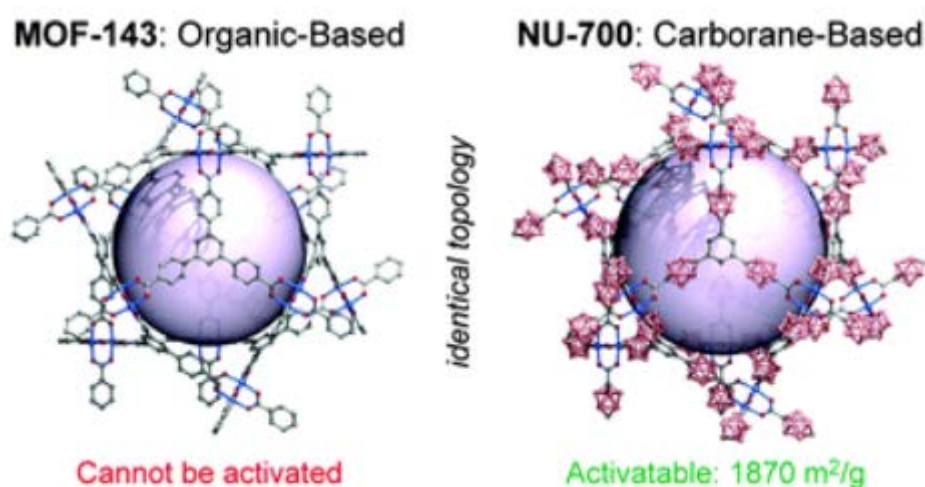


**Figure 1-11.** Comparison of MOF-143 and NU-700 for activation [112].

Apart from *para*-carborane-based linkers, mainly exploited by the groups in Northwestern University, *meta*-carborane (Figure 1-1) has also been used for MOF construction. In 2012, Jin and coworkers firstly reported *meta*-carborane-based MOFs (Figure 1-12) [65]. They synthesized a series of isostructural 2D MOFs which combine prebuilt paddle-wheel  $[\text{Cu}_2(\text{COO})_4]$  nodes with (1,7-dihydroxycarbonyl-1,7-dicarba-closo-dodecaborane; **VI** In Figure 1-10) and extended to the *para*-derivative (**I**) linker by diffusion method at room temperature. The results showed these MOFs preferentially adsorbed  $\text{CO}_2$  over both  $\text{CH}_4$  and  $\text{N}_2$  due to the presence of open metal sites. The same group provided a series of microporous lanthanide coordination polymers with the same ligand (**I**), one of them showing also preferential adsorption of  $\text{CO}_2$  over both  $\text{CH}_4$  and  $\text{N}_2$  [109].

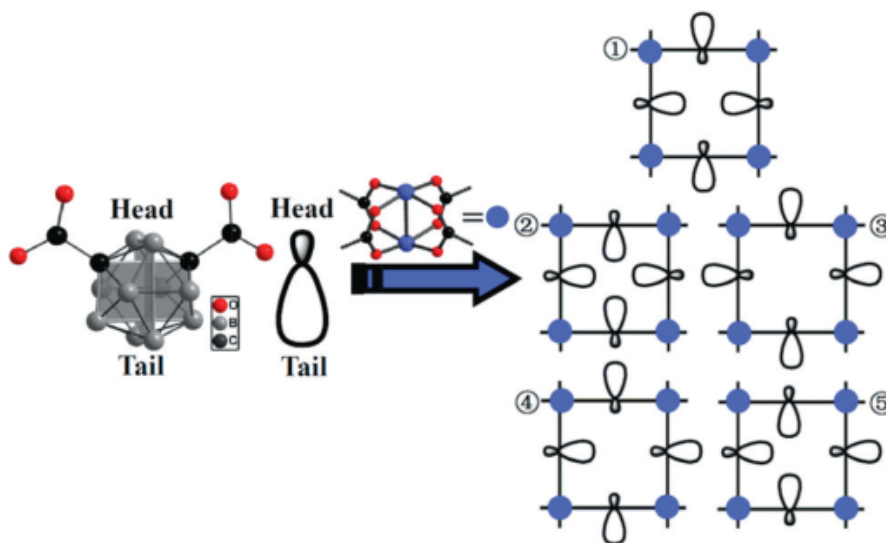


**Figure 1-12.** The formation of 2D structures with five types of rings [65].

Our group reported the first *ortho*-carborane-based MOF back in 2016. The bispyridylalcohol *o*-carborane 1,2-bis{(pyridin-3-yl)methanol}-1,2-dicarba-*closo*-dodecaborane (**VII** in Figure 1-10) provided a 3D Zn-MOF of formula  $[\text{Zn}_4(\mu_4\text{-BDC})_2(\mu_2\text{-VII})_2(\mu_3\text{-O})_2(\text{DMF})_2] \cdot 4\text{DMF}$  (**oCB-MOF-1**).

The highly hydrophobic carborane linker made the MOF stable in liquid water and its crystal-surface showed an unprecedented switch between hydrophobic and superhydrophilic through chemical treatment (Figure 1-13) [113]. Later, our group reported the synthesis and characterization of six new CPs obtained from the reaction between two *m*-carborane bispyridylalcohol ligands (**VIII** in Figure 1-10) and different di-, tri-, and tetracarboxylic linkers with  $M(\text{NO}_3)_2$  salts ( $M = \text{Zn}$  and  $\text{Co}$ ) [114]. One of these compounds ( $[\text{Co}_3(\text{BTB})_2(\text{VIII})_2] \cdot 4\text{DMF}$  (**CB1MOF-1**, Figure 1-14)) acts as a crystalline sponge showing a higher affinity for aromatic guest molecules due to the presence of a large number of host–guest interactions ( $\text{O}-\text{H} \cdots \pi$ ,  $\text{C}-\text{H} \cdots \pi$ ,  $\pi \cdots \pi$ , and weak  $\text{C}-\text{H} \cdots \text{H}-\text{B}$ ). Nanoindentation experiments on this crystalline sponge indicated that a higher number of host–guest contacts has also an effect on the hardness and Young’s moduli values, which can vary by a factor of 5 by exchanging e.g, benzene by chloroform [114]. This same MOF was stable in water for weeks and exhibited interesting reversible SCSC transformations by exchange of the DMF with poor hydrogen bond acceptors or heating in DMF (Figure 1-14) [115]. The flexible and reversible dynamic behavior of this crystalline sponge was unprecedented and opened a new route to encapsulate large molecules that cannot easily diffuse into its structure.

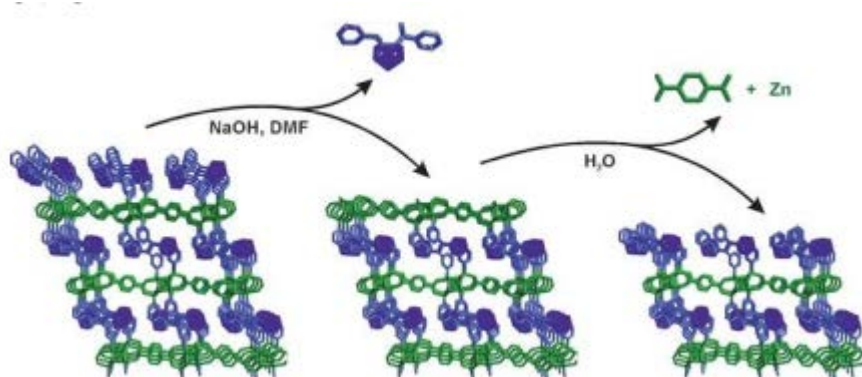


**Figure 1-13.** proposed mechanism for the switchable surface hydrophobicity–hydrophilicity of oCB–MOF-1 [113]. Reprented with permission of John Wiley and Sons.

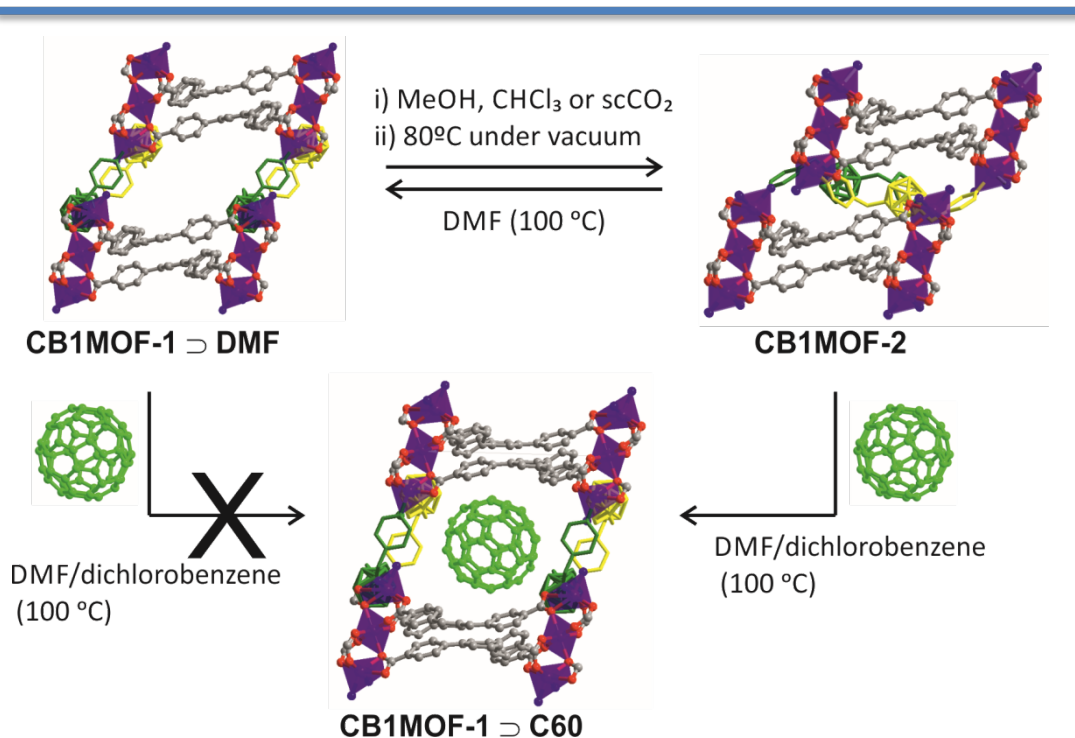


**Figure 1-14.** Optimized conditions for the bulk reversible **CB1MOF-1** to **CB1MOF-2** transformation and C60 encapsulation. 1  $\supset$ DMF [115]. Reprinted with permission of John Wiley and Sons.

Quite recently, Zhang and coworkers reported a novel 3D metal-organic framework BSF-1 comprising the *closo*-dodecaborate cluster  $[B_{12}H_{12}]^{2-}$  prepared by supramolecular assembly of  $CuB_{12}H_{12}$  and 1,2- bis(4-pyridyl)acetylene (Figure 1-15) [116]. The  $[B_{12}H_{12}]^{2-}$  cluster acts as a linker by B–H $\cdots$ Cu interactions and the obtained 3D structure is water stable and also showed good selectivities for gas separation. Excellent separation selectivities for  $C_3H_8/CH_4$ ,  $C_2H_6/CH_4$  and  $C_2H_2/CH_4$  as well as moderately high separation selectivities for  $C_2H_2/C_2H_4$ ,  $C_2H_2/CO_2$  and  $CO_2/CH_4$  were obtained. Moreover, the practical separation performance of  $C_3H_8/CH_4$  and  $C_2H_6/CH_4$  was confirmed by dynamic breakthrough experiments. The good cyclability and high water/thermal stability render it suitable for real industrial application [116].



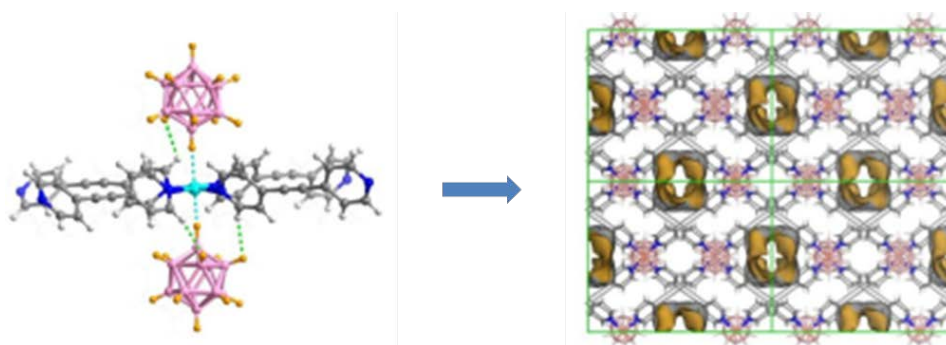


**Figure 1-15.** The structure of BSF-1 based on B-H-M coordination interaction [116]. Reprinted with permission of John Wiley and Sons

All these works show that boranes and carboranes are valuable scaffolds for novel linkers and open new avenues for the synthesis and application of MOFs comprising boron-based cages. Not only higher stabilities are obtained, as compared with the corresponding phenyl analogues, but also higher hydrolytic stabilities are achieved when carboranes are included in the MOF structures. The hydrolytic stability is attributed to the highly hydrophobic nature of carborane residues. The nearly spherical nature of the carborane fragments also facilitate multiple supramolecular contacts that are of a different nature to those found in conventional planar carbon based ligands and provide further stabilization to dynamic MOFs and open new yet unexplored possibilities.

As explained above, MOFs derived from the highly expensive para-carborane are yet the most extensively described, mainly from Northwest University. Thus, new carborane base porous materials from cheaper o- and m-carborane compounds are highly desired if we want to use them for real applications. Thus, the main objective of this thesis is the design, synthesis and study of the properties of novel *meta*-carborane carboxylate-based MOFs, with emphasis on their potential applications.



### 1.4 References

- [1] Hoffmann, R.L., W. N. . *The Journal of Chemical Physics* **1962**, 36, 3489.
- [2] Lipscomb, W.N. *Proceedings of the National Academy of Sciences of the United States of America* **1961**, 47, 1791.
- [3] Longuet-Higgins, H.C.R., M. . *Proceedings of the Royal Society A* **1955**, 230, 110.
- [4] Pitochelli, A.R.H., M. F. *Journal of the American Chemical Society* **1960**, 82, 6909.
- [5] Jemmis, E.D. *Journal of the American Chemical Society* **1982**, 104, 7017.
- [6] Grimes, R.N. *Dalton Transactions* **2015**, 44, 5939.
- [7] Spokoyny, A.M. *Pure and Applied Chemistry* **2013**, 85, 903.
- [8] Dash, B.P.; Satapathy, R.; Maguire, J.A.; Hosmane, N.S. *New Journal of Chemistry* **2011**, 35, 1955.
- [9] Ferrer - Ugalde, A.; González - Campo, A.; Viñas, C.; Rodríguez - Romero, J.; Santillan, R.; Farfán, N.; Sillanpää, R.; Sousa - Pedrares, A.; Núñez, R. *Chemistry – A European Journal* **2014**, 20, 9940.
- [10] Hughes, R.L.S., I. C.; Lawless, E. W. . *In Production of the Boranes and Related Research; Holzmann, R. T., Ed.; Academic Press: New York. 1967.*
- [11] Fein, M.M.B., J.; Mayes, N.; Schwartz, N.; Cohen, M. S. . *Inorganic Chemistry* **1963**, 2, 1111.
- [12] Fein, M.M.G., D.; Paustian, J. E.; Bobinski, J.; Lichstein, B. M.; Mayes, N.; Schwartz, N. N.; Cohen, M. S. . *Inorganic Chemistry* **1963**, 2, 1115.
- [13] Grafstein, D.B., J.; Dvorak, J.; Smith, H.; Schwartz, N. N.; Cohen, M. S.; Fein, M. M. *Inorganic Chemistry* **1963**, 2, 1120.
- [14] Grafstein, D.B., J.; Dvorak, J.; Paustian, J. E.; Smith, H. F.; Karlan, S.; Vogel, C.; Fein, M. M. . *Inorganic Chemistry* **1963**, 2, 1125.
- [15] Grafstein, D.D., J. . *Inorganic Chemistry* **1963**, 2, 1128.
- [16] Alexander, R.P.S., H. A. . *Inorganic Chemistry* **1963**, 2, 1107.
- [17] Heying, T.L.A., J. W.; Clark, S. L.; Alexander, R. P.; Papetti, S.; Reid, J. A.; Trotz, S. I. . *Inorganic Chemistry* **1963**, 2, 1097.
- [18] Heying, T.L.A., J. W.; Clark, S. L.; Mangold, D. J.; Goldstein, H. L.; Hillman, M.; Polak, R. J.; Szymanski, J. W. *Inorganic Chemistry* **1963**, 2, 1089.
- [19] Papetti, S.H., T. L. . *Inorganic Chemistry* **1963**, 2, 1105.
- [20] Schroeder, H.A.H., T. L.; Reiner, J. R. . *Inorganic Chemistry* **1963**, 2, 1092.
- [21] Schroeder, H.V., G. D. . *Inorganic Chemistry* **1963**, 2, 1317.
- [22] Papetti, S.O., C.; Heying, T. L. . *Ind Eng Chem Prod Res Dev* **1966**, 5, 334.
- [23] Stanko, V.I.K., A. I. . *Zh Obshch Khim* **1966**, 36, 2214.
- [24] Dron, P.I.K., W. E.; Michl, J. Z. . *Naturforsch. A* **2014**, 69, 326.
- [25] Davidson, M.G.H., T. G.; Howard, J. A. K.; Mackinnon, A.; Wade, K. *Chemical Communications* **1996**, 2285.
- [26] Hitchcock, A.P.U., S. G.; Wen, A. T.; Kilcoyne, A. L. D.; Tyliszczak, T.R.u., E.; Kosugi, N.; Bozek, J. D.; Spencer, J. T.; McIlroy, D.N.D., P. A. . *The Journal of Physical Chemistry B* **1997**, 101, 3483.
- [27] Turner, A.R.R., H. E.; Borisenko, K. B.; Rankin, D. W. H.; Fox, M.A. *Dalton Transactions* **2005**, 1310.
- [28] Oliva, J.M.K., D. J.; Schleyer, P. v. R.; Serrano-Andres, L. *Pure and Applied Chemistry* **2009**, 81, 719.

- [29] Oliva, J.M.S.-A.e., L.; Klein, D. J.; Schleyer, P. v. R.;; Michl, J. *International Journal of Photoenergy* **2009**, 2009, 1.
- [30] Hutton, B.W.M., F.; Ellis, D.; Herisse, F.; Macgregor, S. A.; McKay, D.P.-A., V.; Rosair, G. M.; Perekalin, D. S.;; Tricas, H.W., A. J. . *Chemical Communications* **2008**, 5345.
- [31] Oliva, J.M.S., P. v. R.; Aullon, G.; Burgos, J. I.;; Fernandez-Barbero, A.A., I. . *Physical Chemistry Chemical Physics* **2010**, 12, 5101.
- [32] Zhao, Y.H.A., M. H.; Zissimos, A. M. . *The Journal of Organic Chemistry* **2003**, 68.
- [33] Ristori, S.O., J.; Grillo, I.; Donati, A.; Spalla, O. . *Biophysical Journal* **2005**, 88, 535.
- [34] Issa, F.; Kassiou, M.; Rendina, L.M. *Chemical Reviews* **2011**, 111, 5701.
- [35] Yamamoto, K.E., Y. . *Bioorganic & Medicinal Chemistry Letters* **2001**, 11, 2389.
- [36] Clegg, W.B., D. A.; Bryan, S. J.; Wade, K. . *Polyhedron* **1984**, 3, 307.
- [37] Planas., J.G. unpublished results.
- [38] Olid, D.; Nunez, R.; Vinas, C.; Teixidor, F. *Chemical Society Reviews* **2013**, 42, 3318.
- [39] Batten, S.R.; Champness, N.R.; Chen, X.-M.; Garcia-Martinez, J.; Kitagawa, S.; Öhrström, L.; O’Keeffe, M.; Suh, M.P.; Reedijk, J.J.P.; Chemistry, A. **2013**, 85, 1715.
- [40] Tomic, E. *Journal of Applied Polymer Science* **1965**, 9, 3745.
- [41] Hoskins, B.; Robson, R. *Journal of the American Chemical Society* **1990**, 112, 1546.
- [42] Yaghi, O.; Li, H. *Journal of the American Chemical Society* **1995**, 117, 10401.
- [43] Li, H.; Eddaoudi, M.; O’Keeffe, M.; Yaghi, O.M. *Nature* **1999**, 402, 276.
- [44] Férey, G.; Mellot-Draznieks, C.; Serre, C.; Millange, F.; Dutour, J.; Surblé, S.; Margiolaki, I. *Science* **2005**, 309, 2040.
- [45] Moghadam, P.Z.; Li, A.; Wiggin, S.B.; Tao, A.; Maloney, A.G.; Wood, P.A.; Ward, S.C.; Fairen-Jimenez, D. *Chemistry of Materials* **2017**, 29, 2618.
- [46] Cho, H.Y.; Yang, D.A.; Kim, J.; Jeong, S.Y.; Ahn, W.S. *Catalysis Today* **2012**, 185, 35.
- [47] Choi, J.S.; Son, W.J.; Kim, J.; Ahn, W.S. *Microporous and Mesoporous Materials* **2008**, 116, 727.
- [48] Jhung, S.H.; Lee, J.H.; Yoon, J.W.; Serre, C.; Férey, G.; Chang, J.S. *Advanced Materials* **2007**, 19, 121.
- [49] Jung, D.W.; Yang, D.A.; Kim, J.; Kim, J.; Ahn, W.S. *Dalton Transactions* **2010**, 39, 2883.
- [50] Kim, J.; Yang, S.T.; Choi, S.B.; Sim, J.; Kim, J.; Ahn, W.S. *Journal of Materials Chemistry* **2011**, 21, 3070.
- [51] Son, W.J.; Kim, J.; Kim, J.; Ahn, W.S. *Chemical Communications*; 2008; pp. 6336.
- [52] Mueller, U.; Schubert, M.; Teich, F.; Puetter, H.; Schierle-Arndt, K.; Pastre, J. *Journal of Materials Chemistry* **2006**, 16, 626.
- [53] Hartmann, M.; Kunz, S.; Himsl, D.; Tangermann, O.; Ernst, S.; Wagener, A. *Langmuir* **2008**, 24, 8634.
- [54] Beldon, P.J.; Fabian, L.; Stein, R.S.; Thirumurugan, A.; Cheetham, A.K.; Friscic, T. *Angewandte Chemie International Edition* **2010**, 49, 9640.
- [55] Klimakow, M.; Klobes, P.; Thünemann, A.F.; Rademann, K.; Emmerling, F. *Chemistry of Materials* **2010**, 22, 5216.
- [56] Friscic, T. *Chemical Society Reviews* **2012**, 41, 3493.
- [57] James, S.L.; Adams, C.J.; Bolm, C.; Braga, D.; Collier, P.; Friscic, T.; Grepioni, F.; Harris, K.D.; Hyett, G.; Jones, W., et al. *Chemical Society Reviews* **2012**, 41, 413.
- [58] Tanabe, K.K.; Cohen, S.M. *Chemical Society Reviews* **2011**, 40, 498.

## Introduction

---

- [59] Karagiari, O.; Bury, W.; Mondloch, J.E.; Hupp, J.T.; Farha, O.K. *Angewandte Chemie International Edition* **2014**, *53*, 4530.
- [60] Lalonde, M.; Bury, W.; Karagiari, O.; Brown, Z.; Hupp, J.T.; Farha, O.K. *Journal of Materials Chemistry A* **2013**, *1*, 5453.
- [61] Stock, N.; Biswas, S. *Chemical Reviews* **2012**, *112*, 933.
- [62] Fujita, M.; Kwon, Y.J.; Washizu, S.; Ogura, K. *Journal of the American Chemical Society* **1994**, *116*, 1151.
- [63] Hoskins, B.F.; Robson, R. *Journal of the American Chemical Society* **1989**, *111*, 5962.
- [64] Guillerm, V.; Gross, S.; Serre, C.; Devic, T.; Bauer, M.; Ferey, G. *Chem. Commun.* **2010**, *46*, 767.
- [65] Huang, S.-L.; Weng, L.-H.; Jin, G.-X. *Dalton Transactions* **2012**, *41*, 11657.
- [66] He, Y.; Li, B.; O'Keeffe, M.; Chen, B. *Chemical Society Reviews* **2014**, *43*, 5618.
- [67] Alezi, D.; Peedikakkal, A.M.P.; Weseliński, Ł.J.; Guillerm, V.; Belmabkhout, Y.; Cairns, A.J.; Chen, Z.; Wojtas, Ł.; Eddaoudi, M. *Journal of the American Chemical Society* **2015**, *137*, 5421.
- [68] Eddaoudi, M.; Kim, J.; O'Keeffe, M.; Yaghi, O.M. *Journal of the American Chemical Society* **2002**, *124*, 376.
- [69] Guillerm, V.; Grancha, T.; Imaz, I.; Juanhuix, J.; MasPOCH, D. *Journal of the American Chemical Society* **2018**, *140*, 10153.
- [70] Guillerm, V.; MasPOCH, D. *Journal of the American Chemical Society* **2019**, *141*, 16517.
- [71] Li, J.R.; Kuppler, R.J.; Zhou, H.C. *Chemical Society Reviews* **2009**, *38*, 1477.
- [72] Lee, J.; Farha, O.K.; Roberts, J.; Scheidt, K.A.; Nguyen, S.T.; Hupp, J.T. *Chemical Society Reviews* **2009**, *38*, 1450.
- [73] Kreno, L.E.; Leong, K.; Farha, O.K.; Allendorf, M.; Van Duyne, R.P.; Hupp, J.T. *Chemical Reviews* **2012**, *112*, 1105.
- [74] Sun, L.; Campbell, M.G.; Dincă, M. *Angewandte Chemie International Edition* **2016**, *55*, 3566.
- [75] DeCoste, J.B.; Peterson, G.W. *Chemical Reviews* **2014**, *114*, 5695.
- [76] Mondloch, J.E.; Katz, M.J.; Isley, W.C.; Ghosh, P.; Liao, P.; Bury, W.; Wagner, G.W.; Hall, M.G.; DeCoste, J.B.; Peterson, G.W., et al. *Nature materials* **2015**, *14*, 512.
- [77] Li, B.; Wen, H.-M.; Zhou, W.; Chen, B. *The Journal of Physical Chemistry Letters* **2014**, *5*, 3468.
- [78] Jiang, J.; Furukawa, H.; Zhang, Y.-B.; Yaghi, O.M. *Journal of the American Chemical Society* **2016**, *138*, 10244.
- [79] Taylor, M.K.; Runčevski, T.; Oktawiec, J.; Gonzalez, M.I.; Siegelman, R.L.; Mason, J.A.; Ye, J.; Brown, C.M.; Long, J.R. *Journal of the American Chemical Society* **2016**, *138*, 15019.
- [80] Chen, Y.; Wu, H.; Liu, Z.; Sun, X.; Xia, Q.; Li, Z. *Industrial Engineering Chemistry Research* **2018**, *57*, 703.
- [81] Aprea, P.; Caputo, D.; Gargiulo, N.; Iucolano, F.; Pepe, F. *Journal of Chemical Engineering Data* **2010**, *55*, 3655.
- [82] Bae, Y.-S.; Farha, O.K.; Hupp, J.T.; Snurr, R.Q. *Journal of Materials Chemistry A* **2009**, *19*, 2131.
- [83] Katz, M.J.; Mondloch, J.E.; Totten, R.K.; Park, J.K.; Nguyen, S.T.; Farha, O.K.; Hupp, J.T. *Angewandte Chemie International Edition* **2014**, *53*, 497.
- [84] Zhu, X.; Li, B.; Yang, J.; Li, Y.; Zhao, W.; Shi, J.; Gu, J. *ACS applied materials & interfaces* **2015**, *7*, 223.
- [85] Gil-San-Millan, R.; López-Maya, E.; Hall, M.; Padial, N.M.; Peterson, G.W.; DeCoste, J.B.; Rodríguez-Albelo, L.M.; Oltra, J.E.; Barea, E.; Navarro, J.A. *ACS Applied Materials & Interfaces* **2017**, *9*, 23967.

- [86] Qadir, N.U.; Said, S.A.M.; Bahaidarah, H.M. *Microporous and Mesoporous Materials* **2015**, *201*, 61.
- [87] Burtch, N.C.; Jasuja, H.; Walton, K.S. *Chemical Reviews* **2014**, *114*, 10575.
- [88] Gelfand, B.S.; Shimizu, G.K.H. *Dalton Transactions* **2016**, *45*, 3668.
- [89] Li, P.; Chen, J.; Zhang, J.; Wang, X. *Separation & Purification Reviews* **2015**, *44*, 19.
- [90] DeCoste, J.B.; Peterson, G.W.; Schindler, B.J.; Killops, K.L.; Browe, M.A.; Mahle, J.J. *Journal of Materials Chemistry A* **2013**, *1*, 11922.
- [91] Ding, N.; Li, H.; Feng, X.; Wang, Q.; Wang, S.; Ma, L.; Zhou, J.; Wang, B. *Journal of the American Chemical Society* **2016**, *138*, 10100.
- [92] Di Salvo, F.; Camargo, B.; Garcia, Y.; Teixidor, F.; Viñas, C.; Giner Planas, J.; Light, M.E.; Hursthouse, M.B. *CrystEngComm* **2011**, *13*, 5788.
- [93] Planas, J.G.; Vinas, C.; Teixidor, F.; Comas-Vives, A.; Ujaque, G.; Lledos, A.; Light, M.E.; Hursthouse, M.B. *Journal of the American Chemical Society* **2005**, *127*, 15976.
- [94] Fox, M.A.; Hughes, A.K. *Coordination Chemistry Reviews* **2004**, *248*, 457.
- [95] Chaari, M.; Kelemen, Z.; Planas, J.G.; Teixidor, F.; Choquesillo-Lazarte, D.; Ben Salah, A.; Viñas, C.; Núñez, R. *Journal of Materials Chemistry C* **2018**, *6*, 11336.
- [96] Zhang, X.; Dai, H.; Yan, H.; Zou, W.; Cremer, D. *Journal of the American Chemical Society* **2016**, *138*, 4334.
- [97] Terrasson, V.; Garcia, Y.; Farras, P.; Teixidor, F.; Viñas, C.; Giner Planas, J.; Prim, D.; Light, M.E.; Hursthouse, M.B. *CrystEngComm* **2010**, *12*, 4109.
- [98] Farha, O.K.; Spokoyny, A.M.; Mulfort, K.L.; Hawthorne, M.F.; Mirkin, C.A.; Hupp, J.T. *Journal of the American Chemical Society* **2007**, *129*, 12680.
- [99] Bae, Y.-S.; Farha, O.K.; Spokoyny, A.M.; Mirkin, C.A.; Hupp, J.T.; Snurr, R.Q. *Chemical Communications* **2008**, 4135.
- [100] Bae, Y.-S.; Spokoyny, A.M.; Farha, O.K.; Snurr, R.Q.; Hupp, J.T.; Mirkin, C.A. *Chemical Communications* **2010**, *46*, 3478.
- [101] Kennedy, R.D.; Krungleviciute, V.; Clingerman, D.J.; Mondloch, J.E.; Peng, Y.; Wilmer, C.E.; Sarjeant, A.A.; Snurr, R.Q.; Hupp, J.T.; Yildirim, T. *Chemistry of Materials* **2013**, *25*, 3539.
- [102] Kennedy, R.D.; Clingerman, D.J.; Morris, W.; Wilmer, C.E.; Sarjeant, A.A.; Stern, C.L.; O’Keeffe, M.; Snurr, R.Q.; Hupp, J.T.; Farha, O.K. *Crystal growth design* **2014**, *14*, 1324.
- [103] Boldog, I.; Bereciartua, P.J.; Bulánek, R.; Kučeráková, M.; Tomandlová, M.; Dušek, M.; Macháček, J.; De Vos, D.; Baše, T. *Crystengcomm* **2016**, *18*, 2036.
- [104] Oleshkevich, E.; Vinas, C.; Romero, I.; Choquesillo-Lazarte, D.; Haukka, M.; Teixidor, F. *Inorganic Chemistry* **2017**, *56*, 5502.
- [105] Hynek, J.; Brázda, P.; Rohlíček, J.; Londesborough, M.G.S.; Demel, J. *Angewandte Chemie International Edition* **2018**, *57*, 5016.
- [106] Boldog, I.; Dušek, M.; Jelínek, T.; Švec, P.; Ramos, F.S.d.O.; Růžička, A.; Bulánek, R. *Microporous and Mesoporous Materials* **2018**, *271*, 284.
- [107] Oleshkevich, E.; Romero, I.; Teixidor, F.; Viñas, C. *Dalton Transactions* **2018**, *47*, 14785.
- [108] Choi, S.; Lee, H.-E.; Ryu, C.H.; Lee, J.; Lee, J.; Yoon, M.; Kim, Y.; Park, M.H.; Lee, K.M.; Kim, M. *Chemical Communications* **2019**, *55*, 11844.
- [109] Huang, S.L.; Lin, Y.J.; Yu, W.B.; Jin, G.X. *ChemPlusChem* **2012**, *77*, 141.
- [110] Farha, O.K.; Spokoyny, A.M.; Mulfort, K.L.; Galli, S.; Hupp, J.T.; Mirkin, C.A. *small* **2009**, *5*, 1727.

## Introduction

---

- [111] Spokoyny, A.M.; Farha, O.K.; Mulfort, K.L.; Hupp, J.T.; Mirkin, C.A. *Inorganica Chimica Acta* **2010**, *364*, 266.
- [112] Clingerman, D.J.; Morris, W.; Mondloch, J.E.; Kennedy, R.D.; Sarjeant, A.A.; Stern, C.; Hupp, J.T.; Farha, O.K.; Mirkin, C.A. *Chemical Communications* **2015**, *51*, 6521.
- [113] Rodríguez - Hermida, S.; Tsang, M.Y.; Vignatti, C.; Stylianou, K.C.; Guillerm, V.; Pérez - Carvajal, J.; Teixidor, F.; Viñas, C.; Choquesillo - Lazarte, D.; Verdugo - Escamilla, C. *Angewandte Chemie International Edition* **2016**, *55*, 16049.
- [114] Tsang, M.Y.; Rodríguez-Hermida, S.; Stylianou, K.C.; Tan, F.; Negi, D.; Teixidor, F.; Viñas, C.; Choquesillo-Lazarte, D.; Verdugo-Escamilla, C.; Guerrero, M. *Crystal Growth & Design* **2017**, *17*, 846.
- [115] Tan, F.; López - Periago, A.; Light, M.E.; Cirera, J.; Ruiz, E.; Borrás, A.; Teixidor, F.; Viñas, C.; Domingo, C.; Planas, J.G. *Advanced Materials* **2018**, *30*, 1800726.
- [116] Zhang, Y.; Yang, L.; Wang, L.; Duttwyler, S.; Xing, H. *Angewandte Chemie International Edition* **2019**, *58*, 8145.

# Chapter 2

---

## *Objectives*



---

## Objectives

As illustrated in **Chapter 1**, the high thermal and chemical stability, hydrophobicity, ease of functionalization and three-dimensional nature of the carborane clusters make them good candidates for designing and synthesizing new carboxylate-based metal-organic frameworks. As compared with the more studied *para*-carborane isomer, the *meta*-carborane fragment has been hardly employed, in spite of its much lower cost. Thus, the main objective of the present thesis is the design, synthesis and application of *meta*-carborane based polycarboxylate ligands for MOF construction. Owing to the spatial disposition of the unique two carbon atoms in the *meta*-carborane icosahedron, it represents an ideal platform for exploring the synthetic possibilities of V-shaped polycarboxylate-based metal-organic frameworks. As explained in the previous chapter, bended or V-shaped ligands have attracted the attention of researchers in recent years due to their unexpected topological structures. In addition to the above general objective, the specific objectives of the present work were:

Explore the construction of MOFs with V-shaped *meta*-carborane based polycarboxylate linkers and different transition metals. It was particularly interesting to investigate the possible influence of geometric configuration of the ligands on the structures of corresponding MOFs and the effect of increasing the connectivity by adding various numbers of carboxylate groups.

Study the influence of elongating the linker on its stability, as compared to the previously reported linker VI (Figure 1-10), and therefore on the stability, hydrophobicity and coordination modes of the new MOFs.

The last objective of the present thesis was to explore the applications of the new V-shaped *meta*-carborane-based MOFs. Especially important was to proof whether the incorporation of the hydrophobic carborane moiety into the MOFs increases their hydrolytic stability and the impact of that on the potential applications.





# Chapter 3

---

*A Reversible Phase Transition of 2D  
Coordination Layers by B–H•••Cu(II)  
Interactions in a Coordination  
Polymer*



---

## A Reversible Phase Transition of 2D Coordination Layers by B-H $\cdots$ Cu(II) Interactions in a Coordination Polymer

### 3.1 Introduction

Porous Coordination Polymers (CPs) or Metal-Organic Frameworks (MOFs) are a class of porous crystalline materials formed by the assembly of metal ions or metal clusters with different types of bridging organic linkers or ligands [1-4]. Open metal sites (OMS) in these materials, where Lewis base molecules can coordinate or interact, are known to play an important role in a variety of applications, ranging from catalysis [5-7] to molecules storage [8,9], separation [10-12] or sensing [13,14]. Such interactions often involve molecules including H<sub>2</sub>O, CO, CO<sub>2</sub>, H<sub>2</sub>, CH<sub>4</sub>, N<sub>2</sub> or H<sub>2</sub> among others and undergo dynamic processes that are difficult to probe directly by spectroscopic experiments such as infrared or Raman spectroscopy [15-17]. Among the MOFs that can easily generate OMS, Cu(II) based paddlewheel MOFs have been extensively studied and exhibit structural diversity and high porosity [18-20]. Solvent molecules bound to the apical position of the Cu<sub>2</sub>-paddlewheel motif (*vide infra*) can be removed to generate unsaturated Cu(II) OMS. Among the various strategies for MOFs activation (removal of pore-filling and metal coordinated solvent), only thermal activation, which consists of applying heat energy and vacuum, has so far been able to dissociate coordinating solvent and generate OMS [15,21,22]. In a series of papers [23-26], N. C. Jeong and coworkers have nicely demonstrated that the Cl atoms of dichloro- or trichloro methane can weakly coordinate to the open metal sites of well-known Cu(II) MOFs such as HKUST-1 (Copper benzene-1,3,5-tricarboxylate) or Cu-MOF-2 (Copper 1,4-benzene-dicarboxylate). Such weak coordination of chloromethanes lead to what the authors termed a *chemical route to active open metal sites by removing coordinating solvent*. They proved the ability of chloromethanes to remove pre-coordinated solvent molecules from OMS, by *in situ* Raman spectroscopy, and therefore leading to MOF activation without the need for thermal activation. Such a mild activation in solution opens new avenues for potential applications of MOFs [24,27].

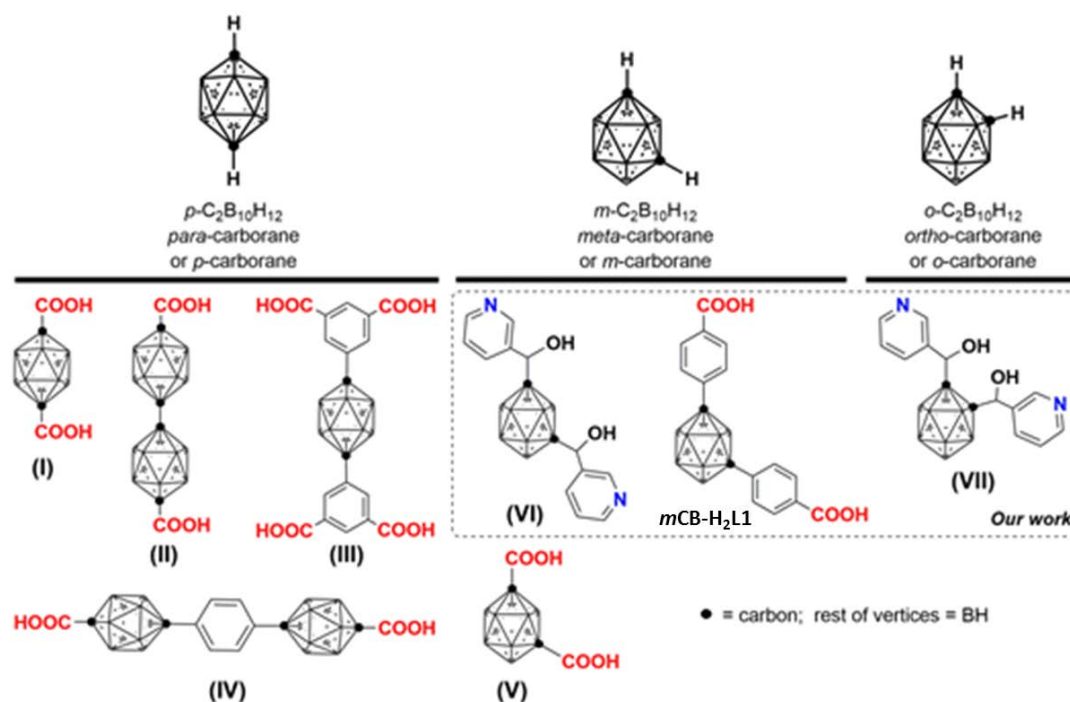
## Introduction

---

Icosahedral boranes and carboranes ( $[\text{B}_{12}\text{H}_{12}]^{2-}$  and  $1,n\text{-C}_2\text{B}_{10}\text{H}_{12}$  ( $n = 2, 7$  or  $12$ ); Scheme 1) are an interesting class of commercially available and exceptionally stable 3D-aromatic boron-rich clusters that possess material-favorable properties such as thermal and chemical stability and hydrophobicity [28-30]. The neutral carboranes are remarkably robust boron clusters with two carbon atoms and possess 26 electrons for 12 vertices. The delocalized electron density is not uniform through the cage, giving rise to extraordinary differences in the electronic effects of the cluster [31]. This unusual electronic structure is often highlighted by regarding carboranes as inorganic three-dimensional “aromatic” analogs of arenes [32]. Such properties make icosahedral carborane clusters valuable ligands for CPs or MOFs. For example, some of us have reported the synthesis and electronic and magnetic properties of purely inorganic CPs based on the monocarboxylic acid of *ortho*-carborane [33-35]. Mirkin and co-workers explored the use of di-, tri- and tetra-carboxylic acid derivatives of *para*-carborane (**I** to **IV** in Scheme 3-1) for CPs synthesis, providing a series of CPs exhibiting unprecedented stabilities with respect to thermal degradation, inherited from the carborane moiety [36-42]. Jin and co-workers also constructed CPs based on the dicarboxylic acid derivatives of *para*- but also of *meta*-carborane linkers (**V** in Scheme 3-1), and studied their adsorption and luminescence properties [43,44]. Dicarboxylic and tricarboxylic derivatives of the smaller carborane *closo*-1,10- $\text{C}_2\text{B}_8\text{H}_{10}$  were also incorporated into porous CPs [38,45]. We have recently designed flexible carborane based ligands for dynamic MOFs (**VI** and **VII** in Scheme 3-1) [46,47]. In addition to water stability [47], the spherical shape of the carborane moiety in these flexible linkers seems to have a noticeable influence in the dynamic behavior of the MOFs. Thus, we previously reported an unusual reversible 3D to 2D transformation of a Cobalt based MOF, incorporating a carborane-based dipyrindine ligand [48]. We argued that contrary to classical flat aromatic ligand based MOFs, spherical-shape linkers such as carboranes, can access extensive conformational space by a combination of low-energy torsion of the substituents and by the spherical core of the ligand. Such spherical carborane based ligands can facilitate multiple supramolecular contacts that are of a different nature to those found in conventional planar carbon based ligands. These include  $\text{B-H}\cdots\text{A}$  ( $\text{A} = \text{H}$  [49-51],  $\text{I}$  [52],  $\pi$  [53,54]) interactions or  $\text{B-H}\cdots\text{Metal}$  [55-62] (agostic) interactions in molecular systems. The latter type of interaction is well documented in icosahedral cages and is considered a preliminary step in many B-H

activation reactions and in hydrogenation or hydroboration [62-64]. The hydridic nature of the H atoms in boranes and carboranes make these BH moieties suitable for metal coordination [65,66]. During the preparation of this manuscript, it was reported a first example of a B–H⋯Cu(II) based MOF from  $[B_{12}H_{12}]^{2-}$  [67].

Here we report the synthesis of a new family of Cu-paddlewheel based 2D coordination polymers incorporating a dicarboxylate *m*-carborane ligand  $[Cu_2(mCB-L1)_2(Solv)_2] \cdot xSolv$  (*mCB-H<sub>2</sub>L1*: 1,7-di(4-carboxyphenyl)-1,7-dicarba-*closo*-dodecaborane; Scheme 1) and an unprecedented reversible phase transition through formation/cleavage of a weak but attractive B–H⋯Cu(II) interactions. We provide evidence for the observed reversible process by a combination of single-crystal (SCXRD), powder (PXRD) X-ray diffraction, Raman spectroscopy and DFT calculations. This reversible transformation is achieved by solvent-guest exchange under ambient conditions in one direction and in DMF solutions at room temperature in the other. The transformation is mediated by B–H⋯Cu(II) interactions, when generating open metal sites during solvent-exchange.



**Scheme 3-1.** Graphical representation of the carborane isomers (*closo*- $C_2B_{10}H_{12}$ ) and their derivatives used as linkers to form CPs.

### 3.2 Results and Discussion

Reaction of  $\text{Cu}(\text{NO}_3)_2$ , and *mCB-H<sub>2</sub>L1* in dimethylformamide (DMF), dimethylacetamide (DMA) or methanol (MeOH) at 80 °C for 48 h afforded greenish crystals for  $[\text{Cu}_2(\textit{mCB-L1})_2(\text{Solv})_2] \cdot x\text{Solv}$  (**1-Solv** = **1-DMF**, **1-DMA** or **1-MeOH**) in good yield. IR spectrum showed the characteristic broad B-H stretching bands from the carborane (in the range 2617~2531  $\text{cm}^{-1}$ ), and the C=O vibration of the carboxylate groups (Figure 3-1). Single-crystal X-ray diffraction (Figure 3-2, Table S3-1) revealed a 2D network for all the compounds. Phase purity was confirmed by elemental analysis and powder X-ray diffraction (PXRD), for **1-DMF** and **1-DMA** (Figure 3-3). Crystals for **1-MeOH** were only stable in the solvent and a rapid phase transition was observed when the crystals were dried in air (*vide infra*).

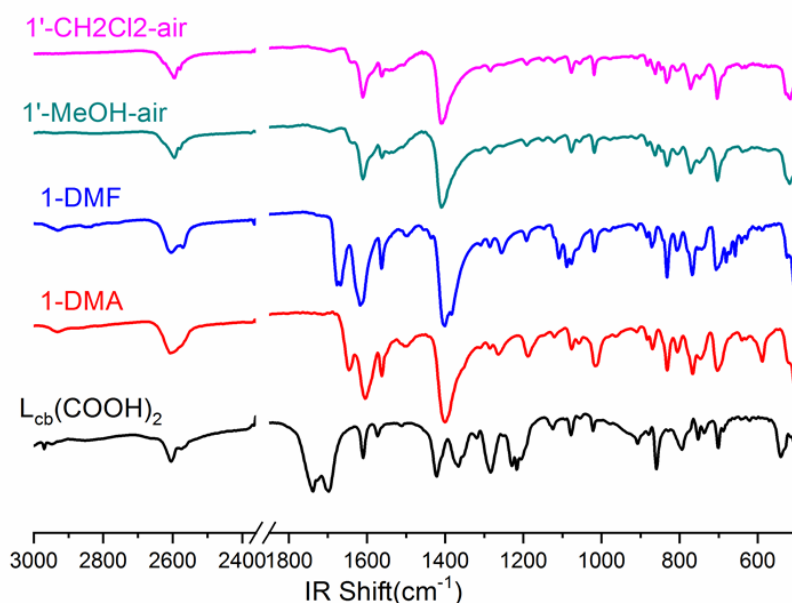


**Figure 3-1.** FT-IR spectra of *mCB-H<sub>2</sub>L1* ligand, **1-DMA**, **1-DMF**, **1'-MeOH-air** and **1'-CH<sub>2</sub>Cl<sub>2</sub>-air**.

The basic unit of **1-Solv** is a  $\text{Cu}_2$ -paddlewheel motif of  $[\text{Cu}_2(\text{COO})_4]$  units (Figure 3-2). The Cu–Cu distances (Table S3-2) in the paddlewheel units are 2.647, 2.642 and 2.620 Å for **1-DMA**, **1-DMF** and **1-MeOH**, respectively. The two copper atoms share four *mCB-L1* linkers at the basal positions and one oxygen atom from the solvent (DMA, DMF or MeOH for **1-DMA**, **1-DMF** and **1-MeOH**, respectively) occupy the apical positions (Figure 3-2A). Cu–OOC and Cu–O<sub>solv</sub> bond lengths (Table S3-2) range from

1.952 to 1.971 Å and 2.081 to 2.137 Å, respectively. The carborane **mCB-L1** linker shows a V-shape ( $\text{OOC-CBcentroid-COO} \approx 111\text{-}115^\circ$ ) and two noncoplanar phenyl rings ( $78\text{-}87^\circ$ ). Thus, the bent **mCB-L1** linkers and noncoplanar phenyl rings in **1-Solv** adopt a  $4^4$ -grid topology by bending alternately above and below the plane containing the paddlewheel  $[\text{Cu}_2(\text{COO})_4]$  units to produce a very corrugated 2D layers. As shown in Figure 3-2B, the 2D  $4^4$  net consists of chair-like units, similar to that found in other related V-shape ditopic linkers [68-70].

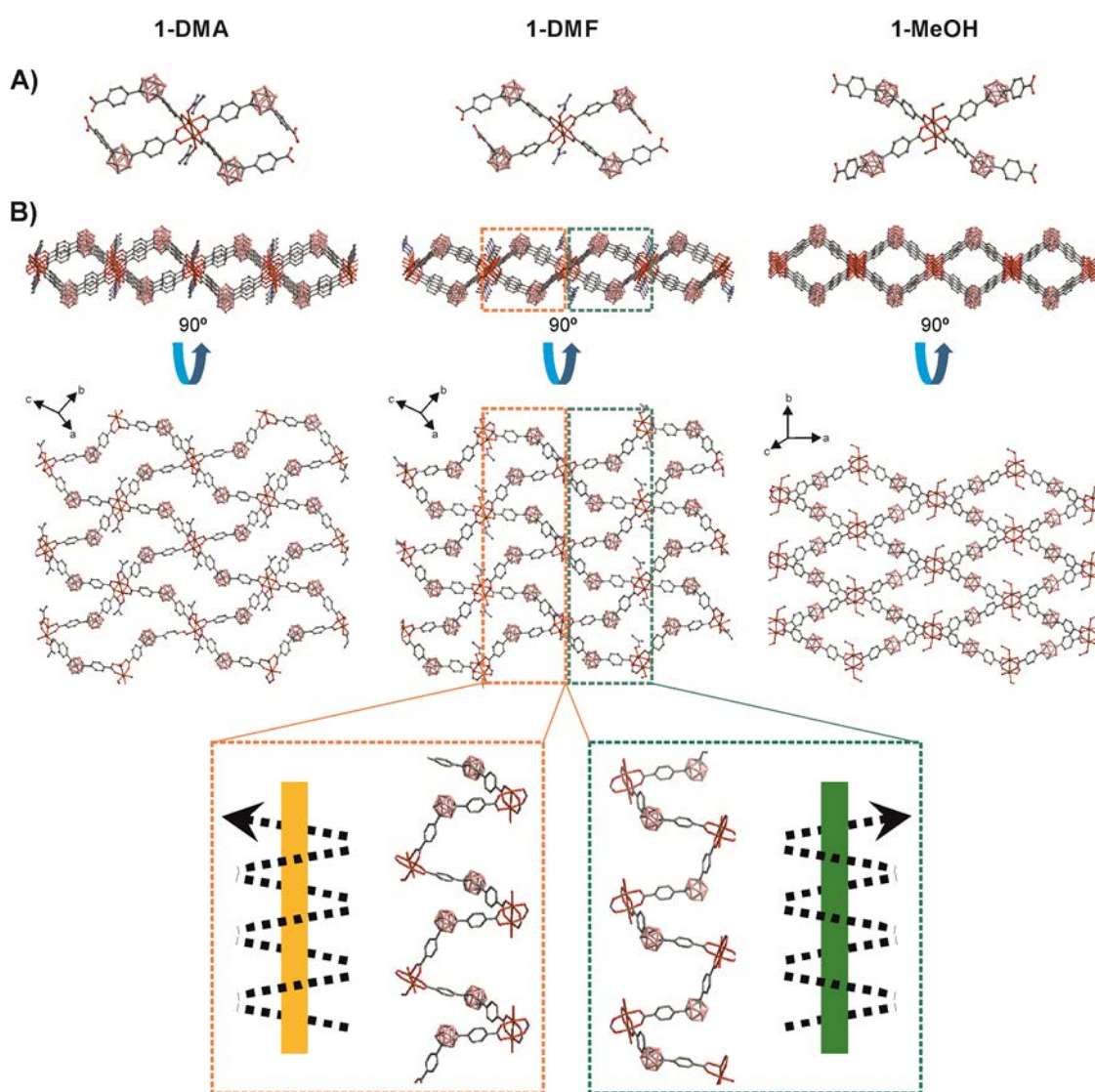


**Figure 3-2.** A comparative view of the crystal structures of **1-DMA**, **1-DMF** and **1-MeOH**. A) View of the Cu<sub>2</sub>-paddlewheel units with **mCB-L1** coordination. b) Two perpendicular views of the extended structures showing the 2D  $4^4$  networks; 1D helical chains with right hand (green) or left hand (orange) are indicated for **1-DMF**. H atoms are omitted for clarity. Color code: B pink; C grey; O red; N blue, Cu orange.



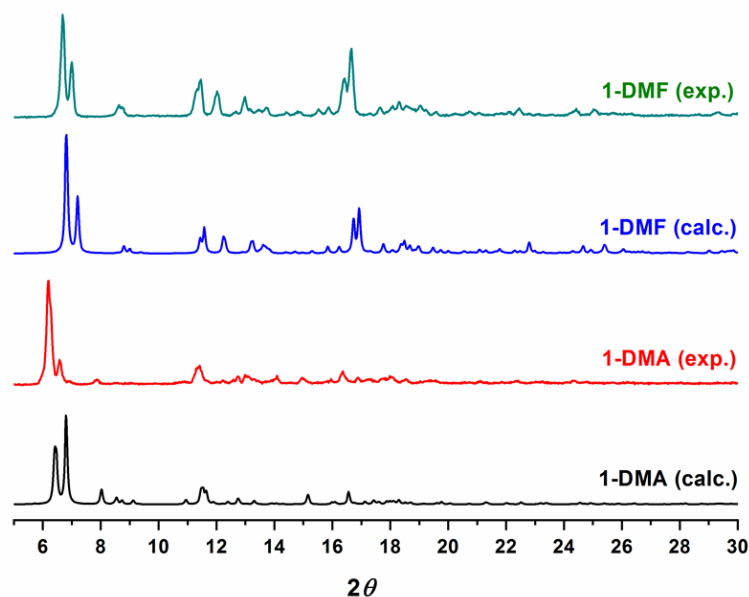


**Figure 3-3.** Comparison of calculated and experimental PXRD for **1-DMF** and **1-DMA**.

Table 3-1 summarizes the parameters for each of the structures in this work and in comparison with some related structures where there is a 1,3-benzene moiety instead of a *m*-carborane unit [68-70]. In each  $4^4$  unit in our structures, two consecutive carborane clusters are above the plane containing the paddlewheel  $[\text{Cu}_2(\text{COO})_4]$  units, and the other two are below the plane. The corrugated layers in **1-Solv** are thick ( $\sim 15\text{-}16$  Å, Table 3-2) and as can be seen in Figure 3-2B, they create nanoscale channels (see colored dotted rectangles in Figure 3-2B). A more detailed analysis of the structures shows that the nanoscale channels are formed by the particular bridging coordination of the V-shape *mCB-L1* linker. Each carborane linker bridges two different paddlewheel units in a way that result in a single-strand helix chain (Figure 3-2), generating the above mentioned channels. These 1D helical chains are alternately connected with each other through the paddlewheel units, constructing the observed 2D networks. The handedness of the  $2_1$  helicity for all descriptions in this paper are determined using a method similar to the supramolecular tilt chirality method (*STC*) [71]. In brief, given a helix in front of the  $2_1$  screw axis inclining to the right, the assemblies can be defined to be right-handed, or inclining to the left are defined to be left-handed. Quite interestingly, the pitches of the helixes are different in each of the new structures. The pitch decreases in the order **1-DMA** (16.2) > **1-DMF** (14.4) > **1-MeOH** (12.5) and correlate with the shorter of the two diagonal paddlewheel to paddlewheel distances in each  $4^4$  chair-like unit (Table 3-1). Such changes in the pitch suggest that a single 2D sheet would stretch

or shrink, depending on the solvent. The analysis of data in Table 3-1 reveals that the larger diagonal paddlewheel to paddlewheel distances in each  $4^4$  chair-like unit vary between 28-30 Å, whereas the variation for the shorter diagonal distances is much smaller (13-20 Å). Interestingly, the corresponding distances for the non-carborane containing CPs, e.g., those having a 1,3-benzene moiety instead of a *m*-carborane unit are longer (ca. 20 x 28 Å) [68-70]. A shorter *m*-carborane dicarboxylic ligand (1,7-dihydroxycarbonyl)-1,7-dicarbocloso-dodecaborane) provided related Cu-Paddlewheel based 2D structures with smaller  $4^4$  nets and shorter diagonal paddlewheel to paddlewheel distances (13-16 Å; Table 3-1) [44]. As mentioned above, the shorter of the two diagonal paddlewheel to paddlewheel distances in each  $4^4$  chair-like unit corresponds to the pitch of the single-strand helix chains in the structures (Figure 3-2B). Larger pitches (or diagonal distances) for the non carborane CPs favor interpenetration in all structures reported in the literature [68-70]. However, no interpenetration is observed for the structures reported in this work. As mentioned above, the pitch in **1-Solv** increases with the size of the solvent molecules. The latter is followed by a concomitant decrease in the layer thickness, as it happens, for example, when one stretches or compresses a coil. Thus, the **1-DMA** and **1-DMF** layer thicknesses are 15.4 and 15.0 Å, respectively, whereas that for **1-MeOH** is 16.3 Å. However, this does not seem to affect the interlayer distances as these are all very close (Table 3-1) and similar to other related 2D Cu(II) coordination polymers [72]. Stacking of the 2D layers gives rise to the 3D structures of the compounds. A comparison of the 3D structures shows only lateral displacements or sliding of the 2D layers as shown in Figure 3-4. Layers in **1-DMA** and **1-DMF** arrange in a way to maximize the nanoscale channels, whereas those in **1-MeOH** are occluded.

**Table 3-1.** Selected crystal parameters for compounds in this work and related 2D structures.

Coordination Polymer	SG <sup>a</sup>	D <sup>b</sup>	$4^4$ nets Diagonal distances (Å) <sup>c</sup>	P (Å) <sup>d</sup>	Layer Thickness <sup>e</sup> (Å)	Interlayer distances (Å)
<b>1-DMA</b> (this work)	<i>P</i> -1	1.262	16.2 x 29.0	16.2	15.41	6.94
<b>1-DMF</b> (this work)	<i>P</i> -1	1.355	14.4 x 29.4	14.4	14.95	6.86
<b>1-MeOH</b> (this work)	<i>P</i> 2 <sub>1</sub> / <i>c</i>	1.367	12.5 x 29.8	12.5	16.29	7.06
PELFOE <sup>f</sup> ([CuL <sup>1</sup> -DMA]DMF)	<i>C</i> 2/ <i>c</i>	1.448	19.7 x 27.6	19.7	-	interpenetrated
MAPLAT <sup>f</sup>	<i>C</i> 2/ <i>c</i>	1.353	19.9 x 27.6	19.9	-	interpenetrated

## Results and Discussion

([CuL <sup>1</sup> ·DMA]H <sub>2</sub> O)						
OFEHOY <sup>f</sup> ([CuL <sup>2</sup> ·DMF]DMF)	C2/c	1.245	19.6 × 27.7	19.6	-	interpenetrated
NEYRIU <sup>f</sup> ([CuL <sup>3</sup> ·MeOH]MeOH)	C2/c	1.261	12.8 × 13.8	12.8	10.313	10.187
NEYREQ <sup>f</sup> ([CuL <sup>3</sup> ·MeOH]DMF)	P2 <sub>1</sub> /n		12.7 × 14.0	12.7	9.827	10.454

<sup>a</sup> Space groups. <sup>b</sup> Calculated density. <sup>c</sup> Paddlewheel to paddlewheel distances in each in each 44 chair-like unit. <sup>d</sup> Pitches of the 21 helices. <sup>e</sup> Measured from H atom to H atom in B-H bonds; See also Figure 3-4. <sup>f</sup> CSD Refcodes. L<sup>1</sup>: 1,3-di(4-carboxyphenyl)benzene; L<sup>2</sup>: 5'-methyl-1,1':3',1''-terphenyl-4,4''-dicarboxylic acid; L<sup>3</sup>: 1,7-dicarba-closo-dodecaborane-1,7-dicarboxylato.

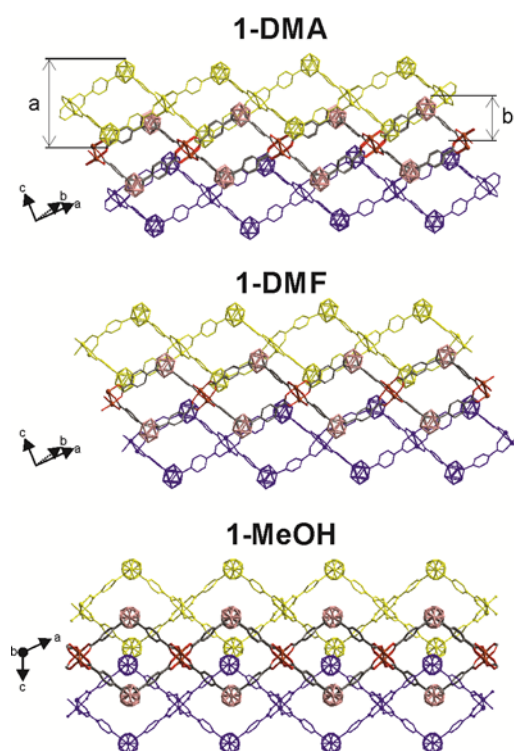


**Figure 3-4.** View of the packing structures for **1-Solv** (Solv = DMA, DMF and MeOH) showing the stacking of 2D layer structures in which the various colors differentiates the contiguous layers. Coordinated solvent molecules are omitted for clarity. Layer thickness (a) and Interlayer distance (b) are only represented in 1-DMA.

Solvent exchange was carried out successively with methanol (MeOH; 2 days) and dichloromethane (CH<sub>2</sub>Cl<sub>2</sub> for 2 days; see Experimental for details) for **1-DMF**. Treatment of large **1-DMF** crystals with MeOH showed a clear macroscopic transformation in the size and color of the crystals to give a new phase **1'-MeOH** (Figure 3-5). Large platelets broke into small pieces, followed with a color change from greenish to sky blue (Figure 3-5b). Immersion of **1'-MeOH** crystals in CH<sub>2</sub>Cl<sub>2</sub>

provoked a color change from sky blue to deep navy ( $1'$ - $\text{CH}_2\text{Cl}_2$ ), consistent with the presence of OMS [24] but no further change of morphology of crystals was observed (Figure 3-5c). In contact with air, deep navy colored crystalline  $1'$ - $\text{CH}_2\text{Cl}_2$  turns within seconds into sky blue color. Thermogravimetric analysis of  $1$ - $\text{DMA}$  and  $1$ - $\text{DMF}$  from room temperature to  $600\text{ }^\circ\text{C}$  shows a continuous drop until  $400\text{ }^\circ\text{C}$  (Figure 3-6a), so that evaporation of the free and coordinated solvent cannot be distinguished from the decomposition of the framework, making the thermal activation difficult. TGA curves for air dried samples of  $1'$ - $\text{MeOH-air}$  and  $1'$ - $\text{CH}_2\text{Cl}_2\text{-air}$  show very similar profiles that are significantly different to that for  $1$ - $\text{DMF}$ ;  $1'$ - $\text{MeOH-air}$  and  $1'$ - $\text{CH}_2\text{Cl}_2\text{-air}$  show a three-step loss, one at  $75$ - $98$ ,  $280$  and another at  $350\text{ }^\circ\text{C}$  (Figure 3-6b).

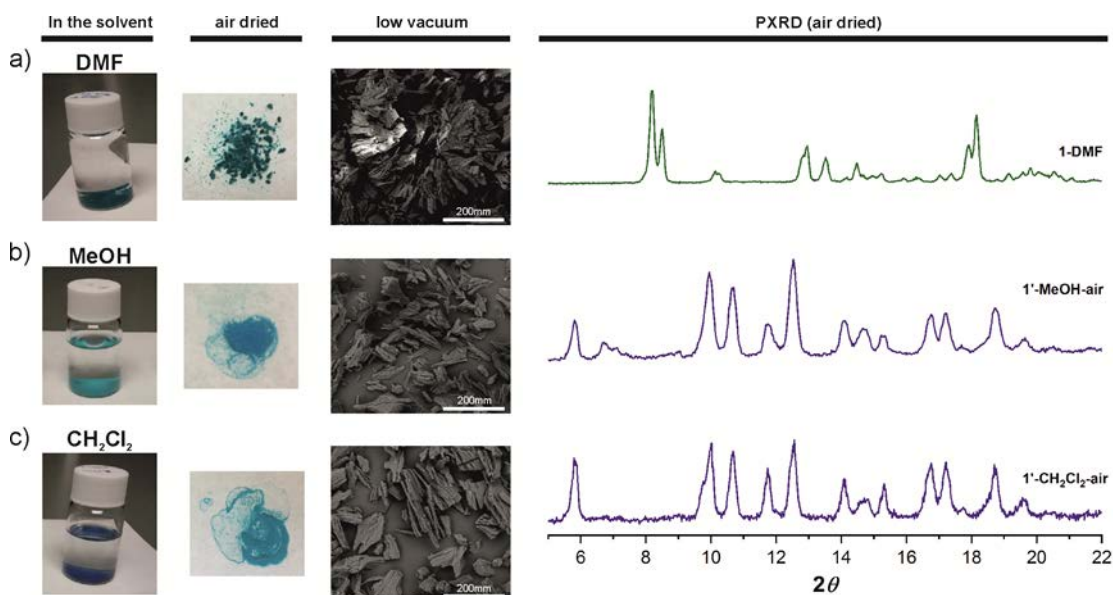


**Figure 3-5.** Left: Photographs and SEM images showing crystals color and morphology of as made  $1$ - $\text{DMF}$  (a), after 2 days in methanol (b) and after 2 days in dichloromethane (c), in the solvent and after being exposed to air. Right: PXRD patterns for  $1$ - $\text{DMF}$ ,  $1'$ - $\text{MeOH-air}$  and  $1'$ - $\text{CH}_2\text{Cl}_2\text{-air}$ .

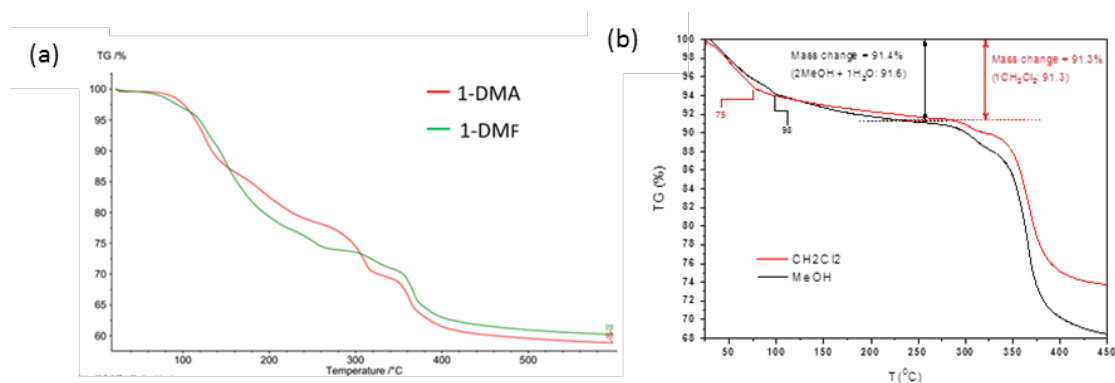


**Figure 3-6.** TGA diagram of as made **1-DMA** (red) and **1-DMF** (green) (a); **1'-MeOH-air** (black) and **1'-CH<sub>2</sub>Cl<sub>2</sub>-air** (red) (b).

Remarkably, PXRD data for **1'-MeOH-air** and **1'-CH<sub>2</sub>Cl<sub>2</sub>-air** show that both correspond to the same phase and those are markedly different to that for **1-DMF** (Figure 3-5). The PXRD data is consistent with a phase transition triggered by immersing **1-DMF** in MeOH, the new crystalline phase remaining stable in CH<sub>2</sub>Cl<sub>2</sub>. Quite interestingly, the PXRD pattern for **1'-MeOH-air** clearly differs from that for the calculated pattern of **1-MeOH** (Figure 3-7). As mentioned above, crystals for **1-MeOH** were only stable in the solvent and a rapid phase transition was observed when the crystals were dried in air; multiple single crystal measurement trials showed a fast change of symmetry on solvent loss. The new symmetry appears to be a centered version of the original cell with a doubling of the *a* parameter, diffraction was too poor to yield more than a rough backbone structure with very high R values. PXRD of the latter crystals exposed to air confirmed that **1-MeOH** transformed into **1'-MeOH-air** (Figure 3-7). Unfortunately, we could not obtain the SCXRD structure of neither **1'-MeOH-air** or **1'-CH<sub>2</sub>Cl<sub>2</sub>-air** even by using synchrotron radiation measurements. Nevertheless, elemental analyses correlate with **1'-MeOH-air** and **1'-CH<sub>2</sub>Cl<sub>2</sub>-air** being  $[\text{Cu}_2(\text{mCBL1})_2(\text{H}_2\text{O})(2\text{MeOH})]$  [73] and  $[\text{Cu}_2(\text{mCBL1})_2(\text{H}_2\text{O})(\text{CH}_2\text{Cl}_2)]$ , respectively. Overall the data suggest the successive exchange of Cu-bound DMF by MeOH and then CH<sub>2</sub>Cl<sub>2</sub> to provide the deep navy colored **1'-CH<sub>2</sub>Cl<sub>2</sub>-wet** having OMS (see Raman discussion below), that on exposure to air rapidly changes to sky blue. As mention in the introduction, such *chemical route to active* OMS species have been widely investigated and showed that owing to the

weak Lewis basicity of  $\text{CH}_2\text{Cl}_2$ , it spontaneously dissociated from the metal and thus provided open metal sites at room temperature [21,23,25,26]. However, we note that whereas the color change from deep navy to sky blue on moist water coordination usually occurs within minutes or hours in the reported examples [25,74], color change from **1'- $\text{CH}_2\text{Cl}_2$ -wet** to **1'- $\text{CH}_2\text{Cl}_2$ -air** takes place within seconds (*vide infra*). Based on the observed color changes and Raman data below, we hypothesize **1'- $\text{CH}_2\text{Cl}_2$ -wet** being  $[\text{Cu}_2(\text{mCBL1})_2] \cdot x\text{CH}_2\text{Cl}_2$ , where the  $\text{CH}_2\text{Cl}_2$  solvent molecules are partially or totally uncoordinated.

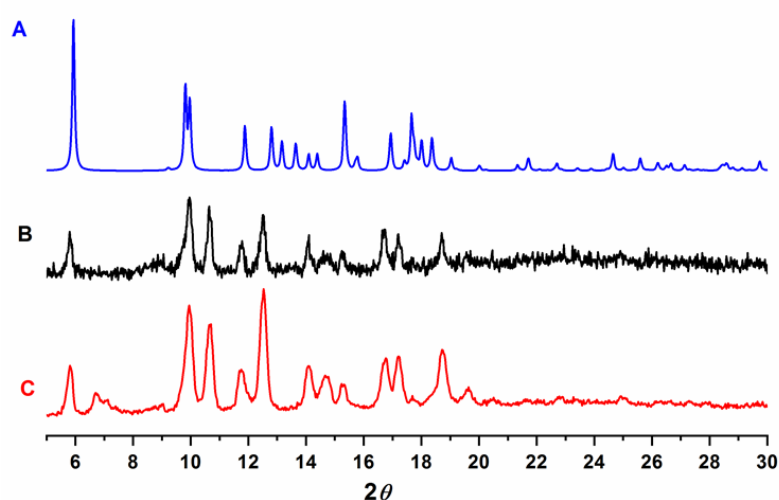


**Figure 3-7.** PXRD comparison for MeOH related compounds. (A) Calculated PXRD from structure **1-MeOH**. (B) PXRD of crystals obtained after exposing **1-MeOH** to air and dried on a filter paper. (C) PXRD of crystals obtained after immersing **1-DMF** into MeOH and then exposed to air and dried on a filter paper. The comparison reveals that **1-MeOH** is not stable out of solvent and rapidly transforms into **1'-MeOH-air**.

**1'- $\text{CH}_2\text{Cl}_2$ -air** was activated at  $120^\circ\text{C}$  under dynamic high vacuum for 20h, affording a deep navy solid, presumably corresponding to desolvated  $[\text{Cu}_2(\text{mCBL1})_2]$  (**1'-activated**), containing OMS. The latter is porous to  $\text{N}_2$  at 77 K (BET surface area:  $301 \text{ m}^2 \text{ g}^{-1}$ ) and also to  $\text{CO}_2$  ( $41 \text{ cm}^3 \text{ g}^{-1}$  STP, Figure S3-1, Figure S3-2) at 273 K and 1 bar.  $\text{N}_2$  sorption-desorption isotherms exhibited a typical reversible type-I behavior with an uptake of  $125 \text{ cm}^3/\text{g}$  (Figure 3-8). The pore width distribution was 6-7 Å (Figures 3-8), suggesting that the micropores from **1'-activated** might correlate with the observed nanoscale channels in **1-solv** (Figure 3-2). Interestingly,  $\text{CO}_2$  sorption capacity of **1'-activated** is twice that measured for the related (but shorter)

carborane-dicarboxylated Cu<sub>2</sub>-paddle wheel CP [44].

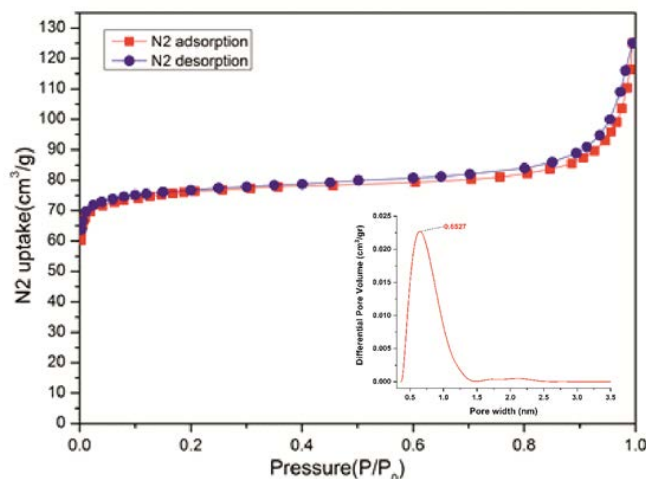


**Figure 3-8.** N<sub>2</sub> adsorption isotherm at 77 K for activated 1'-CH<sub>2</sub>Cl<sub>2</sub>-air. The inset shows the calculated pore-size distribution using a 2D-NLDFT Heterogeneous Surface model.

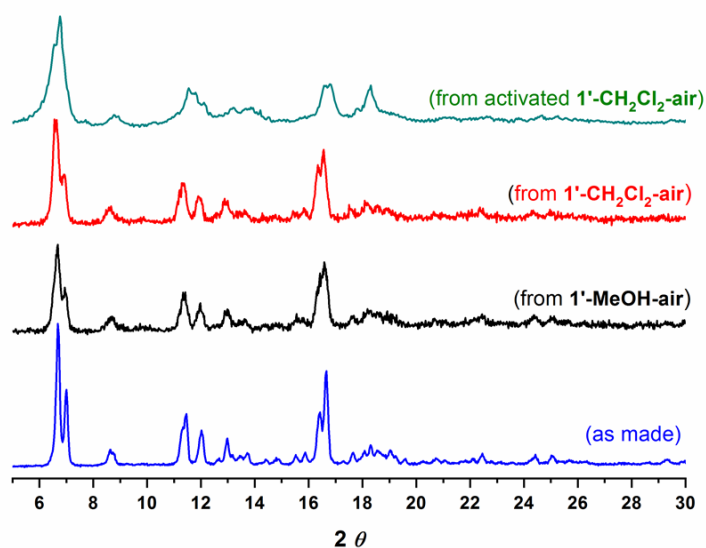


**Figure 3-9.** PXRD patterns showing reversible transformation from different samples of **1-DMF**. Samples for 1'-MeOH-air, 1'-CH<sub>2</sub>Cl<sub>2</sub>-air or activated 1'-CH<sub>2</sub>Cl<sub>2</sub>-air were immersed in DMF, as explained in the experimental section. The PXRD show the conversion in all cases.

Having determined that [Cu<sub>2</sub>(*m*CBL1)<sub>2</sub>] (**1'-activated**) retains porosity, we evaluated the possible structural reversibility. Indeed, 1-DMF could be obtained by immersing samples of **1'-activated**, 1'-CH<sub>2</sub>Cl<sub>2</sub>-air or 1'-MeOH-air into DMF at room temperature (Figure 3-9). Such a reversible transformation under ambient conditions indicates a rather weak interaction between layers in **1'** structures. Intrigued by this reversible phase transition, we further investigated the process by Raman spectroscopy in order to identify the possible changes in the paddlewheel units in **1**.



Therefore, we measured the Raman spectra for **1-DMF**, **1'-MeOH-air**, **1'-CH<sub>2</sub>Cl<sub>2</sub>-air**, and **1'-CH<sub>2</sub>Cl<sub>2</sub>-wet**. A comparison of the complete and selected Raman spectra for all the above compounds is provided in Figures 3-10 and 3-11, respectively. Stretching modes of Cu–Cu vibrations (240-150 cm<sup>-1</sup>) were clearly observed in all the samples as broad bands. Whereas Cu–Cu vibration for **1-DMF** appeared at 162 cm<sup>-1</sup>, that for **1'-CH<sub>2</sub>Cl<sub>2</sub>-wet** appeared at 207 cm<sup>-1</sup>, that is, blue-shifted ca. 50 cm<sup>-1</sup>. Such blue-shift displacement correlates well with that observed for HKUST-1 on chemical activation [26]. As mentioned earlier, exposure of **1'-CH<sub>2</sub>Cl<sub>2</sub>-wet** to air quickly provided **1'-CH<sub>2</sub>Cl<sub>2</sub>-air**. Interestingly, after the sample was exposed to ambient air (within 1 minute) a color change from navy to sky blue was noticed and the Cu–Cu vibration observed for **1'-CH<sub>2</sub>Cl<sub>2</sub>-wet** at 207 cm<sup>-1</sup>, was red-shifted and split into two bands at approximately 180 and 162 cm<sup>-1</sup> in **1'-CH<sub>2</sub>Cl<sub>2</sub>-air** (Figure 3-11). The latter remained unaltered with longer exposure to air. Two bands are also observed in the Raman spectrum of **1'-MeOH-air**, at 182 and 162 cm<sup>-1</sup>. The observed spontaneous red shift on exposing **1'-CH<sub>2</sub>Cl<sub>2</sub>-wet** to air is consistent with a lengthening of the Cu···Cu distances on dissociation of weakly coordinated CH<sub>2</sub>Cl<sub>2</sub> and coordination of other better bonding species, such as e.g., H<sub>2</sub>O from air [23]. The above data is in agreement with previously reported data and proof that DMF-coordinated to Cu in **1** can be effectively and successively dissociated by MeOH and CH<sub>2</sub>Cl<sub>2</sub> [24]. It is noteworthy that no other changes in the Raman signals were observed in the region for the organic moiety of the linker (Figures 3-10 and 3-11). The characteristic double band of  $\nu_{\text{sym}}(\text{COO}^-)$  vibration for the bridged carboxylates at around 1400 and 1420 cm<sup>-1</sup> (Figures 3-10 and 3-11) remains mostly unchanged, demonstrating that there is no significant change in the coordination mode of the carboxylates from the Cu<sub>2</sub>-paddlewheel units during the transformation. There is, however, a clear change in the B-H vibrations, suggesting that the change in the Cu···Cu distances also affects the carborane moieties. Thus, B-H vibrations appear as a broad bands at 2569, 2582 and 2617 cm<sup>-1</sup> in **1-DMF** and change into three broad bands at 2566, 2597 and 2625 cm<sup>-1</sup> in **1'-CH<sub>2</sub>Cl<sub>2</sub>-wet** (Figure 3-11). A clear change was observed when **1'-CH<sub>2</sub>Cl<sub>2</sub>-wet** was exposed to the air, providing **1'-CH<sub>2</sub>Cl<sub>2</sub>-air**.



## Results and Discussion

Thus, new B-H vibrations appear at 2581, 2599, 2607, 2632 and 2667  $\text{cm}^{-1}$  for **1'-CH<sub>2</sub>Cl<sub>2</sub>-air**. As observed in the Cu-Cu vibration region, a nearly identical Raman spectrum to that of **1'-CH<sub>2</sub>Cl<sub>2</sub>-air** is observed in the case of **1'-MeOH-air**.

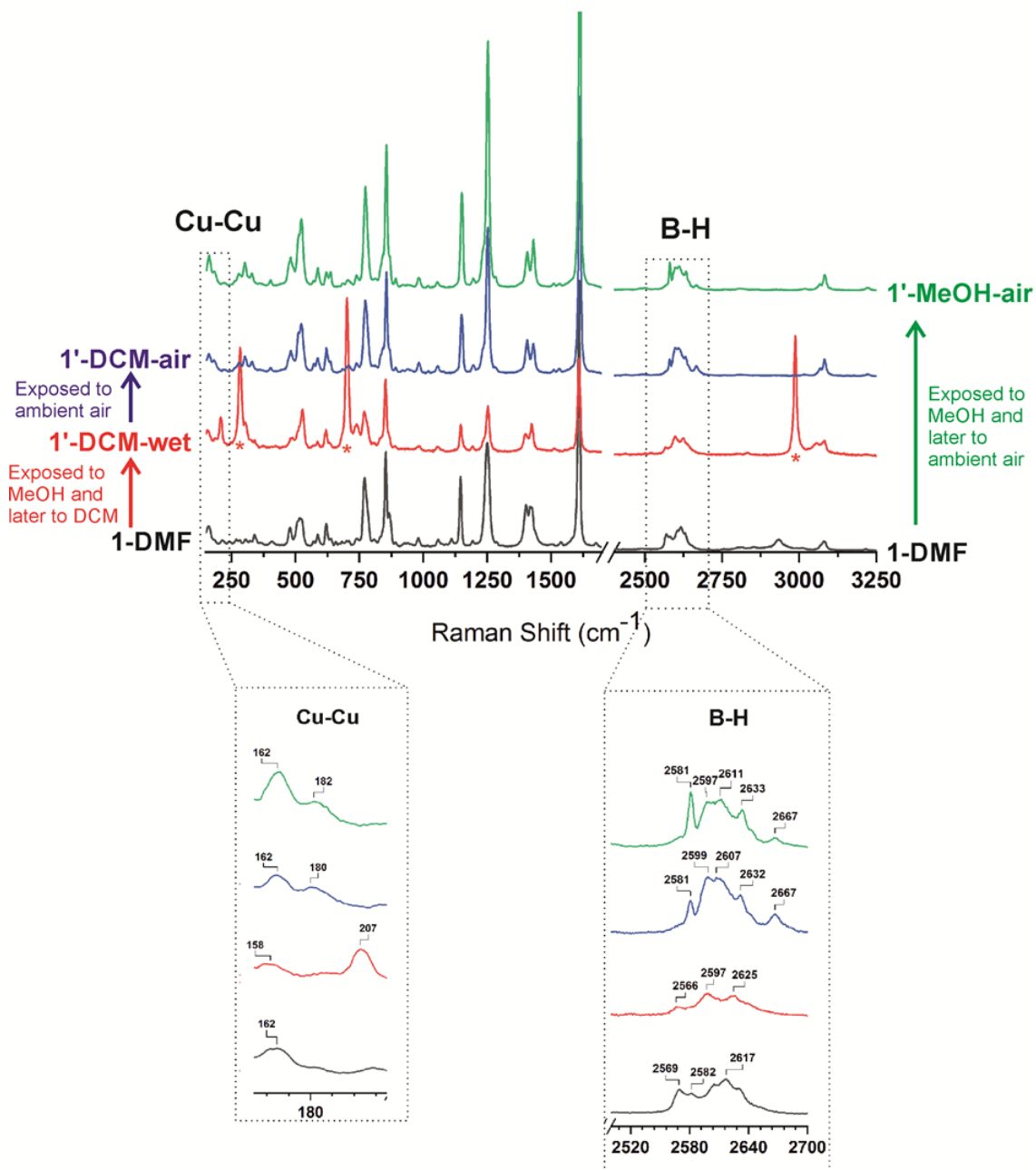


**Figure 3-10.** Comparison of Experimental Raman Spectra of **1-DMF**, **1'-DCM-wet**, **1'-DCM-air** and **1'-MeOH-air**.

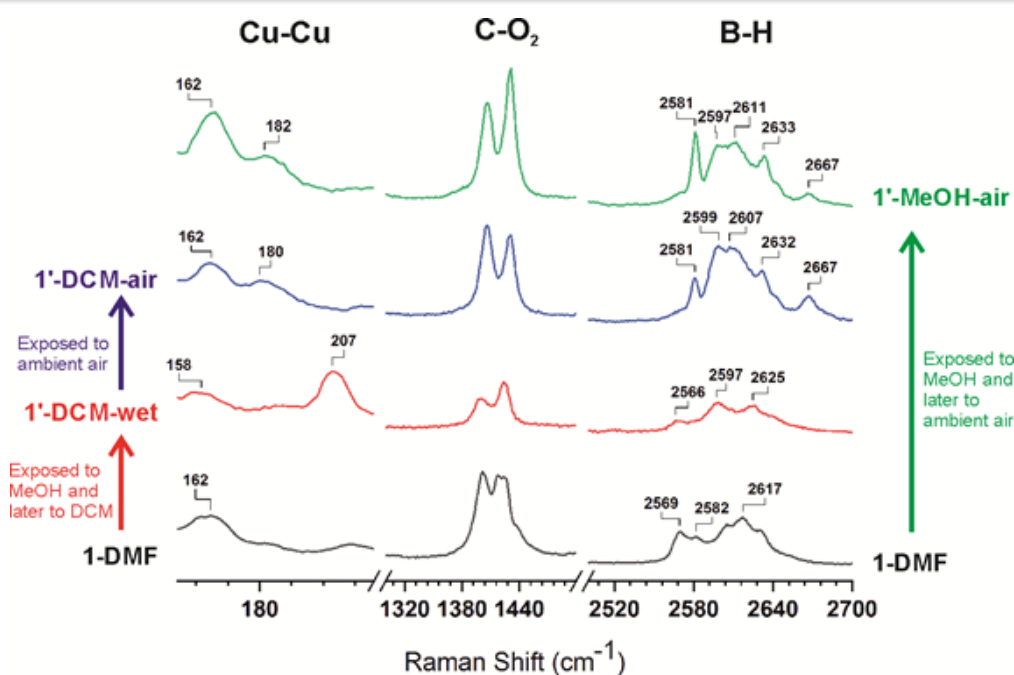


**Figure 3-11.** Successive changes in the Raman spectrum of **1-DMF** after sequential exposure to methanol (MeOH), dichloromethane ( $\text{CH}_2\text{Cl}_2$ ) and ambient air.

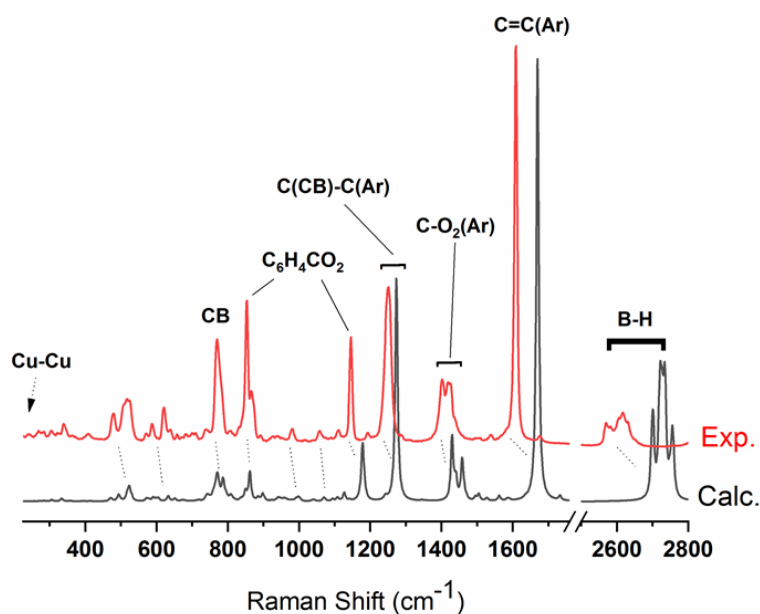
A deep understanding of the vibrational features described in the present work has been obtained by density functional theory (DFT) calculations (See the experimental section for details). In order to simplify the calculations, we used model structures consisting of four monosubstituted carborane based ligands bonded to a  $\text{Cu}_2$ -paddlewheel unit  $[\text{Cu}_2(\text{LCB})_4(\text{Solv})_2]$  ( $\text{LCB} = 1$ -(4-carboxyphenyl)-1,7-dicarba-*closo*-dodecaborane; Solv = DMF, MeOH,  $\text{H}_2\text{O}$ ,  $\text{C}_2\text{B}_{10}\text{H}_{12}$  and none; see Table 3-2, model compounds). We computed bond distances, vibrational frequencies and energies for paddlewheel units having DMF, MeOH,  $\text{H}_2\text{O}$ , none and/or a discrete *m*-carborane moiety bonded to the Cu atoms at the apical positions (Table 3-2). Calculation for the Cu-Cu vibrational frequencies for **1-DMF** resulted in a frequency of  $207 \text{ cm}^{-1}$ , a value significantly higher than the experimental value ( $162 \text{ cm}^{-1}$ ). This disagreement in the Cu-Cu calculated values was also observed in models for HKUST-1 [25]. The calculations however correlate well with the observed raman shifts (*vide infra*), that is, the vibrational frequencies increases as the coordination strength of Lewis base molecules decreases and viceversa. The calculated Raman spectra show a good agreement with the experimental data (Figure 3-12). Regardless of the expected shift between the experimental and calculated

## Results and Discussion

---

Raman spectra, the model provides reliable results in the range 300-3200  $\text{cm}^{-1}$  and allowed identification of all the experimental bands (Figure 3-12). Quite remarkably, the relatively sharp band at 2581  $\text{cm}^{-1}$  in **1'-CH<sub>2</sub>Cl<sub>2</sub>-air** and **1'-MeOH-air** (Figure 3-11) can be attributed to a B-H...Cu(II) agostic interaction, by comparison with our models where at least one hydride of a *m*-carborane molecule is coordinating to one of the Cu(II) atoms of the paddlewheel unit. In addition, the observed weak band at 2667  $\text{cm}^{-1}$  seems to correlate with one of the B-H hydrides in close proximity (although not bonded) to the Cu(II) atoms in the model. Comparison of the B-H Raman region for **1'-CH<sub>2</sub>Cl<sub>2</sub>-air** and **1'-MeOH-air** (Figure 3-11) with that for various models (Figure 3-13) indicates that interactions between 2D layers involve one or perhaps two B-H...Cu(II) interaction per paddlewheel unit. It is possible that not all Cu(II) atoms in each paddlewheel unit are interacting with a hydride, leaving this open to coordinate one water molecule from the air or even remain unsaturated (OMS). In fact, the corrugated shape of the 2D layers might complicate the match between all OMSs and available hydrides between layers. Further evidence for such B-H...Cu(II) interactions is obtained from the DFT calculations on our model compounds. An energy comparison of our DFT models (Table 3-2) reveals a clear stabilization of the fully open metal site model [Cu<sub>2</sub>(L<sub>CB</sub>)<sub>4</sub>] when interacting with one or two B-H hydrides. Thus, stabilization energies of 34.4, 26.7 or 13.6 Kcal/mol were obtained for [Cu<sub>2</sub>(L<sub>CB</sub>)<sub>4</sub>] interacting with one H<sub>2</sub>O and one *m*-carborane molecule, two *m*-carborane molecules or one OMS and one *m*-carborane molecule, respectively. In addition, calculated Cu-Cu vibrational frequencies for our models (Table 3-2) show the same trend that was observed experimentally (Figure 3-11), that is, a blue-shift (from lower to higher frequencies) on generation of open metal sites (or removal of DMF by CH<sub>2</sub>Cl<sub>2</sub> from **1-DMF**) and red-shift displacements (from higher to lower frequencies) on solvent or B-H coordination. Assuming that the observed trend is correct, we hypothesize that the experimentally observed Cu-Cu bands at 162 and 180  $\text{cm}^{-1}$  for **1'-CH<sub>2</sub>Cl<sub>2</sub>-air** and **1'-MeOH-air** correspond to B-H...Cu-Cu...H-B and B-H...Cu-Cu(OMS) species, although we cannot exclude the formation of partially hydrated species. In fact, it seems difficult that all Cu atoms are coordinated to a

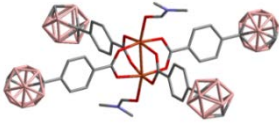
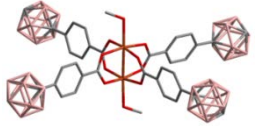
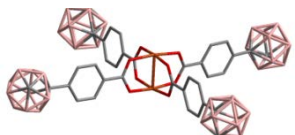
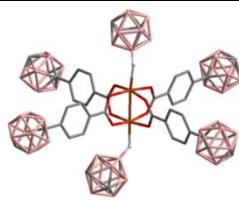
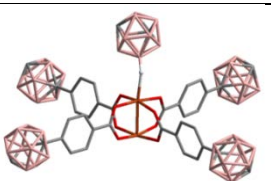
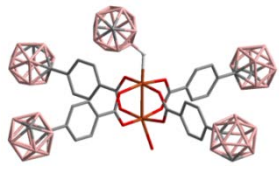
hydride atom, due to the high corrugation of 2D layers. It is also possible that multiple  $(\text{B-H})_x \cdots \text{Cu}$  interactions are taking place. This will certainly stabilize the binding enthalpy of such interactions [75]. A reversible coordination of B-H to a Cu(I) complex has been previously reported for a molecular system [75]. 2D CPs or MOFs present the unique feature of structural isomerism by sliding of layers involving the supramolecular interactions between them and the included solvent [76,77]. However, to our knowledge, no such mediated B-H $\cdots$ Metal transformations have been observed previously in coordination polymers or MOFs. The observed lower stability of crystals for **1-MeOH** than the corresponding ones for **1-DMF** (Figure 3-2), when exposed to air, can be explained by a comparable binding energy for B-H $\cdots$ Cu and Me(H)O $\cdots$ Cu interactions.



**Figure 3-12.** Comparison of Experimental and Calculated Raman for **1-DMF** with  $[\text{Cu}_2(\text{LCB})_4(\text{DMF})_2]$  ( $\text{LCB} = 1\text{-}(4\text{-carboxyphenyl})\text{-}1,7\text{-dicarba-}closo\text{-dodecaborane}$ ).

## Results and Discussion

**Table 3-2.** Calculated Energies, Cu-Cu Bond Lengths and vibrational frequencies for the Model compounds  $[\text{Cu}_2(\text{LCB})_4(\text{Solv})_2]$  (**LCB** = 1-(4-carboxyphenyl)-1,7-dicarba-closo-dodecaborane; Solv = DMF, MeOH, H<sub>2</sub>O, C<sub>2</sub>B<sub>10</sub>H<sub>12</sub> and none). See experimental section for details.

Model compounds (Molecules at the apical positions)	Energy <sup>a</sup> (Kcal/mol)	Cu-Cu distances (Å)		Vibrational Cu-Cu frequencies (cm <sup>-1</sup> )	
		Exp.	Calc.	Exp.	Calc.
 (2 Molecules of DMF)	-41.6	2.641 <sup>b</sup>	2.668	162 <sup>b</sup>	207
 (2 Molecules of MeOH)	-41.0	2.620 <sup>c</sup>	2.597	-	194
 (None)	0	-	2.507	-	223
 (2 Molecules of <i>m</i> -Carborane)	-26.7	-	2.561	-	206
 (1 Molecule of <i>m</i> -Carborane)	-13.6	-	2.536	-	214
 (1 Molecule of <i>m</i> -Carborane 1 molecule of H <sub>2</sub> O)	-34.4	-	2.577	-	192

<sup>a</sup> See DFT calculation section for details. <sup>b</sup> For **1-DMF**. <sup>c</sup> For **1-MeOH**.

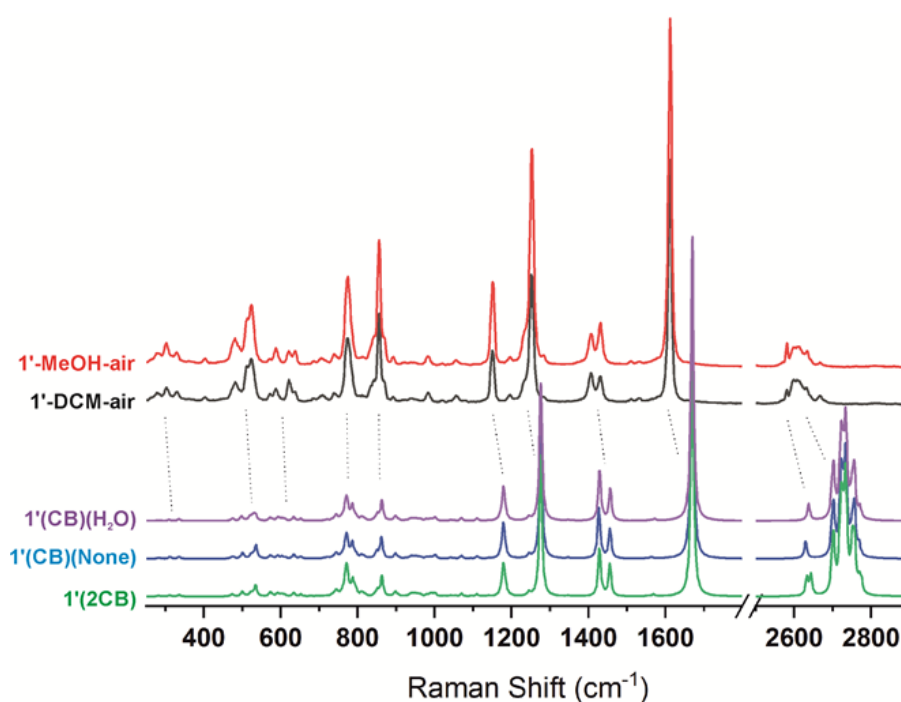


**Figure 3-13.** Comparison of Experimental and Calculated Raman for 1'-CH<sub>2</sub>Cl<sub>2</sub>-air and 1'-MeOH-air with [Cu<sub>2</sub>(LCB)<sub>4</sub>(Solv)<sub>2</sub>] (LCB = 1-(4-carboxyphenyl)-1,7-dicarba-*closo*-dodecaborane; Solv = H<sub>2</sub>O, *m*-C<sub>2</sub>B<sub>10</sub>H<sub>12</sub> and/or none).

### 3.3 Conclusions

In summary, we report the syntheses of 2D **1-Solv** (Solv: DMF, MeOH or CH<sub>2</sub>Cl<sub>2</sub>), a novel family of Cu<sub>2</sub>-paddlewheel CPs that incorporate the flexible ligand 1,7-di(4-carboxyphenyl)-1,7-dicarba-*closo*-dodecaborane (***m*CBL1**). **1-DMF** undergoes a reversible phase transition on solvent exchange and provided a crystalline material that is porous to N<sub>2</sub> and CO<sub>2</sub>. The combination of the experimental and calculated data supports the spontaneous release of the solvent from **1-DMF**, with the consequent generation of OMSs. Sliding of the layers allow the OMSs to be in close proximity to readily available hydride atoms of the many present from the carborane moieties, and thus promote the formation of B–H⋯Cu(II) interactions. The observed phase transition on solvent loss is accompanied by new Raman modes in the B–H and

Cu–Cu region that are in agreement with the formation of B–H···Cu(II) interactions. There is enough flexibility in the solid to move the paddlewheels relative to each other so that the Cu centers can interact with the many available hydride atoms from the carborane moieties in another paddlewheel unit. Such B–H···Cu(II) interactions can be easily disturbed in the presence of a strongly coordinating solvent such as DMF and provide the starting **1-DMF** structure at room temperature. The present work adds unprecedented knowledge to the possible reasons for boranes or carboranes acting to stabilize flexible MOFs [48] but it also discloses another possible mechanism for constructing new flexible architectures or hydride/MOF composites.

### **3.4 Experimental Section**

#### **3.4.1 Characterization and Methods**

Attenuated total reflection Fourier transformed infra-red (ATR-FTIR) spectra were recorded using a PerkinElmer Spectrum One spectrometer equipped with a Universal ATR sampling accessory. Spectra were collected with 2 cm<sup>-1</sup> spectral resolution in the 4000-650 cm<sup>-1</sup> range. Elemental analyses were obtained by using a Thermo (Carlo Erba) Flash 2000 Elemental Analyser, configured for wt.%CHN. Thermogravimetric Analysis (TGA) was performed in N<sub>2</sub>, on an nSTA 449 F1 Jupiter-Simultaneous TGA-DSC or SDT Q600 V8.3 Build 101 instruments (heating rate: 10 °C/min; temperature range: 25 °C to 600 °C). Gas sorption-desorption(CO<sub>2</sub>/273 K and N<sub>2</sub>/77 K) measurements were performed using an ASAP2020 surface area analyzer. Samples were first degassed at 120 °C for 20 h. Powder X-ray Diffraction (PXRD) was recorded at room temperature on a Siemens D-5000 diffractometer with Cu K $\alpha$  radiation Field-emission( $\lambda = 1.54056 \text{ \AA}$ , 45kV, 35mA, increment=0.02°). Morphological features were examined first by optical microscopy and next by scanning electron microscopy (SEM) with a QUANTA FEI 200 FEGSEM microscope. *Raman spectra were recorded* using an LabRam HR800 (Horiba

Jobin-Yvon) dispersive micro-Raman spectrometer coupled with a CCD detector. A solid state laser with a 532 nm wavelength was used as the excitation source and the spectra were measured in a backscattering configuration through an Olympus BXFM objective. Excitation of the samples was performed by focusing the laser beam on crystalline samples with a laser power of 0.5 mW with a 50x magnifying objective lens.

### 3.4.2 Materials

1,7-di(4-carboxyphenyl)-1,7-dicarba-*closo*-dodecaborane ligand was synthesized according to the literature procedure [78]. CPs syntheses were done in air. All chemicals were commercially available and used as received.

Synthesis of  $[\text{Cu}_2(\mathbf{mCB-L1})_2(\text{DMF})_2] \cdot 2\text{DMF} \cdot \text{H}_2\text{O}$  (**1-DMF**).  $\text{Cu}(\text{NO}_3)_2 \cdot 6\text{H}_2\text{O}$  (48.7 mg, 0.167 mmol) was mixed with  $\mathbf{mCB-H_2L1}$  (64.1 mg, 0.167 mmol) in 4 mL of DMF. This mixture was sonicated until all solids were uniformly dissolved, followed by heating at 80 °C for 48 h. Greenish crystals of **1-DMF** were collected and washed with DMF (60 mg, 59.8 %). IR (ATR; selected bands;  $\text{cm}^{-1}$ ): 2605, 2570 (BH); 1672 (C=O from DMF); 1617 (C=O from carboxylate). Elemental analysis (%) calculated for  $\text{Cu}_2(\mathbf{mCB-L1})_2(\text{DMF})_4(\text{H}_2\text{O})$ : C 43.96, H 5.53, N 4.66; Found: C 43.91, H 5.58, N 5.20.

Synthesis of  $[\text{Cu}_2(\mathbf{mCB-L1})_2(\text{DMA})_2] \cdot \text{DMA} \cdot \text{H}_2\text{O}$  (**1-DMA**).  $\text{Cu}(\text{NO}_3)_2 \cdot 6\text{H}_2\text{O}$  (48.7 mg, 0.167 mmol) was mixed with  $\mathbf{mCB-H_2L1}$  (64.1 mg, 0.167 mmol) in 4 mL of DMA. This mixture was sonicated until all solids were uniformly dissolved, followed by heating at 80 °C for 48 h. Greenish crystals of **1-DMA** were collected and washed with DMA (55.0 mg, 56.2 %). IR (ATR; selected bands;  $\text{cm}^{-1}$ ): 2604 (BH); 1646 (C=O from DMA); 1602 (C=O from carboxylate). Elemental analysis (%) calculated for  $\text{Cu}_2(\mathbf{mCB-L1})_2(\text{DMA})_3(\text{H}_2\text{O})$ : C 45.12, H 5.59, N 3.59; Found: C 44.52, H 5.51,



N 4.02.

[Cu<sub>2</sub>(*mCB-L1*)<sub>2</sub>(MeOH)<sub>2</sub>].4MeOH (**1-MeOH**). Cu(NO<sub>3</sub>)<sub>2</sub>.6H<sub>2</sub>O (48.7 mg, 0.167 mmol) was mixed with *mCB-H<sub>2</sub>L1* (64.1 mg, 0.167 mmol) in 4 mL of MeOH. This mixture was sonicated until all solids were uniformly dissolved, followed by heating at 80 °C for 24 h. Light-blue crystals of **1-MeOH** were collected, washed with MeOH and stored in this solvent (46 mg, 50.8 %).

General method for chemical activation of **1-DMF**. As-synthesized greenish crystals of **1-DMF** (10 mg) were immersed in methanol (10 mL), provoking **1-DMF** brake into smaller sky blue crystals of **1'-MeOH**. MeOH was further exchanged once a day for 2 days and replaced by CH<sub>2</sub>Cl<sub>2</sub> (10 mL). The latter provided deep blue crystals for **1'-CH<sub>2</sub>Cl<sub>2</sub>-wet** after 10 minutes. The entire process was performed while maintaining the crystals fully covered with the solvents. When deep blue crystals for **1'-CH<sub>2</sub>Cl<sub>2</sub>-wet** were dried on filter paper at room temperature a very fast color change was observed to sky blue crystals for **1'-CH<sub>2</sub>Cl<sub>2</sub>-air**.

**1'-MeOH-air**: IR (ATR; selected bands; cm<sup>-1</sup>): 2596, 2579 (BH); 1610 (C=O from carboxylate). Elemental analysis (%) calculated for Cu<sub>2</sub>(*mCB-L1*)<sub>2</sub>(H<sub>2</sub>O)(2MeOH): C 41.93, H 4.76; Found: C 41.99, H 4.70.

**1'-CH<sub>2</sub>Cl<sub>2</sub>-air**: IR (ATR; selected bands; cm<sup>-1</sup>): 2596, 25 (BH); 1610 (C=O from carboxylate). Elemental analysis (%) calculated for Cu<sub>2</sub>(*mCB-L1*)<sub>2</sub>(H<sub>2</sub>O)(CH<sub>2</sub>Cl<sub>2</sub>): C 39.84, H 4.05; Found: C 39.71, H 4.26.

Synthesis of **1-DMF** from **1'-Solv-air**. Crystals for freshly made **1'-Solv-air** (10 mg; Solv = MeOH or CH<sub>2</sub>Cl<sub>2</sub>) were suspended in DMF (10 mL) in a capped glass vial and left at room temperature for 3 days. No dissolution of the crystals was observed during this time. The obtained crystals for **1-DMF** were then filtered, washed with DMF and stored in the same solvent.

### 3.4.3 Crystallography

Measured crystals were prepared under inert conditions immersed in perfluoropolyether or paratone as protecting oil for manipulation. Suitable crystals were mounted on MiTeGen Micromounts<sup>TM</sup>, and used for data collection. Crystallographic data for **1-DMA** were collected with a Bruker D8 Venture diffractometer, processed with APEX3 program[79] and corrected for absorption using TWINABS[80]. The structures were solved by direct methods and subsequently refined by correction of  $F^2$  against all reflections. All non-hydrogen atoms were refined with anisotropic thermal parameters by full-matrix least-squares calculations on  $F^2$ [81]. Hydrogen atoms were not located in difference Fourier maps and included as fixed contributions riding on attached atoms with isotropic thermal displacement parameter 1.2 (C-H, B-H) or 1.5 (O-H) times those of the respective atom. **1-DMA** was treated as a two component non-merohedral twin. The twin matrix describes a rotation of 179.8° around the [1 -1 0] direction, given by the matrix (0 -1 0 0 -1 0 0 0 0 -1). The structure of **1-DMA** was solved using direct methods with only the non-overlapping reflections of component 1. The structure was refined using the HKLF 5 routine with all reflections of component 1 (including the overlapping ones), resulting in a BASF value of 0.2356(12). The structure exhibits disorder of the coordinated DMA molecule, which was successfully refined using a two-site model with 0.63:0.37 occupancy ratio. The contribution of the disordered solvent molecules to the diffraction pattern could not be rigorously included in the model and were consequently removed with the SQUEEZE routine of PLATON[82] that suggest the presence of 2 DMA molecules that have not been included in the refined structure but considered for calculation of empirical formula, formula weight, density, linear absorption coefficient and F(000).

Crystallographic data for **1-DMF** and **1-MeOH** were collected on a Rigaku AFC12 4-circle goniometer equipped with a HyPix 6000HE (Hybrid Photon Counting) detector mounted at the window of an FR-E+ SuperBright molybdenum (Mo

$K\alpha_1/K\alpha_2 = 0.71073\text{\AA}$ ) rotating anode generator with VHF Varimax optics (70 $\mu\text{m}$  focus) operating at 2.475kW (45kV, 55mA). Data reduction was performed using the CrysAlisPro (Rigaku, V1.171.40.18b, 2018) software and the structure was solved by Intrinsic Phasing using the ShelXT (Sheldrick, 2015) structure solution program and refined by Least Squares using version 2016/6 of ShelXL (Sheldrick, 2015). In the case of **1-MeOH** the crystal was a non-merohedral twin and data integrated from one component were used for the refinement. Discarding severely overlapped reflections has led to a low completeness.

### 3.4.4 Computational Details

The geometry of all computed systems was optimized by dispersion-corrected (D3)[83] density functional theory (DFT) using the hybrid B3LYP functional[84-86] as implemented in the Gaussian 09 [87]. The Cu atom was described using the scalar relativistic Stuttgart–Dresden SDD pseudopotential and its associated double- $\zeta$  basis set[88], complemented with a set of  $f$  polarization functions [89]. The 6-31G(d) basis sets was used for the rest of atoms [90]. All stationary points were characterized and confirmed by frequency analysis.

Calculations were performed on molecular structures according to the general formula  $[\text{Cu}_2(m\text{CB-L1})_2(\text{Solv})_2]$  where  $m\text{CB-H}_2\text{L1}$  is 1,7-di(4-carboxyphenyl)-1,7-dicarb-*closo*-dodecaborane. Several Solv were considered occupying two coordination sites to investigate their effect on the properties of the system. The Solv molecules computed were DMF, H<sub>2</sub>O, MeOH and *closo*-dodecaborane.

The electronic state of the system was initially investigated for Solv=DMF and MeOH. The closed shell singlets were calculated to be 35.8 kcal/mol and 35.4 kcal/mol higher in energy than the triplets for the complexes with DMF and MeOH as Solv,

respectively. Nevertheless, the open shell singlets states were calculated to be lower in energy than the triplet state by 0.6 kcal/mol for both complexes. This is in agreement with previous DFT studies in the literature for copper paddlewheel based systems [91-95]. Thus, all the structures presented in this work were calculated as open shell singlets (Calculation details see in Table S3-3).

### 3.5 References

- [1] Long, J.R.; Yaghi, O.M. *Chemical Society Reviews* **2009**, *38*, 1213.
- [2] Kitagawa, S.; Kitaura, R.; Noro, S.-i. *Angewandte Chemie International Edition* **2004**, *43*, 2334.
- [3] James, S.L. *Chemical Society Reviews* **2003**, *32*, 276.
- [4] Li, H.; Eddaoudi, M.; O'Keeffe, M.; Yaghi, O.M. *Nature* **1999**, *402*, 276.
- [5] Zhu, L.; Liu, X.-Q.; Jiang, H.-L.; Sun, L.-B. *Chemical Reviews* **2017**, *117*, 8129.
- [6] Kang, Y.-S.; Lu, Y.; Chen, K.; Zhao, Y.; Wang, P.; Sun, W.-Y. *Coordination Chemistry Reviews* **2019**, *378*, 262.
- [7] Dhakshinamoorthy, A.; Li, Z.; Garcia, H. *Chemical Society Reviews* **2018**, *47*, 8134.
- [8] Kumar, K.V.; Preuss, K.; Titirici, M.-M.; Rodríguez-Reinoso, F. *Chemical Reviews* **2017**, *117*, 1796.
- [9] Bobbitt, N.S.; Mendonca, M.L.; Howarth, A.J.; Islamoglu, T.; Hupp, J.T.; Farha, O.K.; Snurr, R.Q. *Chemical Society Reviews* **2017**, *46*, 3357.
- [10] Li, J.-R.; Sculley, J.; Zhou, H.-C. *Chemical Reviews* **2012**, *112*, 869.
- [11] Furukawa, H.; Cordova, K.E.; O'Keeffe, M.; Yaghi, O.M. *Science* **2013**, *341*, 1230444.
- [12] Yu, J.; Xie, L.-H.; Li, J.-R.; Ma, Y.; Seminario, J.M.; Balbuena, P.B. *Chemical Reviews* **2017**, *117*, 9674.
- [13] Gassensmith, J.J.; Kim, J.Y.; Holcroft, J.M.; Farha, O.K.; Stoddart, J.F.; Hupp, J.T.; Jeong, N.C. *Journal of the American Chemical Society* **2014**, *136*, 8277.
- [14] Huang, R.-W.; Wei, Y.-S.; Dong, X.-Y.; Wu, X.-H.; Du, C.-X.; Zang, S.-Q.; Mak, T.C.W. *Nature Chemistry* **2017**, *9*, 689.
- [15] Easun, T.L.; Moreau, F.; Yan, Y.; Yang, S.; Schröder, M. *Chemical Society Reviews* **2017**, *46*, 239.
- [16] Morris, R.E.; Brammer, L. *Chemical Society Reviews* **2017**, *46*, 5444.
- [17] Lee, J.S.; Vlaisavljevich, B.; Britt, D.K.; Brown, C.M.; Haranczyk, M.; Neaton, J.B.; Smit, B.; Long, J.R.; Queen, W.L. *Advanced Materials* **2015**, *27*, 5785.
- [18] Furukawa, H.; Kim, J.; Ockwig, N.W.; O'Keeffe, M.; Yaghi, O.M. *Journal of the American Chemical Society* **2008**, *130*, 11650.
- [19] Eddaoudi, M.; Kim, J.; Vodak, D.; Sudik, A.; Wachter, J.; O'Keeffe, M.; Yaghi, O.M. *Proceedings of the National Academy of Sciences* **2002**, *99*, 4900.
- [20] Köberl, M.; Cokoja, M.; Herrmann, W.A.; Kühn, F.E. *Dalton Transactions* **2011**, *40*, 6834.
- [21] Howarth, A.J.; Peters, A.W.; Vermeulen, N.A.; Wang, T.C.; Hupp, J.T.; Farha, O.K. *Chemistry of Materials* **2017**, *29*, 26.
- [22] Mondloch, J.E.; Karagiari, O.; Farha, O.K.; Hupp, J.T. *CrystEngComm* **2013**, *15*, 9258.
- [23] Choi, J.S.; Bae, J.; Lee, E.J.; Jeong, N.C. *Inorganic Chemistry* **2018**, *57*, 5225.
- [24] Bae, J.; Lee, E.J.; Jeong, N.C. *Chemical Communications* **2018**, *54*, 6458.
- [25] Kim, H.K.; Yun, W.S.; Kim, M.-B.; Kim, J.Y.; Bae, Y.-S.; Lee, J.; Jeong, N.C. *Journal of the American Chemical Society* **2015**, *137*, 10009.
- [26] Bae, J.; Choi, J.S.; Hwang, S.; Yun, W.S.; Song, D.; Lee, J.; Jeong, N.C. *ACS Applied Materials & Interfaces* **2017**, *9*, 24743.
- [27] Ren, J.; Ledwaba, M.; Musyoka, N.M.; Langmi, H.W.; Mathe, M.; Liao, S.; Pang, W. *Coordination Chemistry Reviews* **2017**, *349*, 169.
- [28] Scholz, M.; Hey-Hawkins, E. *Chemical Reviews* **2011**, *111*, 7035.

- [29] Grimes, R.N. Carboranes. In *Carboranes (Third Edition)*, Academic Press: Oxford, 2016.
- [30] Teixidor, F.; Viñas, C. In *Science of Synthesis*, D.E., K., D.S., M., Eds. Thieme: Stuttgart, 2005; Vol. 6, pp. 1325.
- [31] Teixidor, F.; Barberà, G.; Vaca, A.; Kivekäs, R.; Sillanpää, R.; Oliva, J.; Viñas, C. *Journal of the American Chemical Society* **2005**, *127*, 10158.
- [32] Poater, J.; Solà, M.; Viñas, C.; Teixidor, F. *Angewandte Chemie - International Edition* **2014**, *53*, 12191.
- [33] Fontanet, M.; Popescu, A.R.; Fontrodona, X.; Rodríguez, M.; Romero, I.; Teixidor, F.; Viñas, C.; Aliaga-Alcalde, N.; Ruiz, E. *Chemistry - A European Journal* **2011**, *17*, 13217.
- [34] Fontanet, M.; Rodríguez, M.; Romero, I.; Fontrodona, X.; Teixidor, F.; Viñas, C.; Aliaga-Alcalde, N.; Matějček, P. *Dalton Transactions* **2013**, *42*, 7838.
- [35] Fontanet, M.; Rodríguez, M.; Fontrodona, X.; Romero, I.; Teixidor, F.; Viñas, C.; Aliaga-Alcalde, N.; Matějček, P. *Chemistry - A European Journal* **2014**, *20*, 13993.
- [36] Bae, Y.S.; Spokoyny, A.M.; Farha, O.K.; Snurr, R.Q.; Hupp, J.T.; Mirkin, C.A. *Chemical Communications* **2010**, *46*, 3478.
- [37] Bae, Y.-S.; Farha, O.K.; Spokoyny, A.M.; Mirkin, C.A.; Hupp, J.T.; Snurr, R.Q. *Chemical Communications* **2008**, 10.1039/B805785K, 4135.
- [38] Clingerman, D.J.; Morris, W.; Mondloch, J.E.; Kennedy, R.D.; Sarjeant, A.A.; Stern, C.; Hupp, J.T.; Farha, O.K.; Mirkin, C.A. *Chemical Communications* **2015**, *51*, 6521.
- [39] Kennedy, R.D.; Krungleviciute, V.; Clingerman, D.J.; Mondloch, J.E.; Peng, Y.; Wilmer, C.E.; Sarjeant, A.A.; Snurr, R.Q.; Hupp, J.T.; Yildirim, T., et al. *Chemistry of Materials* **2013**, *25*, 3539.
- [40] Spokoyny, A.M.; Farha, O.K.; Mulfort, K.L.; Hupp, J.T.; Mirkin, C.A. *Inorganica Chimica Acta* **2010**, *364*, 266.
- [41] Farha, O.K.; Spokoyny, A.M.; Mulfort, K.L.; Hawthorne, M.F.; Mirkin, C.A.; Hupp, J.T. *Journal of the American Chemical Society* **2007**, *129*, 12680.
- [42] Farha, O.K.; Spokoyny, A.M.; Mulfort, K.L.; Galli, S.; Hupp, J.T.; Mirkin, C.A. *Small* **2009**, *5*, 1727.
- [43] Huang, S.L.; Lin, Y.J.; Yu, W.B.; Jin, G.X. *ChemPlusChem* **2012**, *77*, 141.
- [44] Huang, S.L.; Weng, L.H.; Jin, G.X. *Dalton Transactions* **2012**, *41*, 11657.
- [45] Boldog, I.; Bereciartua, P.J.; Bulánek, R.; Kučeráková, M.; Tomandlová, M.; Dušek, M.; Macháček, J.; De Vos, D.; Baše, T. *CrystEngComm* **2016**, *18*, 2036.
- [46] Tsang, M.Y.; Rodríguez-Hermida, S.; Stylianou, K.C.; Tan, F.; Negi, D.; Teixidor, F.; Viñas, C.; Choquesillo-Lazarte, D.; Verdugo-Escamilla, C.; Guerrero, M., et al. *Crystal Growth & Design* **2017**, *17*, 846.
- [47] Rodríguez-Hermida, S.; Tsang, M.Y.; Vignatti, C.; Stylianou, K.C.; Guillerm, V.; Perez-Carvajal, J.; Teixidor, F.; Vinas, C.; Choquesillo-Lazarte, D.; Verdugo-Escamilla, C., et al. *Angew Chem Int Ed Engl* **2016**, *55*, 16049.
- [48] Tan, F.; López-Periago, A.; Light, M.E.; Cirera, J.; Ruiz, E.; Borrás, A.; Teixidor, F.; Viñas, C.; Domingo, C.; Planas, J.G. *Advanced Materials* **2018**, *30*, 1800726.
- [49] Di Salvo, F.; Camargo, B.; Garcia, Y.; Teixidor, F.; Viñas, C.; Giner Planas, J.; Light, M.E.; Hursthouse, M.B. *CrystEngComm* **2011**, *13*, 5788.
- [50] Planas, J.G.; Vinas, C.; Teixidor, F.; Comas-Vives, A.; Ujaque, G.; Lledos, A.; Light, M.E.; Hursthouse, M.B. *Journal of the American Chemical Society* **2005**, *127*, 15976.
- [51] Fox, M.A.; Hughes, A.K. *Coordination Chemistry Reviews* **2004**, *248*, 457.

## References

---

- [52] Chaari, M.; Kelemen, Z.; Planas, J.G.; Teixidor, F.; Choquesillo-Lazarte, D.; Ben Salah, A.; Viñas, C.; Núñez, R. *Journal of Materials Chemistry C* **2018**, *6*, 11336.
- [53] Zhang, X.; Dai, H.; Yan, H.; Zou, W.; Cremer, D. *Journal of the American Chemical Society* **2016**, *138*, 4334.
- [54] Terrasson, V.; Garcia, Y.; Farras, P.; Teixidor, F.; Viñas, C.; Giner Planas, J.; Prim, D.; Light, M.E.; Hursthouse, M.B. *CrystEngComm* **2010**, *12*, 4109.
- [55] Eleazer, B.J.; Peryshkov, D.V. *Comments on Inorganic Chemistry* **2018**, *38*, 79.
- [56] Riley, L.E.; Chan, A.P.Y.; Taylor, J.; Man, W.Y.; Ellis, D.; Rosair, G.M.; Welch, A.J.; Sivaev, I.B. *Dalton Transactions* **2016**, *45*, 1127.
- [57] Cunha-Silva, L.; Carr, M.J.; Kennedy, J.D.; Hardie, M.J. *Crystal Growth & Design* **2013**, *13*, 3162.
- [58] Teixidor, F.; Flores, M.A.; Viñas, C.; Sillanpää, R.; Kivekäs, R. *Journal of the American Chemical Society* **2000**, *122*, 1963.
- [59] Behnken, P.E.; Marder, T.B.; Baker, R.T.; Knobler, C.B.; Thompson, M.R.; Hawthorne, M.F. *Journal of the American Chemical Society* **1985**, *107*, 932.
- [60] Long, J.A.; Marder, T.B.; Behnken, P.E.; Hawthorne, M.F. *Journal of the American Chemical Society* **1984**, *106*, 2979.
- [61] Knobler, C.B.; Marder, T.B.; Mizusawa, E.A.; Teller, R.G.; Long, J.A.; Behnken, P.E.; Hawthorne, M.F. *Journal of the American Chemical Society* **1984**, *106*, 2990.
- [62] Teixidor, F.; Flores, M.A.; Viñas, C.; Kivekäs, R.; Sillanpää, R. *Angewandte Chemie International Edition in English* **1996**, *35*, 2251.
- [63] Gao, Y.; Guo, S.-T.; Cui, P.-F.; Aznarez, F.; Jin, G.-X. *Chemical Communications* **2019**, *55*, 210.
- [64] Yao, Z.-J.; Deng, W. *Coordination Chemistry Reviews* **2016**, *309*, 21.
- [65] Vinas, C.; Nunez, R.; Flores, M.A.; Teixidor, F.; Kivekas, R.; Sillanpaea, R. *Organometallics* **1995**, *14*, 3952.
- [66] Viñas, C.; Nuñez, R.; Teixidor, F.; Kivekäs, R.; Sillanpää, R. *Organometallics* **1996**, *15*, 3850.
- [67] Zhang, Y.; Yang, L.; Wang, L.; Duttwyler, S.; Xing, H. *Angewandte Chemie International Edition* **2019**, DOI: 10.1002/anie.201903600.
- [68] Zhu, C.; Mao, Q.; Li, D.; Li, C.; Zhou, Y.; Wu, X.; Luo, Y.; Li, Y. *Catalysis Communications* **2018**, *104*, 123.
- [69] Zhang, J.; Wang, B.; Li, M.; Zhao, M.-J.; Xie, Y.-B.; Li, J.-R. *Journal of Coordination Chemistry* **2016**, *69*, 2193.
- [70] He, Z.; Pang, Q.; Rankine, D.; Sumby, C.J.; Zhang, L.; Doonan, C.J.; Li, Q. *CrystEngComm* **2013**, *15*, 9340.
- [71] Sasaki, T.; Hisaki, I.; Miyano, T.; Tohnai, N.; Morimoto, K.; Sato, H.; Tsuzuki, S.; Miyata, M. *Nature Communications* **2013**, *4*, 1787.
- [72] Zhong, R.-Q.; Zou, R.-Q.; Xu, Q. *CrystEngComm* **2011**, *13*, 577.
- [73] Note that it was not possible to differentiate the Cu-coordinated solvent molecules by elemental analysis in this case. Thus, the formula could be either [Cu(L1)2(H2O)(MeOH)].MeOH or [Cu(L1)2(MeOH)2].H2O.
- [74] Wang, X.-F.; Zhang, Y.-B.; Huang, H.; Zhang, J.-P.; Chen, X.-M. *Crystal Growth & Design* **2008**, *8*, 4559.
- [75] Hicken, A.; White, A.J.P.; Crimmin, M.R. *Inorganic Chemistry* **2017**, *56*, 8669.
- [76] Biradha, K.; Hongo, Y.; Fujita, M. *Angewandte Chemie International Edition* **2002**, *41*, 3395.
- [77] Zhang, J.-P.; Liao, P.-Q.; Zhou, H.-L.; Lin, R.-B.; Chen, X.-M. *Chemical Society Reviews* **2014**, *43*,

- 5789.
- [78] Fox, Mark Alexander (1991) Icosahedral carborane derivatives., Durham theses, Durham University.
- [79] Bruker, APEX3 Software, V2016.1; Bruker AXS Inc.: Madison, WI, 2016.
- [80] Sheldrick, G. M. TWINABS; University of Göttingen, Germany, 2012.
- [81] Sheldrick, G. *Acta Crystallographica Section A* **2008**, *64*, 112.
- [82] Spek, A. *Acta Crystallographica Section D* **2009**, *65*, 148.
- [83] Grimme, S.; Antony, J.; Ehrlich, S.; Krieg, H. *The Journal of Chemical Physics* **2010**, *132*, 154104.
- [84] Becke, A.D. *The Journal of Chemical Physics* **1993**, *98*, 5648.
- [85] Lee, C.; Yang, W.; Parr, R.G. *Physical Review B* **1988**, *37*, 785.
- [86] Stephens, P.J.; Devlin, F.J.; Chabalowski, C.F.; Frisch, M.J. *The Journal of Physical Chemistry* **1994**, *98*, 11623.
- [87] Gaussian 09, Revision D.01, M. J. Frisch, G. W. Trucks, H. B. Schlegel, G. E. Scuseria, M. A. Robb, J. R. Cheeseman, G. Scalmani, V. Barone, B. Mennucci, G. A. Petersson, H. Nakatsuji, M. Caricato, X. Li, H. P. Hratchian, A. F. Izmaylov, J. Bloino, G. Zheng, J. L. Sonnenberg, M. Hada, M. Ehara, K. Toyota, R. Fukuda, J. Hasegawa, M. Ishida, T. Nakajima, Y. Honda, O. Kitao, H. Nakai, T. Vreven, J. A. Montgomery, Jr., J. E. Peralta, F. Ogliaro, M. Bearpark, J. J. Heyd, E. Brothers, K. N. Kudin, V. N. Staroverov, T. Keith, R. Kobayashi, J. Normand, K. Raghavachari, A. Rendell, J. C. Burant, S. S. Iyengar, J. Tomasi, M. Cossi, N. Rega, J. M. Millam, M. Klene, J. E. Knox, J. B. Cross, V. Bakken, C. Adamo, J. Jaramillo, R. Gomperts, R. E. Stratmann, O. Yazyev, A. J. Austin, R. Cammi, C. Pomelli, J. W. Ochterski, R. L. Martin, K. Morokuma, V. G. Zakrzewski, G. A. Voth, P. Salvador, J. J. Dannenberg, S. Dapprich, A. D. Daniels, O. Farkas, J. B. Foresman, J. V. Ortiz, J. Cioslowski, D. J. Fox, Gaussian, Inc., Wallingford CT, 2013.
- [88] Andrae, D.; Häußermann, U.; Dolg, M.; Stoll, H.; Preuß, H. *Theoretica chimica acta* **1990**, *77*, 123.
- [89] Ehlers, A.W.; Böhme, M.; Dapprich, S.; Gobbi, A.; Höllwarth, A.; Jonas, V.; Köhler, K.F.; Stegmann, R.; Veldkamp, A.; Frenking, G. *Chemical Physics Letters* **1993**, *208*, 111.
- [90] Francl, M.M.; Pietro, W.J.; Hehre, W.J.; Binkley, J.S.; Gordon, M.S.; DeFrees, D.J.; Pople, J.A. *The Journal of Chemical Physics* **1982**, *77*, 3654.
- [91] Rodríguez-Forteza, A.; Alemany, P.; Alvarez, S.; Ruiz, E. *Chemistry – A European Journal* **2001**, *7*, 627.
- [92] Ali, M.E.; Datta, S.N. *Journal of Molecular Structure: THEOCHEM* **2006**, *775*, 19.
- [93] Bureekaew, S.; Amirjalayer, S.; Schmid, R. *Journal of Materials Chemistry* **2012**, *22*, 10249.
- [94] Tafipolsky, M.; Amirjalayer, S.; Schmid, R. *The Journal of Physical Chemistry C* **2010**, *114*, 14402.
- [95] Alzahrani, K.A.H.; Deeth, R.J. *Dalton Transactions* **2016**, *45*, 11944.



## *References*

---

# Chapter 4

---

*A Highly Water-Stable  
meta-Carborane-Based Copper  
Metal-Organic Framework for  
Efficient High-Temperature Butanol  
Separation*



---

# A Highly Water-Stable *meta*-Carborane-Based Copper Metal-Organic Framework for Efficient High-Temperature Butanol Separation

## 4.1 Introduction

Biofuels are gaining a continual prominence, primarily to augment the security of energy and supply, and thus contribute to the development of a sustainable economy. Biofuels are also emerging as one of the overarching solutions for Bioenergy with Carbon Capture and Storage (BECCS), a negative emission technology for meeting the global warming target[1,2]. It is therefore, not surprising that many countries promote the use of biofuels through supportive legislation, policy measures, and capital investments. Biobutanol is considered as an attractive renewable transportation fuel as it exhibits superior performance and properties when is compared with bioethanol [3]. Biobutanol is less hydroscopic, has higher energy density (30% on a unit volume basis, 98% of that of gasoline), lower vapor pressure, and superior miscibility with gasoline. Also, biobutanol is considered a viable biochemical alternative to synthetic butanol, whose costs are determined by crude oil prices. It can potentially replace petro-butanol, and be an essential precursor for mainstream industrial chemicals and several high-value products like paints, polymers, and plastics. Owing to the prospective multisector applications, there has been an increasing commercial interest in the production of biobutanol. Typically, biobutanol is produced through the Acetone-Butanol-Ethanol (ABE) fermentation process of biomass feedstock. The critical challenge we have to overcome with this process lies in the low yield and productivity, with biobutanol being a dilute alcohol-in-water solution (concentration of < 2 wt%), resulting in prohibitively expensive downstream processing costs. Addressing this challenge can enhance the technical and economic viability of this process. To date, there are two proposed approaches to overcome this:

- i. Through genetic engineering-based modification of microorganisms to enhance the

## ***Introduction***

---

product yield and concentration and thereby reducing the production costs and ii. Through the development of a downstream (hybrid) separation process, which is cost-effective, energy-efficient, and easily integrated with the ABE fermentation reactor in recovering biobutanol [4-6].

The traditional distillation process is identified as the most energy demanding separation technique for the recovery of biobutanol owing to the evaporation of high-water content (>95%) in the feed stream. Additionally, through distillation, azeotropes might be formed. Alternatively, several prospective technologies have been suggested to make the biobutanol recovery process profitable [7-9]. Amongst these, adsorption is identified as one of the energy-efficient alternative [10]. Adsorbent materials such as polymeric resins, activated carbon, zeolites, zeolitic imidazolate frameworks (ZIFs) and metal-organic frameworks (MOFs) have been tested towards biobutanol recovery, and most studies reported in the literature are performed predominantly under liquid-phase conditions [11]. On the other hand, the gas stripping separation technique functions by the selective removal of volatile products, i.e., ABE from the fermentation broth, which is later condensed to yield biobutanol [12]. This stripping is performed with the aid of a sparging gas like N<sub>2</sub>, CO<sub>2</sub> or He. Gas stripping facilitates a higher recovery of ABE in the vapor phase than in the liquid phase. In addition, unlike liquid phase sorption, gas stripping ensures the circumvention of non-volatiles like microbial cells, sugars, and/or reaction intermediates (acetic acid and butyric acid) being removed from broth. However, it suffers from low selectivity and the possibility to form foams within the fermenter.

A hybrid separation technique that combines the merits of gas stripping and vapor phase adsorption and effectively overcomes the demerits of their standalone processes was recently proposed [13,14]. It involves the removal of acetone, butanol, and ethanol in their vapor state from liquid solutions using a sparging gas, and subsequently, through vapor adsorption, the separation of biobutanol is achieved (Figure 4-1). In that respect, a system that uses humid CO<sub>2</sub> to sparge the fermenter and ZIFs as

adsorbents for biobutanol separation becomes the only MOF based system to be reported to date [15]. Overall, the critical issue that has to be addressed is the employment of a suitable adsorbent which has particular prerequisites: **i.** High hydrolytic stability and hydrophobicity with negligible water vapor uptake through the entire activity range, **ii.** High affinity for butanol vapor at low coverage and high uptake capacity, and **iii.** Ease of desorption and regeneration. Though zeolites are widely utilized for a plethora of applications, their hydrophilic nature makes them highly incompetent for this application. The applicability of the hydrophobic silicalite class of zeolites like Si-LTA, Si-CHA for biobutanol recovery in a gas stripping-adsorption system was recently demonstrated[16] and it was found that the selectivity of Si-LTA for butanol/ethanol was affected negatively; this was due to the adsorption of water molecules in the pores. Nonetheless, the separation of butanol was achieved with a reduced selectivity. This characteristic of high sensitivity to even small amounts of water is considered to originate from the hydrophilic defects in zeolites, and the transferability of such defects to bulk synthesis of silicalite zeolites is highly probable. MOFs are comparatively more promising candidates than zeolites for ABE separation as their structures can be tuned and tailor-made to be intrinsically hydrophobic through the application of diverse synthetic options and use of starting materials. Due to their designable structure and the resultant diverse chemical and physical properties, MOFs are useful for a variety of applications [17-28]. Hitherto, in the context of biobutanol recovery, hydrophobic zeolitic imidazolate frameworks (ZIFs), ZIF-8 and ZIF-71 were principally investigated for their adsorptive ABE separation as they have a low affinity for water compared to other hydrophilic ZIFs like ZIF-90 [29-39].

To improve the hydrolytic and thermal stability, as well as the hydrophobicity of MOFs, ligands based on carboranes can be introduced within their structures [40-42]. As described in the first chapter, the spherical nature of the carboranes, with slightly polarized hydrogen atoms and the presence of the hydride-like hydrogens at the B-H vertexes, make the carboranes very hydrophobic.[43] For example, our group has

reported that the hydrophobic properties of carboranes, exploited in a number of medical applications [43-48] but underexploited in materials science, can potentially enhance the hydrolytic stability of CPs and MOFs.

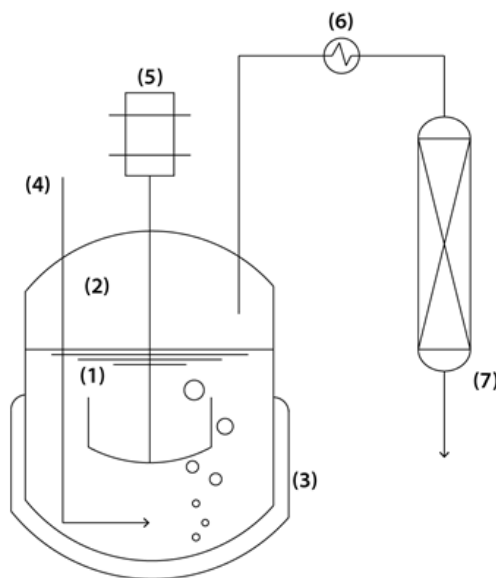


**Figure 4-1.** Schematic illustration of the integrated gas stripping and vapor phase adsorption and separation of butanol from the ABE fermentation process. (1) The ABE fermentation broth, (2) headspace of the bioreactor where ABE vapors are accumulated due to (3) heating jacket which maintains the broth at 313 K, (4) N<sub>2</sub> stripping gas and (5) agitator facilitate the stripping of ABE in their vapor phase as a dilute stream from the broth (6) which is heated to 333 K and (7) transferred as the feed stream to the adsorption column packed with MOFs material.

As we mentioned in Chapter 1, using N-donor linkers as the co-ligand is an effective strategy to construct three-dimension MOFs. Based on the intriguing properties of carboranes and the 2D structure of  $[\text{Cu}_2(\text{mCB-L})_2(\text{Solv})_2] \cdot x\text{Solv}$  coordination polymers from **Chapter 3**, we report here a novel Cu<sub>2</sub>-paddlewheel based MOF with formula  $[\text{Cu}_2(\text{mCB-L1})_2(\text{DABCO})_{0.5}(\text{H}_2\text{O})]$  (**mCB-MOF-1**; mCB-L1: 1,7-di(4-carboxyphenyl)-1,7-dicarba-closo-dodecaborane; DABCO: 1,4-diazabicyclo[2.2.2]octane) for butanol recovery. Our porous and hydrophobic **mCB-MOF-1** retains its porosity when subjected to harsh aqueous conditions (e.g., pH 2-11 for one day or at 90 °C for over two months). Owing to the excellent hydrolytic stability of **mCB-MOF-1**, it was tested as an adsorbent for ABE separation and compared with ZIF-8. The experiments showed that **mCB-MOF-1** is a superior adsorbent for the separation of biobutanol compared to ZIF-8 at 333 K.

## 4.2 Results and Discussion

### 4.2.1 Crystal Structure and Characterization

Reaction of  $\text{Cu}(\text{NO}_3)_2$  with *m*CB- $\text{H}_2\text{L1}$  and DABCO in dimethylformamide (DMF) and ethanol at 80 °C for 48 h afforded greenish crystals for  $[\text{Cu}_2(\textit{m}\text{CB-L1})_2(\text{DABCO})_{0.5}(\text{H}_2\text{O})]$  (***m*CB-MOF-1**) in good yield. IR spectrum showed a characteristic broad B-H stretching band from the carborane ( $2601\text{ cm}^{-1}$ ), and the C=O vibration of the carboxylate groups ( $1716\text{ cm}^{-1}$ ; Figure S4-1). X-ray crystallography reveals that ***m*CB-MOF-1** crystallized in the tetragonal space group *I422* and possesses a 2-fold interpenetrated 3D framework having a rare 5-connected  $(4^4)(6^6)$  (Schläfli symbol) topology (Figure 4-2 and Table S4-1). Phase purity was confirmed by elemental analysis and powder X-ray diffraction (PXRD; Figure 4-4). The basic unit of ***m*CB-MOF-1** is a  $\text{Cu}_2$ -paddlewheel motif of  $[\text{Cu}_2(\text{COO})_4]$  units. The Cu–Cu distance in the paddlewheel unit is  $2.6641(5)\text{ \AA}$ . The two copper atoms share four *m*CB-L linkers at the basal positions and one oxygen atom from a water molecule and a nitrogen atom from a DABCO molecule occupy the apical positions (Figure 4-2a). Cu–OOC and Cu– $\text{O}_{\text{solv}}$  bond lengths range from  $1.937(2)$  to  $1.974(2)\text{ \AA}$  and  $2.188(4)\text{ \AA}$ , respectively. The Cu–N bond length is  $2.180(8)\text{ \AA}$ . The carborane *m*CB-L linker shows a V-shape ( $\text{OOC-CBcentroid-COO} \approx 115^\circ$ ) and two noncoplanar phenyl rings ( $70^\circ$ ). In this structure, each  $\text{Cu}_2$ -paddlewheel cluster is connected to four *m*CB-L ligands forming planar 2D layers with a  $4^4$ -grid topology (Figure 4-2b). Interestingly, the  $[\text{Cu}_2(\textit{m}\text{CB-L1})_2]$  layers were highly corrugated in the absence of DABCO (Figure XX, Chapter 3), while the observed 2D layers in ***m*CB-MOF-1** are flat. These layers were further linked by the pillaring DABCO ligand with a N–N distance of  $2.573(8)\text{ \AA}$ , giving rise to the 5-connected 3D structure shown in Figure 4-2c. The difference of layers arrangement between these structures can be attributed to two reasons: i. In ***m*CB-MOF-1** two twist angles between benzene ring and the reference plane were more close to  $90^\circ$  which is helpful to arrange the



layer in one plane; ii. The co-ligand DABCO separated the adjacent layers to avoid the interaction between layers. Quite remarkable, the DABCO ligands coordinate to only one the two apical sites of each Cu<sub>2</sub>-paddlewheel cluster and alternate above and below the Cu<sub>2</sub>-paddlewheel/*m*CB-L layers (Figures 4-2b, 4-2c). This provides large rectangular channels (18.6 x 4.2 Å), in which the apical positions of the Cu<sub>2</sub>-paddlewheel units are occupied by water molecules. These large rectangular channels are minimized by a 2-fold interpenetration of another 5-connected network, providing square 1D channels (Figure 4-2d) of about 7.0 x 7.0 Å when coordinated water is excluded. The interpenetrated networks are interacting by  $\pi$ -stacking interactions between the centroids of the aromatic rings (3.7174(2) Å) and with an angle of 9.70(14)° between their planes (Figure S4-2).

The structure of ***m*CB-MOF-1** is a rare example of 5-connected (4<sup>4</sup>)(6<sup>6</sup>) topology [49,50] (**sqp**) and represents the first example of such a topology in a Cu<sub>2</sub>-paddlewheel MOF. Indeed, the Cu<sub>2</sub>(O<sub>2</sub>CR)<sub>4</sub>A<sub>2</sub> (A = apical ligands) paddlewheel units serve as lineal, square or octahedral building units, if all dimer cluster coordination sites are occupied by polytopic ligands (i.e., saturated) [51]. In the case of ***m*CB-MOF-1**, the apical positions for each Cu<sub>2</sub>-paddlewheel are occupied by a nitrogen atom of one DABCO and oxygen from water molecules. This rare structural topology [52-54] allows the activation of ***m*CB-MOF-1** by removal of the Cu-coordinated water, leading to an open porous structure. In addition, such interpenetration is unusual when a small pillar ligand such as DABCO is employed [55,56].

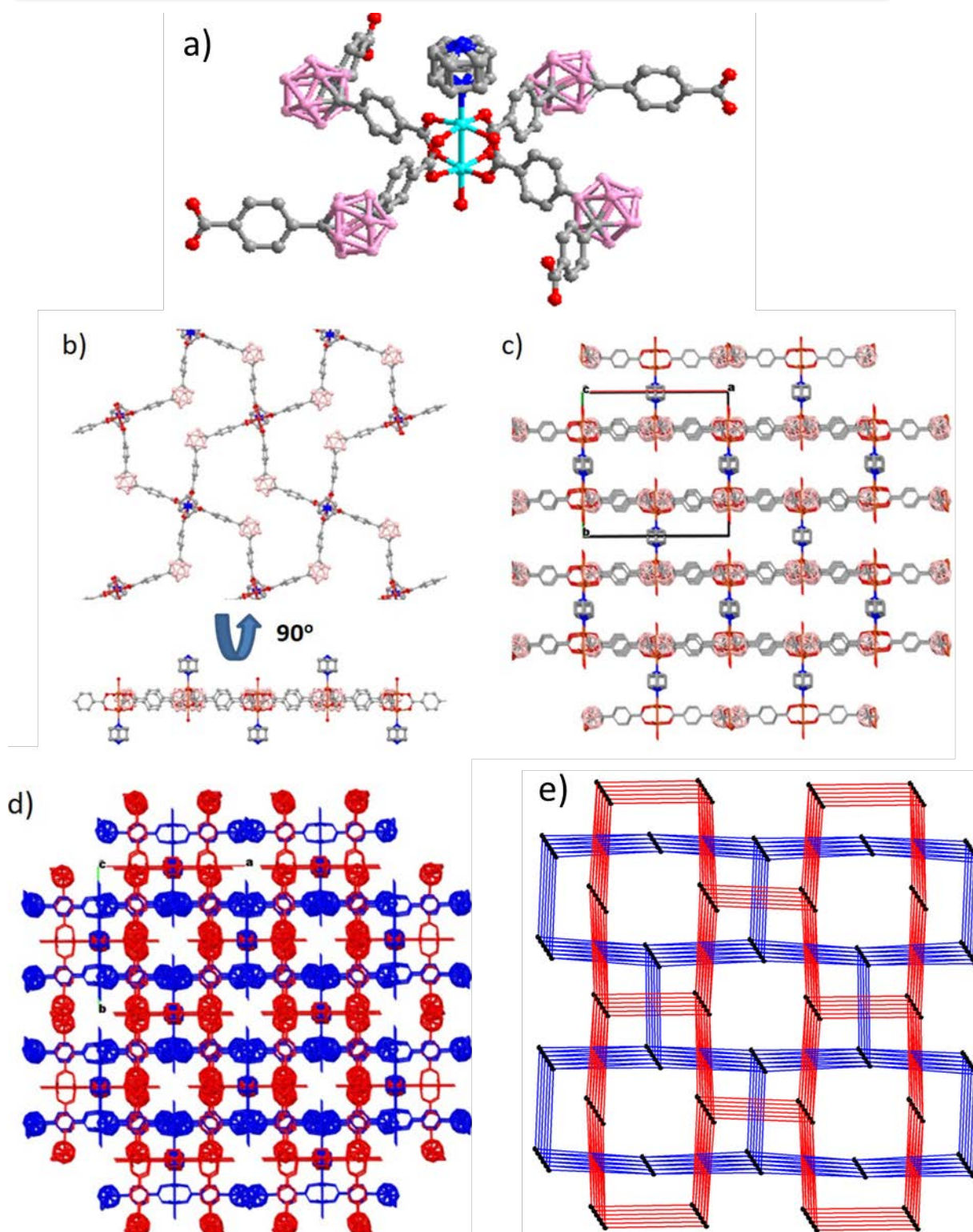


**Figure 4-2.** Crystal structure of *mCB-MOF-1*. a) View of the  $\text{Cu}_2$ -paddlewheel units with *mCB-L* coordination. b) Two perpendicular views of the extended structures showing the 2D  $4^4$  networks. c) 3D framework having a 5-connected  $(4^4)(6^6)$  topology with rectangular 1D channels. d) 2-fold interpenetrated structure with square 1D channels. e) Underlying 2-fold interpenetrated 5-connected nets in the structure of *mCB-MOF-1*; black spheres represent the  $\text{Cu}_2$ -paddlewheel cluster nodes. Interpenetrated networks are colored differently for clarity. H atoms are omitted for clarity. Color code: B pink; C grey; O red; N blue, Cu orange.

Thermogravimetric analysis (TGA) of *mCB-MOF-1* shows a continuous weight loss of 11% from 25 °C to 300 °C, which we attributed to the loss of the guest and coordinated DMF and H<sub>2</sub>O molecules (Figure S4-3). Above 300 °C, this framework decomposes over multiple steps. Variable temperature WAXS measurements showed that *mCB-MOF-1* retains its original structure until 300°C under dynamic vacuum (Figure 4-3). Thus *mCB-MOF-1* was activated at 130°C under dynamic ultrahigh vacuum for 12h, providing *mCB-MOF-1'*. PXRD studies revealed that the structure of the activated *mCB-MOF-1'* is intact upon removal of the guest molecules from its cavities (Figure 4-4). Sorption measurements revealed that desolvated *mCB-MOF-1'* is porous to N<sub>2</sub> (BET surface area: 756 m<sup>2</sup>g<sup>-1</sup>) at 77 K and 1 bar and also to CO<sub>2</sub> (0.16 mmol g<sup>-1</sup>) at 313 K and 150 mbar (Figure S4-4). N<sub>2</sub> adsorption-desorption isotherms indicates the micro-porosity structure of *mCB-MOF-1'*, with a pore width distribution of *ca.* 6 Å, calculated by a non-local density functional theory (NLDFT) method. The latter suggest that the micropores from *mCB-MOF-1'*, correlates with the observed nanoscale channels in *mCB-MOF-1* and support that the coordinated molecules have been removed on activation.

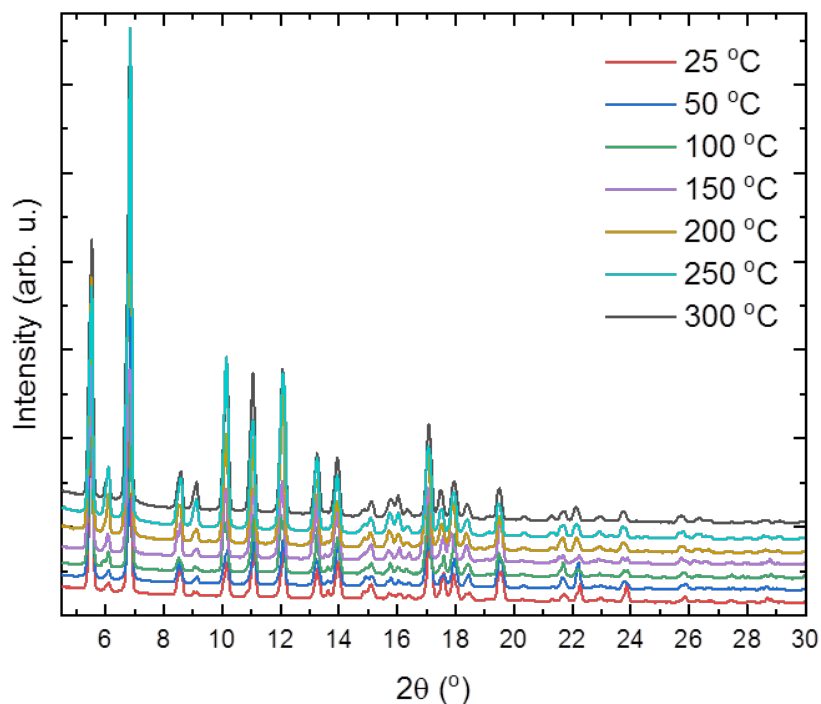


**Figure 4-3.** Variable temperature WAXS patterns of as-synthesized sample of *mCB-MOF-1* under vacuum.

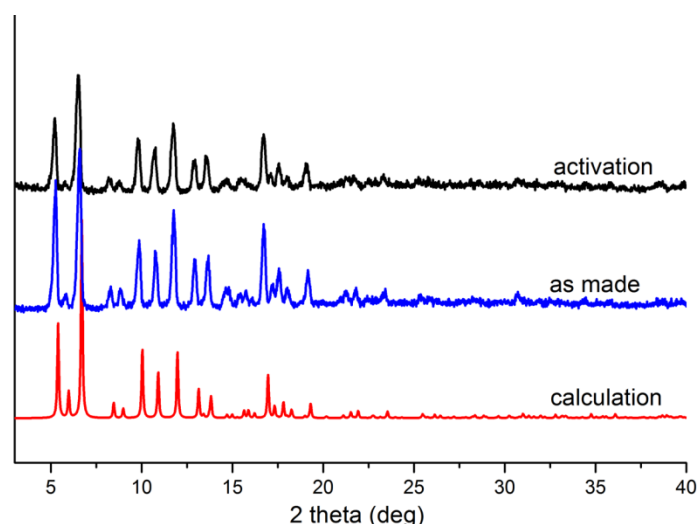


**Figure 4-4.** PXRD patterns of: simulated (red), experimental (blue) of *mCB-MOF-1* and desolvated *mCB-MOF-1'* (black).

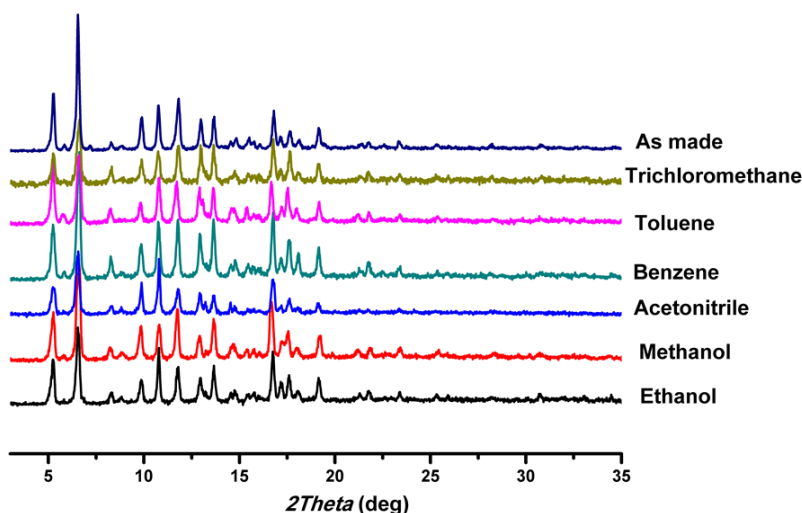


**Figure 4-5.** PXRD patterns of samples of *mCB-MOF-1'* under different solvent treatment.

*mCB-MOF-1* represents a rigid two-fold interpenetrated porous structure and PXRD studies show that no structural changes can occur upon activation (Figure 4-4) or upon its immersion in a variety of organic solvents such as alcohols, benzene, toluene and acetonitrile (Figure 4-5). The rigidity of the framework can be ascribed to two reasons: (a) two nets are linked by strong  $\pi\cdots\pi$  interactions; (b) narrow space of the interpenetrated networks restricts the movement of close 3D nets. The interpenetration [57] and formation of  $\pi$ -stacking motifs [24,58] are known to provide overall stabilization. We reasoned that such rigid structure could also be stable in water as the

highly hydrophobic carborane moieties are decorating the MOF channels, thus providing protection to the Cu<sub>2</sub>-paddlewheel units against hydrolysis or ligand displacement (Figure 4-6) [40,42].

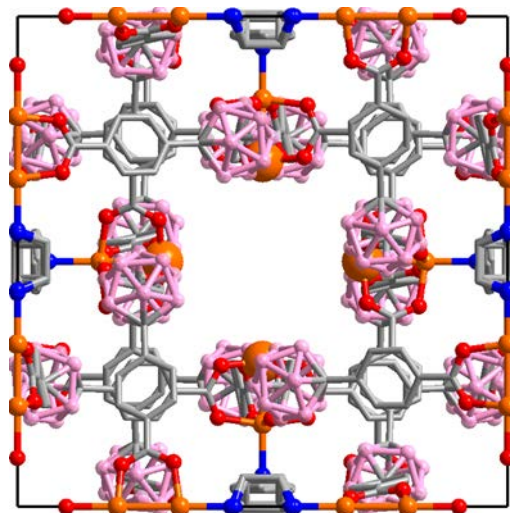


**Figure 4-6.** A view of the crystal structure of *mCB-MOF-1* along the *c* axis showing the environment of four Cu atoms (enlarged orange spheres) in the channels. Color codes: Boron, pink; carbon, grey; nitrogen, blue; oxygen, red. H atoms are omitted for clarity.

### 4.2.2 Hydrolytic Stability and Hydrophobicity

Noteworthy, *mCB-MOF-1*' is stable when incubated in liquid water for at least one month at room temperature. More strikingly, it is fully stable in hot water (90°C) for up to one month as prove by a combination of PXRD, BET, SEM and ICP (Figure 4-7 and Table S4-2). Indeed, PXRD traces of *mCB-MOF-1* before and after incubation for two months at 90°C in water in a closed vial perfectly match the simulated pattern derived from the single crystal structure of *mCB-MOF-1* (Figure 4-7b). However, there is a clear consensus that providing only the PXRD as a proof for water stability is not acceptable and other experimental evidences, such as e.g., gas sorption isotherms and SEM are mandatory for assuring water stability [59]. Thus, stability was also confirmed by N<sub>2</sub> adsorption measurements of the solids after water treatment. Porosity is retained as proved by the BET surface area measurements of the treated samples (Figure 4-7a and Table S4-2). Samples after water treatment for up to two



months at 90°C show negligible changes in their surface area and pore volumes compared with the as made material (see Table S4-2 for details). SEM images of as made *mCB-MOF-1* and the activated sample after being in 90°C water for one month show no significant morphology change of the polyhedral block crystals of *mCB-MOF-1* or evidence of surface cracking (Figure 4-8 and Figure S4-5). Furthermore, the heated sample for two months still shows high porosity and reasonable integrity of the structure (Figure 4-7, 4-8 and Table S4-2). No significant weight loss was observed for the samples treated in the above conditions and consequently, copper leaching is negligible in all the cases (see Table S4-2 for details).

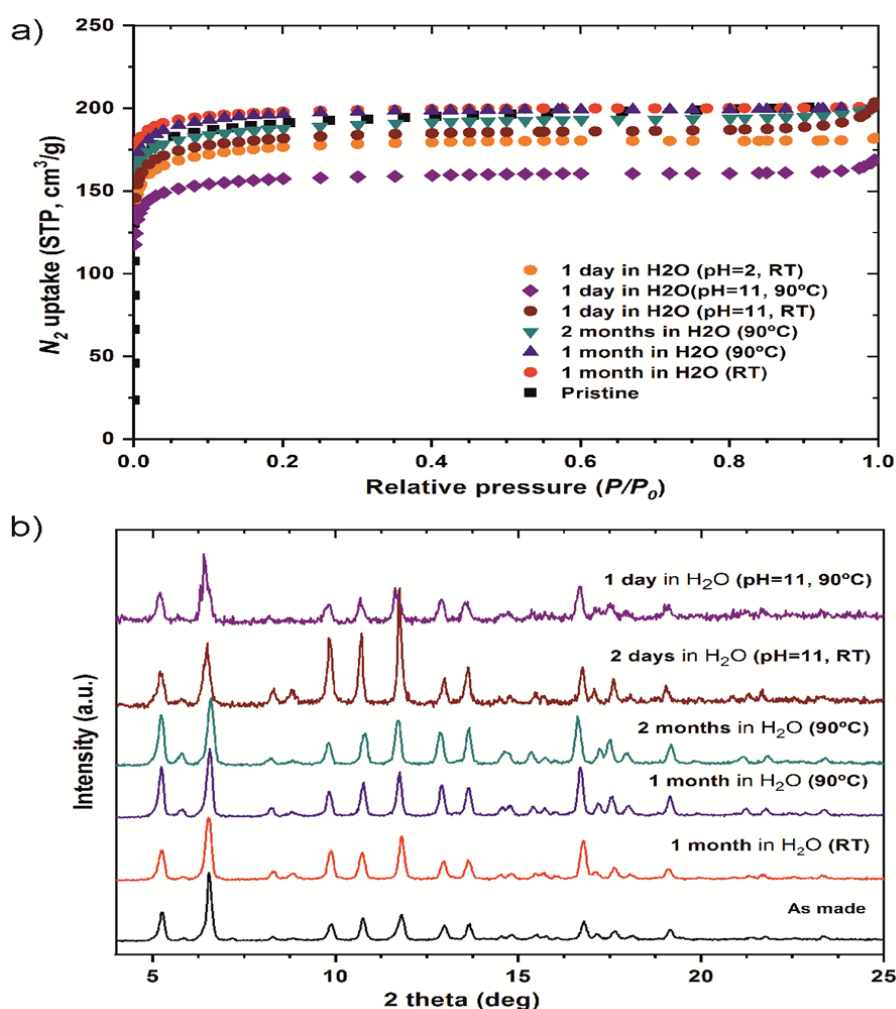


**Figure 4-7.** Comparison of the a)  $N_2$  adsorption isotherms at 77 K and b) PXRD patterns for activated *mCB-MOF-1'* and after being in water at various conditions.

Moreover, *mCB-MOF-1'* is also stable when incubated in liquid water over a wide

pH range (from 2 to 11; pH adjusted with HCl or NaOH) for at least 48 h at room temperature (Figure 4-7, 4-8 and S4-6). PXRD patterns show a somewhat higher stability of **mCB-MOF-1'** in basic than in acid conditions (Figure S4-6). After being in water at pH 2, the surface area and pore volume of **mCB-MOF-1'** decreases from 756 to 698 m<sup>2</sup>g<sup>-1</sup> and 0.31 to 0.28 cm<sup>3</sup>g<sup>-1</sup> in one day (Table S4-2). While in basic conditions (water, pH = 11), the surface area and pore volume of **mCB-MOF-1'** decreases from 756 to 722 m<sup>2</sup>g<sup>-1</sup> and 0.31 to 0.30 cm<sup>3</sup>g<sup>-1</sup> for the same period. Longer exposition to the above conditions shows a fast decrease of surface area and pore volume (see Table S4-2 for details). SEM images of samples being in acidic or basic conditions (Figure 4-8 and S4-7) show a clear change in morphology from polyhedral crystals to small plates in the samples being in acidic aqueous solution but no morphology changes are observed in the samples being in basic conditions. The somewhat higher stability of **mCB-MOF-1'** in basic aqueous solutions prompted us to study the stability under harder conditions. Remarkably, **mCB-MOF-1'** is also stable in basic conditions (pH = 11) at 90°C for at least 24h (Figure 4-7 and S10). When heating under basic conditions for 24h, slight structural changes are already visible (Figure 4-7b). The PXRD pattern for **mCB-MOF-1'** after being at 90°C in water (pH = 11) for one day shows a slight decreasing of peaks at  $2\theta = 8.3, 8.8, 14.5, 14.8$  and  $15.4^\circ$ , and no additional peaks at higher angles were observed. Consistently, SEM images clearly show the presence of cracks on the surface of the polyhedral crystals and the appearance of some spherulites (Figure 4-8 and S4-7) [60,61]. However the presence of spherulites does not reflect a significant change in the PXRD data with respect to the PXRD pattern of the as made material. The heated sample under basic conditions still shows high porosity (629 m<sup>2</sup>g<sup>-1</sup> at 77 K, Figure 4-7 and Table S4-2) with a pore volume of 0.26 cm<sup>3</sup>g<sup>-1</sup>. Quite surprisingly, copper leaching after such hard condition was practically negligible (476 ppb) as determined by ICP.

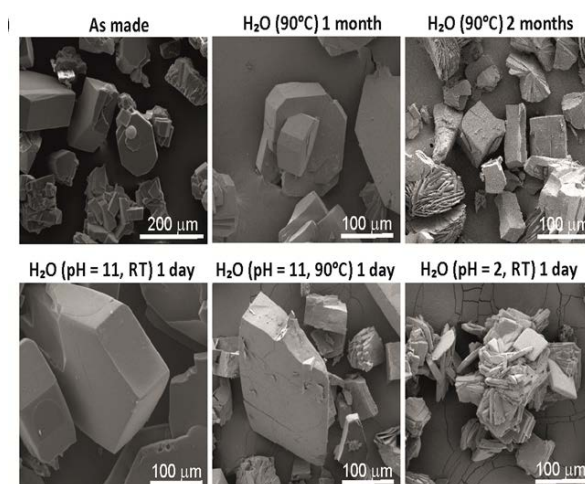


**Figure 4-8.** Comparison of the Scanning Electron Microscopy (SEM) images showing crystals morphology of as made *mCB-MOF-1* and that of *mCB-MOF-1'* after being in water at the indicated conditions.

As mentioned above, we attribute this remarkably high hydrolytic stability to a combination of interpenetration and the hydrophobic nature of the *meta*-carborane residues in the structure *mCB-MOF-1*, which hinder the degradation of the  $\text{Cu}_2$ -paddlewheel units (Figure 4-6). Shimizu and coworkers have recently provided a way to parametrize and grade the hydrolytic stability of MOFs, based on structural and sorption properties [59]. These authors proposed six levels of hardness to water exposure (1 to 6: ambient conditions to boiling water) and four categories (A to D: retention of crystallinity and porosity to loss of porosity and crystallinity) as a way to benchmark both with respect to how the MOF was treated and the post-treatment analysis. Using this stability level, HKUST-1 is classified with a 4B stability (retained some porosity but losses some order when immersed in water), DMOF is classified as 3D (loss of porosity and crystallinity when exposed to intermediate humid conditions), whereas MIL-53 and ZIF-8 are classified as 6B and 6C, respectively (retained some porosity or some order when immersed in boiling water). Following this classification, our  $\text{Cu}_2$ -paddlewheel MOF *mCB-MOF-1* correspond to 6A stability which is, to our knowledge, the highest hydrolytic stability of a Cu-based MOF and surpasses that of the well-known families of ZIF- or Zr-MOFs (Table S4-3) [59,62].

Having determined that *mCB-MOF-1* is robust and permanently porous, we then



## Results and Discussion

evaluated the influence of the carborane units on its hydrophobic properties. The water adsorption isotherm for *m*CB-MOF-1' collected at 313 K (Figure 4-9) exhibits a type-II sorption isotherm, typical of a material with low affinity for water; this is in agreement with the hydrophobic nature of the *m*-carborane residues present in *m*CB-MOF-1 [63]. We then performed water contact-angle measurements of dry *m*CB-MOF-1' in crystalline powder packed on a glass surface and in the form of a disk pellet (diameter = 13 mm), which was fabricated by pressing a dry crystalline powder under a pressure of 10 tons for 5 min [64]. The contact angle ( $\Theta_c$ ) in each case was  $144^\circ$  and  $101^\circ$ , respectively — values which are characteristic of a hydrophobic solid. *m*CB-MOF-1' shows a similar hydrophobicity to that of the other highly hydrophobic MOFs (e.g. ZIF-8,  $\Theta_c = 142^\circ$ ) [65]. We also quantified the contact-angle hysteresis (CAH) that was found to be  $32^\circ$  (Table S4-4). This CAH was attributed to the surface roughness of the disk pellet that can be the responsible for the contact line pinning [66]. Additionally, if a glass substrate bearing *m*CB-MOF-1' powder was inclined after placing a droplet of water on its surface, a *m*CB-MOF-1'-covered water droplet (known as *liquid marble*) was formed (Figure 4-9); this is known to be a common occurrence with hydrophobic powders.[66]

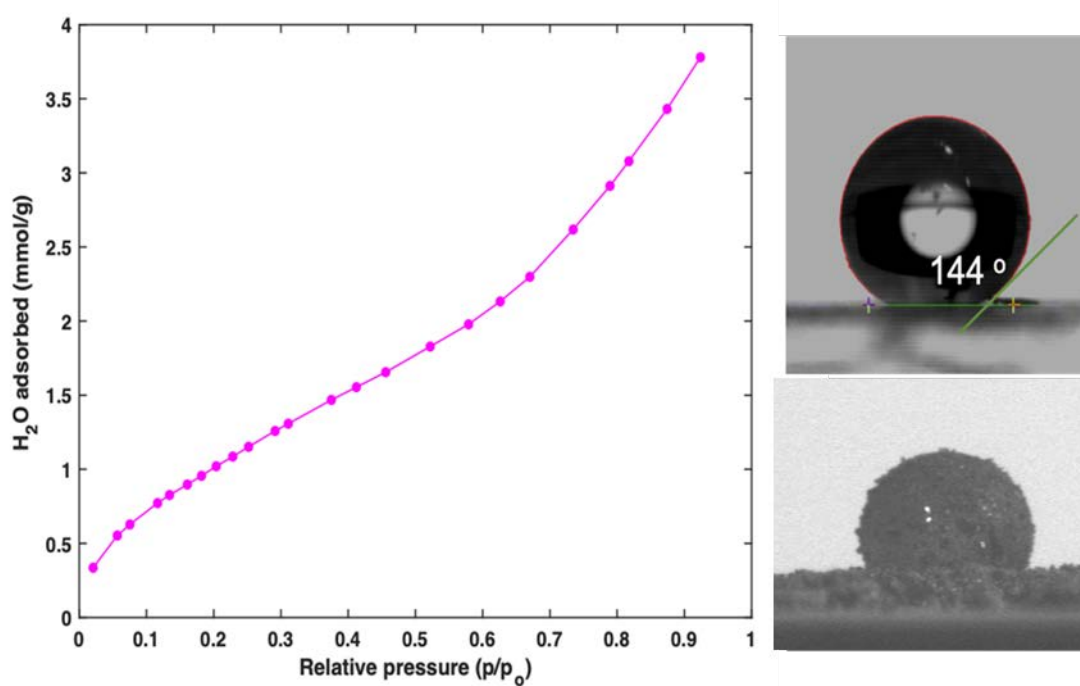


**Figure 4-9.** Left: Type II water vapor adsorption collected on *m*CB-MOF-1' at 313 K, upper right:

---

water contact angle photo of a crystalline powder packed on glass surface, lower right: 9 ml *mCB-MOF-1*-coated water marble.

### 4.2.3 Butanol Separation

The extraordinary water stability of *mCB-MOF-1* and type II water isotherms prompted us to consider this MOF as a candidate for bioalcohol separation from realistic multicomponent aqueous mixtures. With this aim, we proceeded to evaluate the accessibility of its pore structure to the ABE mixture by means of static single component equilibrium isotherms at 313 K, dynamic variable temperature pulse gas chromatography and breakthrough curve measurements. In order to put the results into a broader context we have made a comparison with the well-known ZIF-8 material possessing a related specific pore surface area value and a highly hydrophobic porous network. With this aim, single-component adsorption isotherms of acetone, butanol, ethanol and water have been measured for *mCB-MOF-1* and ZIF-8 at 313 K (Figure 4-10). The results show significant differences between both materials. Firstly, in accordance with their respective porosity features, ZIF-8 exhibits higher saturation uptake for all alcohols which is attributed to its higher surface area and pore volume. Secondly, *mCB-MOF-1* and ZIF-8 behave differently at the critical low-pressure region: there is a steep uptake when *mCB-MOF-1* is used, and there is a negligible uptake when ZIF-8 is used. The type I vapor isotherms for butanol, ethanol and acetone indicate that the pores in *mCB-MOF-1* are readily accessible for these molecules to diffuse in and therefore, *mCB-MOF-1* forms strong interactions with these molecules (Figure 4-10a). Whereas, as shown in Figure 4-10b, ZIF-8 exhibits the characteristic sigmoidal S-shaped isotherms for the alcohol vapors, indicating weak interactions between the ZIF-8 and alcohols at the low-pressure region; biobutanol and other alcohol products are typically dilute solutions in water. In addition, the absence of hysteresis in the isotherms collected on *mCB-MOF-1* facilitates the easier desorption of the adsorbed alcohols.

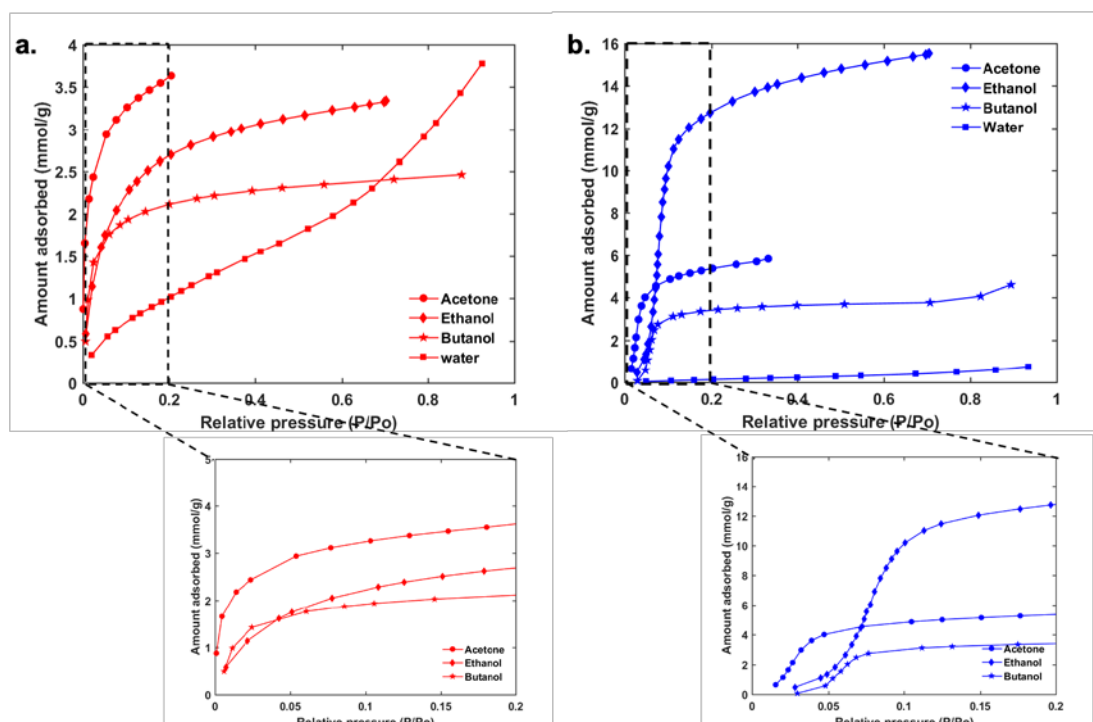


**Figure 4-10.** Acetone (303 K), butanol and ethanol (313K) vapor isotherms collected on *mCB-MOF-1'* (a) and ZIF-8 (b).

The selectivity of butanol over ethanol was evaluated using the Ideal Adsorbed Solution Theory (IAST) [67]. Predictions show a much higher uptake of butanol over ethanol in both *mCB-MOF-1'* and ZIF-8. Remarkably, a higher butanol uptake is observed in *mCB-MOF-1'* than in ZIF-8 in the low-pressure region, and contrary to the latter, *mCB-MOF-1'* shows a negligible ethanol uptake over all pressure range (Figure S4-8). The selectivity results of *mCB-MOF-1'* for butanol over ethanol shows higher than 12.0 in the < 25 kPa and decrease slowly to 7.0 at 100 kPa, being overall larger than that for ZIF-8 (Figure 4-11). Consequently, the overall behavior is in agreement with a higher butanol/ethanol selectivity for *mCB-MOF-1'*.

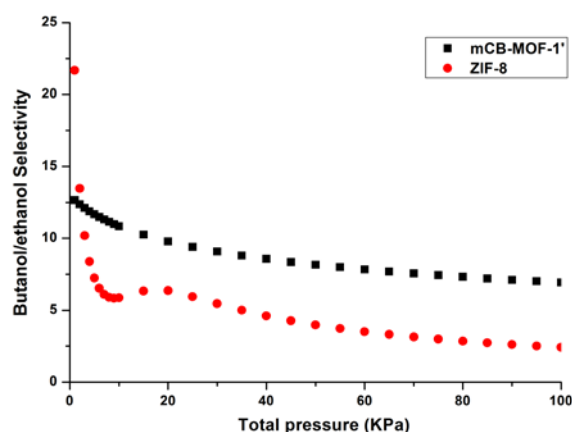


**Figure 4-11.** The IAST predicted selectivity of a binary mixture of Butanol : Ethanol (0.85 : 0.15) at 313 K as a function of the total pressure.

To further characterize the alcohol-MOF interactions, gas-phase pulse chromatographic were performed (Figures 4-12 and 4-13). Both *mCB-MOF-1* and ZIF-8 were packed in separate columns and the experiments were performed at 443 K and 503 K. A broad peak for butanol can be seen in Figure 4-12, which suggests a relatively strong adsorbate (butanol)-adsorbent (*mCB-MOF-1*) interactions. This can be explained by the slow intracrystalline diffusion of the butanol molecules after they diffuse in the pores. To the contrary, acetone peaks are symmetrical for both ZIF-8 and *mCB-MOF-1* suggesting that the acetone molecules are not obstructed by intracrystalline diffusion. NMR experiments were also performed to evaluate the multicomponent vapor uptake capacity of both MOFs. Under atmospheric pressure and at 333 K, we observed that both ZIF-8 and *mCB-MOF-1* uptake comparable amounts of butanol regardless of the difference in their BET surface areas (Table S4-7).

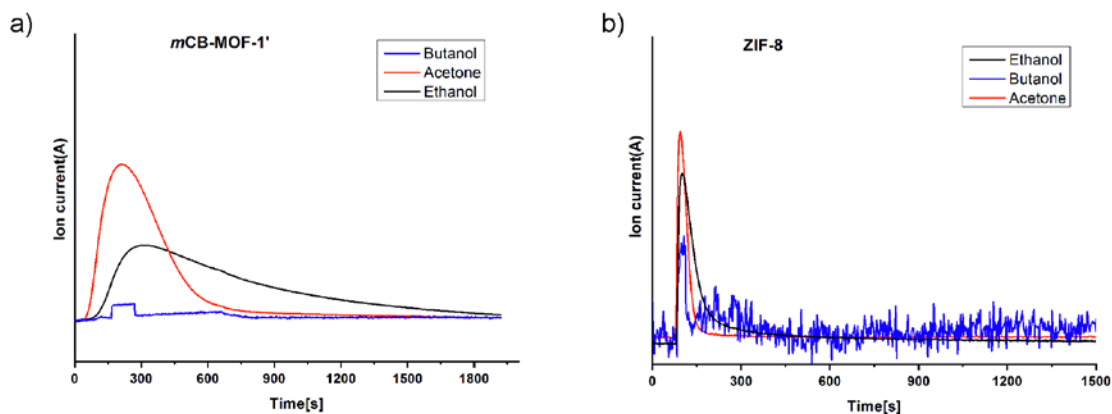


**Figure 4-12.** Pulse gas chromatograms at 443 K of vapor mixture of ABE solution on 10 cm columns (4 mm inner diameter) packed with *mCB-MOF-1* (a) or ZIF-8 (b).

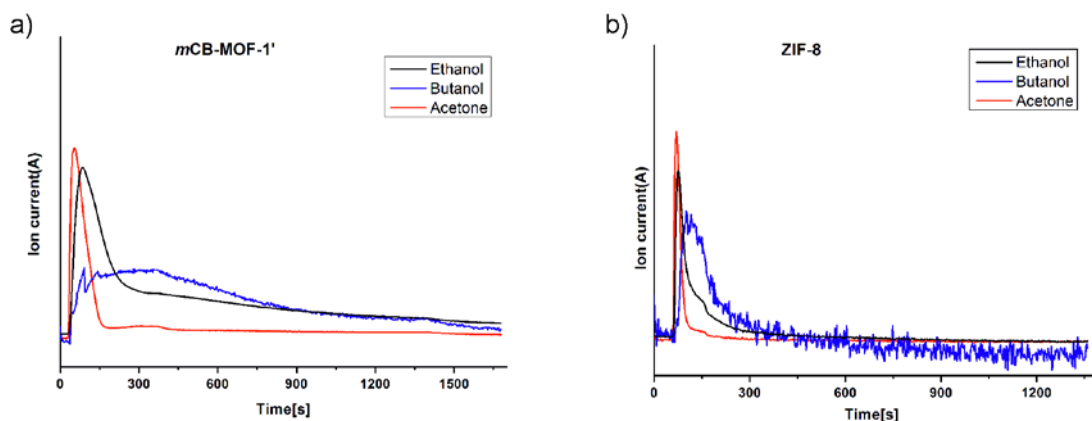


**Figure 4-13.** Pulse gas chromatograms at 503 K of vapor mixture of ABE solution on 10 cm columns (4 mm inner diameter) packed with *mCB-MOF-1* (a) or ZIF-8 (b).

Having established the single component interactions of ABE components with the porous framework, we then proceeded to study the butanol separation under industrially relevant conditions in order to evaluate the effect of competitive adsorption of the different components. With this aim, we studied the separation of butanol through an integrated gas stripping-adsorption process with a model aqueous solution of ABE mixture (composition: acetone 7.04g/l, 0.715wt%; butanol 13.75g/l, 1.39wt%; ethanol 2.56g/l, 0.26wt%; water 960.69g/l, 97.63wt%). 1000 mL of the ABE mixture was thermostated at 313 K and bubbled with helium flow (40 mL min<sup>-1</sup>). The resulting flow of helium, which carried the ABE vapor, was fed as the inlet stream to a thermostated chromatographic column (4 mm inner diameter/10 cm long) packed with *mCB-MOF-1* or ZIF-8 and maintained at 333 K. It is worth

mentioning that the standard ABE fermentation temperature of solventogenic clostridium species in the bioreactor ranges from 308 to 313 K. It is well demonstrated that any operating temperature above 313 K will hamper the production and yield, as it negatively affects the clostridium species. Thus, in our proposed integrated process illustrated in Figure 4-1, we envision that the ABE vapor generated in the bioreactor in concordance with the standard operating conditions of 313 K and 1 atmosphere pressure is stripped by a carrier gas from the headspace of the reactor, and the resultant ABE vapor is externally heated to 333 K before being fed to the fixed adsorbent bed. We chose to set up the temperature of our sorption column at 333 K owing to the observation of comparatively very low adsorption and the concomitant rapid elution of the raffinate – acetone and ethanol from sorption column loaded with *mCB-MOF-1* (Figure S4-9). This finding from a lab scale setup, when extrapolated to an industrial scale process, is considered to be highly meritorious in terms of the overall downstream separation process efficiency and the associated process engineering and economics – capital and operating costs requirements. Thus, the breakthrough curves collected on *mCB-MOF-1* and ZIF-8 are presented in Figure 4-14.

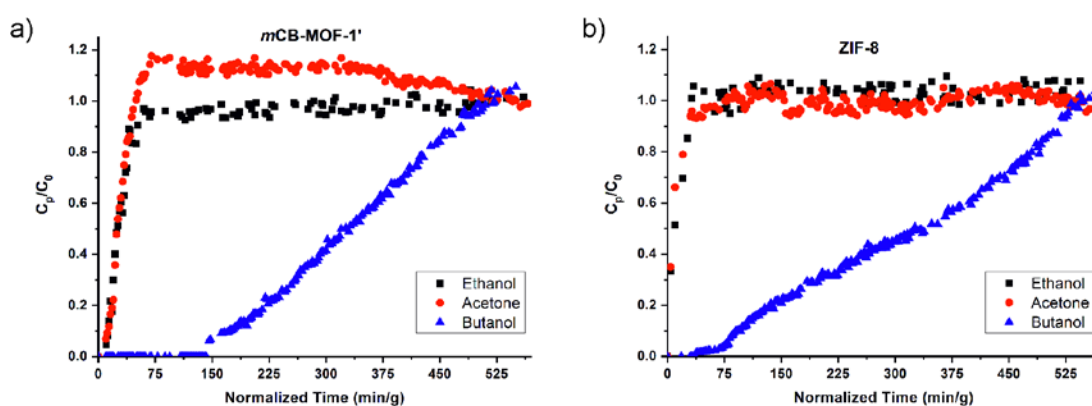


**Figure 4-14.** Breakthrough curves collected at 333K on *mCB-MOF-1'* and ZIF-8. Color code: red: acetone, black: ethanol and blue: butanol.

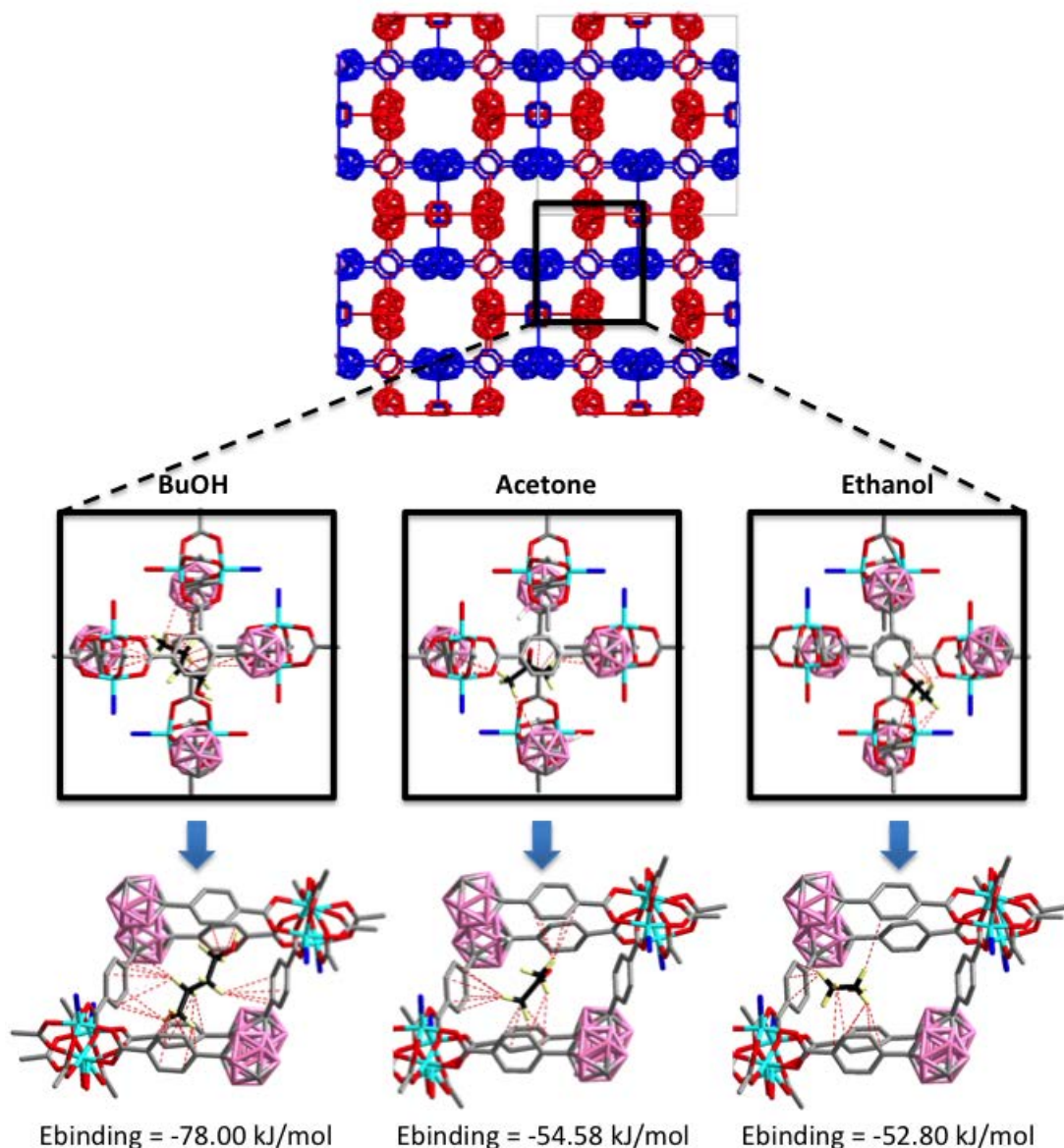


**Figure 4-15.** 2-fold interpenetrated structure with square 1D channels. Black squares represent the portion of the structure where the calculated solvent molecules are located. Intermolecular contacts between the solvent molecules and the framework are shown at the bottom of the image.

The breakthrough curves indicate that at 333 K, acetone, ethanol and butanol are initially co-adsorbed, however, after acetone and ethanol become saturated, butanol replaces these weakly adsorbed components. As can be seen in Figure 4-14, *mCB-MOF-1'* performs better than ZIF-8 as exemplified by the respective breakthrough times of 146 and 80 min/g respectively, which correlates to their adsorption capacity (butanol) at low pressure and strength of adsorbate-adsorbent interactions. It can be therefore, concluded that the butanol interactions with *mCB-MOF-1* pore framework gives rise to a material which can recover butanol



from the ABE mixture at 333 K more efficiently compared to ZIF-8.

Composites	ENER ( A.U. )	$\Delta E$ (kJ/mol)	$\Delta E$ (kcal/mol)	$\Delta E$ (eV)
ethanol	-30.9682			
acetone	-36.6617			
butanol	-44.7325			
<i>mCB-MOF-1'</i>	-2061.2912			
<i>mCB-MOF-1'</i> -ethanol	-2092.2795	<b>-52.7998</b>	<b>-12.6195</b>	<b>-0.55</b>
<i>mCB-MOF-1'</i> -acetone	-2097.9736	<b>-54.5799</b>	<b>-13.0450</b>	<b>-0.57</b>
<i>mCB-MOF-1'</i> -butanol	-2106.0534	<b>-78.0000</b>	<b>-18.6424</b>	<b>-0.81</b>
ZIF-8	-1822.3988			
ZIF-8-ethanol	-1853.3763	<b>-24.3570</b>	<b>-5.8215</b>	<b>-0.25</b>
ZIF-8-acetone	-1859.0729	<b>-32.6239</b>	<b>-7.7973</b>	<b>-0.34</b>
ZIF-8-butanol	-1867.1497	<b>-48.4282</b>	<b>-11.5746</b>	<b>-0.50</b>

**Table 4-1.** CP2K Periodic calculated Energies for the composites.

To shed light on the adsorption mechanism of *mCB-MOF-1'*, we conducted Monte Carlo simulations for butanol, ethanol or acetone adsorbate molecules. The results indicate that the three molecules (butanol, acetone or ethanol) preferentially distribute within the pockets created by the 2-fold interpenetrated structure and away from the 1D channels of *mCB-MOF-1'* (Figure 4-15). In addition, DFT calculations were employed to investigate the interactions between ABE and *mCB-MOF-1'* or ZIF-8. As shown in Table 4-1, the binding energy of butanol (-78.00 kJ/mol) is higher than that for acetone (-54.58 kJ/mol) and ethanol (-52.80 kJ/mol), which shows stronger interactions between butanol and *mCB-MOF-1'*. The order of ABE binding energy with ZIF-8 follows the same that for *mCB-MOF-1'*, with energies of -48.43 kJ/mol for butanol, -32.62 kJ/mol for acetone and -24.36 kJ/mol for ethanol. These results are in agreement with the shape of the single-component adsorption isotherms for both



## Conclusions

---

MOFs (Figure 4-10) and support the observed higher selectivity of butanol over ethanol for **mCB-MOF-1** than for ZIF-8 (Figure 4-11). The higher number of H atoms in the larger alcohol can improve the interactions between the small pores (0.7 nm) of **mCB-MOF-1'**, whereas those are disfavored in the larger pores (1.1 nm) of ZIF-8. The small pores of our carborane-based MOF are fully decorated with low-polar B-H groups and non-polar phenyl rings, and that might certainly explain the preferential adsorption of butanol molecules.

### 4.3 Conclusions

In summary, a new Cu(II) based porous MOF (**mCB-MOF-1**) has been synthesized and characterized. The activated **mCB-MOF-1'** is porous and stable in both basic and acidic aqueous solutions as confirmed by PXRD, BET surface areas, SEM images and ICP. **mCB-MOF-1'** is stable in water at 90 °C for over two months and also stable when incubated in liquid water over a wide pH range (from 2 to 11) for at least 48 h at room temperature and it is also stable in basic conditions (pH 11) at 90 °C for at least 24h. Such hydrolytic stability is attributed to a combination of interpenetration and the highly hydrophobic nature of the meta-carborane residues in the structure **mCB-MOF-1**, which hinder the degradation of the Cu<sub>2</sub>-paddlewheel units. Contact angle and water vapor isotherms indicated that **mCB-MOF-1** exhibits hydrophobicity on both the external crystal surfaces ( $\Theta_c = 144^\circ$ ) and the internal pores (type-II water sorption isotherm). Based on the properties of **mCB-MOF-1**, we tested this material towards butanol recovery from the ABE mixture. Single-component adsorption isotherms of acetone, butanol and ethanol for **mCB-MOF-1'** afforded type I isotherms in the low-pressure region, indicative of a strong affinity for the components of the ABE mixture. The selectivity of **mCB-MOF-1'** for butanol over ethanol, calculated by the Ideal Adsorbed Solution Theory, shows higher than 12.0 in the < 25 kPa and only slowly decrease to 7.0 at 100 kPa, being overall larger than that for ZIF-8. We therefore investigated the separation performance of **mCB-MOF-1'** for ABE aqueous solution (acetone 7.04g/l, 0.715wt%; butanol 13.75g/l, 1.39wt%;

ethanol 2.56g/l, 0.26wt%; water 960.69g/l, 97.63wt%.) separation by an integrated process of gas stripping-vapor phase adsorption process with dynamic breakthrough experiments and compared the separation performance with ZIF-8 under the same conditions. Due to the stronger butanol-*mCB-MOF-1'* interactions, breakthrough curves showcase that *mCB-MOF-1'* recovers butanol more efficiently compared to ZIF-8 at 333 K. Monte Carlo simulations and DFT calculations confirm the stronger binding energy for butanol and our carborane based MOF and show that the adsorbates preferentially distribute within the pockets created by the 2-fold interpenetrated structure and away from the 1D channels of *mCB-MOF-1'*. Our work demonstrates a step forward towards the discovery of novel water stable MOFs for biobutanol recovery from a mostly water-containing ABE mixture. To date, only ZIFs have been tested towards this application and based on our findings, carborane-based MOFs can compete with ZIFs and can even outperform them in the separation of biobutanol. Future work includes the scale up of *mCB-MOF-1* synthesis, shape engineer its powder form into a more industrially favored form, and test its performance using different bed configurations as dictated by process modelling.

## 4.4 Experimental Section

### 4.4.1 Characterization and Methods

Attenuated total reflection Fourier transformed infrared (ATR-FTIR) spectra were recorded using a PerkinElmer Spectrum One spectrometer equipped with a Universal ATR sampling accessory. Spectra were collected with  $2\text{ cm}^{-1}$  spectral resolution in the  $4000\text{-}650\text{ cm}^{-1}$  range. Elemental analyses were obtained by using a Thermo (Carlo Erba) Flash 2000 Elemental Analyser, configured for wt.%CHN. Thermogravimetric Analysis (TGA) was performed in  $\text{N}_2$ , on an nSTA 449 F1 Jupiter-Simultaneous TGA-DSC or SDT Q600 V8.3 Build 101 instruments (heating rate:  $5\text{ }^\circ\text{C}/\text{min}$ ; temperature range:  $25\text{ }^\circ\text{C}$  to  $600\text{ }^\circ\text{C}$ ). Gas sorption-desorption ( $\text{CO}_2/273\text{ K}$  and  $\text{N}_2/77$

## *Experimental Section*

---

K) measurements were performed using IGA001 and ASAP2020 surface area analyzer. The sample was first degassed at 130 °C for 12 h. Crystals for X-ray Diffraction (XRD) were prepared under inert conditions immersed in perfluoropolyether or paratone as protecting oil for manipulation. Suitable crystals were mounted on MiTeGen Micromounts<sup>TM</sup>, and used for data collection at BL13 (XALOC)[68] at the ALBA synchrotron with an undulator source and channel-cut Si(111) monochromator and Kirkpatrick-Baez focusing mirrors with a selected wavelength of 0.72932 Å. An MD2M-Maatel diffractometer fitted with a Dectris Pilatus 6M detector was employed. The sample was kept at 100 K with an Oxford Cryosystems 700 series Cryostream. The structure was solved with the ShelXT 2014/5 (Sheldrick, 2014) structure solution program using the direct phasing methods solution method and by using **Olex2** as the graphical interface.[69] The model was refined with version 2016/6 of **ShelXL** using Least Squares minimisation.[70] Highly disordered solvent, identified as 6 ethanol per formula unit, was treated using a solvent mask (Squeeze). A summary of crystal data is reported in Table S1 in the SI. Powder X-ray Diffraction (PXRD) was recorded at room temperature on a Siemens D-5000 diffractometer with Cu K $\alpha$  radiation ( $\lambda = 1.54056$  Å, 45kV, 35mA, increment=0.02°). Morphological features were examined first by optical microscopy and subsequently by scanning electron microscopy (SEM) with a QUANTA FEI 200 FEGSEM microscope. Water contact-angles were measured using a Krüss DSA 100 device at room temperature using water as the probe fluid (9  $\mu$ L). Inductively Coupled Plasma – Mass Spectrometry (ICP-MS) measurements were carried out in an Agilent ICP-MS 7700x apparatus. Water, ethanol and butanol adsorption isotherms were measured at 313 K while acetone isotherms were collected at 303 K using the Microtrac BELSORP aqua<sup>3</sup> instrument. <sup>1</sup>H NMR spectra were recorded on a Bruker Advance DPX-360 MHz spectrometer in deuterated chloroform, and referenced to the residual solvent peak.

WAXS patterns were recorded on the NCD-SWEET beamline at ALBA synchrotron light source (Spain). An X-ray beam of 8 keV ( $\lambda = 1.54$  Å) was set using a Si (111)

channel cut monochromator. The scattered radiation was recorded using a Rayonix LX-255HS area detector. The sample to detector distance and the reciprocal space calibration were obtained using  $\text{Cr}_2\text{O}_3$  as a standard calibrant. The MOF was introduced in a borosilicate capillary and heated until 300 °C using a Linkam TMS-350 capillary stage (10 °C/min from 25 °C; resting 30 minutes after every 50 °C increase) under dynamic vacuum. Data reduction from 2D images to 1D profiles via azimuthal integration was done using PyFAI [71].

The isothermal parameters were well fitted by the Lagmuir-Freundlich (LF) method from the pure adsorption isotherms at 313K [72,73]. Fitting parameters of LF equation as well as the correlation coefficients ( $R^2$ ) are listed in Tables S4-5 and S4-6. Predicted isotherms and Selectivity for mixtures of butanol and ethanol (0.85:0.15) at 313K was analyzed using IAST.

#### 4.4.2 Materials

1,7-di(4-carboxyphenyl)-1,7-dicarba-*closo*-dodecaborane ligand (*mCB-H<sub>2</sub>L1*) was synthesized according to the literature procedure [74]. Synthesis of ***mCB-MOF-1*** was done in air. All chemicals were commercially available and used as received.

Synthesis of  $[\text{Cu}_2(\textit{mCB-L1})_2(\text{DABCO})_{0.5}(\text{H}_2\text{O})] \cdot 2\text{DMF} \cdot 2\text{H}_2\text{O}$  (***mCB-MOF-1***). *mCB-H<sub>2</sub>L1* (90 mg, 0.234 mmol), DABCO (6.5 mg, 0.059 mmol), DMF (5 mL) and  $\text{H}_2\text{O}$  (1 mL) were added to an 8-dram vial and the mixture was sonicated until dissolution of the solids. Next, an ethanol solution (5 mL) of  $\text{Cu}(\text{NO}_3)_2 \cdot 6\text{H}_2\text{O}$  (68 mg, 0.234 mmol) was added to the mixture. The vial was closed and heated at 80 °C in an oven for 48 h, followed by slow-cooling to room temperature for 5 h. Greenish crystals of ***mCB-MOF-1*** were collected and washed with DMF (100 mg, yield 50 %). IR (ATR; selected bands;  $\text{cm}^{-1}$ ): 2601 (BH); 1716 (C=O from carboxylate). Elemental analysis (%) calculated for  $\text{C}_{41}\text{H}_{32}\text{B}_{20}\text{Cu}_2\text{NO}_9$ : C 42.67, H 4.54, N 3.64; Found: C

42.68, H 4.97, N 3.59.

As synthesized **mCB-MOF-1** crystals were immersed in acetone (20 mL) and replaced once a day for three days, filtered and dried in air. The later was then activated by heating at 130 °C under dynamic ultrahigh vacuum for 12h.

#### **4.4.3 Hydrothermal Stability Tests**

Solvent-exchanged and fully activated **mCB-MOF-1'** was used for all hydrothermal stability tests. All experiments were replicated and the conditions were chosen to test stability in liquid water at room temperature and at 90 °C in closed vials inside an oven (Table S4-2). Such heating conditions were chosen as a more reproducible method than that for the unspecific “boiling water” methods reported in the literature. Samples treated under the different conditions, were filtered, and dried in air. Stability of the treated samples was evaluated by X-ray diffraction, and BET of activated samples. Selected water treated samples were further analyzed for Cu content by ICP or SEM images.

#### **4.4.4 Breakthrough Experiments**

MOFs (500 mg) were packed into a stainless steel column (10 cm long; 4 mm internal diameter) and activated by heating overnight at 403K under a Helium flow (40ml/min) before measurements. Breakthrough measurements were done as follows: a continuous He flow (40 ml/min) was bubbled through the ABE mixture (acetone 7.04 g/l, 0.715 wt%; *n*-butanol 13.75 g/l, 1.39 wt%; ethanol 2.56 g/l, 0.26 wt%; water 960.69 g/l, 97.63 wt%), thermostated at 313K, the forming stream subsequently was flow through the MOF (**mCB-MOF-1** or ZIF-8) packed in the column at 333K.

#### 4.4.5 NMR Experiments

We performed loading experiments (comparable with the breakthrough experiments above) using a 10 cm long, 4 mm internal diameter home-made glass column and nitrogen as gas carrier (flow, 40 ml/min). The loading experiments were performed on *mCB-MOF-1'* (500 mg) and ZIF-8 (450 mg) at 333 K and atmospheric pressure. After 570 min, the corresponding MOFs' adsorbates were extracted with  $\text{CDCl}_3$  and the concentration of each molecule was determined by NMR, using benzene as an internal standard. The results are summarized in Table S4-7.

#### 4.4.6 Adsorbate Location

In order to localize the positions of the butanol, ethanol or acetone molecules within the *mCB-MOF-1'* pores, the Adsorption Locator module of the Materials Studio 6.0 software[75] was employed to perform Monte Carlo simulations. The used forcefield was COMPASS [76], the charge was forcefield assigned and the summation methods were group- and atom-based. The simulations yielded the most stable conformation of the butanol, ethanol or acetone molecules within the pores of *mCB-MOF-1'*.

#### 4.4.7 Binding Energy Calculation

Periodic DFT calculations were carried out using the CP2K code [77]. All calculations employed a mixed Gaussian and planewave basis sets. Core electrons were represented with norm-conserving Goedecker-Teter-Hutter pseudopotentials [78-80], and the valence electron wavefunction was expanded in a double-zeta basis set with polarization functions [81] along with an auxiliary plane wave basis set with an energy cutoff of 400 eV. The generalized gradient approximation exchange-correlation functional of Perdew, Burke, and Enzerhof (PBE) [82] was used. Test calculations showed that the total energy change of the reactive system was negligible ( $<0.01$  eV)

## *Experimental Section*

---

when the maximum force convergence criteria of 0.001 hartree/bohr was used. Each reaction state configuration was optimized with the Broyden-Fletcher-Goldfarb-Shanno (BGFS) algorithm with SCF convergence criteria of  $1.0 \times 10^{-8}$  au. To compensate the long-range van der Waals dispersion interaction between the adsorbate and the MOF, the DFT-D3 scheme[83] with an empirical damped potential term was added into the energies obtained from exchange-correlation functional in all calculations. The value of binding energies (BE) were calculated as the energy difference before and after adsorption in the adsorption process, as defined by

$$BE = E_{\text{MOF+vapor}} - E_{\text{MOF}} - E_{\text{vapor}}$$

where  $E_{\text{MOF+vapor}}$  is the total energy of the MOF/ABE adsorption system in equilibrium state, while  $E_{\text{MOF}}$  and  $E_{\text{vapor}}$  are the energy of the adsorbate-free MOF structures and the vapor adsorbate, respectively. A negative value of BE suggests an exothermic adsorption of the vapor molecule over MOF.

## 4.5 References

- [1] V. Masson-Delmotte, P.Z., H. O. Pörtner, D. Roberts, J. Skea, P. R. Shukla, A. Pirani, W. Moufouma-Okia, C. Péan, R. Pidcock, S. Connors, J. B. R. Matthews, Y. Chen, X. Zhou, M. I. Gomis, E. Lonnoy, T. Maycock, M. Tignor, T. Waterfield (eds.). *World Meteorological Organization, Geneva, Switzerland, 32 pp.* **2018**.
- [2] Gough, C. *UK: John Wiley & Sons Ltd.* **2018**.
- [3] Lampe, A.I.; Dittmar, A.K.; Heyen, C.; Kiefer, J. *Fuel* **2018**, *222*, 312.
- [4] Demirbas, A. *Energy Conversion and Management* **2008**, *49*, 2106.
- [5] Ni, Y.; Sun, Z. *Applied Microbiology and Biotechnology* **2009**, *83*, 415.
- [6] Xue, C.; Zhao, X.-Q.; Liu, C.-G.; Chen, L.-J.; Bai, F.-W. *Biotechnology Advances* **2013**, *31*, 1575.
- [7] Kujawska, A.; Kujawski, J.; Bryjak, M.; Kujawski, W. *Renewable and Sustainable Energy Reviews* **2015**, *48*, 648.
- [8] Huang, H.-J.; Ramaswamy, S.; Liu, Y. *Separation and Purification Technology* **2014**, *132*, 513.
- [9] Friedl, A. *FEMS Microbiology Letters* **2016**, *363*.
- [10] Oudshoorn, A.; van der Wielen, L.A.M.; Straathof, A.J.J. *Industrial & Engineering Chemistry Research* **2009**, *48*, 7325.
- [11] Abdehagh, N.; Tezel, F.H.; Thibault, J. *Adsorption* **2013**, *19*, 1263.
- [12] Qureshi, N.; Hp, B. *Recovery of butanol from fermentation broth by gas stripping*; 2018.
- [13] Abdehagh, N.; Dai, B.; Thibault, J.; Handan Tezel, F. *Journal of Chemical Technology & Biotechnology* **2017**, *92*, 245.
- [14] Pyrgakis, K.A.; de Vrije, T.; Budde, M.A.W.; Kyriakou, K.; López-Contreras, A.M.; Kokossis, A.C. *Biochemical Engineering Journal* **2016**, *116*, 176.
- [15] Bhattacharyya, S.; Jayachandrababu, K.C.; Chiang, Y.; Sholl, D.S.; Nair, S. *ACS Sustainable Chemistry & Engineering* **2017**, *5*, 9467.
- [16] Van der Perre, S.; Gelin, P.; Claessens, B.; Martin-Calvo, A.; Cousin Saint Remi, J.; Duerinck, T.; Baron, G.V.; Palomino, M.; Sánchez, L.Y.; Valencia, S., et al. *ChemSusChem* **2017**, *10*, 2968.
- [17] Ding, M.; Flaig, R.W.; Jiang, H.-L.; Yaghi, O.M. *Chemical Society Reviews* **2019**, *48*, 2783.
- [18] Trickett, C.A.; Helal, A.; Al-Maythalyony, B.A.; Yamani, Z.H.; Cordova, K.E.; Yaghi, O.M. *Nature Reviews Materials* **2017**, *2*.
- [19] Furukawa, H.; Cordova, K.E.; O'Keeffe, M.; Yaghi, O.M. *Science* **2013**, *341*, 974.
- [20] Lin, R.-B.; Xiang, S.; Xing, H.; Zhou, W.; Chen, B. *Coordination Chemistry Reviews* **2019**, *378*, 87.
- [21] Mínguez Espallargas, G.; Coronado, E. *Chemical Society Reviews* **2018**, *47*, 533.
- [22] Wang, H.; Zhu, Q.-L.; Zou, R.; Xu, Q. *Chem* **2017**, *2*, 52.
- [23] Lustig, W.P.; Mukherjee, S.; Rudd, N.D.; Desai, A.V.; Li, J.; Ghosh, S.K. *Chemical Society Reviews* **2017**, *46*, 3242.
- [24] Chen, B.; Eddaoudi, M.; Hyde, S.T.; O'Keeffe, M.; Yaghi, O.M. *Science* **2001**, *291*, 1021.
- [25] Boyd, P.G.; Chidambaram, A.; García-Díez, E.; Ireland, C.P.; Daff, T.D.; Bounds, R.; Gładysiak, A.; Schouwink, P.; Moosavi, S.M.; Maroto-Valer, M.M., et al. *Nature* **2019**, *576*, 253.
- [26] Ebrahim, F.M.; Nguyen, T.N.; Shyshkanov, S.; Gładysiak, A.; Favre, P.; Zacharia, A.; Itskos, G.; Dyson, P.J.; Stylianou, K.C. *Journal of the American Chemical Society* **2019**, *141*, 3052.
- [27] Kampouri, S.; Nguyen, T.N.; Spodaryk, M.; Palgrave, R.G.; Züttel, A.; Smit, B.; Stylianou, K.C.



## References

---

- Advanced Functional Materials* **2018**, *28*, 1806368.
- [28] Shyshkanov, S.; Nguyen, T.N.; Ebrahim, F.M.; Stylianou, K.C.; Dyson, P.J. *Angewandte Chemie International Edition* **2019**, *58*, 5371.
- [29] Cousin Saint Remi, J.; Rémy, T.; Van Hunskerken, V.; van de Perre, S.; Duerinck, T.; Maes, M.; De Vos, D.; Gobechiya, E.; Kirschhock, C.E.A.; Baron, G.V., et al. *ChemSusChem* **2011**, *4*, 1074.
- [30] Zhang, K.; Lively, R.P.; Dose, M.E.; Brown, A.J.; Zhang, C.; Chung, J.; Nair, S.; Koros, W.J.; Chance, R.R. *Chemical Communications* **2013**, *49*, 3245.
- [31] Li, K.; Olson, D.H.; Seidel, J.; Emge, T.J.; Gong, H.; Zeng, H.; Li, J. *Journal of the American Chemical Society* **2009**, *131*, 10368.
- [32] Gao, C.; Wu, J.; Shi, Q.; Ying, H.; Dong, J. *Microporous and Mesoporous Materials* **2017**, *243*, 119.
- [33] Cousin-Saint-Remi, J.; Denayer, J.F.M. *Chemical Engineering Journal* **2017**, *324*, 313.
- [34] Cousin-Saint-Remi, J.; Finoult, A.-L.; Jabbour, C.; Baron, G.V.; Denayer, J.F.M. *Microporous and Mesoporous Materials* **2019**, <https://doi.org/10.1016/j.micromeso.2019.02.009>, 109322.
- [35] Cousin-Saint-Remi, J.; Van der Perre, S.; Segato, T.; Delplancke, M.-P.; Goderis, S.; Terryn, H.; Baron, G.; Denayer, J. *ACS Applied Materials & Interfaces* **2019**, *11*, 13694.
- [36] Liu, X.; He, L.; Zheng, J.; Guo, J.; Bi, F.; Ma, X.; Zhao, K.; Liu, Y.; Song, R.; Tang, Z. *Advanced Materials* **2015**, *27*, 3273.
- [37] Liu, X.-L.; Li, Y.-S.; Zhu, G.-Q.; Ban, Y.-J.; Xu, L.-Y.; Yang, W.-S. *Angewandte Chemie International Edition* **2011**, *50*, 10636.
- [38] Bai, Y.; Dong, L.; Zhang, C.; Gu, J.; Sun, Y.; Zhang, L.; Chen, H. *Separation Science and Technology* **2013**, *48*, 2531.
- [39] Li, Y.; Wee, L.H.; Martens, J.A.; Vankelecom, I.F.J. *Journal of Materials Chemistry A* **2014**, *2*, 10034.
- [40] Tan, F.; López-Periago, A.; Light, M.E.; Cirera, J.; Ruiz, E.; Borrás, A.; Teixidor, F.; Viñas, C.; Domingo, C.; Planas, J.G. *Advanced Materials* **2018**, *30*, 1800726.
- [41] Tsang, M.Y.; Rodríguez-Hermida, S.; Stylianou, K.C.; Tan, F.; Negi, D.; Teixidor, F.; Viñas, C.; Choquesillo-Lazarte, D.; Verdugo-Escamilla, C.; Guerrero, M., et al. *Crystal Growth & Design* **2017**, *17*, 846.
- [42] Rodríguez-Hermida, S.; Tsang, M.Y.; Vignatti, C.; Stylianou, K.C.; Guillerm, V.; Perez-Carvajal, J.; Teixidor, F.; Vinas, C.; Choquesillo-Lazarte, D.; Verdugo-Escamilla, C., et al. *Angew Chem Int Ed Engl* **2016**, *55*, 16049.
- [43] Scholz, M.; Hey-Hawkins, E. *Chemical Reviews* **2011**, *111*, 7035.
- [44] Issa, F.; Kassiou, M.; Rendina, L.M. *Chemical Reviews* **2011**, *111*, 5701.
- [45] In *Boron-Based Compounds. Potential and Emerging applications in Medicine*, Teixidor, E.H.-H.a.C.V., Ed. John Wiley & Sons Ltd: UK, 2018; 10.1002/9781119275602.
- [46] Clara, V.; Rosario, N.; Ines, B.; Francesc, T. *Current Medicinal Chemistry* **2019**, *26*, 5036.
- [47] Hosmane, N. In *Boron Science*, CRC Press: Boca Raton, 2012; <https://doi.org/10.1201/b11199>.
- [48] *Handbook of Boron Chemistry in Organometallics, Catalysis, Materials and Medicine*; Hosmane, N.a.E.R., Ed. Imperial College Press/World Scientific Publishing Ltd.: UK, 2018; pp. 1400.
- [49] Zhan, C.-H.; Feng, Y.-L. *Journal of Solid State Chemistry* **2010**, *183*, 1226.
- [50] Wang, J.; Wu, X.-R.; Liu, J.-Q.; Li, B.-H.; Singh, A.; Kumar, A.; Batten, S.R. *CrystEngComm* **2017**,

- 19, 3519.
- [51] Eubank, J.F.; Wojtas, L.; Hight, M.R.; Bousquet, T.; Kravtsov, V.C.; Eddaoudi, M. *Journal of the American Chemical Society* **2011**, *133*, 17532.
- [52] Wang, H.-N.; Meng, X.; Yang, G.-S.; Wang, X.-L.; Shao, K.-Z.; Su, Z.-M.; Wang, C.-G. *Chemical Communications* **2011**, *47*, 7128.
- [53] Klein, N.; Senkovska, I.; Baburin, I.A.; Grünker, R.; Stoeck, U.; Schlichtenmayer, M.; Streppel, B.; Mueller, U.; Leoni, S.; Hirscher, M., et al. *Chemistry – A European Journal* **2011**, *17*, 13007.
- [54] Müller, P.; Wisser, F.M.; Freund, P.; Bon, V.; Senkovska, I.; Kaskel, S. *Inorganic Chemistry* **2017**, *56*, 14164.
- [55] Chung, H.; Barron, P.M.; Novotny, R.W.; Son, H.-T.; Hu, C.; Choe, W. *Crystal Growth & Design* **2009**, *9*, 3327.
- [56] Jiang, H.-L.; Makal, T.A.; Zhou, H.-C. *Coordination Chemistry Reviews* **2013**, *257*, 2232.
- [57] Jasuja, H.; Walton, K.S. *Dalton Transactions* **2013**, *42*, 15421.
- [58] Park, S.S.; Hendon, C.H.; Fielding, A.J.; Walsh, A.; O’Keeffe, M.; Dincă, M. *Journal of the American Chemical Society* **2017**, *139*, 3619.
- [59] Gelfand, B.S.; Shimizu, G.K.H. *Dalton Transactions* **2016**, *45*, 3668.
- [60] Shtukenberg, A.G.; Punin, Y.O.; Gunn, E.; Kahr, B. *Chemical Reviews* **2012**, *112*, 1805.
- [61] DeCoste, J.B.; Peterson, G.W.; Schindler, B.J.; Killups, K.L.; Browe, M.A.; Mahle, J.J. *Journal of Materials Chemistry A* **2013**, *1*, 11922.
- [62] He, H.; Sun, Q.; Gao, W.; Perman, J.A.; Sun, F.; Zhu, G.; Aguila, B.; Forrest, K.; Space, B.; Ma, S. *Angewandte Chemie - International Edition* **2018**, *57*, 4657.
- [63] Canivet, J.; Fateeva, A.; Guo, Y.; Coasne, B.; Farrusseng, D. *Chemical Society Reviews* **2014**, *43*, 5594.
- [64] PXRD experiments confirmed the stability of the MOF after being shaped into a pellet.
- [65] Sann, E.E.; Pan, Y.; Gao, Z.; Zhan, S.; Xia, F. *Separation and Purification Technology* **2018**, *206*, 186.
- [66] Jayaramulu, K.; Geyer, F.; Schneemann, A.; Kment, S.; Otyepka, M.; Zboril, R.; Vollmer, D.; Fischer, R.A. *Adv Mater* **2019**, *31*, e1900820.
- [67] Myers, A.L.; Prausnitz, J.M. *AIChE Journal* **1965**, *11*, 121.
- [68] Juanhuix, J.; Gil-Ortiz, F.; Cuni, G.; Colldelram, C.; Nicolas, J.; Lidon, J.; Boter, E.; Ruget, C.; Ferrer, S.; Benach, J. *Journal of Synchrotron Radiation* **2014**, *21*, 679.
- [69] Dolomanov, O.V.; Bourhis, L.J.; Gildea, R.J.; Howard, J.A.K.; Puschmann, H. *Journal of Applied Crystallography* **2009**, *42*, 339.
- [70] Sheldrick, G. *Acta Crystallographica Section C* **2015**, *71*, 3.
- [71] Kieffer, J.; Karkoulis, D. *Journal of Physics: Conference Series* **2013**, *425*, 202012.
- [72] Babarao, R.; Hu, Z.; Jiang, J.; Chempath, S.; Sandler, S.I. *Langmuir* **2007**, *23*, 659.
- [73] Goetz, V.; Pupier, O.; Guillot, A. *Adsorption* **2006**, *12*, 55.
- [74] Fox, M.A. *Durham theses, Durham University*. **1991**.
- [75] Biovia Materials Studio 6.0: San Diego: Dassault Systèmes 2018.
- [76] Sun, H. *The Journal of Physical Chemistry B* **1998**, *102*, 7338.
- [77] Vandevonede, J.; Krack, M.; Mohamed, F.; Parrinello, M.; Chassaing, T.; Hutter, J. *Computer Physics Communications* **2005**, *167*, 103.
- [78] Goedecker, S.; Teter, M. *Physical Review B - Condensed Matter and Materials Physics* **1996**, *54*, 1703.

## References

---

- [79] Hartwigsen, C.; Goedecker, S.; Hutter, J. *Physical Review B - Condensed Matter and Materials Physics* **1998**, *58*, 3641.
- [80] Krack, M.; Parrinello, M. *Physical Chemistry Chemical Physics* **2000**, *2*, 2105.
- [81] VandeVondele, J.; Hutter, J. *The Journal of Chemical Physics* **2007**, *127*, 114105.
- [82] Perdew, J.P.; Burke, K.; Ernzerhof, M. *Physical Review Letters* **1997**, *78*, 1396.
- [83] Grimme, S.; Antony, J.; Ehrlich, S.; Krieg, H. *Journal of Chemical Physics* **2010**, *132*.

# Chapter 5

---

*Selective Adsorptive  
Separation of Gases and  
Efficient Oil-Water Separation  
by a Hydrophobic  
Carborane-Based  
Metal-Organic Framework*

*The gas sorption and separation experiments in this Chapter have been carried out at the Instituto de Ciencia Molecular (ICMol)-Universidad de Valencia as part of a collaboration with Dr Guillermo Minguez Espallargas.*



---

## Selective Adsorptive Separation of Gases and Efficient Oil-Water Separation by a Hydrophobic Carborane-Based Metal-Organic Framework

### 5.1 Introduction

The global greenhouse effect, which is caused by the emission of CO<sub>2</sub> into the atmosphere, has attracted more and more attention [1]. According to the NASA's report in 2017 [2,3], the CO<sub>2</sub> concentration in the atmosphere is reaching alarming levels. During the past 10-15 years, the atmosphere CO<sub>2</sub> concentration has increased from 365 ppm to 475 ppm [3]. Apart from natural processes, the consumption of carbon-base fossil fuels is mainly responsible for generating the CO<sub>2</sub> emission [2,3]. In 2009, the U.S. Department of Energy (DOE) issued a carbon sequestration program for achieving 90% CO<sub>2</sub> capture at an increase in the cost of electricity of less than 35% for the post-combustion process by 2020 [4]. Post-combustion CO<sub>2</sub> process usually involves the fuel gas. Fuel gas mainly contains *ca.* 15% CO<sub>2</sub>, *ca.* 75% N<sub>2</sub>, *ca.* 3-4% O<sub>2</sub> as well as saturated water vapor and small amounts of acid gases such as SO<sub>x</sub>, NO<sub>x</sub>, with a total pressure of 1 atm and a temperature of 40-80 °C [5]. Moreover, the separation of CO<sub>2</sub> from biogas and natural gas is also promising for utilizing these gases as alternative cleaner fuels. Biogas mainly consists of *ca.* 60-70% CH<sub>4</sub> and *ca.* 30-40% CO<sub>2</sub> at ambient temperature and pressure [6]. Natural gas mainly consists of CH<sub>4</sub> and small amounts of CO<sub>2</sub> (usually *ca.* 1%) which is produced at 30-60 °C and 50-70 bar [7]. Therefore, developing economical methods to efficiently capture and separate CO<sub>2</sub> from flue gas and purify CH<sub>4</sub> from biogas or natural gas are highly desirable.

So far, a number of technologies and materials have been developed toward CO<sub>2</sub> capture and separation, such as aqueous ammonia and amine functionalized solids adsorption [8-10], membrane separation [11,12], and cryogenics distillation [13-15]

among others. Compared with traditional techniques, adsorption-based methods using porous materials to capture or separate CO<sub>2</sub> with less energy consumption and cost shows great advantages among these technologies. Activated carbon, zeolites, and carbon molecular sieves have been extensively studied as adsorbents for CO<sub>2</sub>/N<sub>2</sub> and CO<sub>2</sub>/CH<sub>4</sub> separation [16-18]. However, the drawback of these materials is their low adsorption capacities or difficult regeneration process. Metal-organic frameworks (MOFs), exhibit outstanding separation performance toward CO<sub>2</sub>/N<sub>2</sub> and CO<sub>2</sub>/CH<sub>4</sub> binary mixtures due to their large surface areas, tunable pore-size and pore surface, and existing open metal sites [19-22]. To date, many MOFs have been reported for CO<sub>2</sub>/N<sub>2</sub> and CO<sub>2</sub>/CH<sub>4</sub> separation. But most of them are fragile when exposed to water conditions, such as HKUST-1 [23] and MOF-5 [24], two of the most famous MOFs. Additionally, MOFs have been considered to be promising candidates for the application of oil-spills which have caused severe water pollution leading to a threat to marine species and human life due to its degradability and harmlessness [25-27]. Thus it is very important to develop water-stable or hydrophobic MOFs for these separation applications in environmental field.

Recently, Zhang and co-workers [28] presented a water-stable borane-based MOF, BSF-1, which showed good separation performance toward C1-C3 gases mixture. Encouraged by his work, we have investigated our hydrophobic *meta*-carborane-based MOF (***mCB-MOF-1***; described in Chapter 4) for a series of gases adsorption and binary gas mixture separation, as well as for oil-water separation. In this work, we show that ***mCB-MOF-1*** exhibits excellent performance for CO<sub>2</sub>/N<sub>2</sub> separation validated by breakthrough experiments and is a potential candidate for efficient oil-water separation.

## **5.2 Results and Discussion**

Full characterization and stability of ***mCB-MOF-1*** is described in Chapter 4 of the

present thesis.

### 5.2.1 Adsorption Isotherms of CO<sub>2</sub>, CH<sub>4</sub>, H<sub>2</sub> and N<sub>2</sub> on *mCB-MOF-1*

To investigate the potential gas adsorption and separation of *mCB-MOF-1*, the single-component adsorption isotherms of CO<sub>2</sub>, CH<sub>4</sub>, and N<sub>2</sub> were collected at various temperatures at a pressure range of 2 bar (Figure 5-1, Figure S5-1, and S5-2). CO<sub>2</sub> uptakes on *mCB-MOF-1* at 2 bar were 2.14, 1.66, 1.44, and 1.23 mmol/g at 273, 293, 303, and 313 K, respectively, these values being compatible with other ultramicroporous MOFs [29]. When compared with CH<sub>4</sub> and N<sub>2</sub> the uptakes, the CO<sub>2</sub> adsorption capacity for *mCB-MOF-1* was much higher under all different temperatures and pressures, as shown in Figures 5-2 and 5-3. At 2 bar and 273 K, CO<sub>2</sub> and CH<sub>4</sub> adsorption amounts were 2.14, 1.14 mmol/g, respectively. CO<sub>2</sub> and N<sub>2</sub> adsorption uptakes at 1 bar and 313K were 0.80, 0.12 mmol/g, respectively. These results demonstrate that CO<sub>2</sub> molecules have stronger interactions with *mCB-MOF-1* compared to CH<sub>4</sub> and N<sub>2</sub>, highlighting its advantage for highly effective separation of CO<sub>2</sub> from CH<sub>4</sub> and N<sub>2</sub>. We also determined the hydrogen adsorption isotherms at low pressure at 77 K and at high pressure at 273 K, 298 K, and 323 K for *mCB-MOF-1* (Figure 5-4). It was observed that the maximum adsorption capacities reached 2.05, 1.48 mmol/g at 153 bar at 273, 298 K, respectively, and 1.11 mmol/g at 142 bar and 323 K. The relatively low hydrogen adsorption amounts indicate its potential for CO<sub>2</sub>-H<sub>2</sub> gas mixtures' separation.



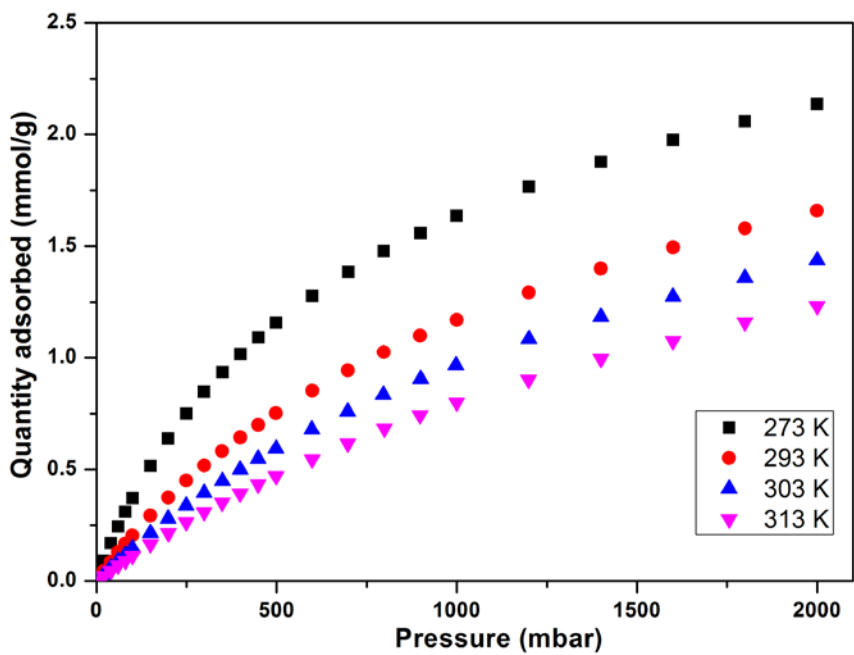


Figure 5-1. CO<sub>2</sub> adsorption isotherms on *mCB*-MOF-1 at 273-313 K.

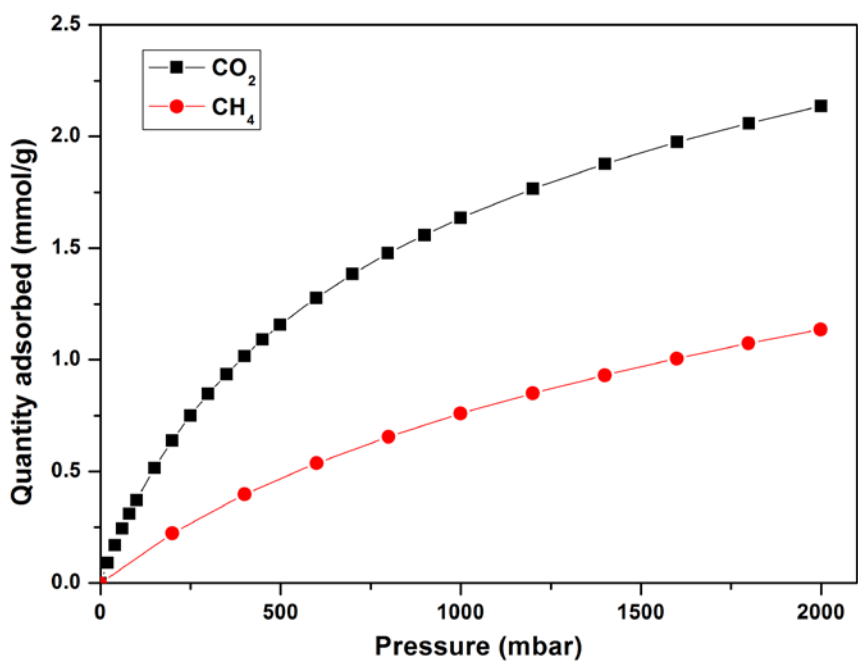


Figure 5-2. Comparison of CO<sub>2</sub> and CH<sub>4</sub> adsorption isotherms on *mCB*-MOF-1 at 273 K.

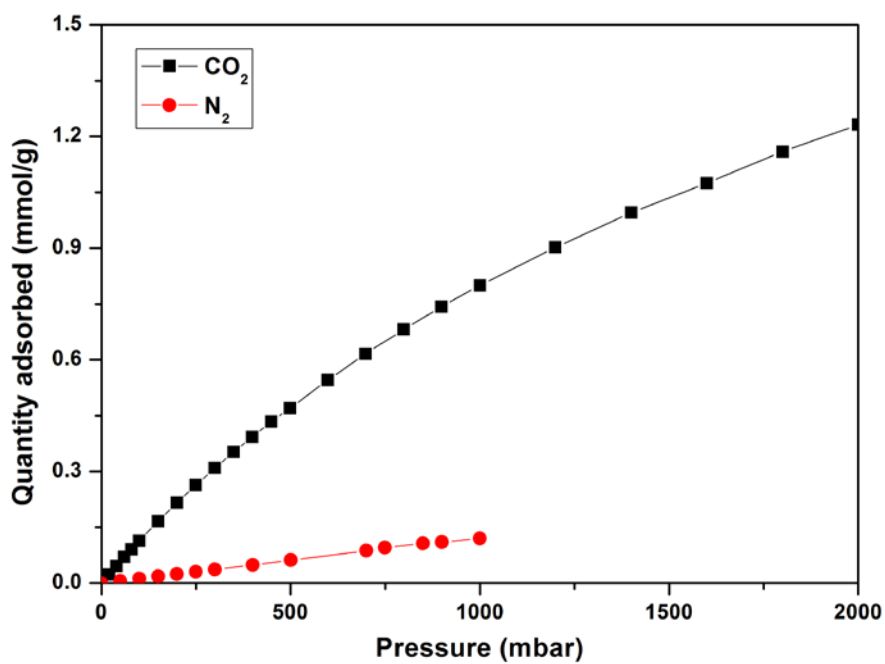


Figure 5-3. Comparison of CO<sub>2</sub> and N<sub>2</sub> adsorption isotherms on *mCB-MOF-1* at 313 K.

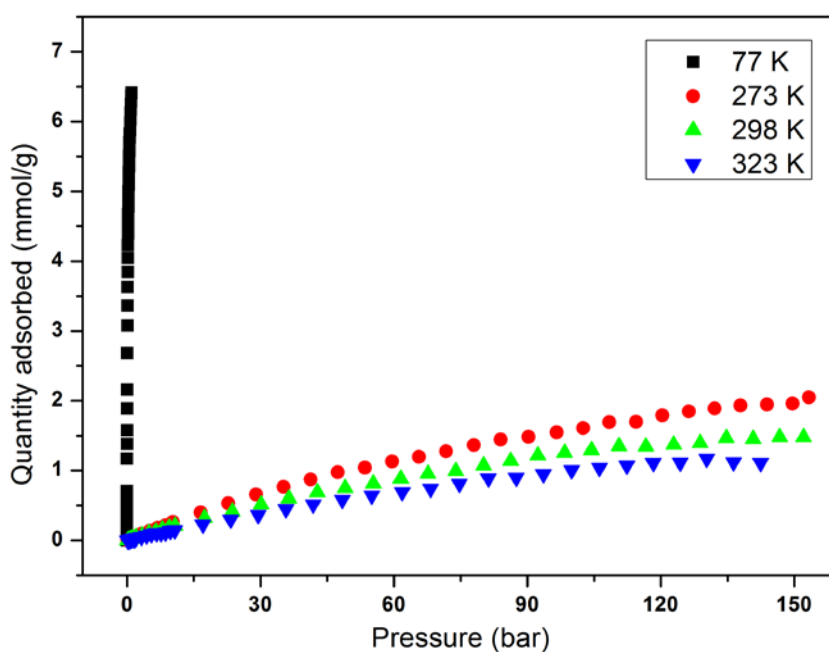
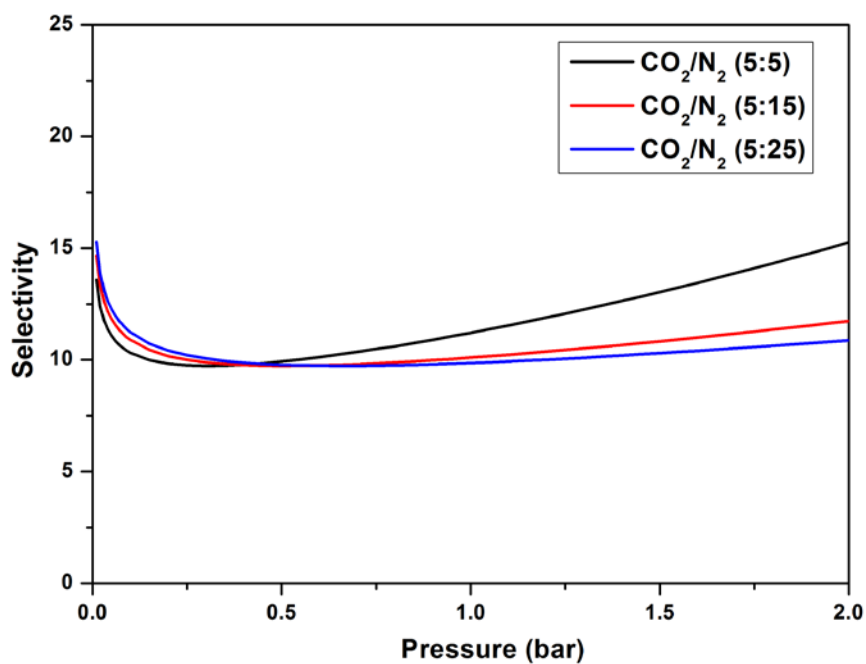


Figure 5-4. H<sub>2</sub> adsorption isotherms on *mCB-MOF-1* at 77 K at low pressure and at 273-323 K at high pressure.

### 5.2.2 IAST Predicted Adsorption Selectivities of CO<sub>2</sub>/N<sub>2</sub> and CO<sub>2</sub>/CH<sub>4</sub> on *mCB-MOF-1*

The adsorption differences in *mCB-MOF-1* encouraged us to investigate the CO<sub>2</sub> selectivity over CH<sub>4</sub> and N<sub>2</sub>. Ideal adsorbed solution theory (IAST) [30] was employed to predict the adsorption selectivity of theoretical CO<sub>2</sub>/N<sub>2</sub> and CO<sub>2</sub>/CH<sub>4</sub> gas mixtures. The adsorption isotherms of CO<sub>2</sub>, CH<sub>4</sub>, and N<sub>2</sub> were fitted by different Langmuir-Freundlich isotherm models (see details in SI). The obtained fitting parameters are summarized in Table S5-1, S5-2 and S5-3. It was noticed that all regression coefficients  $R^2$  were higher than 0.999, indicating the excellent fitting of the data. Figure 5-5 and 5-6 exhibits predicted IAST selectivities for CO<sub>2</sub>/CH<sub>4</sub> binary mixtures (5:5, 5:15, or 5:25, v/v) at 273 K and CO<sub>2</sub>/N<sub>2</sub> binary mixtures (5:5, 5:15, or 5:25, v/v) at 313 K over the pressure range 0-2 bar. It was observed that both CO<sub>2</sub>/CH<sub>4</sub> and CO<sub>2</sub>/N<sub>2</sub> adsorption selectivities decreased sharply along with the increase of pressure in the low pressure region. However, in the high pressure region, there was no significant change when the pressure was increasing for CO<sub>2</sub>/CH<sub>4</sub> mixture (5:15, or 5:25) and CO<sub>2</sub>/N<sub>2</sub> mixture (5:15, or 5:25) adsorption selectivities, while a gradual increase was observed for equimolar CO<sub>2</sub>/CH<sub>4</sub> mixture (5:5) and CO<sub>2</sub>/N<sub>2</sub> mixture (5:5) adsorption selectivity (Figure 5-5 and 5-6). Furthermore, it should be pointed out that the differences in ratio of CO<sub>2</sub>/CH<sub>4</sub> and CO<sub>2</sub>/N<sub>2</sub> had negligible influence on the binary gas mixtures adsorption selectivities at low pressures. The CO<sub>2</sub>/CH<sub>4</sub> adsorption selectivity at 273 K was in the range 3.92-5.3, with a value of 3.9 at 1 bar. The adsorption selectivity of CO<sub>2</sub>/N<sub>2</sub> at 313 K was in the range 9.7-15.3, which is comparable to other reported MOFs. These results indicate that *mCB-MOF-1* may exhibit good selective adsorption of CO<sub>2</sub> over CH<sub>4</sub> and N<sub>2</sub>.



**Figure 5-5.** IAST predicted selectivities of CO<sub>2</sub>/N<sub>2</sub> (5:5, 5:15, and 5:25, v/v) on *mCB*-MOF-1 at 313 K.

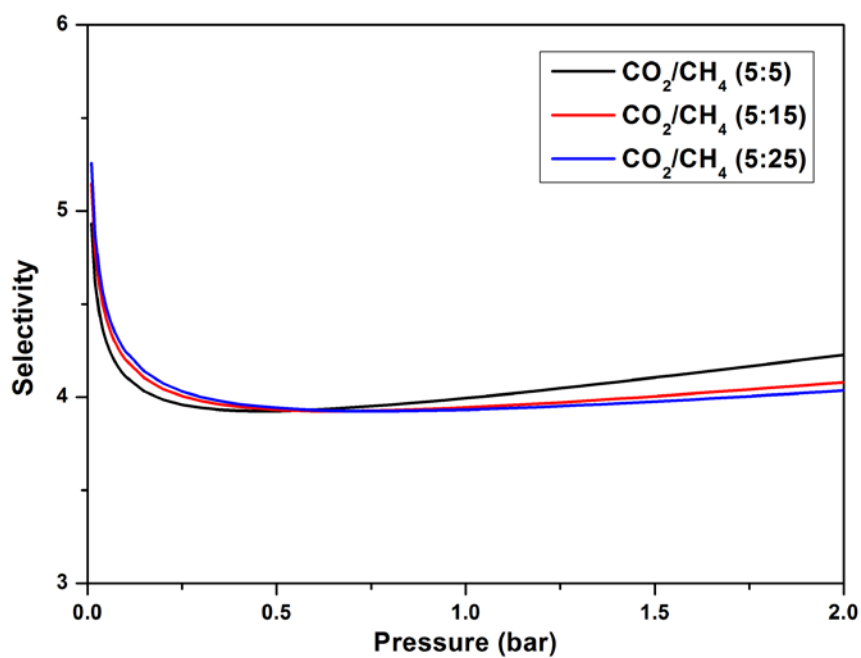


**Figure 5-6.** IAST predicted selectivities of CO<sub>2</sub>/CH<sub>4</sub> (5:5, 5:15, and 5:25, v/v) on *mCB*-MOF-1 at 273K.

### 5.2.3 Isothermic Heat of Adsorption

As an important parameter to evaluate the adsorption affinity of the adsorbate–adsorbent, the isosteric heats of adsorption ( $Q_{st}$ ) of CO<sub>2</sub>, CH<sub>4</sub>, N<sub>2</sub>, and H<sub>2</sub> were derived from isotherm data at different temperatures on the basis of the virial method (see details in SI) [14]. As shown in Figure 5-7, the  $Q_{st}$  values of CO<sub>2</sub>, CH<sub>4</sub>, N<sub>2</sub>, and H<sub>2</sub> for *mCB-MOF-1* with gas loadings were obtained. The  $Q_{st}$  value of CO<sub>2</sub> was in the range of 22.4–25.6 kJ/mol, while the value of  $Q_{st}$  for CH<sub>4</sub>, N<sub>2</sub>, H<sub>2</sub> were in the range of 16.3–18.3, 8.2–8.5, and 9.6–10.6 kJ/mol, respectively. Thus the  $Q_{st}$  value of CO<sub>2</sub>, CH<sub>4</sub>, N<sub>2</sub>, and H<sub>2</sub> followed the order CO<sub>2</sub> > CH<sub>4</sub> > H<sub>2</sub> > N<sub>2</sub>. These results indicate the CO<sub>2</sub> molecules have stronger interactions with *mCB-MOF-1* compared to other gases. The zero-coverage  $Q_{st}$  for CO<sub>2</sub> was 25.6 kJ/mol which was lower than the same Cu<sub>2</sub> paddle-wheel cluster MOF HKUST-1[31]. The relative low  $Q_{st}$  for CO<sub>2</sub> suggested that the regeneration process of *mCB-MOF-1* would be easy to complete and consume less energy. At higher pressure, the  $Q_{st}$  for CO<sub>2</sub> gradually decreased with increasing adsorption which suggested that the preferable adsorption sites within the framework were occupied gradually. However, these  $Q_{st}$  values indicated that the adsorption for CO<sub>2</sub>, CH<sub>4</sub>, N<sub>2</sub>, and H<sub>2</sub> were physisorption and the differences in interactions would be a key factor for CO<sub>2</sub> separation over CH<sub>4</sub> or N<sub>2</sub>.

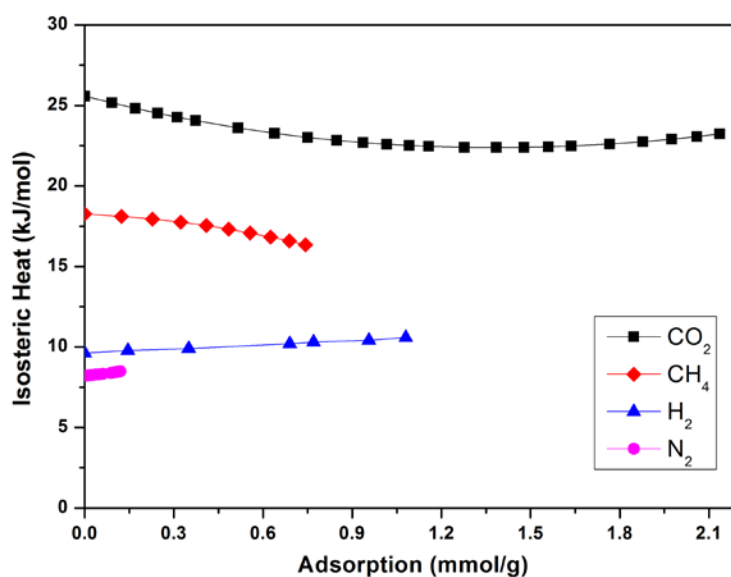


Figure 5-7. Isothermic heat of adsorption of CO<sub>2</sub>, CH<sub>4</sub>, H<sub>2</sub>, and N<sub>2</sub> on *mCB-MOF-1*.

## 5.2.4 Breakthrough Experiments of Binary CO<sub>2</sub>/N<sub>2</sub>, CO<sub>2</sub>/CH<sub>4</sub>, and C<sub>3</sub>H<sub>8</sub>/C<sub>3</sub>H<sub>6</sub> Gas Mixtures on *mCB-MOF-1*

To further evaluate the realistic performance of *mCB-MOF-1*, the dynamic breakthrough experiments of binary CO<sub>2</sub>/N<sub>2</sub> mixture (5:5, 5:15 and 5:25, v/v) and CO<sub>2</sub>/CH<sub>4</sub> mixture (5:5, 5:15 and 5:25, v/v) were performed on an adsorbent bed packed with activated *mCB-MOF-1* at 1 bar. Usually, in the realistic gas mixture separation process, temperature has an important role in the working capacity and the separation ratio. So the temperatures in breakthrough experiments were set to 283, 298, and 323 K for comparison of separation performance. During the experiments, helium (2ml/min) was used as a tracer.

As shown in Figure 5-8, at 298 K *mCB-MOF-1* exhibited excellent separation performance for binary CO<sub>2</sub>/N<sub>2</sub> mixture (5:5) with the CO<sub>2</sub> adsorption capacity of 17.78 ml/g. It was observed that the breakthrough time of N<sub>2</sub> was much shorter than that of CO<sub>2</sub>, indicating that CO<sub>2</sub> was preferentially adsorbed. Figure 5-9 and Table 5-1 summarized the adsorption capacity and selectivity results with various compositions at different temperatures. Both cases of 5:5 CO<sub>2</sub>/N<sub>2</sub> at 298 K and 5:15 CO<sub>2</sub>/N<sub>2</sub> at 283 K breakthrough experiments exhibited excellent selectivities with the values more than 1000, which implied almost all N<sub>2</sub> molecules were kept out of the framework and *mCB-MOF-1* could successfully separate nitrogen from carbon dioxide, being able to obtain a very pure stream of nitrogen. This very high CO<sub>2</sub>/N<sub>2</sub> selectivity of *mCB-MOF-1* has surpassed most reported MOFs as listed in Table 5-2 and represents the highest selectivity among Cu<sub>2</sub> paddle-wheel MOFs so far. Moreover, it was noted that concentration effect did not exhibit a high affinity of a framework toward carbon dioxide. At 298 K, nitrogen adsorption became competitive at low CO<sub>2</sub> concentration which certainly would reduce the CO<sub>2</sub>/N<sub>2</sub> selectivity. However, *mCB-MOF-1* still showed good selectivity for 5:15 CO<sub>2</sub>/N<sub>2</sub> mixture at 298 K with the number of about 81. As we can see, temperature also can influence the CO<sub>2</sub>/N<sub>2</sub> separation performance.

At low temperature CO<sub>2</sub> adsorption was enhanced due to its thermodynamic dominant role, while N<sub>2</sub> adsorption was allowed for competitive adsorption at high temperature because of its kinetic role which would decrease the separation selectivity. The experimental mixed gas CO<sub>2</sub>/N<sub>2</sub> separation selectivity were not completely the same with the results predicted by the IAST calculations, which may be attributed to the used temperature difference and the non-ideality of gas CO<sub>2</sub>/N<sub>2</sub> mixtures deviating from an ideal solution[32]. Anyway, *mCB-MOF-1* has showed great potential in binary CO<sub>2</sub>/N<sub>2</sub> gas separation.

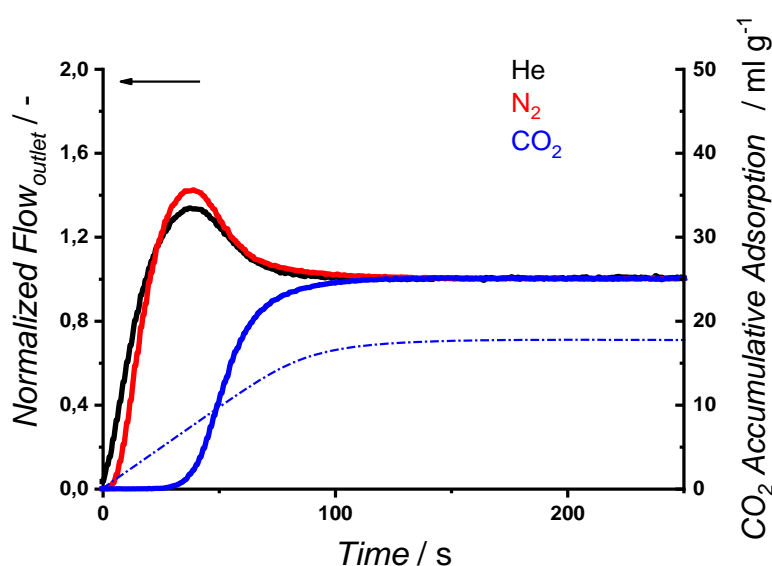


**Figure 5-8.** Breakthrough exit normalized flowrates (solid line, left axis), and CO<sub>2</sub> accumulative adsorbed amount (dash line, right axis) vs. time, at 298 K and 1 bar, on *mCB-MOF-1*. Inlet composition corresponds to a 10 ml min<sup>-1</sup> CO<sub>2</sub>/N<sub>2</sub> (5:5) mixture. Time zero is set with the first detection of helium (tracer).

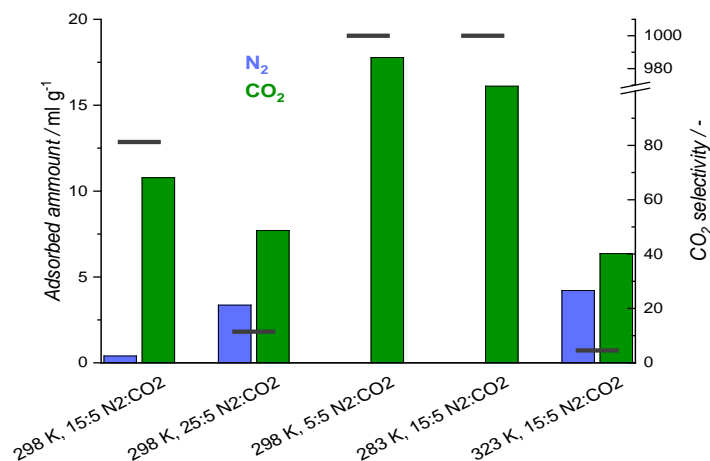


**Figure 5-9.** Breakthrough measurements adsorption and selectivity results summary; performed in an experimental fixed bed reactor (breakthrough setup), for CO<sub>2</sub>/N<sub>2</sub> gas mixtures at different inlet conditions.

**Table 5-1.** Breakthrough measurements adsorption and selectivity results summary; performed in an experimental fixed bed reactor (breakthrough setup), for CO<sub>2</sub>/N<sub>2</sub> gas mixtures at different inlet conditions. Replica measurements included.

Temperature (K)	Flow inlet (ml/min)				Adsorbed Amounts (ml/g)		
	N <sub>2</sub>	CO <sub>2</sub>	He	Ar	N <sub>2</sub>	CO <sub>2</sub>	
298	15	5	2	40	0,40	10,78	81,26
298	15	5	2	40	0,34	10,77	95,43
298	25	5	2	40	3,36	7,70	11,46
298	25	5	2	40	4,68	7,92	8,47
298	5	5	2	40	0,00	17,78	-
298	5	5	2	40	0,00	17,78	-
283	15	5	2	40	0,00	16,11	-
283	15	5	2	40	0,00	15,93	-
323	15	5	2	40	4,21	6,36	4,54
323	15	5	2	40	3,87	6,21	4,81

**Table 5-2.** CO<sub>2</sub> adsorption performance comparisons on the selected MOFs at 1 bar.

MOFs	BET area (m <sup>2</sup> /g)	T/K	CO <sub>2</sub> uptake (mmol/g)	Selectivity CO <sub>2</sub> /N <sub>2</sub> (1:1,v/v)	Ref.
<b>Mg-MOF-74</b>	1775	298	8.78	83.2	[23,33,34]
<b>SIFSIX-2-Cu</b>	3140	298	1.85	13.7 (10:90,v/v)	[19]
<b>SIFSIX-2-Cu-i</b>	735	298	5.41	140 (10:90,v/v)	[19]
<b>SIFSIX-3-Zn</b>	-	298	2.55	1818 (10:90,v/v)	[19]
<b>HKUST-1</b>	1193	273	6.85	101.5	[35]
<b>Al(OH)(NDC)</b>	761	273	1.61	19.6	[36]
<b>PCN-80</b>	3850	296	2.52	11.8	[37]
<b>IISERP-MOF4</b>	692	303	2.69	410	[38]
<b>ZJU-8a</b>	2501	298	2.13	10.5 (15:85,v/v)	[39]
<b>mmen-CuBTTri</b>	870	298	4.2	165/327 (1:5,v/v)	[40]
<b>en-Cu-BTTri</b>	345	298	1.27	44 (1:5,v/v)	[41]



## Results and Discussion

<b>Cu-BTtri</b>	1900	298	3.24	19 (1:5,v/v)	[41]
<b>UiO-66-NH<sub>2</sub></b>	1112	298	2.97	58	[29]
<b>UiO-66-EA</b>	567	298	1.69	365	[29]
<b>mCB-MOF-1</b>	756	298	1.17	~ 1000	This work

It should be pointed out that **mCB-MOF-1** could also separate CO<sub>2</sub>/CH<sub>4</sub> (5:5, 5:15 and 5:25) gas mixtures. As shown in Figure 5-10, the breakthrough time for CH<sub>4</sub> was shorter than that for CO<sub>2</sub> in the 5:5 CO<sub>2</sub>/CH<sub>4</sub> binary mixture separation at 298 K. The observed breakthrough time for CH<sub>4</sub> indicates a stronger competitive adsorption of this gas than that of N<sub>2</sub> in the CO<sub>2</sub>/N<sub>2</sub> mixtures (Figure 5-8 and 5-10). The overall data is consistent with the calculated higher Q<sub>st</sub> for CH<sub>4</sub> than that for N<sub>2</sub>. This can be further explained that methane molecule is more polarizable than nitrogen, although the kinetic diameter of methane is slightly larger than that of nitrogen. Furthermore, unlike the CO<sub>2</sub>/N<sub>2</sub> mixture separation, the CO<sub>2</sub> concentration and temperature barely affected the CO<sub>2</sub>/CH<sub>4</sub> separation ratio (Figure 5-11 and Table 5-3), demonstrating the stronger thermodynamic competition between CO<sub>2</sub> and CH<sub>4</sub>. At 298 K, the CO<sub>2</sub>/CH<sub>4</sub> selectivity of about 3.5 was close to the value (3.9) by IAST prediction at 273 K, indicating the good reliability of the results of the IAST CO<sub>2</sub>/CH<sub>4</sub> selectivity calculations.

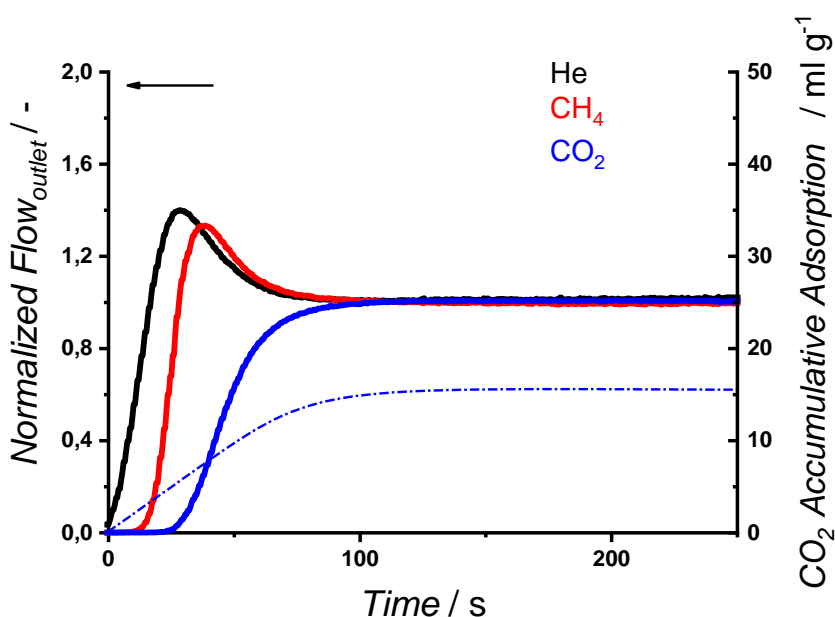


**Figure 5-10.** Breakthrough exit normalized flowrates (solid line, left axis), and CO<sub>2</sub> accumulative adsorbed amount (dash line, right axis) vs. time, at 298 K and 1 bar, on *mCB-MOF-1*. Inlet composition corresponds to a 10 ml min<sup>-1</sup> CO<sub>2</sub>/CH<sub>4</sub> (5:5) mixture. Time zero is set with the first detection of helium (tracer).

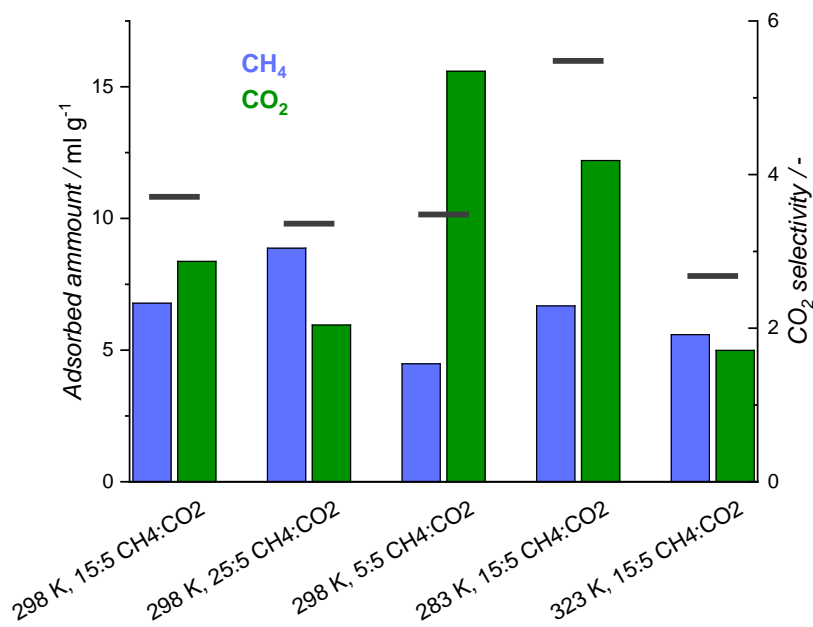


**Figure 5-11.** Breakthrough measurements adsorption and selectivity results summary; performed in an experimental fixed bed reactor (breakthrough setup), for CO<sub>2</sub>/CH<sub>4</sub> gas mixtures at different inlet conditions.

**Table 5-3.** Breakthrough measurements adsorption and selectivity results summary; performed in an experimental fixed bed reactor (breakthrough setup), for CO<sub>2</sub>/CH<sub>4</sub> gas mixtures at different inlet conditions. Replica measurements included.

Temperature (K)	Flow inlet (ml/min)				Adsorbed Amounts (ml/g)		
	CH <sub>4</sub>	CO <sub>2</sub>	He	Ar	CH <sub>4</sub>	CO <sub>2</sub>	
298	15	5	2	40	6,78	8,37	3,71
298	15	5	2	40	6,75	8,95	3,98
298	25	5	2	40	8,87	5,95	3,36
298	25	5	2	40	8,66	6,00	3,47
298	5	5	2	40	4,48	15,59	3,48
298	5	5	2	40	4,23	15,14	3,58
283	15	5	2	40	6,68	12,20	5,48
283	15	5	2	40	6,74	12,71	5,66
323	15	5	2	40	5,59	4,99	2,68
323	15	5	2	40	6,04	5,16	2,56

Propane/propylene separation is one of the most challenging separations in chemical

## Results and Discussion

engineering industry, not only for the high demand of the propylene as feedstock, but specially, due to the similarities of the components in this mixture [42]. Both hydrocarbons share similarities in physical and chemical properties (although the double bond in the alkene makes it more reactive to metals in a MOF framework). Molecular size is also a dominant parameter, the difference is so small and so critical, that even the definition of diameter alter, not only the actual value, but also the order in volume (propylene ‘kinetic diameter’ is larger than propane’s (0.45 nm versus 0.43 nm); but, for both, the ‘van der Waals diameter’ and ‘critical molecular diameter’ propylene is now smaller than propane (corresponding to 0.40 nm and 0.27 nm; and 0.42 nm and 0.28 nm; respectively).

Similar to CO<sub>2</sub>/N<sub>2</sub> and CO<sub>2</sub>/CH<sub>4</sub> separation, the dynamic breakthrough experiments of C<sub>3</sub>H<sub>6</sub>/C<sub>3</sub>H<sub>8</sub> binary mixture (4:4 and 4:12) at 283, 298, and 323 K also have been explored. To some extent, *mCB-MOF-1* presented selectivity toward propylene (Figure 5-12), even though the separation ratio was really low. As shown in Figure 5-13 and Table 5-4, both gases presented similar thermodynamic behaviour, temperature affected both of them (and their sum) in the same expected trend: low temperature always promoted an exothermal adsorption process. The double bond slightly increased the affinity to the alkene, especially at low temperature. Overall, unfortunately *mCB-MOF-1* is not a good candidate for C<sub>3</sub>H<sub>6</sub>/C<sub>3</sub>H<sub>8</sub> separation.

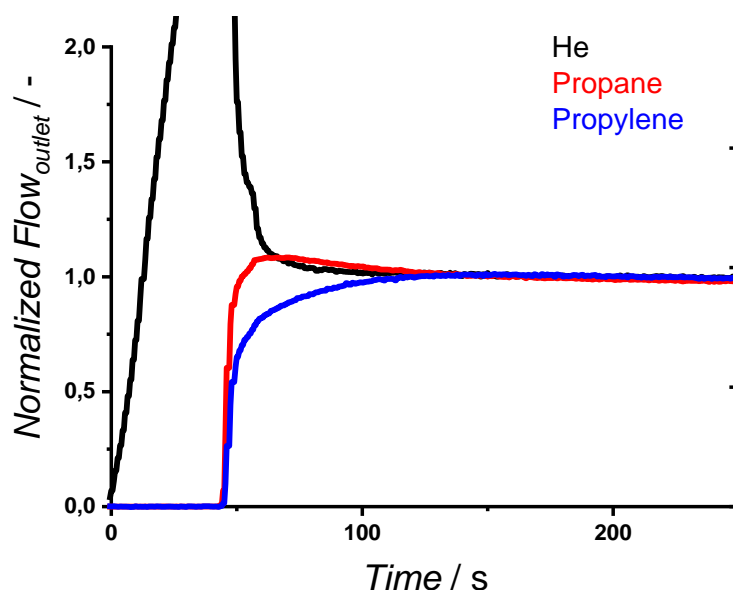


**Figure 5-12.** Breakthrough exit normalized flowrates (solid line, left axis) vs. time, at 298 K and 1 bar, on *mCB-MOF-1*. Inlet composition corresponds to a 16 ml min<sup>-1</sup> mixture propane:propylene (3:1). Time zero is set with the first detection of helium (tracer).

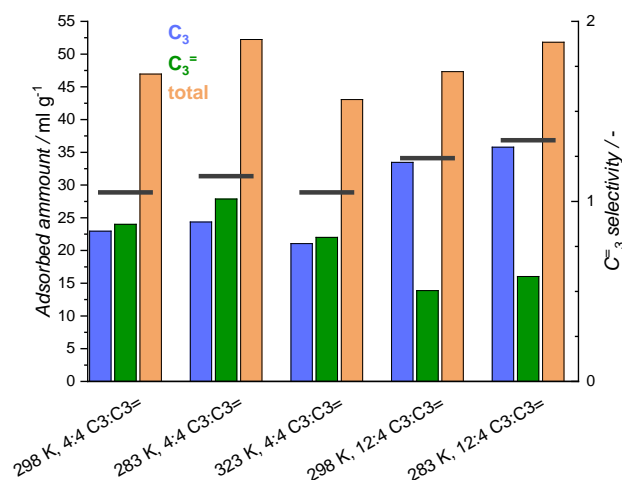


**Figure 5-13.** Breakthrough measurements adsorption and selectivity results summary; performed in an experimental fixed bed reactor (breakthrough setup), for propane:propylene gas mixtures at different inlet conditions.

**Table 5-4.** Breakthrough measurements adsorption and selectivity results summary; performed in an experimental fixed bed reactor (breakthrough setup), for propane:propylene gas mixtures at different inlet conditions. Replica measurements included.

Temperature (K)	Flow inlet (ml/min)		He	Ar	Adsorbed Amounts (ml/g)			
	C <sub>3</sub>	C <sub>3</sub> =			C <sub>3</sub>	C <sub>3</sub> =	mixture	
298	4	4	2	40	22,96	24,00	46,96	1,05
298	12	4	2	40	33,46	13,87	47,33	1,24
283	4	4	2	40	24,36	27,87	52,23	1,14
283	12	4	2	40	35,78	16,03	51,81	1,34
323	12	4	2	40	35,26	16,51	51,77	1,40
323	4	4	2	40	21,05	22,00	43,05	1,05
323	12	4	2	40	29,91	12,20	42,11	1,22

## 5.2.5 Oil-water Separation

As we described in Chapter 4, *mCB-MOF-1* shows high hydrophobicity (water contact angle of 144°) and also oleophilicity (hexane contact angle of 17.5°), which

## Results and Discussion

encouraged us to investigate its oil-water separation performance. Bearing this approach in mind, separation devices were generated by loading a **mCB-MOF-1** sample on a syringe to generate simple filters [43]. The device was placed slantways to solve the problem of no contact of the light oil with the **mCB-MOF-1** sample due to the lower density of light oil than that of water (Figure 5-14). For heavy oil, it could be separated from oil-water mixture under the force of gravity directly. Briefly, water was dyed by methylene blue for clear observation, benzene was selected as a model of light oil and chloroform was selected as a model of heavy oil to test its oil-water separation performance, respectively. The separation devices before and after the oil-water separation were demonstrated in Figure 5-14. During the separation process, it could be observed that benzene or chloroform quickly passed through the **mCB-MOF-1** sample and fell into the vial, but water was repelled and stayed in the syringe. After the separation, no visible organic liquids were observed in the water phase, suggesting that the oil-water separation of **mCB-MOF-1** is highly efficient. The PXRD pattern (Figure 5-15) also revealed that the structural integrity of **mCB-MOF-1** remained well after the separation. All these results make **mCB-MOF-1** a promising oil-water separation material for practical applications.

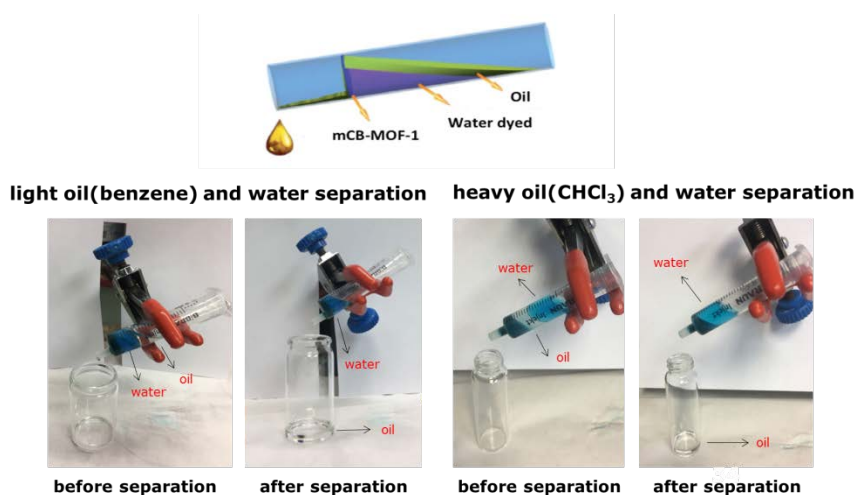


**Figure 5-14.** Photographs showing the oil/water separation experiments. Water was colored with methylene blue.

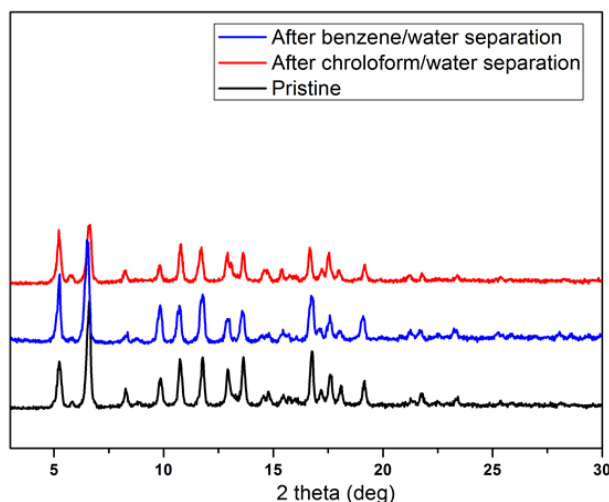


Figure 5-15. PXRD patterns of *mCB-MOF-1* after oil/water separation.

### 5.3 Conclusions

In conclusion, the hydrophobic carborane-based metal-organic framework, *mCB-MOF-1*, was reported for CO<sub>2</sub>, CH<sub>4</sub>, N<sub>2</sub>, and H<sub>2</sub> adsorption and separation at various temperatures. This ultra-microporous material exhibited moderate CO<sub>2</sub> adsorption uptake and relative low isosteric heat of CO<sub>2</sub> adsorption ( $Q_{st-zero}=25.6$  kJ/mol). IAST calculations combined with breakthrough experiments demonstrated that *mCB-MOF-1* preferentially adsorbed CO<sub>2</sub> over N<sub>2</sub> and CH<sub>4</sub>. Notably, this MOF showed very excellent CO<sub>2</sub>/N<sub>2</sub> selectivity (~1000) at 298 K at 1 bar, suggesting its great potential for realistic sequestering CO<sub>2</sub> from CO<sub>2</sub>/N<sub>2</sub> mixture in industrial separation. We are currently studying the separation under realistic humid conditions. Binary CO<sub>2</sub>/CH<sub>4</sub> and C<sub>3</sub>H<sub>8</sub>/C<sub>3</sub>H<sub>6</sub> separation have also been investigated on *mCB-MOF-1* with separation selectivity of 3.5 for CO<sub>2</sub>/CH<sub>4</sub> and low separation performance for C<sub>3</sub>H<sub>8</sub>/C<sub>3</sub>H<sub>6</sub> at 298 K at 1 bar. The adsorption isotherms and isosteric heat of adsorption for H<sub>2</sub> implied that *mCB-MOF-1* could be used for CO<sub>2</sub>/H<sub>2</sub> mixture separation. Moreover, the hydrophobic and oleophilic *mCB-MOF-1* showed good oil-water separation performance without external pressure. We envision that *mCB-MOF-1* could be promising material for potential applications in the environmentally process in the future.

## **5.4 Experimental Section**

### **5.4.1 Characterization and Methods**

Thermogravimetric Analysis (TGA) was performed in N<sub>2</sub>, on an nSTA 449 F1 Jupiter-Simultaneous TGA-DSC or SDT Q600 V8.3 Build 101 instruments (heating rate: 5 °C/min; temperature range: 25 °C to 600 °C). Gas sorption-desorption measurements were performed using IGA001 and ASAP2020 surface area analyzer. The sample was first degassed at 130 °C for 12 h. Powder X-ray Diffraction (PXRD) was recorded at room temperature on a Siemens D-5000 diffractometer with Cu K $\alpha$  radiation ( $\lambda = 1.54056 \text{ \AA}$ , 45kV, 35mA, increment=0.02°).

The isothermal parameters were well fitted by the double-site Lagmuir-Freundlich (DSLFF) method from the pure adsorption isotherms for CO<sub>2</sub> at 273K, single-site Lagmuir (SSL) method from the pure adsorption isotherms for CH<sub>4</sub> at 273K, single-site Lagmuir-Freundlich (SSLF) method from the pure adsorption isotherms for both CO<sub>2</sub> and N<sub>2</sub> at 313K. Fitting parameters of these equations as well as the correlation coefficients ( $R^2$ ) are listed in Tables S5-1. Predicted selectivity for binary mixtures of CO<sub>2</sub>/N<sub>2</sub> (5:5, 5:15, and 5:25, v/v) at 313 K and CO<sub>2</sub>/CH<sub>4</sub> (5:5, 5:15, and 5:25, v/v) at 273 K was analyzed using IAST.

### **5.4.2 Materials**

As synthesized *mCB-MOF-1* crystals (see chapter 4) were immersed in acetone (20 mL) and replaced once a day for three days, filtered and dried in air. The later was then activated by heating at 130 °C under dynamic ultrahigh vacuum for 12h.

### 5.4.3 Breakthrough Experiments

An ABR (*HIDEN Isochema*) setup was responsible for the performance of those experiments. It is an automated breakthrough analyzer, based on a fixed-bed adsorption column. In a typical experiment, pressure, temperature and inlet composition are set and controlled. In order to determine the adsorption dynamic behaviour of gas mixtures, the outlet flow composition is analysed by an integrated mass spectrometer (HPR-20 *QIC*). The column was filled with 257 mg of *mCB-MOF-1*. Before every measurement, the sample was regenerated at atmospheric temperature and pressure, in  $30 \text{ ml min}^{-1}$  Ar flow for 20 minutes. Regeneration temperature was increased to 353 K for hydrocarbons mixtures, as those gases were more strongly attached to the *mCB-MOF-1* framework. Operation conditions ranged 283–323 K at 1 bar. The inlet mixture consisted in a dilution of carbon dioxide in nitrogen or methane (1:1, 3:1, 5:1;  $\text{N}_2/\text{CH}_4/\text{CO}_2$ ); and, in 1:1 and 3:1 mixtures for propane:propylene measurements. In all situations, gas mixtures resemble expected natural or industrial compositions. Time zero, in the analysis, is set with the first detection of helium, due to its use as a tracer ( $2 \text{ ml min}^{-1}$  of He in the feed flow).



### 5.5 References

- [1] Yang, H.; Xu, Z.; Fan, M.; Gupta, R.; Slimane, R.B.; Bland, A.E.; Wright, I. *Journal of Environmental Sciences* **2008**, *20*, 14.
- [2] Singh, D.; Croiset, E.; Douglas, P.L.; Douglas, M.A. *Energy conversion Management* **2003**, *44*, 3073.
- [3] *Statistics, IEA %J IEA, Paris* <http://www.iea.org/co2highlights/co2highlights.pdf> **2011**.
- [4] Ciferno, J.P.; Fout, T.E.; Jones, A.P.; Murphy, J.T. *Chemical Engineering Progress* **2009**, *105*, 33.
- [5] D'Alessandro, D.M.; Smit, B.; Long, J.R. *Angew. Chem., Int. Ed.* **2010**, *49*, 6058.
- [6] Chaemchuen, S.; Kabir, N.A.; Zhou, K.; Verpoort, F. *Chemical Society Reviews* **2013**, *42*, 9304.
- [7] Adewole, J.; Ahmad, A.; Ismail, S.; Leo, C. *International Journal of Greenhouse Gas Control* **2013**, *17*, 46.
- [8] Yamasaki, A. *Journal of Chemical Engineering of Japan* **2003**, *36*, 361.
- [9] Yeh, J.T.; Resnik, K.P.; Rygle, K.; Pennline, H.W. *Fuel Processing Technology* **2005**, *86*, 1533.
- [10] Xu, X.; Song, C.; Andresen, J.M.; Miller, B.G.; Scaroni, A.W. *Energy Fuels* **2002**, *16*, 1463.
- [11] Rodrigues, M.A.; de Souza Ribeiro, J.; de Souza Costa, E.; de Miranda, J.L.; Ferraz, H.C. *Separation Purification Technology* **2018**, *192*, 491.
- [12] Jian, Y.; Yin, H.; Chang, F.; Cheng, L.; Yang, J.; Mu, W.; Li, X.; Lu, J.; Zhang, Y.; Wang, J. *Journal of Membrane Science* **2017**, *522*, 140.
- [13] Rocha, L.A.; Andreassen, K.A.; Grande, C.A. *Chemical Engineering Science* **2017**, *164*, 148.
- [14] Hu, Z.; Gami, A.; Wang, Y.; Zhao, D. *Advanced Sustainable Systems* **2017**, *1*, 1700092.
- [15] Grande, C.A.; Roussanaly, S.; Anantharaman, R.; Lindqvist, K.; Singh, P.; Kemper, J. *Energy Procedia* **2017**, *114*, 2259.
- [16] Belmabkhout, Y.; Serna-Guerrero, R.; Sayari, A. *Chemical Engineering Science* **2009**, *64*, 3721.
- [17] Akten, E.D.; Siriwardane, R.; Sholl, D.S. *Energy Fuels* **2003**, *17*, 977.
- [18] Choi, B.-U.; Choi, D.-K.; Lee, Y.-W.; Lee, B.-K.; Kim, S.-H. *Journal of Chemical Engineering Data* **2003**, *48*, 603.
- [19] Nugent, P.; Belmabkhout, Y.; Burd, S.D.; Cairns, A.J.; Luebke, R.; Forrest, K.; Pham, T.; Ma, S.; Space, B.; Wojtas, L., et al. *Nature* **2013**, *495*, 80.
- [20] Lv, D.; Wang, H.; Chen, Y.; Xu, F.; Shi, R.; Liu, Z.; Wang, X.; Teat, S.J.; Xia, Q.; Li, Z.J. *ACS Applied Materials&Interfaces* **2018**, *10*, 6031.
- [21] Chen, Y.; Wu, H.; Liu, Z.; Sun, X.; Xia, Q.; Li, Z. *Industrial Engineering Chemistry Research* **2018**, *57*, 703.
- [22] Liang, L.; Chen, Q.; Jiang, F.; Yuan, D.; Qian, J.; Lv, G.; Xue, H.; Liu, L.; Jiang, H.-L.; Hong, M. *Journal of Materials Chemistry A* **2016**, *4*, 15370.
- [23] DeCoste, J.B.; Peterson, G.W.; Schindler, B.J.; Killops, K.L.; Browe, M.A.; Mahle, J.J. *Journal of Materials Chemistry A* **2013**, *1*, 11922.
- [24] Ding, N.; Li, H.; Feng, X.; Wang, Q.; Wang, S.; Ma, L.; Zhou, J.; Wang, B. *Journal of the American Chemical Society* **2016**, *138*, 10100.
- [25] Chu, T.; Belding, L.; van der Est, A.; Dudding, T.; Korobkov, I.; Nikonov, G.I. *Angewandte Chemie International Edition* **2014**, *53*, 2711.
- [26] Jin, M.; Wang, J.; Yao, X.; Liao, M.; Zhao, Y.; Jiang, L. *Advanced Materials* **2011**, *23*, 2861.
- [27] Horcajada, P.; Gref, R.; Baati, T.; Allan, P.K.; Maurin, G.; Couvreur, P.; Ferey, G.; Morris, R.E.;

- Serre, C. *Chemical Reviews* **2012**, *112*, 1232.
- [28] Zhang, Y.; Yang, L.; Wang, L.; Duttwyler, S.; Xing, H. *Angewandte Chemie International Edition* **2019**, *58*, 8145.
- [29] Shalini, S.; Nandi, S.; Justin, A.; Maity, R.; Vaidhyanathan, R. *Chemical Communications* **2018**, *54*, 13472.
- [30] Myers, A.L.; Prausnitz, J.M. *AIChE Journal* **1965**, *11*, 121.
- [31] Teo, H.W.B.; Chakraborty, A.; Kayal, S. *Applied Thermal Engineering* **2017**, *110*, 891.
- [32] Lv, X.; Li, L.; Tang, S.; Wang, C.; Zhao, X. *Chemical Communications* **2014**, *50*, 6886.
- [33] Yu, J.; Balbuena, P.B. *The Journal of Physical Chemistry C* **2013**, *117*, 3383.
- [34] Valenzano, L.; Civalleri, B.; Chavan, S.; Palomino, G.T.; Areán, C.O.; Bordiga, S. *The Journal of Physical Chemistry C* **2010**, *114*, 11185.
- [35] Xu, F.; Yu, Y.; Yan, J.; Xia, Q.; Wang, H.; Li, J.; Li, Z. *Chemical Engineering Journal* **2016**, *303*, 231.
- [36] Zhang, J.; Sun, L.; Xu, F.; Li, F.; Zhou, H.-Y.; Liu, Y.-L.; Gabelica, Z.; Schick, C. *Chemical Communications* **2012**, *48*, 759.
- [37] Lu, W.; Yuan, D.; Makal, T.A.; Li, J.R.; Zhou, H.C. *Angewandte Chemie* **2012**, *124*, 1612.
- [38] Nandi, S.; Haldar, S.; Chakraborty, D.; Vaidhyanathan, R. *Journal of Materials Chemistry A* **2017**, *5*, 535.
- [39] Cai, J.; Wang, H.; Wang, H.; Duan, X.; Wang, Z.; Cui, Y.; Yang, Y.; Chen, B.; Qian, G. *Rsc Advances* **2015**, *5*, 77417.
- [40] McDonald, T.M.; D'Alessandro, D.M.; Krishna, R.; Long, J.R. *Chemical Science* **2011**, *2*, 2022.
- [41] Demessence, A.; D'Alessandro, D.M.; Foo, M.L.; Long, J.R. *Journal of the American Chemical Society* **2009**, *131*, 8784.
- [42] Wang, H.; Dong, X.; Colombo, V.; Wang, Q.; Liu, Y.; Liu, W.; Wang, X.L.; Huang, X.Y.; Proserpio, D.M.; Sironi, A. *Advanced Materials* **2018**, *30*, 1805088.
- [43] Zhang, M.; Xin, X.; Xiao, Z.; Wang, R.; Zhang, L.; Sun, D. *Journal of Materials Chemistry A* **2017**, *5*, 1168.

## *References*

---

# Chapter 6

---

*Highly Efficient Adsorptive  
Removal of Toxic  
Organophosphorus Compounds by  
a New Carborane-Based Zirconium  
Metal-Organic Framework*

*The pesticides' removal experiments in this Chapter have been carried out at the Institute of Chemical Sciences and Engineering, École Polytechnique Fédérale de Lausanne (EPFL Valais), 1951 Sion, Switzerland as part of a collaboration with Dr Kyriakos C. Stylianou.*



---

# Highly Efficient Adsorptive Removal of Toxic Organophosphorus Compounds by a New Carborane-Based Zirconium Metal-Organic Framework

## 6.1 Introduction

Organophosphorus Compounds are a group of highly toxic synthetic compounds [1], which include organophosphorus pesticides (OPs) and organophosphorus chemical warfare agents (CWAs) and/or their nerve agent simulants. Their high toxicity is from the ability of binding to acetylcholinesterase which results in neuromuscular paralysis and death of living beings [2-4]. OPs are widely used in agriculture to protect crops and kill insects. However, their common use leading to massive residues in groundwater and food put public health in a dangerous situation [5]. Therefore, developing effective technologies to remove toxic OPs from water is highly desirable. To date, various methods and materials have been studied for OPs removal such as electrochemistry, extraction, adsorption, enzymatic biodegradation, and photocatalytic degradation [6-14]. However, all studied methods for OPs removal process present some drawbacks; for example, degradation products of glyphosate (Figure 6-1), one of the most common OPs, usually provides aminomethylphosphonic acid which is even more toxic than glyphosate itself. Among these strategies, adsorption is regarded as a promising technique due to its simple operation, low energy and time consumption. Thus developing adsorption-based materials is of great significance in the field of OPs pollution control. Organophosphorus CWAs (Figure 6-2) have been used on and off the battlefield such as terrorist attacks which is a great threat to the society. Therefore, developing more effective materials to detect and degrade toxic organophosphorus CWAs has attracted a great number of research interests among scientists in the past few years. Activated carbons supplemented with metal nanoparticles and/or organic amines have been used for organophosphorus CWAs adsorption, but they have limitation due to deactivation problems [15,16]. Some

## Introduction

---

methods such as catalytically active metal oxides have also been explored, however, most of them exhibit low adsorption capacities[17]. Other techniques are used for efficient organophosphorus CWAs degradation but they are usually incompatible with applications where corrosion would occur [18]. Therefore, developing technologies that can degrade organophosphorus CWAs with advanced self-detoxifying materials capable of adsorbing and degrading toxic agents in actual application is necessary.

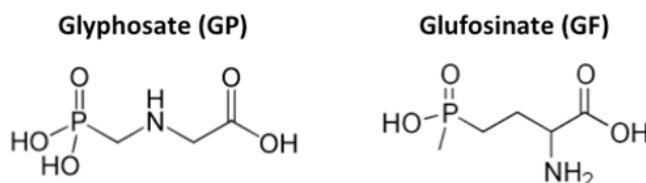
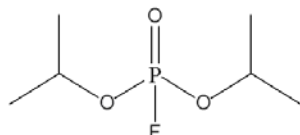


**Figure 6-1.** Chemical structures of Glyphosate (left) and Glufosinate (right).

Metal-organic framework (MOFs) are a highly versatile class of porous materials which consist of metal ions/clusters and organic linkers (Chapter 1). In contrast to traditional porous materials, MOFs have the great advantage of tunable pore sizes and catalytic active sites. These features make MOFs good platforms for detection, capture and degradation of toxic organophosphorus compounds [19-21]. Among them, zirconium-based MOFs have shown promising performance for organophosphorus compounds adsorption [22-25]. Zhu and coworkers [26] firstly reported organophosphorus pesticides adsorptive removal with UiO-67. The Zr-O(H) groups in the MOF nodes serve as natural binding sites for the phosphoric groups in the pesticides, leading to effective adsorption and removal of this type of OPs. In biology, a bimetallic hydroxidebridged zinc(II)-containing enzyme is utilized to catalytically hydrolyze phosphate ester bonds[27]. Inspired by this biological phenomenon, the combination of Lewis-acidic Zr(IV) and basic hydroxide groups in Zr-MOFs have been successfully investigated for degradation of organophosphorus CWAs by scientists [22-25,28]. Therefore, stable Zr-MOFs are promising solid adsorptive catalyst for organophosphorus compounds capture.

Diisopropylfluorophosphate (DIFP)



Dimethyl 4-nitrophenyl phosphate (DMNP)

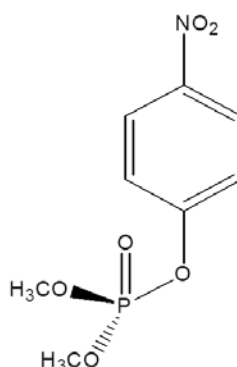


**Figure 6-2.** Chemical structures of Diisopropylfluorophosphate (left) and Dimethyl 4-nitrophenyl phosphate (right).

As described in previous chapters, carborane-based MOFs usually show outstanding stabilities in aqueous conditions. Here we expand the family of V-shaped carboxylate carborane linkers and synthesize a new tetracarboxylic acid ligand *m*CB-H<sub>4</sub>L<sub>2</sub>. In the present chapter we describe the preparation of a new Zr-MOF [Zr<sub>6</sub>(μ<sub>3</sub>-O)<sub>4</sub>(μ<sub>3</sub>-OH)<sub>4</sub>(OH)<sub>4</sub>(H<sub>2</sub>O)<sub>4</sub>(*m*CB-L<sub>2</sub>)<sub>2</sub>•6DMF•3H<sub>2</sub>O (*m*CB-MOF-2) and explore its properties for OPs adsorption and organophosphorus nerve agents degradation.

## 6.2 Results and Discussion

### 6.2.1 Synthesis and Characterization

A new V-type (bended) bis-phenyl tetracarboxylic acid derived from the *m*-carborane cluster (*m*CB-H<sub>4</sub>L<sub>2</sub>: 1,7-di(3,5-dicarboxyphenyl)-1,7-dicarba-closo-dodecaborane), was synthesized via Cu(I) coupling and oxidation, adapted from a reported procedure and isolated in 63% yield. Solvothermal reaction of *m*CB-H<sub>4</sub>L<sub>2</sub> with ZrCl<sub>4</sub> in the presence of formic acid in *N,N*-dimethylformamide (DMF) at 120 °C for 48 h yielded single clear colorless prism-shaped crystals of *m*CB-MOF-2. Single-crystal X-ray diffraction (SCXRD) studies revealed that *m*CB-MOF-2 crystallizes in the space group *P6/mmm* and has the **csq** topology (Figure 6-3). Such topology is the most



commonly observed in Zr-MOF structures with planar tetracarboxylic linkers (e.g., NU-1000, PCN-222, MOF-545 or MMMPF-6) [29]. Thus, *mCB-MOF-2* framework consists of octahedral  $Zr_6$  clusters linked by the bended *mCB-L2* ligands (Figure 6-3). Each octahedral  $Zr_6$  cluster is capped by  $\mu_3$ -OH groups providing a  $Zr_6O_8$  core. Eight of the octahedral edges of each  $Zr_6O_8$  core are connected to eight *mCB-MOF-2* units with the remaining Zr coordination sites occupied by terminal OH/OH<sub>2</sub> ligands.[30] The resultant MOF has the molecular formula  $[Zr_6(\mu_3-O)_4(\mu_3-OH)_4(OH)_4(H_2O)_4(mCB-L2)_2]$  and contain typical hexagonal (1.2 nm) and triangular (0.8 nm) channels observed for the *csq* topology (Figure 6-3). The V-shape of our ligand imposes a shrink of the resultant network, as compared with the commonly described planar tetracarboxylic linkers (e.g., NU-1000 [31] contains 3 nm hexagonal and 1.2 nm triangular channels). Nevertheless, the total solvent-accessible volume of *mCB-MOF-2*, after removing the free solvent molecules, was calculated to be 52.5% by PLATON [32].

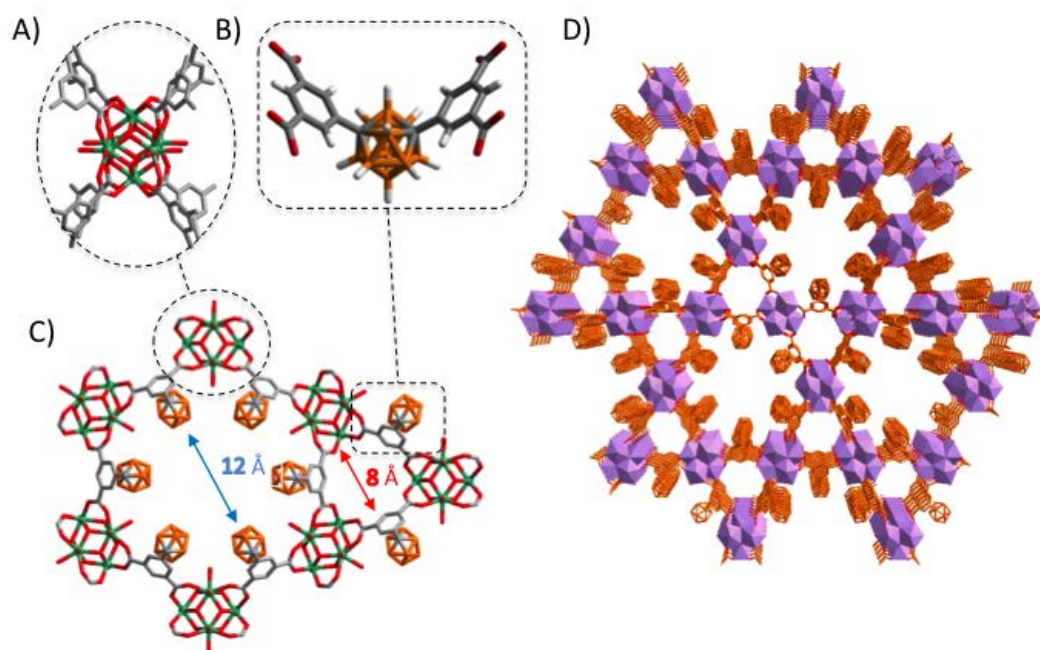


**Figure 6-3.** Crystal structure of *mCB-MOF-2*. A) View of the 8-connected  $Zr_6$ -cluster. B) *mCB-L2* linker. C) Detail view of the hexagonal and triangular 1D channels. D) 3D framework with hexagonal and triangular 1D channels;  $Zr_6O_x$  clusters are shown as violet polyhedra. Except in B), H atoms are omitted for clarity. Color code: B orange; C grey; O red; Zr green.

The bulk phase and analytical purity of the as made **mCB-MOF-2** were confirmed by powder X-ray diffraction (PXRD, Figure 6-4), elemental analysis, thermogravimetric analysis (TGA) and infrared spectroscopy. IR spectra showed the characteristic (Zr)O–H/O–H<sub>2</sub> stretching bands (in the range 3600-3700 cm<sup>-1</sup>)[30,31,33], and B–H stretching band for the carborane fragments at 2606 cm<sup>-1</sup> (Figure S6-1). TGA of the as-synthesized **mCB-MOF-2** after soaking in acetone revealed a plateau in the range 100-270 °C (Figure S6-2). Variable temperature Synchrotron Wide Angle X-ray Scattering (WAXS) measurements showed that **mCB-MOF-2** retains its original structure up to 270 °C under dynamic vacuum (Figure 6-5). PXRD studies revealed that the structure of the activated **mCB-MOF-2'** is intact upon removal of the guest molecules from its cavities (Figure 6-4A). Type I N<sub>2</sub> isotherms collected at 77K and 1 bar confirmed the microporous nature of **mCB-MOF-2'**, with a N<sub>2</sub> uptake of 285 cm<sup>3</sup>g<sup>-1</sup>(STP) and a BET surface area of 1095 m<sup>2</sup>g<sup>-1</sup> (Figure 6-4B). The experimental total pore volume of 0.44 cm<sup>3</sup>g<sup>-1</sup> is in agreement with the calculated pore volume (0.57 cm<sup>3</sup>g<sup>-1</sup>). Evaluation of a density functional theory (DFT) simulation of the N<sub>2</sub> isotherm indicates the presence of a type of pores of 0.8 nm, consistent with the average value of the observed triangular and hexagonal channels (Figure 6-3). **mCB-MOF-2'** is also porous to CO<sub>2</sub>, with the maximum uptake amount of *ca.* 2.4 mmol g<sup>-1</sup> at 313 K and 4.4 mmol g<sup>-1</sup> at 273 K (Figure 6-4C). CH<sub>4</sub> and H<sub>2</sub> adsorption isotherms were also measured over wide pressure ranges (Figure 6-6). At 77 K the maximum H<sub>2</sub> uptake is about 6.5 mmol g<sup>-1</sup>, while the H<sub>2</sub> uptake remains almost the same amount over high pressure ranges for different temperatures 273-323 K, which indicates thermodynamics is negligible compared to kinetic effect for high pressure H<sub>2</sub> adsorption. At room temperature, the maximum CH<sub>4</sub> uptake is about 1.2 mmol g<sup>-1</sup> at 2 bar while the adsorption amount is 6.0 mmol g<sup>-1</sup> at 100 bar.

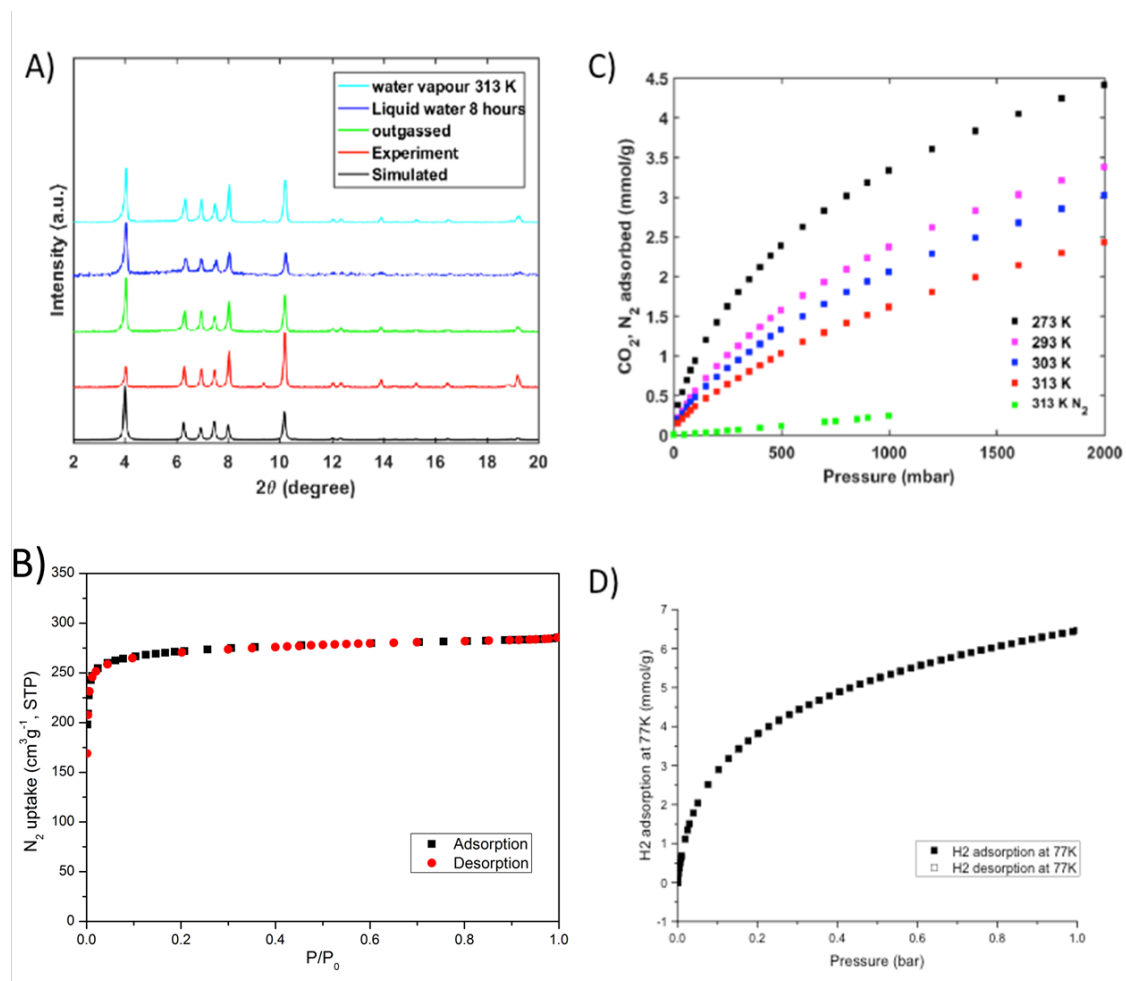


**Figure 6-4.** Characterization data for *mCB*-MOF-2. A) PXRD patterns for activated *mCB*-MOF-2' and after being in water at various conditions. B)  $N_2$  adsorption isotherms at 77 K. C)  $CO_2$  adsorption isotherms at 313 K and D)  $H_2$  adsorption isotherms at 77 K for *mCB*-MOF-2'.

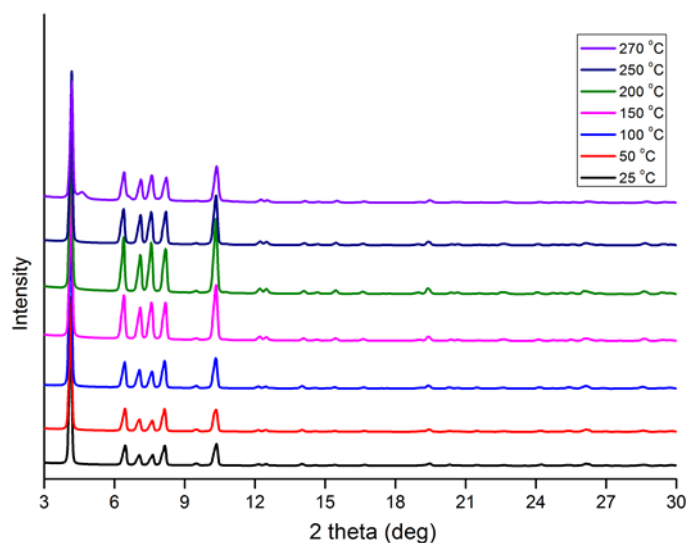


**Figure 6-5.** Variable temperature WAXS measurements of *mCB*-MOF-2 under dynamic vacuum.

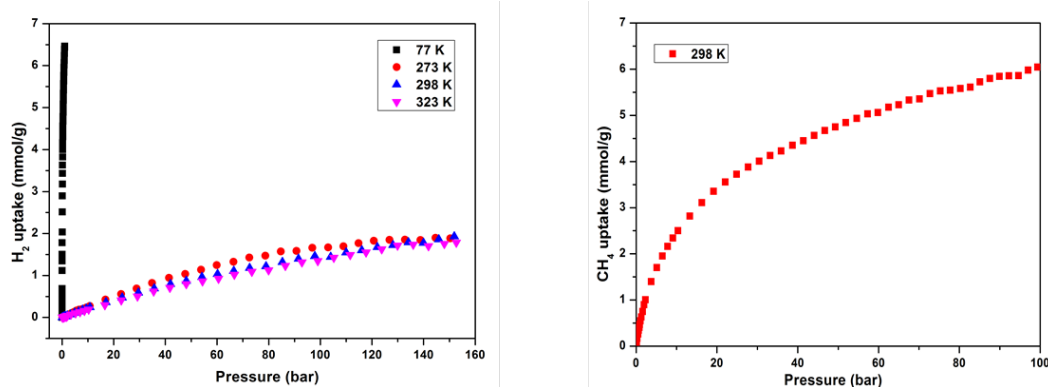


**Figure 6-6.** Left: H<sub>2</sub> adsorption isotherms at 77, 273, 298, and 323 K; right: CH<sub>4</sub> adsorption isotherms at 298 K for *mCB-MOF-2'*.

Having determined that activated *mCB-MOF-2'* is a robust microporous material, we then evaluated the stability in various media. *mCB-MOF-2'* is stable in liquid water at various conditions (RT to 90 °C or acid and based conditions) for 48h. *mCB-MOF-2'* stability under the above mentioned conditions was proved by PXRD and BET (Figure 6-7, 6-8). PXRD traces of *mCB-MOF-2'* before and after incubation for 48 h at RT or 90 °C in water in a closed vial perfectly match the simulated pattern derived from the single crystal structure of *mCB-MOF-2* (Figure 6-7). Samples show negligible changes in their PXRD patterns after water treatment under acidic (HCl, pH =1) or basic (NaOH, pH = 11) conditions or even in 12M *conc.* HCl condition for 24h (Figure 6-7). Samples crystallinity remained excellent after those treatments (Figure 6-7) and porosity is retained as proved by the BET surface area measurements of the treated samples (Figure 6-8 and Table S6-1). The overall data proofs an excellent chemical and hydrolytic stability of *mCB-MOF-2*, in line with Zr cluster and carborane containing MOFs [34,35] and carborane containing MOFs [35-37].

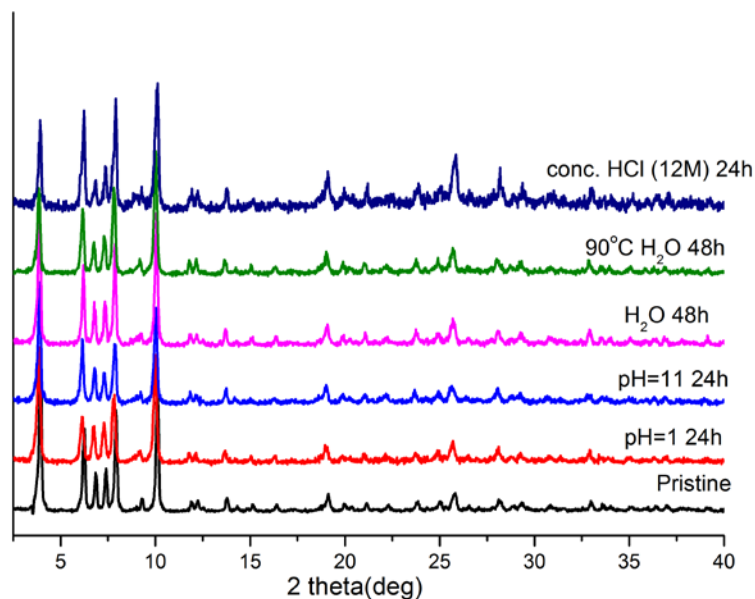


Figure 6-7. PXRD patterns for *mCB-MOF-2'* under different treatments.

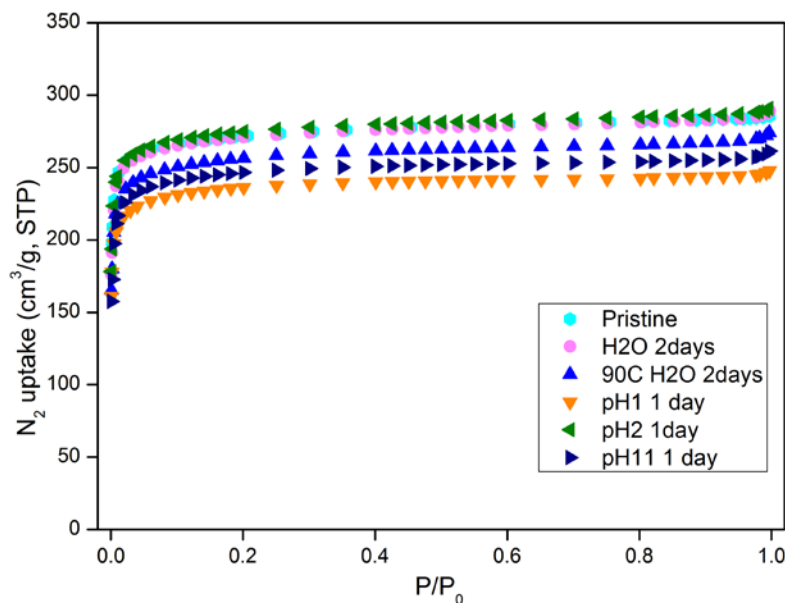


Figure 6-8. Comparison of the  $N_2$  adsorption isotherms for *mCB-MOF-2'* at 77 K

## 6.2.2 Water Adsorption

We also evaluated the possible influence of the carborane units on its hydrophobic properties. Contact angle ( $\Theta_c \sim 0^\circ$ ) measurements clearly indicate that the surface of

**mCB-MOF-2** is hydrophilic. The water isotherms provide useful information on the hydrophilic/hydrophobic properties of the porous materials as well as relevant information on the adsorption mechanism and strength of the interaction between water and the porous material framework [38-40]. The water adsorption isotherm for **mCB-MOF-2'** collected at 298 K (Figure 6-9) exhibits a two-step process, which can be correlated to the filling of the different cavities present in the structure. The adsorbed amount of water gradually increases with increasing up to at  $P/P_0 = 0.1$ , followed by a somewhat abrupt water uptake in the pressure range from  $P/P_0 = 0.1$  to 0.2 and an uptake of  $150 \text{ cm}^3 \text{ g}^{-1}$ . At  $P/P_0=0.4$  water filled the pores with the uptake amount of  $190 \text{ cm}^3 \text{ g}^{-1}$ , closely followed by the second step, then the cavities reached saturated water adsorption at  $P/P_0=0.9$  with a total water capacity of  $370 \text{ cm}^3 \text{ g}^{-1}$  (29.7wt%) which is comparable with other reported Zr-MOFs [39]. More importantly, for on-board heat exchange systems, the water adsorption for a material in the low-pressure region ( $P/P_0=0.1$ ) has a practicable significance. For **mCB-MOF-2'**, the uptake of water is  $55 \text{ cm}^3 \text{ g}^{-1}$  at  $P/P_0=0.1$  which is higher than that of the famous Zr-MOF UiO-66, with a number of  $20 \text{ cm}^3 \text{ g}^{-1}$ [39]. Compared with the second step, adsorption rate is higher and uptake amount is similar for the first step, which is related to the different affinity of water to the different surface of MOF material. From the water adsorption isotherm, we calculated that **mCB-MOF-2'** can capture 86 water molecules per unit cell, including 44 water molecules from first step and 42 water molecules from second step.

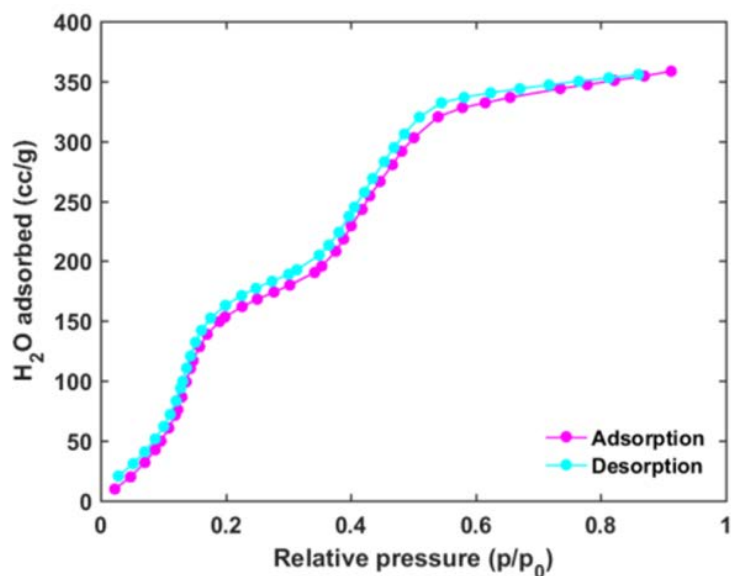


Figure 6-9. Water adsorption isotherms for *mCB-MOF-2'* at 298 K.

The above results provide valuable insight into the water adsorption behavior of biporous MOFs (with hydrophobic and hydrophilic pores). Such MOFs, only a handful of which have been reported, present different chemical environments within a single material that can be exploited for a number of applications [41-44]. The water isotherm profile for *mCB-MOF-2'* is certainly consistent with the different nature of the pores. In order to further proof the influence of the pores' nature on the water adsorption, we set out to determine location of guest water molecules by Synchrotron SXR. Prior to studying the location of water, we collected diffraction data for a crystal of acetone exchanged *mCB-MOF-2-a*, which was prepared by solvent exchange (see experimental section). Solvent molecules were highly disordered in both channels and could not be fully refined. However, the electron density distribution provides a glimpse of the arrangement of the acetone molecules in the pores of *mCB-MOF-2-a* (Figure 6-10A, 6-10B). The results demonstrate the presence of residual electron density in both cavities of *mCB-MOF-2-a*, indicating that all channels are occupied by guest molecules. Fully activated *mCB-MOF-2'* crystals were then immersed in water for 24h to provide *mCB-MOF-2-w*. The diffraction data of the later (Figure 6-10C, 6-10D) clearly shows that residual electron density is only



found in the hydrophilic cavities, where the  $[\text{Zr}_6(\mu_3\text{-O})_4(\mu_3\text{-OH})_4(\text{OH})_4(\text{H}_2\text{O})_4]$  clusters are located. There is no appreciable residual electron density in the carborane decorated hydrophobic channels, being this consistent with the different nature of the pores and the biporous nature of the MOF.

Quite interesting, in the hexagonal channels there exists a set of carborane on each inner surface of the channel while in the triangular channel it consists of benzene rings on the wall of the channel which give hydrophobic pores and hydrophilic pores in the framework. This special feature of the pores probably will balance the performance and efficiency for the application of wastewater treatment.

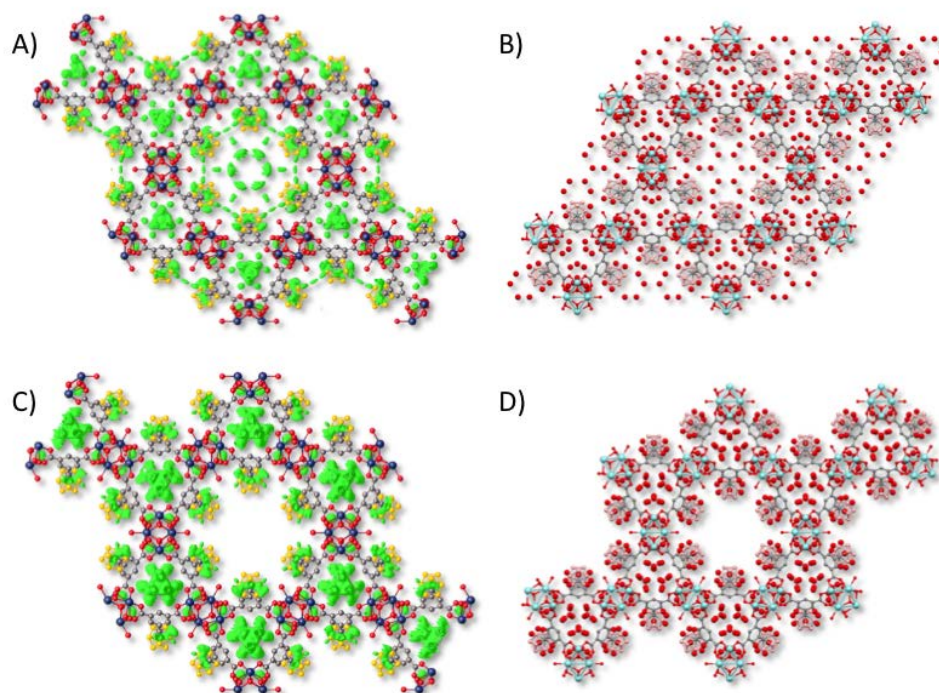


**Figure 6-10.** Residual electron density surface at  $1.7 \text{ e}\text{\AA}^{-3}$  and the ten highest electron density peaks refined as oxygen for acetone exchanged *mCB-MOF-2-a* (A and B, respectively) and water exchanged *mCB-MOF-2-w* (C and D, respectively).

### 6.2.3 Removal of Organophosphorus Pesticides

The industrialization of agriculture during the 20th century pervaded surface and



groundwater sources with agrochemicals (herbicides and pesticides) [19]. We first decided to explore two of the most frequently used OPs in agriculture, Glyphosate (GP, N-phosphonomethyl glycine) and glugosinate (GF, DL-homoalanin-4-(methyl) phosphonic acid) (Figure 6-1). These pesticides are of great concern owing to their indiscriminate used, water solubility and negative effects on human health. However, only three reports have been published so far on adsorption of these particular pesticides on the Zr-MOFs UiO-67 and NU-1000 [26,45,46].

We first tested the room temperature adsorption isotherms of GP and GF on **mCB-MOF-2'** after their adsorption for a sufficient period of time (Figure 6-11A). The isotherms reveal the relationship between the equilibrium concentration ( $C_e$ ) of the system and the amount of pesticides adsorbed ( $q_e$ ) on the MOF. In order to thoroughly understand the adsorption behavior, the experimental isotherms were evaluated by two generally used isothermal models—the Langmuir and Freundlich models—in this study. The Langmuir isothermal model is based on the assumption of monolayer adsorption, in which the adsorbate only combines with a finite number of open active sites that are identical and equivalent[47]. However, the Freundlich isothermal model is only an empirical model whose earliest known relationship describes the non-ideal and reversible adsorption, which can be applied to multilayer adsorption without being restricted to the formation of a monolayer [48]. Lagmuir adsorption has the following mathematical expression

$$\frac{C_e}{q_e} = \frac{1}{K_L q_{max}} + \frac{C_e}{q_{max}} \quad (1)$$

where  $C_e$  is the equilibrium concentration of pesticides ( $\text{mmol L}^{-1}$ ),  $q_e$  is the amount of adsorbed OPs at equilibrium ( $\text{mmol g}^{-1}$ ),  $K_L$  represents the Langmuir constant ( $\text{L mmol}^{-1}$ ) that relates to the adsorption energy and affinity of binding sites, and  $q_{max}$  denotes the maximum adsorption capacity ( $\text{mmol g}^{-1}$ ). Freundlich adsorption mathematical expression is as follows

$$\ln q_e = \ln K_F + n \ln C_e \quad (2)$$

where  $K_F$  ( $\text{mmol}^{1-n} \text{L}^n \text{g}^{-1}$ ) represents the Freundlich constant, which is related to the adsorption capacity of the adsorbent and  $n$  is a parameter that indicates the adsorption intensity. The value of  $n$  reflects the type of isotherm to be favorable ( $0 < n < 1$ ), irreversible ( $n = 0$ ) or unfavorable ( $n > 1$ ).

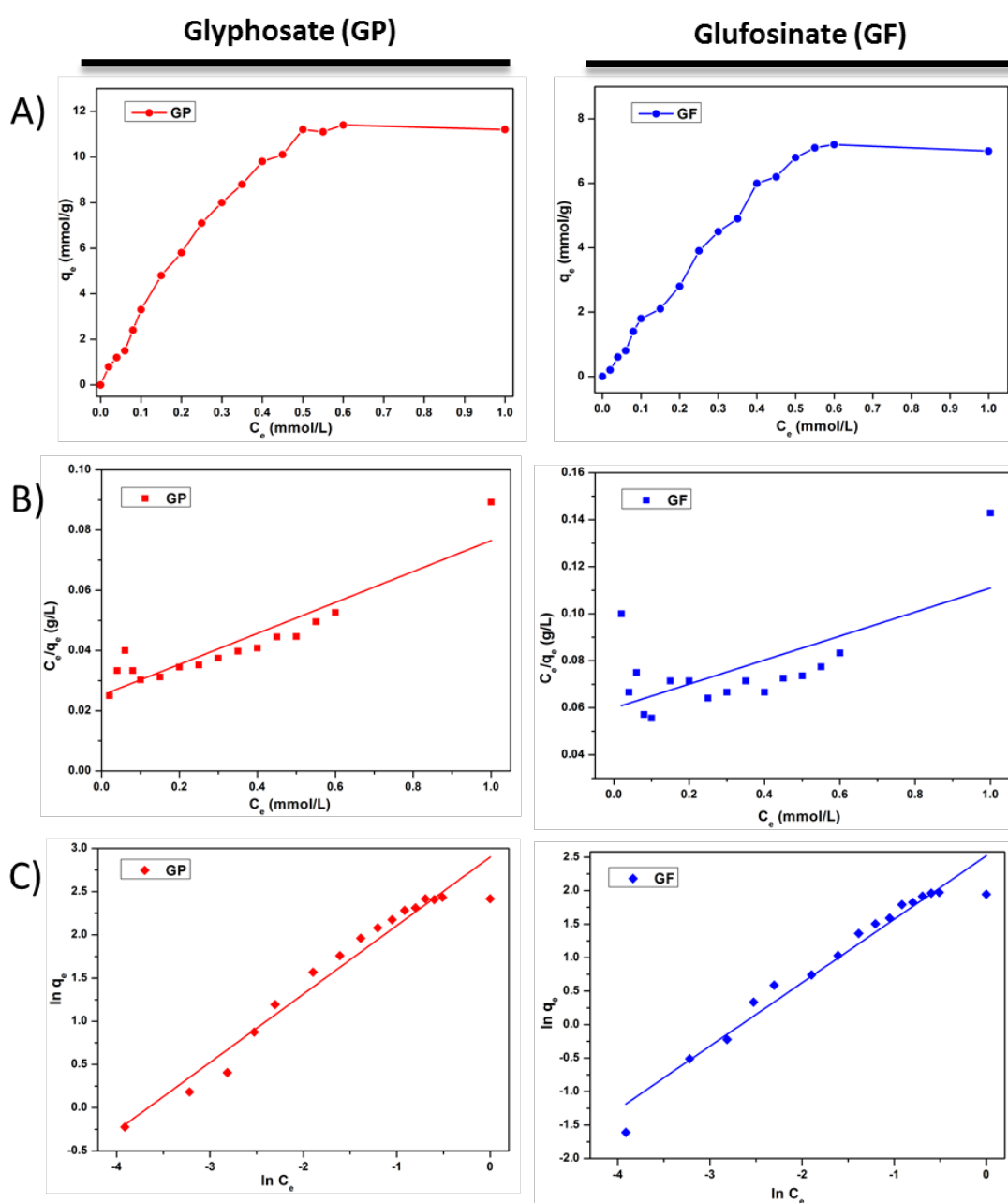


**Figure 6-11.** Adsorption isotherms of Glyphosate and Glufosinate on *mCB-MOF-2'* (A),

## Results and Discussion

Langmuir model plots (B) and Freundlich model plots (C).

**Table 6-1.** Langmuir and Freundlich Parameters of *mCB-MOF-2'* for GP and GF Adsorption.

OPs	Langmuir model			Freundlich model		
	$K_L$ (Lmmol <sup>-1</sup> )	$q_{max}$ (mmolg <sup>-1</sup> )	$R^2$	$K_F$ (mmol <sup>1-n</sup> L <sup>n</sup> g <sup>-1</sup> )	$n$	$R^2$
Glyphosate	2.04±0.40	19.46±2.21	0.83758	18.10±1.50	0.79±0.04	0.95715
Glufosinate	0.85±0.34	19.59±6.10	0.38543	12.43±1.25	0.94±0.05	0.95589

The adsorption isotherms for the GP and GF (both the Langmuir and Freundlich models) on *mCB-MOF-2'* are provided in Figure 6-11. The obtained parameters and the correlation coefficients ( $R^2$ ) are presented in Table 6-1. The results showed that the empirical Freundlich model has a better fit than the Langmuir model in both cases, which is contrary to the adsorptions on UiO-67 or NU-1000 [26,45,46]. Thus, our data suggests that the adsorption of GP and GF on *mCB-MOF-2'* follows the Freundlich isothermal model, which indicates the heterogeneity of the adsorption sites and that those are not energetically equivalent. Both  $n$  values were less than 1.0, demonstrating that adsorption of GP and GF on *mCB-MOF-2'* are favorable. We also observed high  $K_F$  values indicating that *mCB-MOF-2'* showed high adsorption performance for both GP and GF. The maximum adsorption capacities of GP and GF on *mCB-MOF-2'* are calculated to be  $q_{max}=11.4$  mmolg<sup>-1</sup> and 7.2 mmolg<sup>-1</sup>, respectively. The higher adsorption value for GP indicates that the *mCB-MOF-2'* present different affinities to OPs with different molecular structures. As mentioned earlier, the Zr metal nodes of the MOFs are Lewis acids and have a high affinity for the phosphate functional groups of GP and GF, which are Lewis base [46,49]. Thus, the Zr metal nodes in the framework are expected to act as the adsorption sites for the herbicides. The Zr-O(H) groups in these nodes also serve as natural binding sites for the phosphoric groups in the pesticides. Thus, the presence of methyl on the phosphorus atom of the GF (not present in GP; Figure 6-1) might diminish its bonding with the Zr-OH groups in *mCB-MOF-2'*, as already observed in the case of UiO-67 [26]. Nevertheless, the

adsorption capacities of GP and GF on *mCB-MOF-2'* are much higher than all other reported materials up to date (Table 6-2). Quite remarkable, GP adsorption capacity is much higher than that of the same topological but mesoporous MOF NU-1000 ( $q_{\max}=8.97 \text{ mmol g}^{-1}$ ) [46]. A comparison of the adsorption capacities of GP and GF on different porous materials is shown in Table 6-2, which reveals that *mCB-MOF-2'* is a good candidate as potential materials for effective organophosphorus pesticides adsorptive removal in environmental pollution management.

**Table 6-2.** Comparison of the Adsorption Capacities of GP and GF onto Various Adsorbents.

OPs	Adsorbent	$q_{\max}$ ( $\text{mmol g}^{-1}$ )	Reference
GP	MnFe <sub>2</sub> O <sub>4</sub> -graphene	0.23	[50]
GP	MnO <sub>x</sub> /Al <sub>2</sub> O <sub>3</sub>	0.69	[51]
GP	dendro biochar	0.26	[52]
GP	chitosan/alginate membrane	4.73 X 10 <sup>-5</sup>	[53]
GP	polyaniline/ZSM-5	0.58	[54]
GP	montmorillonite	0.295	[55]
GP	alum sludge	0.67	[56]
GP	Ni <sub>2</sub> AlNO <sub>3</sub>	1.02	[57]
GP	$\alpha$ -FeOOH	0.23	[58]
GP	MgAl-LDH	1.09	[59]
GP	UiO-67	3.18	[26]
GP	UiO-67 (100-200 nm)	7.90	[46]
GP	Fe <sub>3</sub> O <sub>4</sub> @SiO <sub>2</sub> @UiO-67	1.52	[60]
GP	UiO-67@GO	2.855	[45]
GP	NU-1000 (100-200nm)	8.97	[46]
GP	<i>mCB-MOF-2'</i>	11.4	This work

GF	UiO-67	1.98	[26]
GF	<i>m</i> CB-MOF-2'	7.2	This work

To evaluate the stability, PXRD patterns from *m*CB-MOF-2' after adsorption in 0.05 mmolL<sup>-1</sup> GP solution for 48 h were also investigated. As shown in Figure 6-12, *m*CB-MOF-2' retained its structure after the adsorption of GP. Moreover, the regeneration and reusability were investigated to evaluate its performance to the removal of GP and GF molecules. As shown in Figure 6-13, no significant decrease was observed in adsorption capacity for GP and GF after at least three adsorption cycles, demonstrating that *m*CB-MOF-2' could be recycled and reused for economically GP and GF treatment from polluted water.

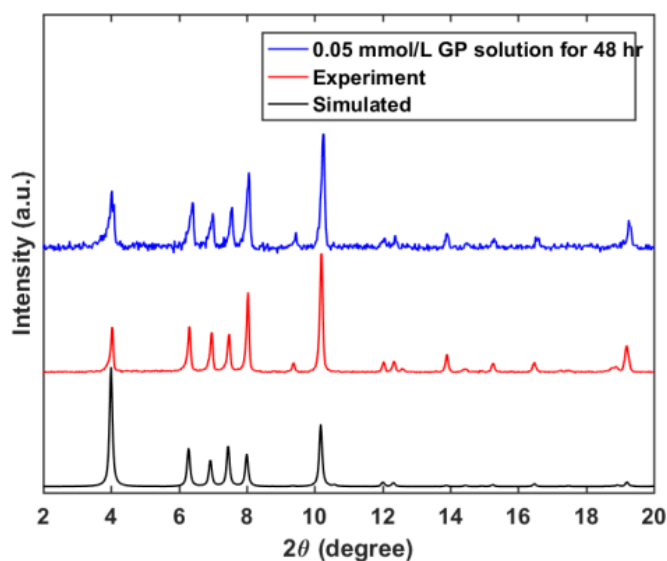


**Figure 6-12.** PXRD patterns of *m*CB-MOF-2' after GP adsorption.

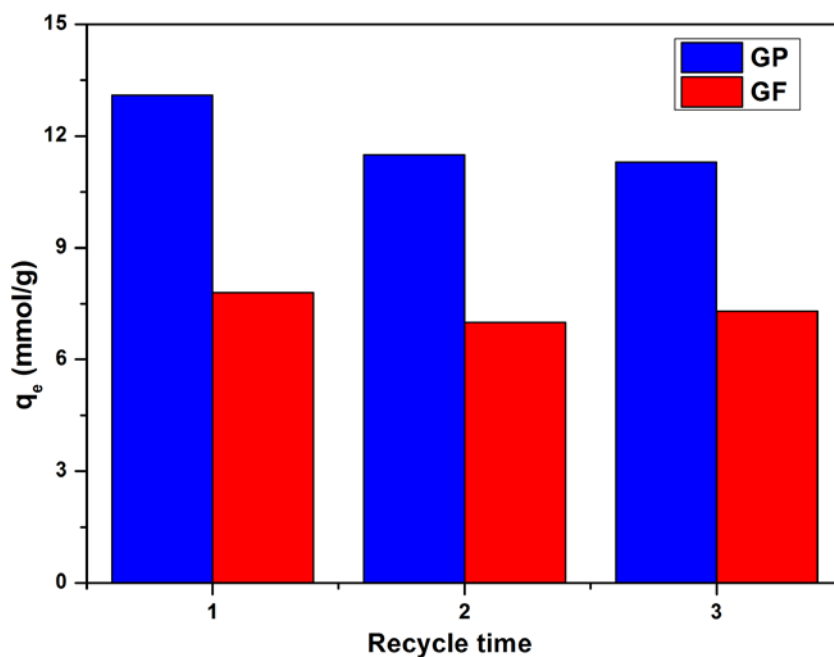


Figure 6-13. Regeneration cycles on the adsorption capacity of *mCB-MOF-2'* for GP and GF.

## 6.2.4 Catalytic Hydrolysis of Organophosphorus Nerve Agent Simulants

Since *mCB-MOF-2'* has a good acid stability, so we explored the catalytic degradation ability of *mCB-MOF-2'* toward the nerve agent simulant diisopropylfluorophosphate (DIFP). The material was tested on the catalytic hydrolysis of DIFP by using a 1:1 stoichiometric ratio of Zr cluster and DIFP molecule in non-buffered aqueous solutions and the concentration of DIFP was recorded by GC mass spectrometry. The profiles of degradation of DIFP are shown in Figure 6-14.

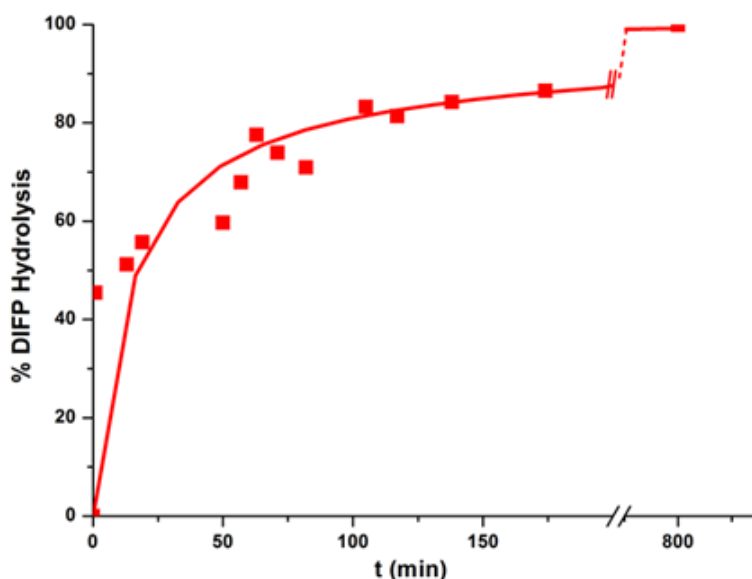
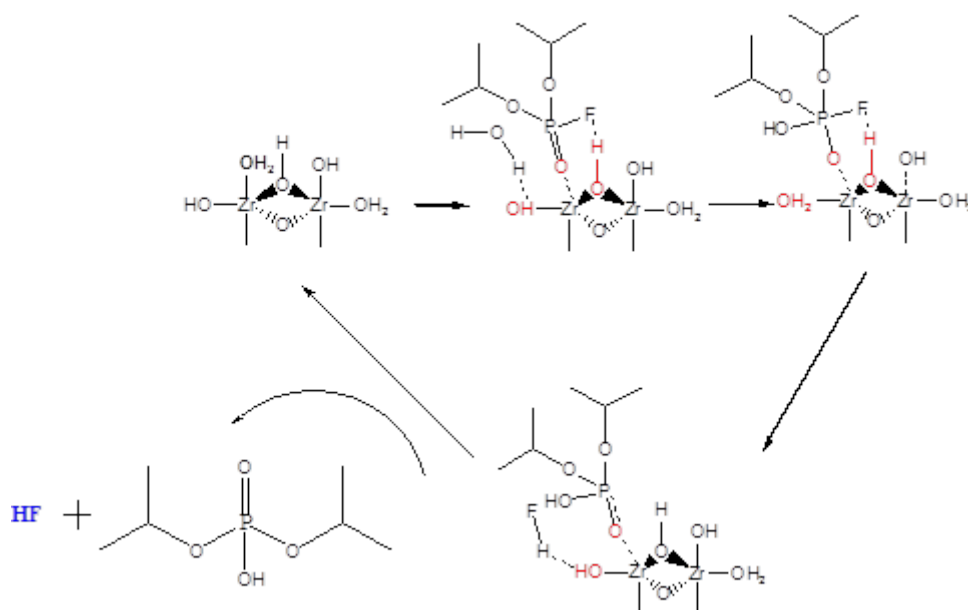


Figure 6-14. Profiles of catalytic hydrolytic degradation of DIFP upon exposure to *mCB-MOF-2'*

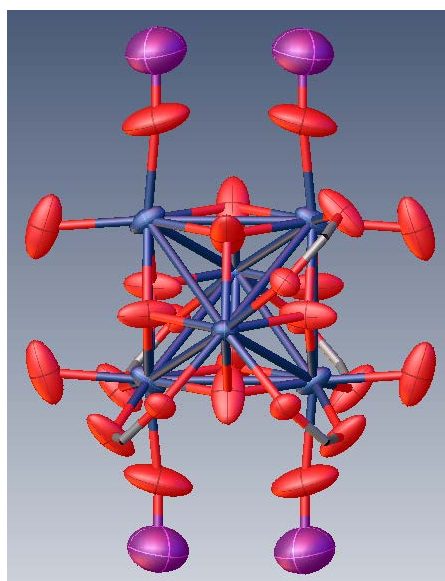
The results show a very fast initial degradation speed of DIFP by *mCB-MOF-2'*, with a half-life time  $t_{1/2} = 16$  min. 87% of the DIFP is degraded after about 200 min with the 100% reached after 800 minutes. The relatively long time for complete degradation can be explained by the formation of HF as byproduct during the degradation reaction. Nevertheless the degradation of DIFP by *mCB-MOF-2'* outperforms any other undecorated Zr-MOFs such as UiO-66, UiO-67 or NU-1000 [61].



Scheme 6-1. Proposed mechanism for the hydrolysis of DIFP by *mCB-MOF-2'*.

A proposed hydrolysis mechanisms for *mCB-MOF-2'* is summarized in Scheme 6-1.

The bridging  $\mu_3$ -OH groups is bonded to the F atom from DIFP by hydrogen bonding, and a terminal water molecule near the neighboring Zr atom moves to the terminal –OH site by hydrogen bonding, so the unsaturated coordinated Zr atom act as a Lewis acid to attack the DIFP with P=O bond. Upon rehydration of the Zr SBU, hydrofluoric acid and diisopropyl phosphate are released which are not toxic to the natural environment. In order to proof the function of the Zr clusters in the degradation process, we have tried to get suitable single crystals of the degradation intermediates by SCXRD measurement. Since we noticed that relatively long exposition times to aqueous DIFP solutions affected the crystallinity of the samples, we quickly collected synchrotron data for samples after five minutes of exposition to DIFP. Analysis of the data showed that there was significant electron density in the expected position for the P atoms of the DIFP molecules to be coordinated to Zr atoms. The electron density of the whole DIFP fragments was however diffusely spread out and could not be refined. Anisotropic refinement at full occupancy as phosphorus results however in a reasonable model for the presence of P atoms bonded to Zr in *mCB-MOF-2'* (Figure 6-15). The latter provides evidence for the coordination of the P=O bond of the DIFP molecules to the  $Zr_6O_x$  clusters as a preliminary step for its degradation. This preliminary data represents the first experimental observation of an intermediate of degradation of CWAs.

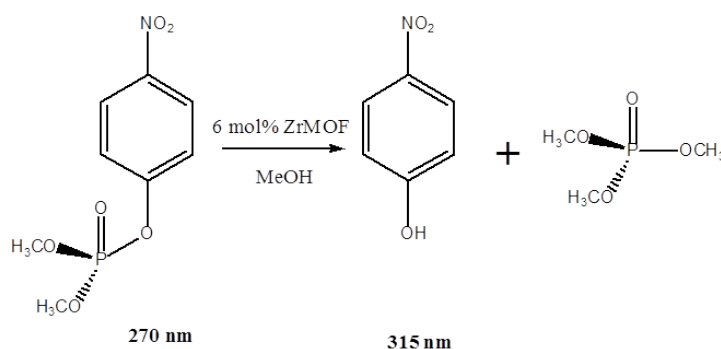




## Results and Discussion

**Figure 6-15.** Anisotropic refinement of the largest residual electron density peaks close to the  $Zr_6O_x$  clusters. Color code: P violet; O red; Zr blue.

Encouraged by the excellent activity of **mCB-MOF-2'** in catalytic hydrolysis of DIFP, we decided to investigate the catalytic activity of another nerve agent simulant methyl paraoxon (dimethyl 4-nitrophenyl phosphate, DMNP; Scheme 6-2) in methanol solution. The formation of UV/blue-absorbing nitrophenol makes for straightforward monitoring of the reaction progress by using UV/Vis spectroscopy (Figure 6-15). The **mCB-MOF-2'** catalytic hydrolysis of DMNP experiment were carried out at room temperature by stirring a 6 mol% slurry of **mCB-MOF-2'** sample in methanol. The methanolysis of DMNP stops at trimethylphosphate with formation of *p*-nitrophenol (Scheme 6-2). As shown in Figure 6-16, the formation of a new absorbance peak at 315 nm (*p*-nitrophenol) is followed by a concomitant decrease in the absorption of methyl paraoxon at 270 nm from UV-Vis experiments. The conversion profiles for DMNP are shown in Figure 6-17, to be noted, DMNP does not degrade at all in methanol solution, but a high initial rate of degradation confirms its comparable catalytic activity of **mCB-MOF-2'** for DMNP. These studies are still in progress in our group.



**Scheme 6-2.** Hydrolysis of DMNP by **mCB-MOF-2'** in methanol solution.

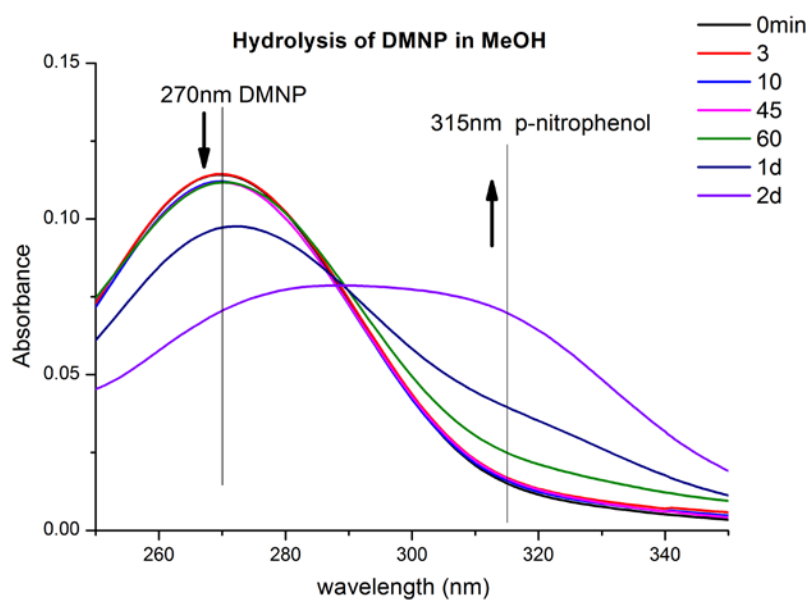


Figure 6-16. UV-Vis trace of the methanolysis of DMNP by *mCB-MOF-2'*.

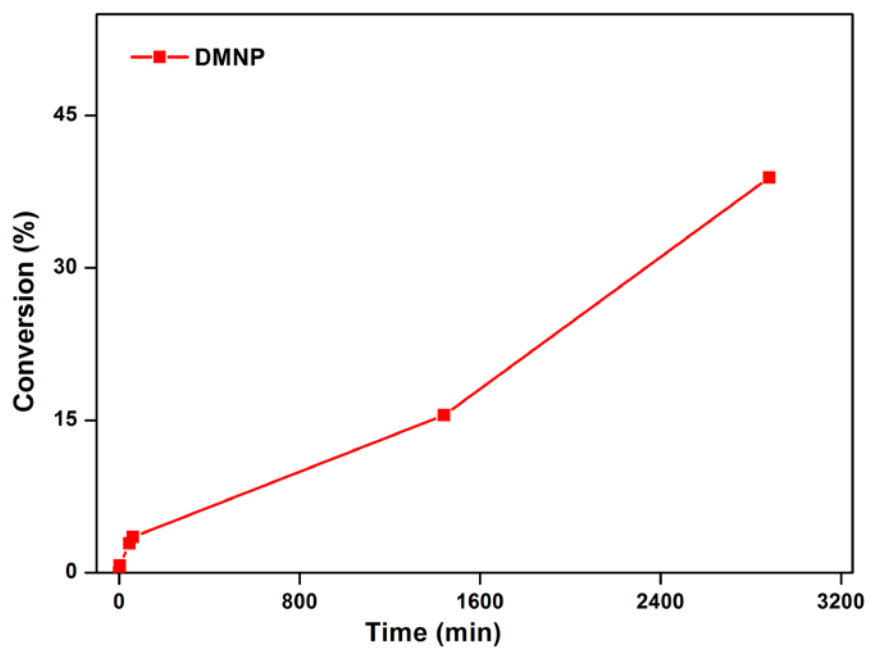


Figure 6-17. Conversion profiles for the methanolysis of DMNP by *mCB-MOF-2'*.

### 6.3 Conclusions

In summary, a new V-shaped tetradentate carboxylate carborane-based ligand has been designed and synthesized, along with the first carborane-based Zr-MOF (**mCB-MOF-2**) so far. It crystallizes in the space group *P6/mmm* and has a **csq** topology, commonly observed in other Zr-MOF structures such as for example in the mesoporous NU-1000. The activated **mCB-MOF-2'** is porous (BET surface of 1095 m<sup>2</sup>g<sup>-1</sup>; CO<sub>2</sub>, H<sub>2</sub>, CH<sub>4</sub>....) and stable in both basic and strong acidic aqueous solutions as confirmed by PXRD and BET surface area measurements. **mCB-MOF-2'** is stable in water at 90 °C for over two days and also stable when incubated in liquid water over a wide pH range (from 1 to 11) for at least 24 h at room temperature and it is also stable in high concentrated (12M) HCl solutions for at least 24h. Such hydrolytic stability is attributed to the highly hydrophobic nature of the *meta*-carborane residues in the structure, as in the case of **mCB-MOF-1** (Chapter 4), and the robustness of Zr clusters in the framework. The feature of both hydrophobic and hydrophilic channels in **mCB-MOF-2** can be observed in the stepwise water adsorption, with an adsorption capacity of 370 cm<sup>3</sup>g<sup>-1</sup>(STP). Electronic density maps from synchrotron measurements proved the presence of two water adsorption sites in the structure. Very excellent adsorption of organophosphorus pesticides including GP and GF have been observed on **mCB-MOF-2**, with the highest reported uptake of 11.4 and 7.2 mmol g<sup>-1</sup>, respectively. The Freundlich models of the OPs adsorption imply its special interaction between OPs and **mCB-MOF-2** compared with other MOFs, such as e.g. NU-1000, which follows a conventional Langmuir adsorption model. Quite remarkably, microporous **mCB-MOF-2** adsorb more GP than the mesoporous UN-1000. The recyclability of **mCB-MOF-2** indicates its good potential for economical OPs removal application. Moreover, **mCB-MOF-2** also can efficiently catalyze the degradation of organophosphorus nerve agent simulants DIFP completely and DMNP. Synchrotron measurements after DIFP adsorption firstly give direct evidence for confirmation of interaction between Zr cluster and DIFP molecules. Future work

for organophosphorus compounds treatment includes chemical warfare agents such as sarin and soman.

## 6.4 Experimental Section

### 6.4.1 Characterization and Methods

Attenuated total reflection Fourier transformed infrared (ATR-FTIR) spectra were recorded using a PerkinElmer Spectrum One spectrometer equipped with a Universal ATR sampling accessory. Spectra were collected with  $2\text{ cm}^{-1}$  spectral resolution in the  $4000\text{-}650\text{ cm}^{-1}$  range. Elemental analyses were obtained by using a Thermo (Carlo Erba) Flash 2000 Elemental Analyser, configured for wt.%CHN. Thermogravimetric Analysis (TGA) was performed in  $\text{N}_2$ , on an nSTA 449 F1 Jupiter-Simultaneous TGA-DSC or SDT Q600 V8.3 Build 101 instruments (heating rate:  $5\text{ }^\circ\text{C}/\text{min}$ ; temperature range:  $25\text{ }^\circ\text{C}$  to  $600\text{ }^\circ\text{C}$ ). Gas sorption-desorption ( $\text{CO}_2/273\text{ K}$  and  $\text{N}_2/77\text{ K}$ ) measurements were performed using IGA001 and ASAP2020 surface area analyzer. The sample was first degassed at  $130\text{ }^\circ\text{C}$  for 12 h. Crystals for X-ray Diffraction (XRD) were prepared under inert conditions immersed in perfluoropolyether or paratone as protecting oil for manipulation. Suitable crystals were mounted on MiTeGen Micromounts<sup>TM</sup>, and used for data collection at BL13 (XALOC)[62] at the ALBA synchrotron with an undulator source and channel-cut Si(111) monochromator and Kirkpatrick-Baez focusing mirrors with a selected wavelength of  $0.72932\text{ \AA}$ . An MD2M-Maatel diffractometer fitted with a Dectris Pilatus 6M detector was employed. The sample was kept at  $100\text{ K}$  with an Oxford Cryosystems 700 series Cryostream. The structure was solved with the ShelXT 2014/5 (Sheldrick, 2014) structure solution program using the direct phasing methods solution method and by using **Olex2** as the graphical interface.[63] The model was refined with version 2016/6 of **ShelXL** using Least Squares minimisation.[64] Highly disordered solvent, identified as 6 ethanol per formula unit, was treated using a

## ***Experimental Section***

---

solvent mask (Squeeze). A summary of crystal data is reported in Table S6-2 in the SI. Powder X-ray Diffraction (PXRD) was recorded at room temperature on a Siemens D-5000 diffractometer with Cu K $\alpha$  radiation ( $\lambda = 1.54056 \text{ \AA}$ , 45kV, 35mA, increment=0.02 $^\circ$ ). Morphological features were examined first by optical microscopy and subsequently by scanning electron microscopy (SEM) with a QUANTA FEI 200 FEGSEM microscope. Water contact-angles were measured using a Krüss DSA 100 device at room temperature using water as the probe fluid (9 L). Inductively Coupled Plasma – Mass Spectrometry (ICP-MS) measurements were carried out in an Agilent ICP-MS 7700x apparatus. Water, ethanol and butanol adsorption isotherms were measured at 313 K while acetone isotherms were collected at 303 K using the Microtrac BELSORP aqua<sup>3</sup> instrument.

WAXS patterns were recorded on the NCD-SWEET beamline at ALBA synchrotron light source (Spain). An X-ray beam of 8 keV ( $\lambda = 1.54 \text{ \AA}$ ) was set using a Si (111) channel cut monochromator. The scattered radiation was recorded using a Rayonix LX-255HS area detector. The sample to detector distance and the reciprocal space calibration were obtained using Cr<sub>2</sub>O<sub>3</sub> as a standard calibrant. The MOF was introduced in a borosilicate capillary and heated until 300 °C using a Linkam TMS-350 capillary stage (10 °C/min from 25 °C; resting 30 minutes after every 50 °C increase) under dynamic vacuum. Data reduction from 2D images to 1D profiles via azimuthal integration was done using PyFAI [65].

### **6.4.2 Materials**

All chemicals were commercially available and used as received. All Synthetic procedures were carried out in air unless noted. Infrared (IR) ATR spectra were recorded on a Perkin–Elmer Spectrum One spectrometer. <sup>1</sup>H, <sup>13</sup>C and <sup>11</sup>B nuclear magnetic resonance (NMR) spectra were recorded with a Bruker Advance-400

spectrometer in deuterated dimethylsulfoxide, unless noted, and referenced to the residual solvent peak for  $^1\text{H}$  and  $^{13}\text{C}$  NMR or to  $\text{BF}_3\cdot\text{OEt}_2$  as an external standard for  $^{11}\text{B}$  NMR. Chemical shifts are reported in ppm and coupling constants in Hertz. Multiplets nomenclature is as follows: s, singlet; d, doublet; t, triplet; br, broad; m, multiplet.

Synthesis of 1, 7-di (3, 5-dimethylphenyl)-1,7-dicarba-closo-dodecaborane (***mCB-L2'***). The procedure was adapted from a literature procedure[66] with little modification. The experiment was carried out under a nitrogen atmosphere in round-bottomed flasks equipped with a magnetic stirring bar. 1.00 g (6.93 mmol) *meta*-carborane (*m*-CB) was added to an oven dried Schlenk flask. The flask was evacuated and backfilled with  $\text{N}_2$  three times. 50 mL of dimethoxyethane were added to the schlenk flask. Once the *m*-CB was totally solved 10.2 mL (1.6 M) of *n*-BuLi in hexane was added dropwise at  $0^\circ\text{C}$ . The mixture was then stirred at room temperature for 30 min and then 2.38 g of CuCl was added into the solution. The mixture was stirred for 20 min and then 0.6 mL pyridine and 2.01 mL (13.86 mmol) of 5-*I*-*m*-xylene were added. The solution was heated and fluxed at  $85^\circ\text{C}$  until the TLC showed the original compound was almost consumed completely. The cooled mixture was diluted with 200 mL ether and allowed to stand for 2 h. The precipitate was filtered off and the solution was extracted three times with an HCl (3 M) solution. The diethyl ether was removed in the rotatory evaporator, then sticky solid filtered through a silica gel column (ethyl acetate: petroleum ether = 1:10) and the filtrate was concentrated by using a rotary evaporator to obtain 1.54 g (63.04%) of ***mCB-L2'***.

Yield: 1.54 g (63.04 %), white solid  $^1\text{H}\{^{11}\text{B}\}$  NMR (400 MHz,  $\text{CDCl}_3$ ):  $\delta$  2.32 (s, 6H,  $\text{CH}_3$ ),  $\delta$  2.61 (br, 5H, BH),  $\delta$  6.94 (s, 2H,  $\text{C}_6\text{H}_3$ ),  $\delta$  7.09 (s, 4H,  $\text{C}_6\text{H}_3$ );  $^{11}\text{B}\{^1\text{H}\}$  NMR (400 MHz,  $\text{CDCl}_3$ ):  $\delta$  -6.10 (s, 2B),  $\delta$  -10.73 (s, 5B),  $\delta$  -13.27 (s, 2B),  $\delta$  -15.26 (s, 1B). IR (ATR; selected bands;  $\text{cm}^{-1}$ ):  $\nu$  3061 (CH); 2915 (CH); 2599 (BH)

Synthesis of 1,7-di(3,5-dicarboxyphenyl)-1,7-dicarba-closo-dodecaborane

## Experimental Section

---

**(mCB-H<sub>4</sub>L<sub>2</sub>)**. The procedure was adapted from a literature procedure.[66]

6.93 g (69.3 mmol) of CrO<sub>3</sub> was added in small portions to a stirred mixture of 1.54 g (4.37 mmoles) **mCB-L<sub>2</sub>'**, 60 ml glacial acetic acid, 30 ml acetic anhydride and 6.23 ml *conc.* H<sub>2</sub>SO<sub>4</sub>. The dark green mixture was stirred at 20°C for 2 hours then poured into 100 ml distilled water. A precipitate appeared which was filtered off and washed with distilled water to remove the green chromium residues. The off-white solid was recrystallized dissolving the solid in a Na<sub>2</sub>CO<sub>3</sub> solution, filtering the solution and then acidifying again the solution with an HCl (3M) aqueous solution. The white precipitate that appears was filtered off and recrystallized from acetone: water mixture to yield 1.89 g of **mCB-H<sub>4</sub>L<sub>2</sub>**.

Yield: 1.89 g (57.6%), white solid <sup>1</sup>H{<sup>11</sup>B} NMR (400 MHz, DMSO-*d*<sub>6</sub>): δ 2.52 (br, 10H, B-H), δ 8.45 (s, 2H, C<sub>6</sub>H<sub>3</sub>), δ 13.66 (br s, 4H, CO OH); <sup>11</sup>B{<sup>1</sup>H} NMR (400 MHz, DMSO-*d*<sub>6</sub>): δ -8.51 (br, 10B); IR (ATR; selected bands; cm<sup>-1</sup>): ν 3081 br (OH, CH); 2607 (BH); 1693 (C=O from carboxylate). Elemental analysis (%) calculated for C<sub>18</sub>H<sub>20</sub>B<sub>10</sub>O<sub>8</sub>: C 45.76, H 4.27; Found: C 45.03, H 4.85.

Synthesis of [Zr<sub>6</sub>(μ<sub>3</sub>-O)<sub>4</sub>(μ<sub>3</sub>-OH)<sub>4</sub>(OH)<sub>4</sub>(H<sub>2</sub>O)<sub>4</sub>(mCB-L<sub>2</sub>)<sub>2</sub>] •6DMF•3H<sub>2</sub>O

**(mCB-MOF-2)**. **mCB-H<sub>4</sub>L<sub>2</sub>** (20 mg, 0.0423 mmol) and ZrCl<sub>4</sub>(29mg, 0.1269 mmol) were dissolved in DMF (5 mL), then formic acid(2.0 mL) was added to the mixture solution in an 8-dram vial. The vial was closed and heated at 120 °C in an oven for 48 h, followed by slow-cooling to room temperature for 10 h. Colorless crystals of **mCB-MOF-2** were collected and washed with DMF (25 mg, yield 52.6 %). IR (ATR; selected bands; cm<sup>-1</sup>): 2606 (BH); 1656 (C=O from carboxylate); 3600-3700 (-OH/H<sub>2</sub>O from Zr cluster). Elemental analysis (%) calculated for Zr<sub>6</sub>C<sub>54</sub>B<sub>20</sub>H<sub>96</sub>O<sub>41</sub>N<sub>6</sub>: C 28.84, H 4.30, N 3.74; Found: C 28.64, H 4.03, N 3.89.

As synthesized **mCB-MOF-2** crystals were immersed in acetone (20 mL) and replaced once a day for three days then filtered and dried in air. The later was further activated by heating at 130 °C under dynamic ultrahigh vacuum for 12h to form **mCB-MOF-2'**.

### 6.4.3 Pesticides Adsorption Experiments

An aqueous stock solution of GP or GF (200 ppm) was prepared by dissolving GP ( $C_3H_8NO_5P$ , MW: 169.07) or GF ( $C_5H_{12}NO_4P$ , MW: 181.1) in deionized water. GP or GF solutions with different concentrations of 0.01-0.5 mmol L<sup>-1</sup> (0.01, 0.03, 0.05, 0.1, 0.15, 0.2, 0.3, 0.4, and 0.5) were prepared by the dilution of the stock solution with water. The GP or GF concentrations were determined by measuring the phosphorus using ICP-AES. The adsorption experiments were conducted at 25 °C, and 10 mg of *mCB-MOF-2'* was added to 10 mL of OPs solution then let it stir for 48 hour to determine the adsorption capacity of MOF. The amounts of adsorbed GP or GF were measured from the difference between the initial ( $C_0$ ) and equilibrium ( $C_e$ ) concentrations in the supernatant after centrifugation. The equilibrium uptake was calculated by equation:

$$q_e = \frac{V(C_0 - C_e)}{W}$$

Where  $q_e$  (mmol g<sup>-1</sup>) is equilibrium adsorption capacity of GP or GF on *mCB-MOF-2'*.  $V$  presents the volume of the used OPs solution (L), and  $W$  is the weight of the used adsorbents (g).

### 6.4.4 Organophosphorus Nerve Agent Simulants Degradation Experiments

The degradation of DIFP was conducted by employing 20 mg *mCB-MOF-2'* suspended in 0.5 mL distill water. Afterwards, 2.5 μL of DMSO (used as internal reference) and 2.5 μL DIFP were added to the suspension. The concentration of DIFP was followed at room temperature by means of gas chromatography employing an Agilent 30 m-column (0.53 mm internal diameter) and taking 0.2 μL aliquots of the supernatant solution.



## *Experimental Section*

---

The catalytic degradation experiments of DMNP were carried out at room temperature. A solid sample of ***mCB-MOF-2'*** (2.6 mg, 6 mol%, 0.0015 mmol) was added to an aliquot of methanol (1 mL) in a 1.5 mL vial. The resulting mixture was stirred for 30 min to finely disperse the ***mCB-MOF-2'***. To this suspension was then added methyl paraoxon (6.2 mg, 0.025 mmol). Periodic monitoring was carried out by removing each 20 mL aliquot from the reaction mixture and diluting it with methanol (10 mL) for UV-Vis measurements.

## 6.5 References

- [1] Eddleston, M.; Buckley, N.A.; Eyer, P.; Dawson, A.H. *The Lancet* **2008**, *371*, 597.
- [2] Vera, M.S.; Lagomarsino, L.; Sylvester, M.; Pérez, G.L.; Rodríguez, P.; Mugni, H.; Sinistro, R.; Ferraro, M.; Bonetto, C.; Zagarese, H. *Ecotoxicology* **2010**, *19*, 710.
- [3] Marrs, T.C. *Pharmacology Therapeutics* **1993**, *58*, 51.
- [4] Mercey, G.; Verdelet, T.; Renou, J.; Kliachyna, M.; Baati, R.; Nachon, F.; Jean, L.; Renard, P.-Y. *Accounts of Chemical Research* **2012**, *45*, 756.
- [5] Aragay, G.; Pino, F.; Merkoçi, A. *Chemical Reviews* **2012**, *112*, 5317.
- [6] Samet, Y.; Agengui, L.; Abdelhédi, R. *Chemical Engineering Journal* **2010**, *161*, 167.
- [7] Arapoglou, D.; Vlyssides, A.; Israilides, C.; Zorpas, A.; Karlis, P. *Journal of hazardous materials* **2003**, *98*, 191.
- [8] Martínez-Huitle, C.A.; De Battisti, A.; Ferro, S.; Reyna, S.; Cerro-López, M.n.; Quiro, M.A.J. *Environmental Science Technology* **2008**, *42*, 6929.
- [9] Cycoń, M.; Żmijowska, A.; Wójcik, M.; Piotrowska-Seget, Z. *Journal of Environmental Management* **2013**, *117*, 7.
- [10] Wei, W.; Du, J.; Li, J.; Yan, M.; Zhu, Q.; Jin, X.; Zhu, X.; Hu, Z.; Tang, Y.; Lu, Y. *Advanced Materials* **2013**, *25*, 2212.
- [11] Chen, S.; Liu, C.; Peng, C.; Liu, H.; Hu, M.; Zhong, G. *PLoS One* **2012**, *7*, e47205.
- [12] Hossaini, H.; Moussavi, G.; Farrokhi, M. *Water Research* **2014**, *59*, 130.
- [13] Negishi, N.; Sano, T.; Hirakawa, T.; Koiwa, F.; Chawengkijwanich, C.; Pimpha, N.; Echavia, G.-R.M. *Applied Catalysis B: Environmental* **2012**, *128*, 105.
- [14] Echavia, G.R.M.; Matzusawa, F.; Negishi, N. *Chemosphere* **2009**, *76*, 595.
- [15] Daoud, W.A. *Self-cleaning materials and surfaces: a nanotechnology approach*; John Wiley & Sons: 2013.
- [16] Smith, J.; Romero, J.; Dahn, T.; Dunphy, K.; Croll, L.; Dahn, J. *Journal of hazardous materials* **2012**, *235*, 279.
- [17] Bandoz, T.J.; Laskoski, M.; Mahle, J.; Mogilevsky, G.; Peterson, G.W.; Rossin, J.A.; Wagner, G.W. *The Journal of Physical Chemistry C* **2012**, *116*, 11606.
- [18] Jang, Y.J.; Kim, K.; Tsay, O.G.; Atwood, D.A.; Churchill, D.G. *Chemical Reviews* **2015**, *115*, PR1.
- [19] Rojas, S.; Horcajada, P. *Chemical Reviews* **2020**.
- [20] Dhaka, S.; Kumar, R.; Deep, A.; Kurade, M.B.; Ji, S.-W.; Jeon, B.-H. *Coordination Chemistry Reviews* **2019**, *380*, 330.
- [21] Bobbitt, N.S.; Mendonca, M.L.; Howarth, A.J.; Islamoglu, T.; Hupp, J.T.; Farha, O.K.; Snurr, R.Q. *Chemical Society Reviews* **2017**, *46*, 3357.
- [22] López - Maya, E.; Montoro, C.; Rodríguez - Albelo, L.M.; Aznar Cervantes, S.D.; Lozano - Pérez, A.A.; Cenís, J.L.; Barea, E.; Navarro, J.A.R. *Angewandte Chemie International Edition* **2015**, *54*, 6790.
- [23] Drout, R.J.; Robison, L.; Chen, Z.; Islamoglu, T.; Farha, O.K. *Trends in Chemistry* **2019**, *1*, 304.
- [24] Kirlikovali, K.O.; Chen, Z.; Islamoglu, T.; Hupp, J.T.; Farha, O.K. *ACS applied materials & interfaces* **2020**, *12*, 14702.
- [25] Gil-San-Millan, R.; López-Maya, E.; Platero-Prats, A.E.; Torres-Pérez, V.; Delgado, P.; Augustyniak, A.W.; Kim, M.K.; Lee, H.W.; Ryu, S.G.; Navarro, J.A.R. *Journal of the American*

## References

---

- Chemical Society* **2019**, *141*, 11801.
- [26] Zhu, X.; Li, B.; Yang, J.; Li, Y.; Zhao, W.; Shi, J.; Gu, J. *ACS applied materials & interfaces* **2015**, *7*, 223.
- [27] Wong, K.-Y.; Gao, J. *Biochemistry* **2007**, *46*, 13352.
- [28] Katz, M.J.; Mondloch, J.E.; Totten, R.K.; Park, J.K.; Nguyen, S.T.; Farha, O.K.; Hupp, J.T. *Angewandte Chemie* **2014**, *53*, 497.
- [29] Chen, Z.; Hanna, S.L.; Redfern, L.R.; Alezi, D.; Islamoglu, T.; Farha, O.K. *Coordination Chemistry Reviews* **2019**, *386*, 32.
- [30] Planas, N.; Mondloch, J.E.; Tussupbayev, S.; Borycz, J.; Gagliardi, L.; Hupp, J.T.; Farha, O.K.; Cramer, C.J. *The Journal of Physical Chemistry Letters* **2014**, *5*, 3716.
- [31] Mondloch, J.E.; Bury, W.; Fairen-Jimenez, D.; Kwon, S.; DeMarco, E.J.; Weston, M.H.; Sarjeant, A.A.; Nguyen, S.T.; Stair, P.C.; Snurr, R.Q., et al. *Journal of the American Chemical Society* **2013**, *135*, 10294.
- [32] Spek, A.; PLATON, A. *Journal of Applied Crystallography* **2003**, *36*.
- [33] Yang, D.; Bernales, V.; Islamoglu, T.; Farha, O.K.; Hupp, J.T.; Cramer, C.J.; Gagliardi, L.; Gates, B.C. *Journal of the American Chemical Society* **2016**, *138*, 15189.
- [34] Bai, Y.; Dou, Y.; Xie, L.-H.; Rutledge, W.; Li, J.-R.; Zhou, H.-C. *Chemical Society Reviews* **2016**, *45*, 2327.
- [35] Gan, L.; Chidambaram, A.; Fonquernie, P.G.; Light, M.E.; Choquesillo-Lazarte, D.; Huang, H.; Solano, E.; Fraile, J.; Viñas, C.; Teixidor, F. *Journal of the American Chemical Society* **2020**, *142*, 8299.
- [36] Tsang, M.Y.; Rodríguez-Hermida, S.; Stylianou, K.C.; Tan, F.; Negi, D.; Teixidor, F.; Viñas, C.; Choquesillo-Lazarte, D.; Verdugo-Escamilla, C.; Guerrero, M. *Crystal Growth & Design* **2017**, *17*, 846.
- [37] Rodríguez - Hermida, S.; Tsang, M.Y.; Vignatti, C.; Stylianou, K.C.; Guillerm, V.; Pérez - Carvajal, J.; Teixidor, F.; Viñas, C.; Choquesillo - Lazarte, D.; Verdugo - Escamilla, C. *Angewandte Chemie International Edition* **2016**, *55*, 16049.
- [38] Kalmutzki, M.J.; Diercks, C.S.; Yaghi, O.M. *Advanced Materials* **2018**, *30*, 1704304.
- [39] Furukawa, H.; Gándara, F.; Zhang, Y.-B.; Jiang, J.; Queen, W.L.; Hudson, M.R.; Yaghi, O.M. *Journal of the American Chemical Society* **2014**, *136*, 4369.
- [40] Canivet, J.; Fateeva, A.; Guo, Y.; Coasne, B.; Farrusseng, D. *Chemical Society Reviews* **2014**, *43*, 5594.
- [41] Gładysiak, A.; Deeg, K.S.; Dovgaliuk, I.; Chidambaram, A.; Ordiz, K.; Boyd, P.G.; Moosavi, S.M.; Ongari, D.; Navarro, J.A.R.; Smit, B., et al. *ACS Applied Materials and Interfaces* **2018**, *10*, 36144.
- [42] Chaudhari, A.K.; Mukherjee, S.; Nagarkar, S.S.; Joarder, B.; Ghosh, S.K. *CrystEngComm* **2013**, *15*, 9465.
- [43] Sapchenko, S.A.; Samsonenko, D.G.; Dybtsev, D.N.; Fedin, V.P. *Inorganic Chemistry* **2013**, *52*, 9702.
- [44] Ohmori, O.; Kawano, M.; Fujita, M. *Angewandte Chemie - International Edition* **2005**, *44*, 1962.
- [45] Yang, Q.; Wang, J.; Zhang, W.; Liu, F.; Yue, X.; Liu, Y.; Yang, M.; Li, Z.; Wang, J. *Chemical Engineering Journal* **2017**, *313*, 19.
- [46] Pankajakshan, A.; Sinha, M.; Ojha, A.A.; Mandal, S. *ACS omega* **2018**, *3*, 7832.

- [47] Langmuir, I. *Journal of the American Chemical Society* **1916**, *38*, 2221.
- [48] Freundlich, H. *The Journal of Physical Chemistry* **1906**, *57*, 1100.
- [49] Gul-E-Noor, F.; Jee, B.; Poppl, A.; Hartmann, M.; Himsl, D.; Bertmer, M. *Phys. Chem. Chem. Phys.* **2011**, *13*, 7783.
- [50] Yamaguchi, N.U.; Bergamasco, R.; Hamoudi, S. *Chemical Engineering Journal* **2016**, *295*, 391.
- [51] Zheng, T.; Sun, Y.; Lin, Y.; Wang, N.; Wang, P. *Chemical Engineering Journal* **2016**, *298*, 68.
- [52] Mayakaduwa, S.; Kumarathilaka, P.; Herath, I.; Ahmad, M.; Al-Wabel, M.; Ok, Y.S.; Usman, A.; Abduljabbar, A.; Vithanage, M. *Chemosphere* **2016**, *144*, 2516.
- [53] Carneiro, R.T.; Taketa, T.B.; Neto, R.J.G.; Oliveira, J.L.; Campos, E.V.; de Moraes, M.A.; da Silva, C.M.; Beppu, M.M.; Fraceto, L.F. *Journal of Environmental Management* **2015**, *151*, 353.
- [54] Milojević-Rakić, M.; Janošević, A.; Krstić, J.; Vasiljević, B.N.; Dondur, V.; Ćirić-Marjanović, G. *Microporous mesoporous materials* **2013**, *180*, 141.
- [55] Khoury, G.A.; Gehris, T.C.; Tribe, L.; Sánchez, R.M.T.; dos Santos Afonso, M. *Applied Clay Science* **2010**, *50*, 167.
- [56] Hu, Y.; Zhao, Y.; Sorohan, B. *Desalination* **2011**, *271*, 150.
- [57] Khenifi, A.; Derriche, Z.; Mousty, C.; Prévot, V.; Forano, C. *Applied Clay Science* **2010**, *47*, 362.
- [58] Jonsson, C.M.; Persson, P.; Sjöberg, S.; Loring, J.S. *Environmental Science Technology* **2008**, *42*, 2464.
- [59] Li, F.; Wang, Y.; Yang, Q.; Evans, D.G.; Forano, C.; Duan, X. *Journal of hazardous materials* **2005**, *125*, 89.
- [60] Yang, Q.; Wang, J.; Chen, X.; Yang, W.; Pei, H.; Hu, N.; Li, Z.; Suo, Y.; Li, T.; Wang, J. *Journal of Materials Chemistry A* **2018**, *6*, 2184.
- [61] Gil-San-Millan, R.; López-Maya, E.; Hall, M.; Padial, N.M.; Peterson, G.W.; DeCoste, J.B.; Rodríguez-Albelo, L.M.; Oltra, J.E.; Barea, E.; Navarro, J.A. *ACS Applied Materials&Interfaces* **2017**, *9*, 23967.
- [62] Juanhuix, J.; Gil-Ortiz, F.; Cuni, G.; Colldelram, C.; Nicolas, J.; Lidon, J.; Boter, E.; Ruget, C.; Ferrer, S.; Benach, J. *Journal of Synchrotron Radiation* **2014**, *21*, 679.
- [63] Dolomanov, O.V.; Bourhis, L.J.; Gildea, R.J.; Howard, J.A.K.; Puschmann, H. *Journal of Applied Crystallography* **2009**, *42*, 339.
- [64] Sheldrick, G. *Acta Crystallographica Section C* **2015**, *71*, 3.
- [65] Kieffer, J.; Karkoulis, D. *Journal of Physics: Conference Series* **2013**, *425*, 202012.
- [66] Fox, M.A. *Durham theses, Durham University.* **1991**.

## *References*

---

# **Supporting Information**



## Supporting Information for Chapter 3

**Table S3-1.** Crystal and Structure Refinement data for **1-Solv** (Solv = DMA, DMF or MeOH).

Compound	<b>1-DMA</b>	<b>1-DMF</b>	<b>1-MeOH</b>
Empirical formula	C <sub>48</sub> H <sub>72</sub> B <sub>20</sub> N <sub>4</sub> O <sub>12</sub> Cu <sub>2</sub>	C <sub>44</sub> H <sub>64</sub> B <sub>20</sub> N <sub>4</sub> O <sub>12</sub> Cu <sub>2</sub>	C <sub>38</sub> H <sub>60</sub> B <sub>20</sub> O <sub>14</sub> Cu <sub>2</sub>
Formula weight	1240.37	1184.27	1084.14
Crystal system	Triclinic	Triclinic	Monoclinic
Space group	P-1	P-1	P21/c
CCDC ref	1901504	1899491	1859468
Wavelength (Å)	Cu Kα (1.5418)	Mo Kα (0.71073)	Mo Kα (0.71073)
a (Å)	15.2205(5)	14.4079(13)	16.2198(5)
b (Å)	15.5001(6)	14.5172(12)	12.5200(3)
c (Å)	15.5639(5)	15.4994(11)	14.1322(5)
α (deg)	82.435(2)	86.242(6)	90
β (deg)	87.787(2)	89.578(7)	113.426(4)
γ(deg)	63.755(2)	63.842(8)	90
V (Å <sup>3</sup> )	5897(2)	2901.8(4)	2633.30(16)
Z	2	2	2
F (000)	1284	1220.0	1116.0
θ (range)	2.865 - 67.266	3.735 - 25.027	2.126-28.499
Max./min. transmission	0.752817/ 0.615490	1.00000/0.59033	1.000/0.798
Ind refln (R <sub>int</sub> )	11538 (-)	10188 (-)	5966 (0.0714)
R1 (I > 2(I))	0.0469	0.0863	0.0455



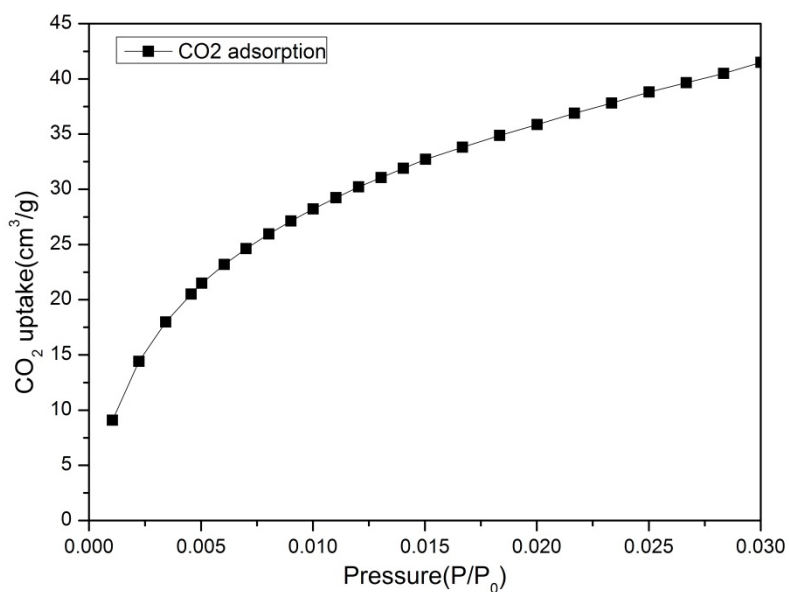
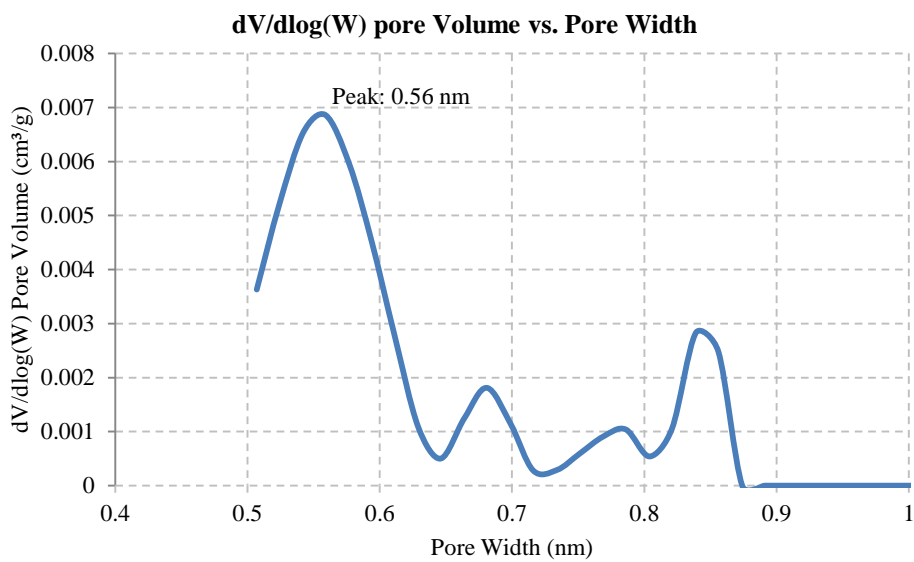
Supporting Information for Chapter 3

R1 (all data)	0.0604	0.1603	0.0576
wR2	0.1122	0.1718	0.1220
Wr2 (all data)	0.1191	0.2062	0.1268

**Table S3-2.** Selected distances (Å) and angles (°) for **1-Solv** (Solv = DMA, DMF or MeOH).

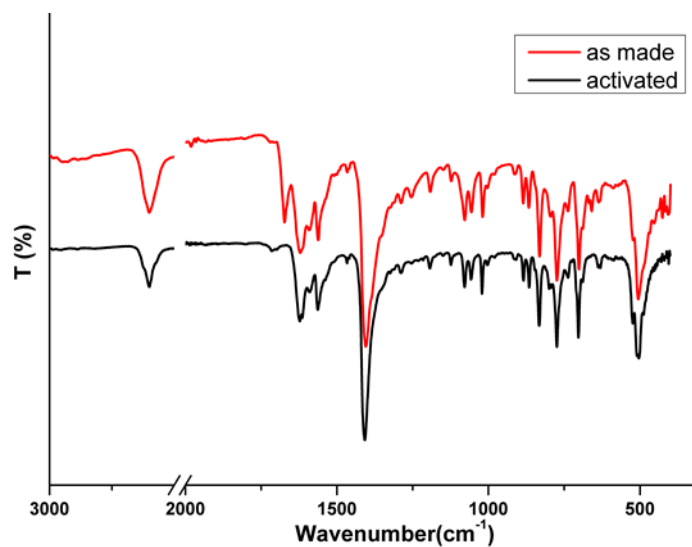
Compound	Cu–Cu	Cu–O <sub>2</sub> C	Cu–O <sub>solv</sub>	O <sub>2</sub> C–CB <sub>centroid</sub> –CO <sub>2</sub> <sup>a</sup>	Ph–Ph <sup>b</sup>
<b>1-DMA</b>	2.643	1.952	2.081	112.62	86.76
	2.647	1.959	2.124	115.43	86.45
		1.961			
		1.962			
		1.964			
		1.965			
		1.977			
		1.983			
<b>1-DMF</b>	2.607(2)	1.941(4)	2.111(5)	110.54	82.21
	2.641(2)	1.948(4)	2.138(4)	114.98	77.7(2)
		1.959(5)			
		1.966(4)			
		1.972(4)			
		1.974(4)			
		1.981(5)			
		1.991(4)			
<b>1-MeOH</b>	2.620(50)	1.951(2)	2.130(2)	112.22	87.29(30)
		1.958(2)			
		1.962(2)			
		1.983(2)			

<sup>a</sup> Carboxylated Carbon to carborane centroid angle. <sup>b</sup> Angle between C6H4 rings in the mCB-L1 ligand.

**Figure S3-1.** CO<sub>2</sub> adsorption isotherm at 273 K for activated 1'-activated.**Figure S3-2.** Pore Distribution by Density Functional Theory Model: CO<sub>2</sub>-DFT Slit Geometry for activated 1'-activated.



## Supporting Information for Chapter 4

**Figure S4-1.** FT-IR spectra of as-made *mCB-MOF-1* (red) and activated *mCB-MOF-1'* (black).**Table S4-1.** Crystal and Structure Refinement data for *mCB-MOF-1*

Compound <sup>a</sup>	<i>mCB-MOF-1</i>
Empirical formula <sup>a</sup>	C <sub>35</sub> H <sub>44</sub> B <sub>20</sub> Cu <sub>2</sub> N O <sub>9</sub>
Formula weight	965.99
Crystal system	Tetragonal
Space group	<i>I</i> 422
CCDC ref	1966753
Wavelength (Å)	Synchrotron ( 0.72932 )
Temperature	100(2)K
a (Å)	20.9233(5)
c (Å)	26.34200(10)
V (Å <sup>3</sup> )	11532.1(6)
Z	8

$\rho(\text{calc})$ (g/cm <sup>3</sup> )	1.113
F (000)	3928
$\theta$ range (deg)	1.62 - 34.16
Max./min. transmission	1.00000 / 0.12269
Ind refln ( $R_{\text{int}}$ )	10372 0.0727
Goodness-of-fit on $F^2$	1.066
$R_1^b$ ( $I > 2\sigma(I)$ )	0.0456
$R_1^b$ (all data)	0.0470
$wR_2^c$ ( $I > 2\sigma(I)$ )	0.1396
$wR_2^c$ (all data)	0.1413

<sup>a</sup>Based on the formula without uncoordinated solvent molecules.

<sup>b</sup> $R_1 = \Sigma(|F_o| - |F_c|) / \Sigma|F_o|$ .

<sup>c</sup> $wR_2 = [\Sigma w(|F_o|^2 - |F_c|^2)^2 / \Sigma w(F_o^2)]^{1/2}$ .

**Figure S4-2.** A view of the  $\pi$ -stacking in *m*CB-MOF-1.

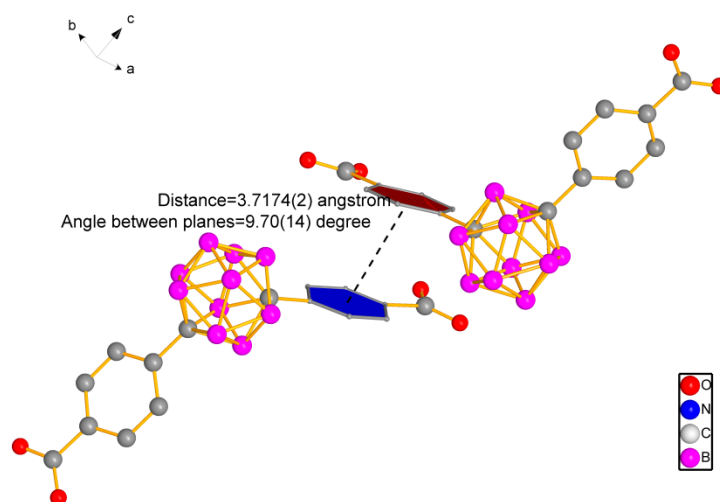


**Figure S4-3.** TGA diagrams of: as made *mCB-MOF-1* (black) and desolvated *mCB-MOF-1'* (red).

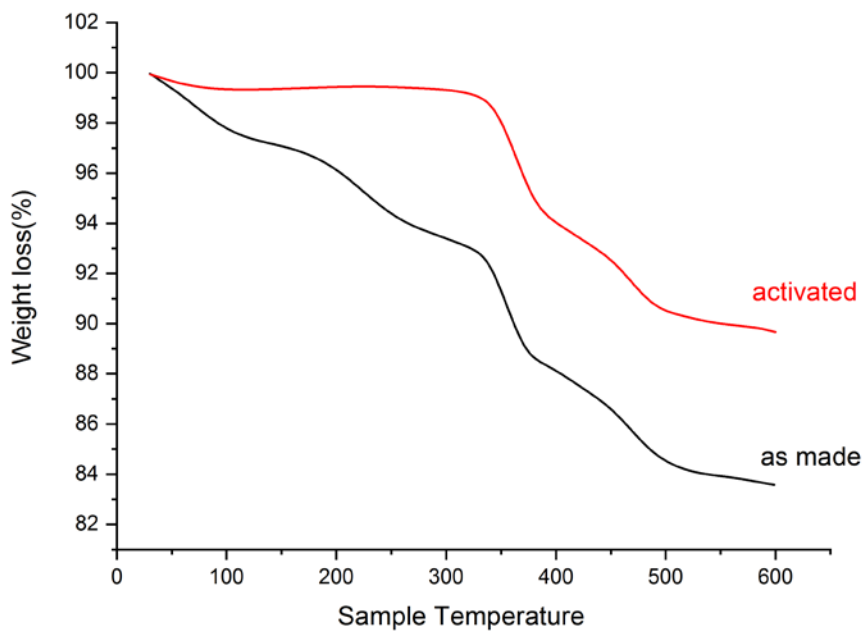


**Figure S4-4.** CO<sub>2</sub> adsorption isotherms at various temperatures for activated *mCB-MOF-1'*.

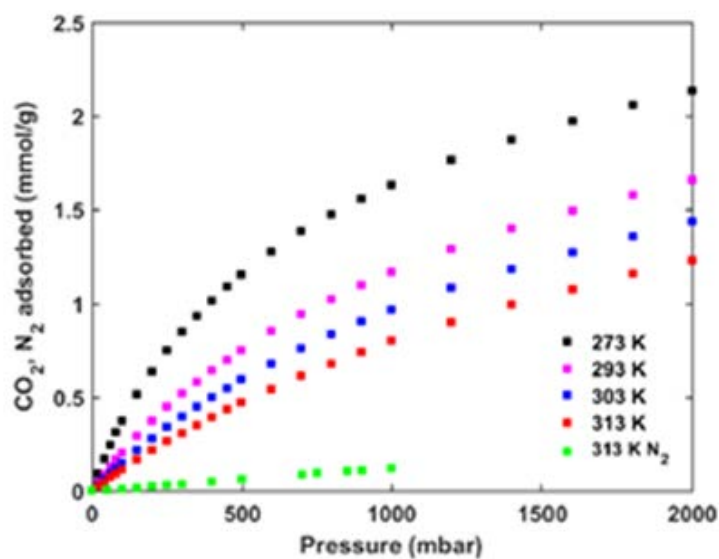


**Table S4-2.** Surface areas, N<sub>2</sub> uptakes, total pore volumes and ICP results for samples of **mCB-MOF-1'** treated under various conditions.

Conditions	BET surface area (m <sup>2</sup> /g)	N <sub>2</sub> uptake (STP cm <sup>3</sup> g <sup>-1</sup> ) <sup>a</sup>	Pore volume (cm <sup>3</sup> /g) <sup>b</sup>	[Cu] <sup>c</sup>
130°C, vacuum, 12h	756	200	0.31	-
20 days in water (90°C)	-	-	-	530 ppb
30 days in water (rt)	803	202	0.31	23.2 ppb
30 days in water (90°C)	787	200	0.31	792 ppb
60 days in water (90°C)	751	196	0.31	20.5 ppm
1 day, pH=2 (rt)	698	181	0.28	6.2 ppm
2 days, pH=2 (rt)	381	125	0.19	-
1 day, pH=11 (rt)	722	203	0.30	-
2 days, pH=11 (rt)	366	123	0.19	-
1 day, pH=11 (90°C)	629	169	0.26	476 ppb

<sup>a</sup> Measurement was taken at P/P0 = 0.95. <sup>b</sup> Calculated by single point method. <sup>c</sup> ICP-MS measurements of the concentration of Cu in the aqueous phase during the stability tests of **mCB-MOF-1'** at different conditions (aqueous blank sample contained 0.6 ppb of Cu).

**Figure S4-5. Scanning Electron Microscopy (SEM) images showing crystals morphology of: A) as made *mCB-MOF-1* and that of *mCB-MOF-1'* after being in water at 90°C for: B) one month and C) two months.**

A new crystalline phase forming spherulites [1] begin to appear in *mCB-MOF-1* samples that have been in 90°C water for two months (Figure S4-5C). Nevertheless, the heated sample for two months still shows high porosity and reasonable integrity of the structure. Such evidence for earlier detection of MOF aging via SEM than by PXRD has been previously observed [2].

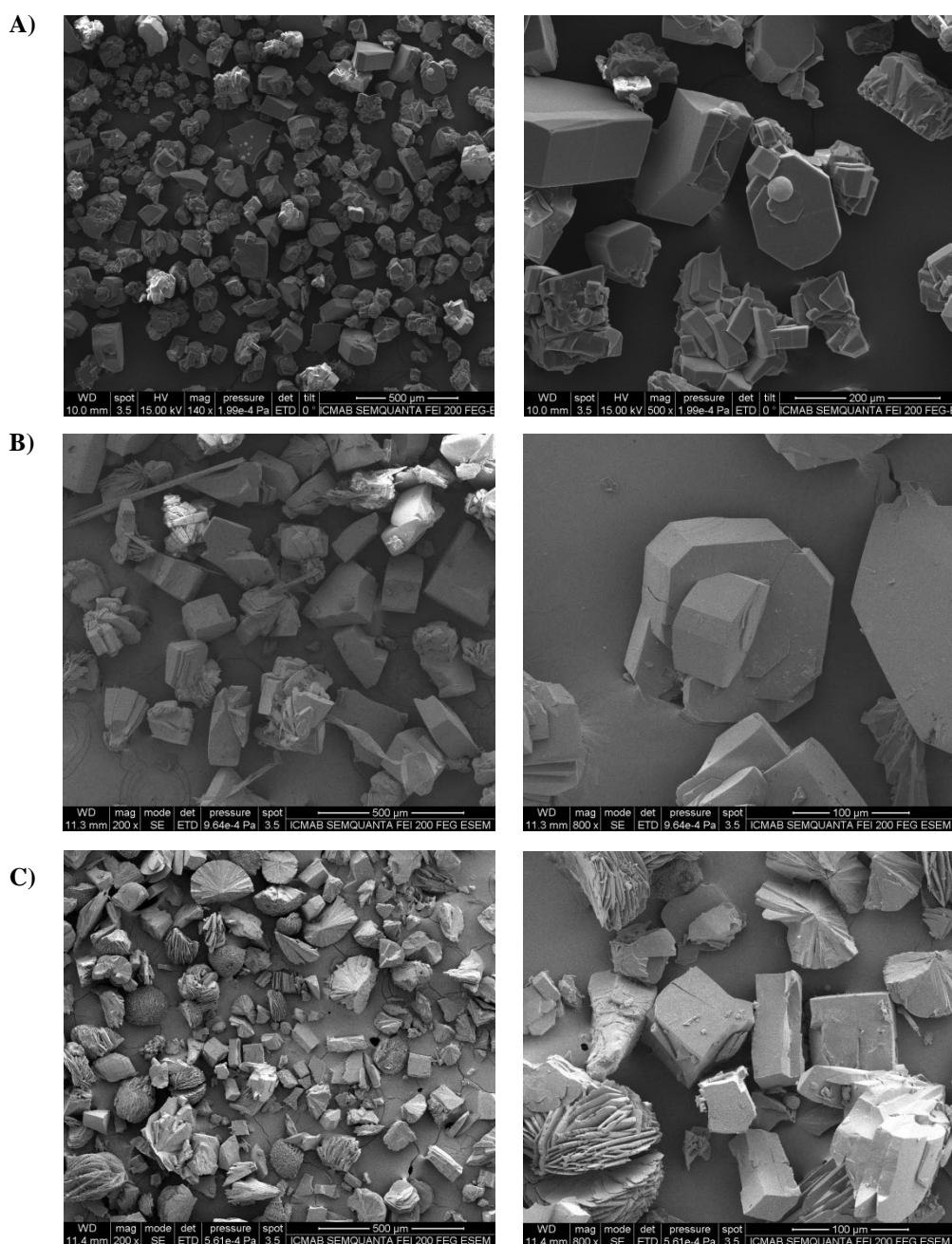




**Figure S4-6.** Comparison of the PXRD patterns of the activated *mCB-MOF-1'* after immersion in non-neutral water solutions at various conditions.

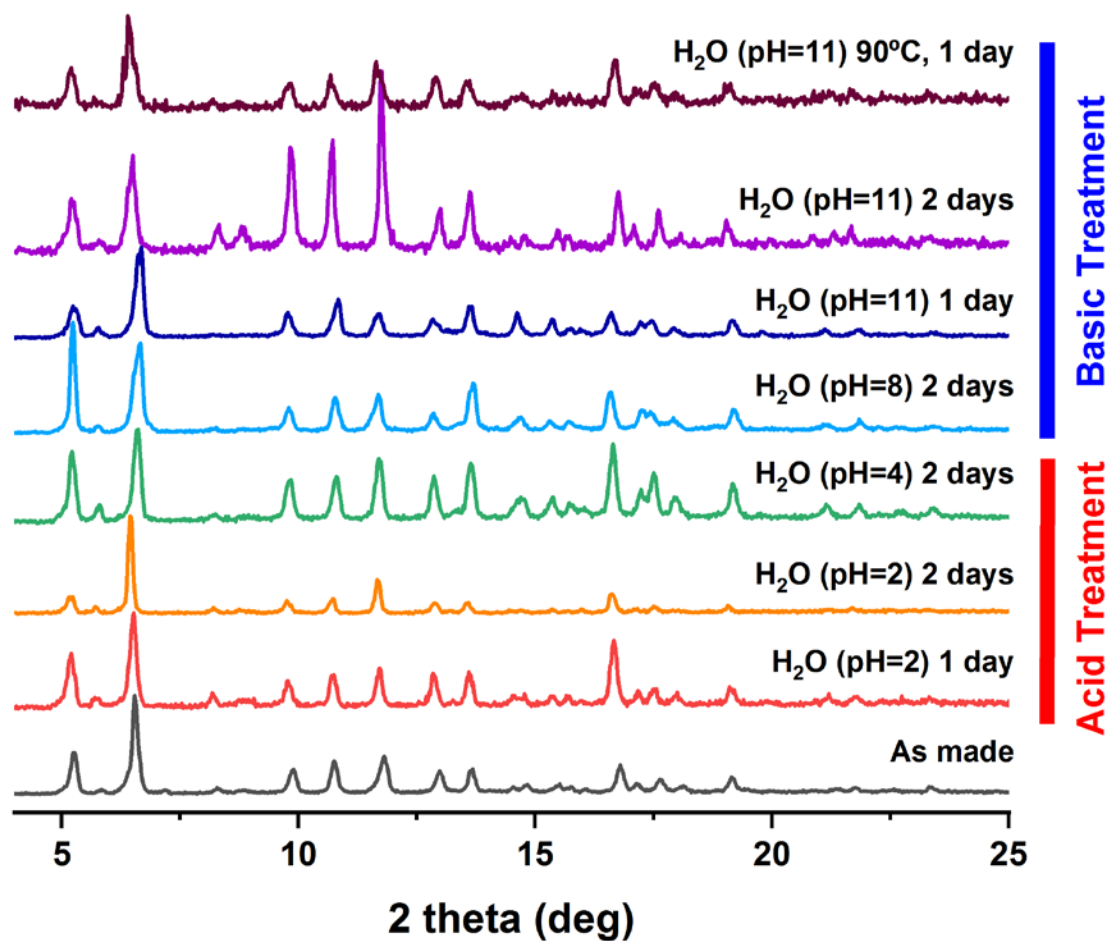


**Figure S4-7.** Scanning Electron Microscopy (SEM) images showing crystals morphology of: mCB-MOF-1' after being for one day in aqueous A) NaOH (pH = 11) at RT, B) NaOH (pH = 11) at 90°C and C) HCl (pH = 2) at RT. Scale bars correspond to 500  $\mu\text{m}$  (left column images) or 100  $\mu\text{m}$  (right column images).

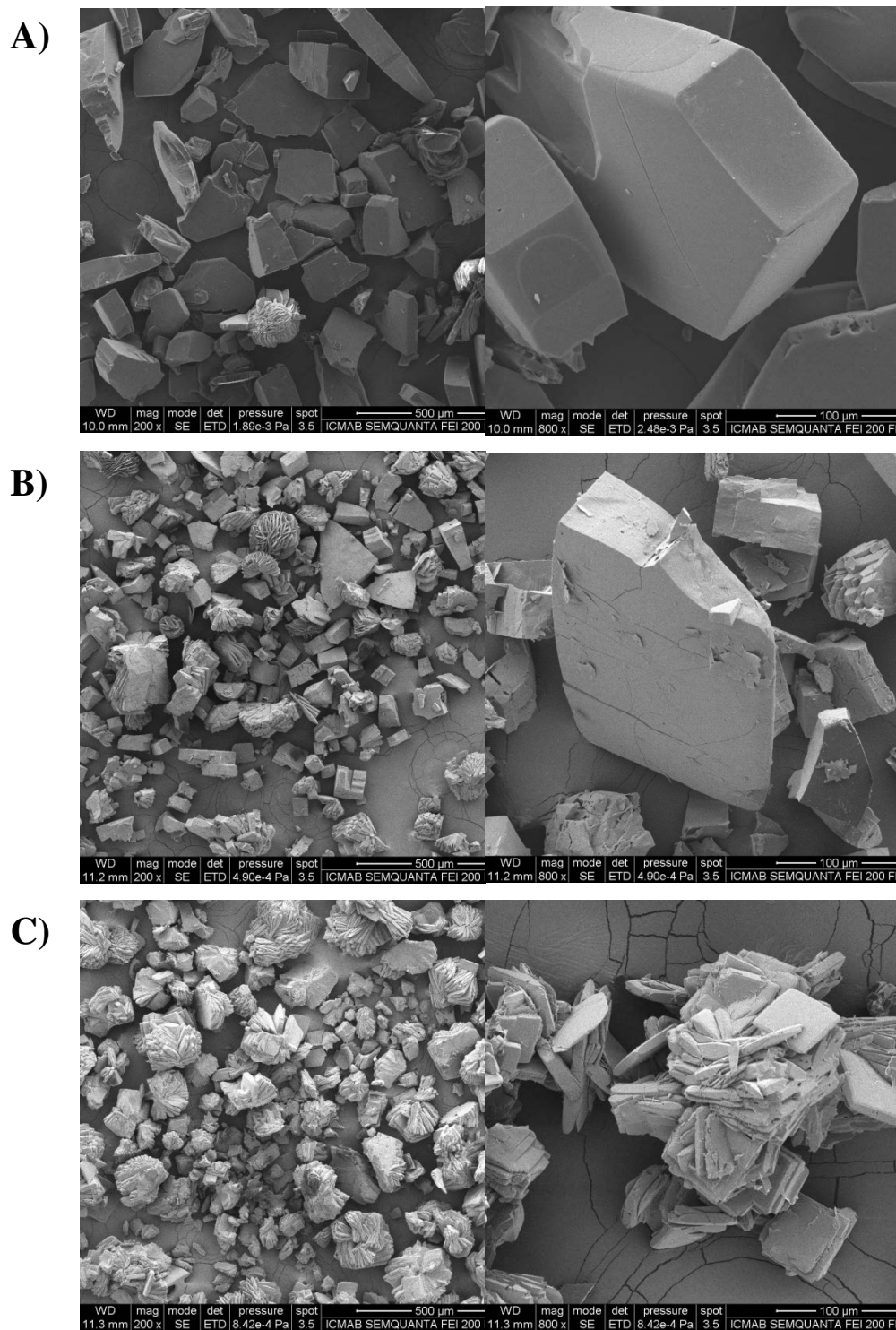


**Table S4-3.** Comparison of  $S_{\text{BET}}$ , chemical stability conditions, and stability level of selected stable MOFs.

MOFs	$S_{\text{BET}}$ ( $\text{m}^2/\text{g}$ )	Stable conditions	Stability level <sup>a</sup>	Ref.
MIL-53(AI)	900	80 °C, water, 6 h; 0.07 M NaOH, 0.07 M HCl, 2 h	6B	[3]
ZIF-8	1630	Boiling Water, 7 days; 8 M NaOH, boiling, 24 h	6C	[4]
ZIF-68	1090	Boiling water, 7 days	6C	[5]
ZIF-69	950	Boiling water, 7 days	6C	[6]
ZIF-70	1730	Boiling water, 7 days	6C	[6]
CALF-25	385	80 °C, 80% RH	4D	[6]
UiO-66	1187	Boiling water, 4 h	6A	[7]
DUT-67	1064/810	RT, Water, 24 h; 1 M HCl, 3 days	5A	[8]
DUT-68	891/749	RT, Water, 24 h; 1 M HCl, 3 days	5A	[9]
PCN-124	1372	RT, Water, 3 days	5A	[9]
PCN-222	2200	Concentrate HCl or boiling water for 24 h	6A	[10]
NU-1000	2320	RT, Water, 24 h	5A	[11]
NU-1100	4020	RT, Water, 24 h	5A	[12]
NU-1103	5646	RT, Water, 18 h	5A	[13]
MOF-802	1145	RT, Moisture	3A	[14]
MOF-841	1390	RT, Moisture	3A	[14]
Cu(BTtri)	1770	Boiling water 3 days; HCl (pH = 3) RT, 24 h	6B	[15,16]
Cu(BTT)	701	RT, Water, 24 h	5A	[17]
Cu(BTP)	1860	Boiling water 10 days	6B	[18]
HKUST-1	1340	RT, in air less than 1 day	3D	[18]
<b>mCB-MOF-1</b>	756	90 °C, water, 2 months; RT, pH=2, 48 h, 90 °C pH=11, 24 h	6A	This work

<sup>a</sup> According to B. S. Gelfand, G. K. H. Shimizu, *Dalton Trans.* **2016**, 45, 3668-3678.)

**Table S4-4.** Contact angles (°) for powder and as-made disk pellets of *mCB-MOF-1*.

	Static	Advancing	Receding	Contact Angle Hysteresis (CAH)
<b>Powder</b>	144.2 ± 0.4	-	-	-
<b>As-made pellet</b>	100.9 ± 0.1	101.1	69.1	32

**Ideal Adsorbed Solution Theory (IAST) selectivity studies** [19,20]

In order to compare the separation efficiency of 1-butanol/ethanol mixtures for *mCB-MOF-1* and ZIF-8, IAST method was used to predict the molar loadings at specific partial pressures by using pure single component isotherm fits. The adsorption isotherms of 1-butanol and ethanol in *mCB-MOF-1* at 313 K were fitted with the single-site Langmuir (SSL) model:

$$q = \frac{q_{sat}bp}{1 + bp}$$

Here,  $q$  is molar uptake of adsorbate (mmol/g),  $q_{sat}$  is saturation uptake (mmol/g),  $b$  is the parameter in single component Langmuir isotherm ( $\text{KPa}^{-1}$ ),  $p$  is the pressure of bulk gas.

For the adsorption isotherms of 1-butanol and ethanol in ZIF-8 at 313 K, they were fitted with double-site Langmuir-Freundlich (DSLFF) model:

$$q = \frac{q_{sat,1}b_1pc_1}{1 + b_1pc_1} + \frac{q_{sat,2}b_2pc_2}{1 + b_2pc_2}$$

Here,  $q_{sat,1}$  and  $q_{sat,2}$  are saturation uptake (mmol/g) for sites 1 and 2,  $b_1$  and  $b_2$  are the affinity coefficients of sites 1 and 2,  $c_1$  and  $c_2$  are the parameters for the deviations of an ideal homogeneous surface.

Ideal Adsorbed Solution Theory (IAST) two-gas adsorption selectivity could be

calculated from single-component isotherm fitting parameters, defined as following:

$$Sads = \frac{q1/q2}{p1/p2}$$

**Table S4-5.** Langmuir fitting parameters of 1-butanol and ethanol adsorption isotherms of *mCB-MOF-1'* at 313 K.

<i>mCB-MOF-1</i>	$q_{sat}$ (mmol/g)	$b$ (KPa <sup>-1</sup> )	Adj. R <sup>2</sup>
1-butanol	2.389638	0.200323	0.98324
ethanol	3.483847	0.010583	0.99099

**Table S4-6.** Langmuir fitting parameters of 1-butanol and ethanol adsorption isotherms of ZIF-8 at 313 K.

ZIF-8	$q_{sat,1}$ (mmol/g)	$b_1$ (KPa <sup>-1</sup> )	$c_1$	$q_{sat,2}$ (mmol/g)	$b_2$ (KPa <sup>-1</sup> )	$c_2$	Adj. R <sup>2</sup>
1-butanol	1284.1288	1.4043E-7	1.61024	3.2489	6.4983E-9	6.9879	0.98813
ethanol	12.7473	1.2282E-11	5.08214	2.8909	1.0705E-11	3.88035	0.99761

**Figure S4-8.** The IAST predicted isotherms of *mCB-MOF-1'* (a), ZIF-8 (b) of a binary mixture of Butanol : Ethanol (0.85 : 0.15) at 313 K as a function of the total pressure.

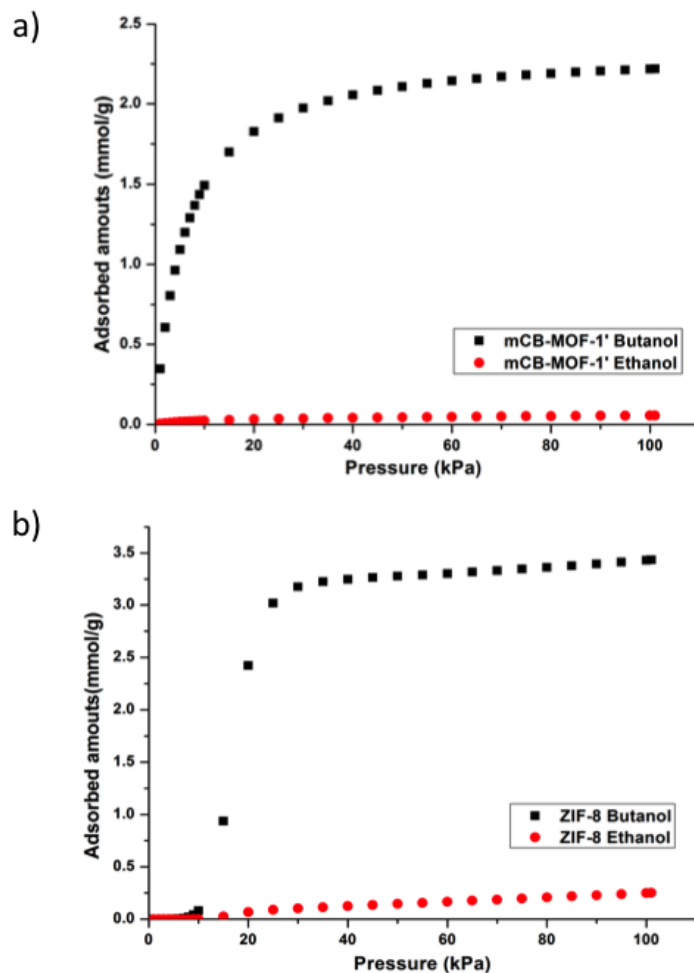
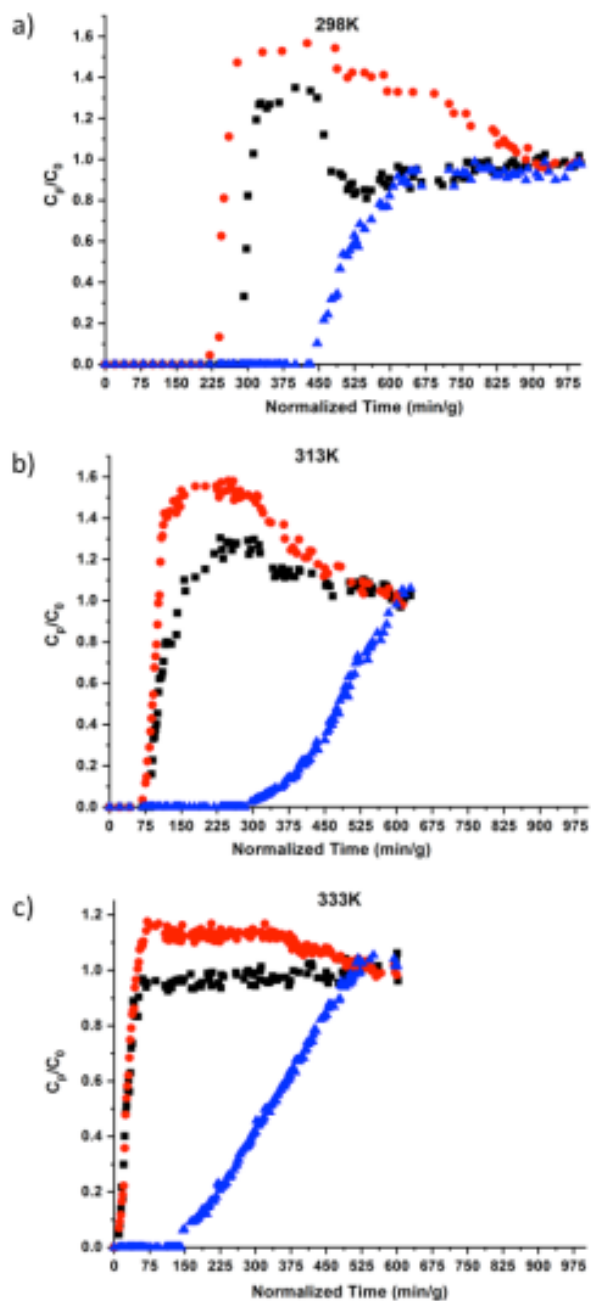


**Table S4-7.** Parameters obtained from the NMR breakthrough experiments (See experimental section for details).

Adsorption capacity	<i>mCB-MOF-1</i>	ZIF-8
Butanol	15.0072mg (0.4056mmol/g)	15.6288mg (0.4693mmol/g)

Ethanol	0.5796mg (0.0252mmol/g)	0.6716mg (0.0324mmol/g)
Acetone	8.1954 mg (0.2826mmol/g)	1.1252 mg (0.0431mmol/g)
H <sub>2</sub> O	9.117mg (1.013mmol/g)	9.2448mg (1.1413mmol/g)
Weight increased from the NMR	32.8992 mg	26.6704mg
Real weight increased	43.6 mg	21.4 mg
Selectivity(B/E)	2.77	2.49
Selectivity(B/A)	0.97	7.39

**Figure S4-9.** Comparison of breakthrough curves for separation of butanol collected from columns at a) 298K, b) 313K and c) 333K. Codes: Butanol (blue triangles), ethanol (black squares), acetone (red circles).

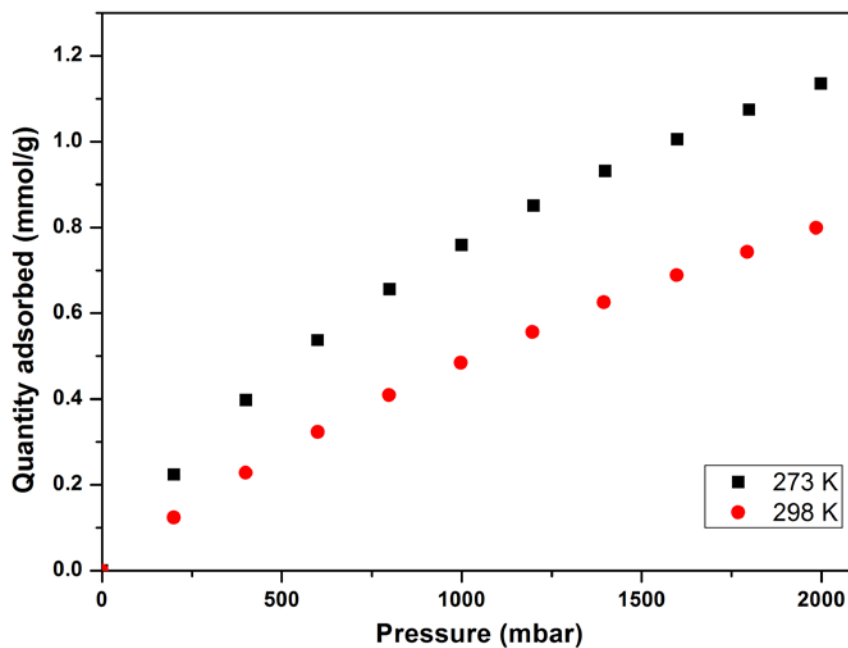
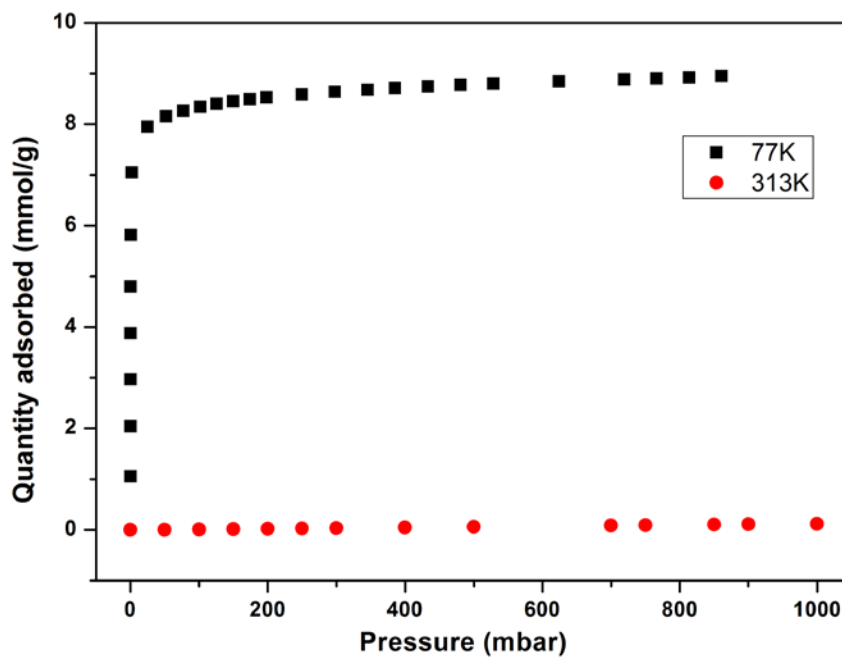




## References

- [1] Shtukenberg, A.G.; Punin, Y.O.; Gunn, E.; Kahr, B. *Chemical Reviews* **2012**, *112*, 1805.
- [2] DeCoste, J.B.; Peterson, G.W.; Schindler, B.J.; Killops, K.L.; Browe, M.A.; Mahle, J.J. *Journal of Materials Chemistry A* **2013**, *1*, 11922.
- [3] Bezverkhyy, I.; Ortiz, G.; Chaplais, G.; Marichal, C.; Weber, G.; Bellat, J.-P. *Microporous and Mesoporous Materials* **2014**, *183*, 156.
- [4] Park, K.S.; Ni, Z.; Côté, A.P.; Choi, J.Y.; Huang, R.; Uribe-Romo, F.J.; Chae, H.K.; O'Keeffe, M.; Yaghi, O.M. *Proceedings of the National Academy of Sciences* **2006**, *103*, 10186.
- [5] Banerjee, R.; Phan, A.; Wang, B.; Knobler, C.; Furukawa, H.; O'Keeffe, M.; Yaghi, O.M. *Science* **2008**, *319*, 939.
- [6] Taylor, J.M.; Vaidhyanathan, R.; Iremonger, S.S.; Shimizu, G.K.H. *Journal of the American Chemical Society* **2012**, *134*, 14338.
- [7] Cavka, J.H.; Jakobsen, S.; Olsbye, U.; Guillou, N.; Lamberti, C.; Bordiga, S.; Lillerud, K.P. *Journal of the American Chemical Society* **2008**, *130*, 13850.
- [8] Bon, V.; Senkovska, I.; Baburin, I.A.; Kaskel, S. *Crystal Growth & Design* **2013**, *13*, 1231.
- [9] Park, J.; Li, J.-R.; Chen, Y.-P.; Yu, J.; Yakovenko, A.A.; Wang, Z.U.; Sun, L.-B.; Balbuena, P.B.; Zhou, H.-C. *Chemical Communications* **2012**, *48*, 9995.
- [10] Feng, D.; Gu, Z.Y.; Li, J.R.; Jiang, H.L.; Wei, Z.; Zhou, H.C. *Angewandte Chemie International Edition* **2012**, *51*, 10307.
- [11] Mondloch, J.E.; Bury, W.; Fairen-Jimenez, D.; Kwon, S.; DeMarco, E.J.; Weston, M.H.; Sarjeant, A.A.; Nguyen, S.T.; Stair, P.C.; Snurr, R.Q. *Journal of the American Chemical Society* **2013**, *135*, 10294.
- [12] Gutov, O.V.; Bury, W.; Gomez - Gualdrón, D.A.; Krungleviciute, V.; Fairen - Jimenez, D.; Mondloch, J.E.; Sarjeant, A.A.; Al - Juaid, S.S.; Snurr, R.Q.; Hupp, J.T. *Chemistry – A European Journal* **2014**, *20*, 12389.
- [13] Wang, T.C.; Bury, W.; Gómez-Gualdrón, D.A.; Vermeulen, N.A.; Mondloch, J.E.; Deria, P.; Zhang, K.; Moghadam, P.Z.; Sarjeant, A.A.; Snurr, R.Q. *Journal of the American Chemical Society* **2015**, *137*, 3585.
- [14] Furukawa, H.; Gandara, F.; Zhang, Y.-B.; Jiang, J.; Queen, W.L.; Hudson, M.R.; Yaghi, O.M. *Journal of the American Chemical Society* **2014**, *136*, 4369.
- [15] Demessence, A.; D'Alessandro, D.M.; Foo, M.L.; Long, J.R. *Journal of the American Chemical Society* **2009**, *131*, 8784.
- [16] Sumida, K.; Rogow, D.L.; Mason, J.A.; McDonald, T.M.; Bloch, E.D.; Herm, Z.R.; Bae, T.-H.; Long, J.R. *Chemical Reviews* **2012**, *112*, 724.
- [17] Dong, B.X.; Zhang, S.Y.; Liu, W.L.; Wu, Y.C.; Ge, J.; Song, L.; Teng, Y.L. *Chemical Communications* **2015**, *51*, 5691.
- [18] Colombo, V.; Galli, S.; Choi, H.J.; Han, G.D.; Maspero, A.; Palmisano, G.; Masciocchi, N.; Long, J.R. *Chemical Science* **2011**, *2*, 1311.
- [19] Lu, W.; Sculley, J.P.; Yuan, D.; Krishna, R.; Wei, Z.; Zhou, H.C. *Angewandte Chemie* **2012**, *124*, 7598.
- [20] Myers, A.L.; Prausnitz, J.M. *AIChE Journal* **1965**, *11*, 121.

## Supporting Information for Chapter 5

Figure S5-1. CH<sub>4</sub> adsorption isotherms on *mCB*-MOF-1 at 273 and 298 K.Figure S5-2. N<sub>2</sub> adsorption isotherms on *mCB*-MOF-1 at 77 and 313 K.

### Ideal Adsorbed Solution Theory (IAST) selectivity

In order to investigate the separation efficiency of CO<sub>2</sub>/N<sub>2</sub> and CO<sub>2</sub>/CH<sub>4</sub> mixtures for **mCB-MOF-1**, IAST method was used to predict the molar loadings at specific partial pressures by using pure single component isotherm fits. The adsorption isotherm of CH<sub>4</sub> on **mCB-MOF-1** at 273 K was fitted with the single-site Langmuir (SSL) model:

$$q = \frac{q_{sat}bp}{1 + bp}$$

Here,  $q$  is molar uptake of adsorbate (mmol/g),  $q_{sat}$  is saturation uptake (mmol/g),  $b$  is the parameter in single component Langmuir isotherm (KPa<sup>-1</sup>),  $p$  is the pressure of bulk gas.

For the adsorption isotherm of CO<sub>2</sub> on **mCB-MOF-1** at 273 K, it was fitted with double-site Langmuir-Freundlich (DSLFL) model:

$$q = \frac{q_{sat,1}b_1p^{c_1}}{1 + b_1p^{c_1}} + \frac{q_{sat,2}b_2p^{c_2}}{1 + b_2p^{c_2}}$$

Here,  $q_{sat,1}$  and  $q_{sat,2}$  are saturation uptake (mmol/g) for sites 1 and 2,  $b_1$  and  $b_2$  are the affinity coefficients of sites 1 and 2,  $c_1$  and  $c_2$  are the parameters for the deviations of an ideal homogeneous surface.

For the adsorption isotherms of CO<sub>2</sub> and N<sub>2</sub> on **mCB-MOF-1** at 313 K, they were fitted with single-site Langmuir-Freundlich (SSLFL) model:

$$q = \frac{q_{sat}bp^c}{1 + bp^c}$$

Here,  $c$  is the parameter for the deviations of an ideal homogeneous surface.

Ideal Adsorbed Solution Theory (IAST) two-gas adsorption selectivity could be calculated from single-component isotherm fitting parameters, defined as following:

$$S_{ads} = \frac{q_1/q_2}{p_1/p_2}$$

**Table S5-1.** Single-site Langmuir fitting parameters of CH<sub>4</sub> adsorption isotherm on **mCB-MOF-1** at 273 K.

<b>mCB-MOF-1</b>	$q_{sat}$ (mmol/g)	$b$ (KPa <sup>-1</sup> )	Adj. R <sup>2</sup>
CH <sub>4</sub>	2.14503	0.00554	0.99969

**Table S5-2.** Double-site Langmuir-Freundlich fitting parameters of CO<sub>2</sub> adsorption isotherm on *mCB-MOF-1* at 273 K.

<i>mCB-MOF-1</i>	$q_{sat,1}$ (mmol/g)	$b_1$ (KPa <sup>-1</sup> )	$c_1$	$q_{sat,2}$ (mmol/g)	$b_2$ (KPa <sup>-1</sup> )	$c_2$	Adj. R <sup>2</sup>
CO <sub>2</sub>	3.18295	0.00524	0.76244	1.78534	0.01879	0.99736	1

**Table S5-3.** Single-site Langmuir-Freundlich fitting parameters of CO<sub>2</sub> and N<sub>2</sub> adsorption isotherms on *mCB-MOF-1* at 313 K.

<i>mCB-MOF-1</i>	$q_{sat}$ (mmol/g)	$b$ (KPa <sup>-1</sup> )	$c$	Adj. R <sup>2</sup>
CO <sub>2</sub>	2.77376	0.00456	0.97379	0.99997
N <sub>2</sub>	0.58574	0.00146	1.12781	0.99933

**Isosteric heat of adsorption**

In order to evaluate the interactions between *mCB-MOF-1* and these gas molecules (CO<sub>2</sub>, CH<sub>4</sub>, H<sub>2</sub> and N<sub>2</sub>), the isosteric heat of adsorption  $Q_{st}$  was calculated. In detail,  $Q_{st}$  was obtained by fitting adsorption isotherms of CO<sub>2</sub> at 273, 293, and 303 K, CH<sub>4</sub> at 273 and 298 K, H<sub>2</sub> at 273, 298, and 323 K, N<sub>2</sub> at 77 and 313 K with the **eq 1**. Then, the  $Q_{st}$  was calculated by **eq 2**.

$$\ln p = \ln N + \left(\frac{1}{T}\right) \sum_{i=0}^m a_i N^i + \sum_{j=0}^n b_j N^j \quad (\text{eq 1})$$

$$Q_{st} = -R \sum_{i=0}^m a_i N^i \quad (\text{eq 2})$$

where  $p$  and  $N$  represent the pressure (Torr) and the quantity adsorbed (mg/g),  $T$  refers to the temperature (K),  $a_i$  and  $b_j$  represent empirical parameters,  $m$  and  $n$  represent the number of coefficients required to give a good fit to the isotherms, and  $R$  the ideal gas constant (J·K<sup>-1</sup>·mol<sup>-1</sup>).



## Supporting Information for Chapter 6

**Figure S6-1.** FT-IR spectra of as-made *mCB-MOF-2* (black) and activated *mCB-MOF-2'* (red).

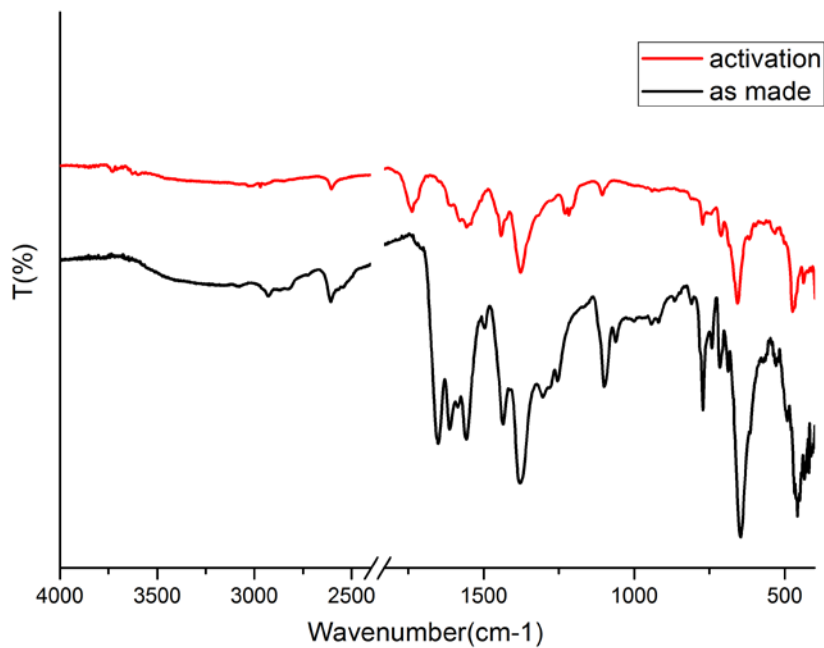


**Figure S6-2.** TGA diagrams of as-made *mCB-MOF-2* (black) and activated *mCB-MOF-2'* (red).

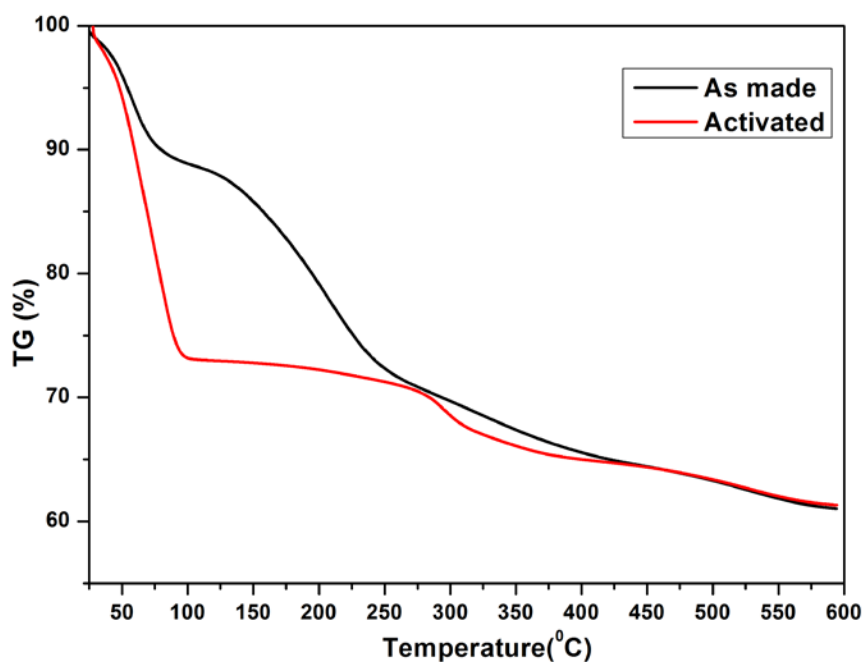


**Table S6-1.** Surface areas, N<sub>2</sub> uptakes, and total pore volumes for samples of *mCB-MOF-2'* treated under various conditions.

Conditions	BET surface area (m <sup>2</sup> /g)	N <sub>2</sub> uptake (STP cm <sup>3</sup> g <sup>-1</sup> ) <sup>a</sup>	Pore volume (cm <sup>3</sup> /g) <sup>b</sup>
130°C, vacuum, 12h	1095	288	0.45
2 days in water (rt)	1088	288	0.45
2 days in water (90°C)	1024	274	0.42
1 day, pH=1 (rt)	945	248	0.38
1 day, pH=2 (rt)	923	289	0.45
1 day, pH=11 (rt)	829	261	0.40

<sup>a</sup> Measurement was taken at P/P<sub>0</sub> = 0.95. <sup>b</sup> Calculated by single point method.

**Table S6-2.** Crystal and Structure Refinement data for *mCB-MOF-2*

Compound	<i>mCB-MOF-2</i>
Empirical formula	C18 H16 B10 O16 Zr3
Formula weight	870.07
Crystal system	Hexagonal
Space group	<i>P6/mmm</i>
Wavelength (Å)	Synchrotron ( 0.72932 )
Temperature	100(2)K
a (Å)	25.5012(4)
b (Å)	25.5012(4)
c (Å)	14.0513(2)
V (Å <sup>3</sup> )	7913.5(3)
Z	6
ρ <sub>(calc)</sub> (g/cm <sup>3</sup> )	1.095

F (000)	2532
$\theta$ range (deg)	1.763 - 28.498
Absorp.coeff. ( $\text{mm}^{-1}$ )	0.626
Ind refln	3546
( $R_{\text{int}}$ )	0.0344
Goodness-of-fit on $F^2$	1.117
$R_1$ ( $I > 2\sigma(I)$ )	0.0503
$R_1$ (all data)	0.0516
$wR_2$ ( $I > 2\sigma(I)$ )	0.1455
$wR_2$ (all data)	0.1469





# **General Conclusions**



## General Conclusions

The results in this Thesis expand the up to now very limited family of *meta*-carborane-based MOFs and in particular those from carboxylate carborane-based MOFs. This work proof that the incorporation of polycarboxylate *meta*-carborane-based ligands into coordination polymers or MOFs endows those with excellent chemical and hydrolytic stabilities.

Firstly, it was synthesized a new family of Cu-paddlewheel based 2D coordination polymers  $[\text{Cu}_2(\mathbf{mCB-L1})_2(\text{Solv})_2] \cdot x\text{Solv}$  (**1-DMF**, **1-DMA**, **1-MeOH**) based on a dicarboxylate *m*-carborane ligand 1,7-di(4-carboxyphenyl)-1,7-dicarba-*closo*-dodecaborane (**mCB-H<sub>2</sub>L1**). Their structures were determined by SCXRD analysis, and revealed that the V-shaped linker **mCB-L1** displayed non-coplanar phenyl rings, resulting in a very corrugated 2D layers. The basal positions at the Cu<sub>2</sub>-paddlewheel units were occupied by various solvents, such as DMF, DMA or MeOH, providing **1-DMF**, **1-DMA** or **1-MeOH**, respectively. **1-DMF** undergoes a reversible phase transition on solvent exchange and provided a crystalline material that is porous to N<sub>2</sub> and CO<sub>2</sub>. The combination of the experimental and calculated data supports the spontaneous release of the solvent from **1-DMF**, with the consequent generation of OMSs. Sliding of the layers allows the OMSs to be in close proximity to readily available hydride atoms of the many present from the carborane moieties, and thus promote the formation of B–H···Cu(II) interactions. The observed phase transition on solvent loss is accompanied by new Raman modes in the B–H and Cu–Cu region that are in agreement with the formation of B–H···Cu(II) interactions. There is enough flexibility in the solid to move the paddlewheels relative to each other so that the Cu centers can interact with the many available hydride atoms from the carborane moieties in another paddlewheel unit. Such B–H···Cu(II) interactions can be easily disturbed in the presence of a strongly coordinating solvent such as DMF and provide the starting **1-DMF** structure at room temperature. The present work adds unprecedented knowledge to the possible reasons

## General Conclusions

---

for boranes or carboranes acting to stabilize flexible MOFs but it also discloses another possible mechanism for constructing new flexible architectures or hydride/MOF composites.

Secondly, based on the 2D layered structure from **1**, we synthesized a new Cu<sub>2</sub>-paddlewheel based MOF **mCB-MOF-1** which was constructed by **mCB-L1** (1,7-di(4-carboxyphenyl)-1,7-dicarba-closo-dodecaborane) and DABCO (1,4-diazabicyclo[2.2.2]octane) and characterized by a series of characterization techniques including SCXRD, PXRD, FTIR, TGA, and N<sub>2</sub> adsorption. The SCXRD analysis revealed that **mCB-MOF-1** presents a pillar-layer structure with the two apical sites of each Cu<sub>2</sub>-paddlewheel cluster were occupied by DABCO ligands and H<sub>2</sub>O molecules, respectively. **mCB-MOF-1** shows a 2-fold interpenetration structure with square 1D channels. The activated **mCB-MOF-1'** is porous with a BET surface area of 756 m<sup>2</sup>g<sup>-1</sup>. Due to the structural interpenetration and protective effect of hydrophobic *meta*-carborane toward Cu<sub>2</sub>-paddlewheel cluster hydrolysis, **mCB-MOF-1'** exhibits an extraordinary stability in basic and acidic aqueous solutions, and even in water at 90 °C for over two months. **mCB-MOF-1'** it is also stable when incubated in liquid water over a wide pH range (from 2 to 11) for at least 48 h at room temperature and also in basic conditions (pH11) at 90 °C for at least 24 h. The hydrophobicity of **mCB-MOF-1** also was indicated by a contact angle ( $\theta_c = 144^\circ$ ) and type-II water vapor isotherms. Furthermore, single-component adsorption isotherms of acetone, butanol, and ethanol for **mCB-MOF-1** afforded type I isotherms in the low-pressure region, indicative of a strong affinity for the components of the ABE mixture. The IAST selectivity for butanol over ethanol shows higher than 12.0 at <25 kPa and only slowly decreases 7.0 at 100 kPa, being overall larger than that for ZIF-8. Monte Carlo and DFT calculations show that **mCB-MOF-1'** has higher affinity for butanol than ZIF-8, and show that the adsorbates preferentially distribute within the pockets created by the 2-fold interpenetrated structure of **mCB-MOF-1'**. The results from an integrated process of gas stripping–vapor-phase adsorption process with dynamic breakthrough experiments for the separation of ABE aqueous

solution (acetone 7.04 g/L, 0.715 wt%; butanol 13.75 g/L, 1.39 wt%; ethanol 2.56 g/L, 0.26 wt%; water 960.69 g/L, 97.63 wt%) at 333K on both MOFs show a more efficient butanol recovery for **mCB-MOF-1'** compared to ZIF-8 under the same conditions. This work demonstrates the potential of carborane containing MOFs for creating water stable MOFs and their potential for industrial applications.

Subsequently, based on the microporous nature and highly stable property of **mCB-MOF-1'**, it was further explored the gas adsorption toward CO<sub>2</sub>, CH<sub>4</sub>, N<sub>2</sub>, and H<sub>2</sub> at various temperatures at a pressure range of 2 bar. The single-component adsorption isotherms showed the CO<sub>2</sub> adsorption performance on **mCB-MOF-1'** was much better than that of CH<sub>4</sub> or N<sub>2</sub> under the same conditions. The IAST selectivities for CO<sub>2</sub>/CH<sub>4</sub> binary mixtures (5:5, 5:15, or 5:25, v/v) at 273 K and CO<sub>2</sub>/N<sub>2</sub> binary mixtures (5:5, 5:15, or 5:25, v/v) at 313 K over the pressure range 0-2 bar indicated good selective adsorption of CO<sub>2</sub> over CH<sub>4</sub> and N<sub>2</sub>. Moreover, the Q<sub>st</sub> value of CO<sub>2</sub>, CH<sub>4</sub>, and N<sub>2</sub> indicated that the CO<sub>2</sub> molecules have stronger interactions with **mCB-MOF-1'** compared to other gases. In addition, a combination of adsorption isotherms and isosteric heat of adsorption for H<sub>2</sub> implied that **mCB-MOF-1'** could be used for CO<sub>2</sub>/H<sub>2</sub> separation. Notably, breakthrough experiments demonstrated that **mCB-MOF-1'** had very excellent CO<sub>2</sub>/N<sub>2</sub> separation performance with a selectivity of ~1000 at 298 K at 1 bar which surpassed most reported MOFs, but moderate CO<sub>2</sub>/CH<sub>4</sub> selectivity and low C<sub>3</sub>H<sub>8</sub>/C<sub>3</sub>H<sub>6</sub> separation performance at 298 K at 1 bar. Besides, good oil-water separation performance was observed on **mCB-MOF-1'** due to its hydrophobic and oleophilic property.

Finally, a new tetracarboxylic acid ligand 1,7-di(3,5-dicarboxyphenyl)-1,7-dicarba-*closo*-dodecaborane (**mCB-H<sub>4</sub>L<sub>2</sub>**) was designed and synthesized. Then the first carborane-based Zr-MOF (**mCB-MOF-2**) was synthesized and characterized by a series of characterization techniques including SCXRD, PXRD, FTIR, TGA, and N<sub>2</sub> adsorption. The SCXRD analysis revealed that **mCB-MOF-2** is formed by Zr<sub>6</sub> clusters connected to eight V-shaped **mCB-L<sub>2</sub>** ligands

## *General Conclusions*

---

to produce a 3D **csq** topology MOF with hydrophobic hexagonal and hydrophilic triangular 1D channels. The activated **mCB-MOF-2'** is porous to CO<sub>2</sub>, H<sub>2</sub>, CH<sub>4</sub> with a BET surface area of 1095 m<sup>2</sup>g<sup>-1</sup>. **mCB-MOF-2'** exhibited high stability in water at 90 °C for over two days and also in liquid water over a wide pH range (from 1 to 11) for at least 24 h at room temperature and it is also stable in high concentrated (12M) HCl solutions for at least 24 h. The hydrolytic stability can be attributed to the hydrophobic property of *meta*-carborane and the robustness of Zr<sub>6</sub> clusters. The stepwise water adsorption isotherm provided an adsorption capacity of 370 cm<sup>3</sup>g<sup>-1</sup>(STP) on **mCB-MOF-2'**. The adsorptive removals of organophosphorus pesticides including GP and GF in aqueous solutions were evaluated by Freundlich models, and the adsorption capacities have surpassed all reported MOFs including its mesoporous analogue NU-1000. Moreover, **mCB-MOF-2'** also showed good performance on catalytic degradation of organophosphorus nerve agent simulants DIFP and DMNP.

# **List of Publications**

---





**List of Publications**

- 1) **L. Gan**, P. G. Fonquernie, M. E. Light, G. Norjmaa, G. Ujaque, D. Choquesillo-Lazarte, J. Fraile, F. Teixidor, C. Viñas and J. G. Planas, *Molecules* **2019**, *24*, 3204.
  
- 2) **L. Gan**, A. Chidambaram, P. G. Fonquernie, M. E. Light, D. Choquesillo-Lazarte, H. Huang, E. Solano, J. Fraile, C. Viñas, F. Teixidor, J. A. Navarro, K. Stylianou, J. G. Planas, *J. Am. Chem. Soc* **2020**, *142*, 8299-8311.